

# Solitons and dynamics of frequency comb formation in optical microresonators

THÈSE N° 5877 (2013)

PRÉSENTÉE LE 9 SEPTEMBRE 2013  
À LA FACULTÉ DES SCIENCES DE BASE  
LABORATOIRE DE PHOTONIQUE ET MESURES QUANTIQUES (SB/STI)  
PROGRAMME DOCTORAL EN PHOTONIQUE

ÉCOLE POLYTECHNIQUE FÉDÉRALE DE LAUSANNE

POUR L'OBTENTION DU GRADE DE DOCTEUR ÈS SCIENCES

PAR

Tobias HERR

acceptée sur proposition du jury:

Prof. T. Lasser, président du jury  
Prof. T. Kippenberg, directeur de thèse  
Prof. J. M. Dudley, rapporteur  
Prof. K. S. Eikema, rapporteur  
Prof. C. Moser, rapporteur



ÉCOLE POLYTECHNIQUE  
FÉDÉRALE DE LAUSANNE

Suisse  
2013



Meiner Familie gewidmet.



# Acknowledgements

I thank my adviser **Prof. Tobias Kippenberg** for four years of outstanding research opportunities and support. I am moreover grateful for his enthusiasm, his constant availability for discussion and the many ideas that arose as a result. In addition, I would like to thank him for the freedom and his trust when defining and designing the experiments. I genuinely enjoyed being part of his lab.

I thank **Prof. Michael Gorodetsky** who has substantially contributed to all research projects contained in this thesis. In particular I thank him for sharing his deep physical insight and brilliant ideas in countless mostly late night phone discussion (even later for the Moscow time zone). Michael is the theoretical backbone of this work.

I would also like to thank my thesis committee **Prof. John Dudley**, **Prof. Kjeld Eikema**, **Prof. Christophe Moster** and **Prof. Theo Lasser** for their interest in my work, their time and helpful comments.

I thank **Prof. Theodor Hänsch** and **Nathalie Picqué** for hosting the mid-infrared experiment at MPQ.

I thank my colleagues for their support ideas and helping me with their skills. They have significantly contributed to this thesis. It has been an honor and a great pleasure for me to work with them:

**Pascal Del'Haye** introduced me to the field of microresonator based combs and taught me many of the decisive tricks to make things work. His talent to tweak an experimental system is legendary. I enjoyed working with him in the small MPQ D.139 lab on the octave spanning spectrum and also on more creative, unofficial physics side projects. I am very happy that later on so called competing research interest could not affect our friendship.

**Johann Riemensberger** has been a constant source of ideas, which in combination with his excellent experimental skills has been a great help particular in the context of dispersion measurement and Kerr comb reconstruction. I highly value the many discussion we had when trying to understand the broad beatnote on the screen in front of us. In addition I owe thanks to Johann for carefully proof-reading my thesis and his insightful comments. Besides, I

## Acknowledgements

---

appreciate Johann's Bavarian character and our friendship.

**Klaus Hartinger** established heroically the  $\text{Si}_3\text{N}_4$  resonator platform at EPFL in many long cleanroom hours. His  $\text{Si}_3\text{N}_4$  resonators were crucial to show the platform-independence of the comb formation dynamics. Moreover, the soliton experiments benefited from his knowledge and advice in dispersion compensation.

I thank **Christine Wang** for fruitful collaboration on the mid-infrared project at MPQ and her support in  $\text{MgF}_2$  resonator fabrication.

**Victor Brasch** has contributed to the dispersion measurements in both  $\text{MgF}_2$  and  $\text{Si}_3\text{N}_4$  resonators, which are important in understanding the soliton dynamics. His instinct to question established concepts at the right point has led to very interesting and enlightening discussion particularly in the context of solitons. His comments have greatly improved this thesis. Besides work I value him as a friend and I enjoyed the many hours spent together on sailing boats, road bikes and around camp fires.

I thank **John Jost** for our very constructive and already successful work on the spectral broadening experiment. His constructive and supportive character and his experimental skills are a great enrichment for the comb team.

While not part of the comb team I would like to thank **Stefan Weis** for valuable help and advice in many technical aspects of the experiment, as well as, proof reading of this thesis. Stefan has become a close friend over the last years and I thank him for the great time we spent together in the lab, the kitchen of Estudiantines, in the mountains and on the water.

For support in the fabrication of  $\text{SiO}_2$  and  $\text{MgF}_2$  resonators I thank **Emanuel Gavartin** and **Johannes Hofer**.

I wish all the best to the current and new comb team **Victor Brasch**, **John Jost**, **Martin Pfeiffer** and **Eva-Katharina Dietsche** and thank them for proof-reading of this thesis.

In 2010 the lab moved from MPQ to EPFL into a completely empty lab. Building the new lab was only possible through a collaborative effort. I would like to thank my colleagues, particularly **Samuel Deléglise**, **Jens Dobrindt**, **Emanuel Gavartin** and **Stefan Weis** for their help during this time.

For equipment and support in the early phase of this work I thank **Ronald Holzwarth**.

I thank **Prof. Alex Gaeta** and **Reza Salem** for lending us free of charge the temporal magnifier device, which enabled a single shot characterization of the solitons.

I would like to thank **Hélène Laurens, Patricia Marti-Rochat, Christina Becker, Sabine Wirtz** and **Ainhoa Echeverria** for precious administrative support. Moreover, I would like to thank the EPFL photonics doctoral program, in particular **Prof. Olivier Martin, Cathy Buchs** and **Pierrette Paulou-Vaucher**. I would also like to thank the electrical and mechanical workshops, particularly **Helmut Brückner, Charly Linner** and **Wolfgang Simon** at MPQ, as well as **Gilles Grandjean** and **Martial Doy** at EPFL. For computing support I would like to thank **Florence Hagen**.

I would like to thank **Johannes Beck, Leonhard Neuhaus, Nicolas Piro, Rémi Rivière, Vivishek Sudhir, Ewold Verhagen, Pierre Verlot, Dalziel Wilson** and **Xiaoqing Zhou** for discussions, ideas and coffee breaks.

Last but not least I would like to thank my parents, my sister, my brother and Anne-Lise for their unconditional support far beyond the scope of this thesis.

*Lausanne, June 2013*

T. H.





# Abstract

Frequency combs, that is spectra of equidistant optical lines, are powerful tools in spectroscopy and optical frequency metrology. Conventionally, these combs are generated in mode-locked lasers, where a train of ultra-short pulses in the temporal domain corresponds to a comb spectrum in the optical frequency domain. Recently, a novel class of frequency comb generators was discovered based on parametric frequency conversion in Kerr-nonlinear high-Q microresonators. Here, a continuous wave pump laser is coupled to the microresonator and converted into hundreds of comb lines via parametric four-wave mixing. These microresonator based frequency combs are uniquely characterized by their wide mode spacing, their compactness and their independence from broadband laser gain media or saturable absorbers. Due to their distinct properties microresonators based combs hold promise for novel application including spectroscopy, telecommunications, optical waveform synthesis and microwave photonics. However, mastering the novel frequency comb technology is a challenging endeavor tightly connected to fundamental scientific question arising from the complex nonlinear dynamics of the system. After rapid initial progress the development of microresonator frequency combs had come to a halt, threatened by unexplained frequency noise questioning the applicability of microresonator based combs.

In this thesis the origin of the frequency noise is investigated based on a unique comparative approach combining experiments in three different resonator systems namely fused silica, magnesium fluoride and silicon nitride microresonators. Applying precision spectroscopy and techniques of optical frequency metrology, it is revealed that the noise is due to multiple inconsistent combs forming at the same time in the microresonator. Combining the experimental observations with a theoretical analysis we identify the ratio  $\kappa/D_2$  of resonator linewidth  $\kappa$  to anomalous resonator dispersion  $D_2$  as a critical design parameter for comb formation and hence low-noise performance of the system. For a ratio of  $\kappa/D_2 \sim 1$  low noise performance can be expected.

Having identified a regime of low noise operation, we utilize this to implement low noise frequency combs in the mid-infrared wavelength regime, which is difficult to access with conventional technology. The mid-infrared spectral range, also known as the ‘molecular fingerprint’ region is of high technological and scientific importance. We employ magnesium fluoride microresonators, which exhibit high anomalous dispersion  $D_2$  in the mid-infrared regime such that  $\kappa/D_2 \sim 1$  is achieved. We pump the microresonators with a continuous wave laser at a wavelength of 2.5 micron derived from an optical parametric oscillator. Heterodyne beatnote measurements with a second optical parametric oscillator confirm the low noise

## Acknowledgements

---

performance. The achievement of low noise frequency comb generation in the strongly anomalous dispersion demonstrates the potential of microresonator based combs for mid-infrared applications.

Regarding the temporal domain one of the most interesting question is, whether microresonator comb generators can provide ultra-short pulses, similar to conventional frequency combs. In this work we unveil experimentally and theoretically that this is indeed possible and connected to the formation of temporal dissipative cavity solitons in anomalous dispersion microresonators. This constitutes the first observation of temporal, dissipative solitons in a microresonator. The formation of solitons manifests itself as discrete state transition of the system. The solitons form spontaneously when the pump laser is scanned through the effective zero detuning point of a microcavity resonance into the red-detuned pumping regime. We develop a laser-tuning method that allows to reliably generate soliton states. The generated solitons remain stable until the pump laser is switched off. This remarkable stability despite the usually destabilizing thermal effects under red-detuned pumping conditions is explained. The number of solitons propagating inside the microresonator can be controlled by the pump laser detuning. The results are in excellent agreement with numerical simulations and soliton theory. Stable long-term operation allows continuous out-coupling of a train of femto-second pulses that corresponds to a low noise frequency comb in the spectral domain. Combs based on solitons constitute a novel method of microresonator based comb generation, qualitatively different from previous work. In particular, single soliton combs are characterized by a smooth spectral envelope, which is unprecedented in microresonator based frequency combs and essential to the envisioned application. Moreover, utilizing the ultra-short pulses we demonstrate the generation of supercontinua extending over more than two thirds of an octave, which could lead to so far unattained self-referencing of microresonator based combs.

### Keywords:

- optical frequency combs
- optical microresonators
- nonlinear optics
- mid-infrared
- temporal dissipative cavity solitons
- ultra-short optical pulses

# Zusammenfassung

Optische Frequenzkämme sind Spektren bestehend aus einer grossen Zahl an Laserlinien, die im optischen Frequenzraum äquidistant angeordnet sind. Diese Spektren haben eine zentrale Bedeutung in der optischen Präzisionsspektroskopie. Erzeugt werden Frequenzkämme normalerweise in Moden-gekoppelten Lasern, deren periodisch emittierte Pulse im Zeitbereich, einem Kamm-Spektrum im Frequenzbereich entsprechen. Eine neue Methode zur Erzeugung von Frequenzkämmen beruht auf parametrischer Frequenzumwandlung in optisch nicht-linearen Mikroresonatoren hoher Güte. Hierzu wird ein monochromatischer Laser in einen Mikroresonator eingekoppelt und dort durch Vier-Wellen-Mischen in mehrere hundert Kamm-Linien umgewandelt. Gegenüber anderen Systemen, zeichnen sich die kompakten, Mikroresonator-basierten Frequenzkämme sowohl durch einen grossen Frequenzabstand der Kammlinien, als auch durch die Unabhängigkeit von breitbandigen Laser-Verstärkungsmedien und saturierbaren Absorbern aus. Dadurch eignen sich Mikroresonator-Frequenzkämme für eine Vielzahl neuartiger Anwendungen in der Spektroskopie, der Telekommunikation, der Erzeugung optischer Signale und der Mikrowellen-Photonik. Obwohl vielversprechend, ist diese neue Technologie noch mit Schwierigkeiten behaftet. Insbesondere gibt es noch viele offene wissenschaftliche Fragen, die sich aus der komplexen nicht-linearen Dynamik des physikalischen Systems ergeben. Nach anfänglich raschem Fortschritt, hat das unerwartete und unerklärliche Auftreten von Frequenzrauschen, die prinzipielle Eignung der Mikroresonator-Technologie für die geplanten Anwendungen in Frage gestellt.

In dieser Arbeit wird der Ursprung dieses Frequenzrauschen untersucht. Diese Untersuchung basiert auf dem engen Vergleich verschiedener Mikroresonator-Systeme, die es durch ihre verschiedenen Eigenschaften ermöglichen ein Verständnis des Frequenzrauschen zu erlangen. Hierzu werden Methoden der optischen Frequenzmetrologie und Laser basierte Präzisionsspektroskopie angewandt. Dabei stellt sich heraus, dass das Auftreten von Frequenzrauschen eng verknüpft ist mit dem Ablauf der Frequenzkamm-Erzeugung. Hierbei kann es zur gleichzeitigen Ausbildung mehrerer, inkonsistenter Frequenzkämme kommen, die durch Wechselwirkung für das Frequenzrauschen verantwortlich sind. Durch experimentelle und theoretische Analyse, wird das Verhältnis  $\kappa/D_2$  von Resonanzbreite  $\kappa$  und anomaler Dispersion  $D_2$  als kritischer Design-Parameter identifiziert, der über die Rauscheigenschaften des Systems entscheidet. Für ein Verhältnis von  $\kappa/D_2 \sim 1$  wird ein nur geringes Rauschen vorhergesagt. Basierend auf dem Verständnis des Frequenzrauschen ist es möglich Frequenzkämme mit geringem Frequenzrauschen im mittleren Infrarot Spektralbereich zu erzeugen. Hierzu werden Mikroresonatoren aus Magnesiumfluorid verwendet, die sich durch eine hohe Disper-

## Acknowledgements

---

sion  $D_2$  im mittleren Infraroten auszeichnen. Dadurch ergibt sich ein Verhältnis  $\kappa/D_2 \sim 1$ . In Verbindung mit einem optischen parametrischen Oszillator der als Laserquelle dient, gelingt es Frequenzkämme bei einer Wellenlänge von etwa  $2.5 \mu\text{m}$  zu erzeugen. Wie erwartet weisen die so erzeugten Frequenzkämme nur geringes Frequenzrauschen auf. Letzteres wird durch eine Heterodyn-Messung mit einem zweiten optischen parametrischen Oszillator nachgewiesen. Dieses Ergebnis zeigt, dass sich Mikroresonatoren gut eignen, um Frequenzkämme im wichtigen, aber nur schwer zugänglichen mittleren Infrarot, zur Verfügung zu stellen. Eine der interessantesten Fragen im Bereich der Mikroresonatorkämme ist die nach der direkten Erzeugung von optischen Pulsen im Mikroresonator, vergleichbar mit konventionellen Frequenzkämmen. Die vorliegende Arbeit zeigt, dass dies in der Tat möglich ist durch die Bildung von zeitlichen, dissipativen Solitonen im anormalen Dispersionsbereich des Mikroresonators. Dies stellt die erste Beobachtung von zeitlichen, dissipativen Solitonen in Mikroresonatoren dar. Ein oder mehrere Solitonen bilden sich spontan, wenn die Laserquelle mit einer zeitlich abnehmenden optischen Frequenz die effektive Resonanzfrequenz des Mikroresonators durchschreitet, was zu einem effektiv rot-verstimmten Laser führt. Durch eine spezielle Methode, bei der die optische Frequenz des Lasers, gezielt verändert wird, ist es möglich stabile Solitonen-Zustände zu erreichen. Diese bleiben erhalten bis der Laser ausgeschaltet wird. Die überraschende Stabilität der Solitonen bei rot-verstimmten Laser wird erklärt. Die Anzahl der Solitonen lässt sich durch die optische Laserfrequenz bestimmen. Die experimentellen Beobachtungen stimmen hervorragend mit numerischen Simulationen und analytischer Theorie überein. Die Langzeitstabilität der Solitonen ermöglicht es, kontinuierlich periodisch wiederkehrende Femto-Sekunden Pulse, die einem Frequenzkamm entsprechen, aus dem Mikroresonator auszukoppeln. Die Erzeugung von Frequenzkämmen über Solitonen-Zustände ist qualitativ verschieden vom bisherigen Ansatz zur Erzeugung von Frequenzkämmen in Mikroresonatoren. Wenn nur ein einziges Soliton im Resonator umläuft, besitzt der erzeugte Frequenzkamm eine glatte spektrale Intensitätsverteilung, die bisher im Bereich der Mikroresonatorkämme nicht erreicht werden konnte. Die spektrale Glattheit ist von essentieller Bedeutung für die Anwendungen Mikroresonator-basierter Frequenzkämme. Die Erzeugung ultra-kurzer Pulse erlaubt es, das optische Kamm-Spektrum in einer hoch nicht-linearen Faser zu mehr als zwei Dritteln einer Oktave zu verbreitern. Letzteres eröffnet neue Möglichkeiten zur bisher unerreichten Selbstreferenzierung von Mikroresonator-Frequenzkämmen.

### Schlüsselwörter:

- optischer Frequenzkamm
- optischer Mikroresonator
- nicht-lineare Optik
- mittleres Infrarot
- zeitlich, dissipative Resonator Solitonen
- ultra-kurze optische Pulse

# List of publications

- <sup>1</sup> Tobias Herr, Victor Brasch, John D. Jost, Christine Y. Wang, Nikita M. Kondratiev, Michael L. Gorodetsky and Tobias J. Kippenberg. “Temporal soliton formation in optical microresonators.”, *submitted*, partly published as arXiv 1211.0733.
- <sup>2</sup> Christine Y. Wang\*, Tobias Herr\*, Pascal Del’Haye, Albert Schliesser, Johannes Hofer, Ronald Holzwarth, Theodor W. Hänsch, Nathalie Picqué and Tobias J. Kippenberg. “Mid-infrared optical frequency combs based on crystalline microresonators.”, *Nature Communications* **4**, 1345 (2013).
- <sup>3</sup> Tobias Herr, Klaus Hartinger, Johann Riemensberger, Christine Y. Wang, Emanuel Gavartin, Ronald Holzwarth, Michael L. Gorodetsky and Tobias J. Kippenberg. “Universal formation dynamics and noise of Kerr-frequency combs in microresonators.”, *Nature Photonics* **6**, 480-487 (2012).
- <sup>4</sup> Johann Riemensberger, Klaus Hartinger, Tobias Herr, Victor Brasch, Ronald Holzwarth and Tobias J. Kippenberg. “Dispersion engineered high-Q silicon nitride ring-resonators via atomic layer deposition.”, *Optics Express* **20**, 25, 27661-27669 (2012).
- <sup>5</sup> Pascal Del’Haye\*, Tobias Herr\*, Emanuel Gavartin, Michael L. Gorodetsky, Ronald Holzwarth and Tobias J. Kippenberg. “Octave spanning tunable frequency comb from a microresonator.”, *Physical Review Letters* **107**, 063901 (2011).

---

\*These authors contributed equally to this work.



# List of presentations

In 2013:

- **Nonlinear Optics Conference (NLO), Kohala Coast, Hawaii, USA, 21-26 July 2013 (invited)**  
Tobias Herr, Victor Brasch, John D. Jost, Christine Y. Wang, Nikita M. Kondratiev, Michael L. Gorodetsky and Tobias J. Kippenberg.  
“Mode-locking via soliton formation in optical microresonators”
- **International Frequency Control Symposium (IFCS) and European Frequency and Time Forum (EFTF), Prague, Czech Republic, 21-25 July 2013 (invited)**  
Tobias Herr, Victor Brasch, John D. Jost, Christine Y. Wang, Nikita M. Kondratiev, Michael L. Gorodetsky and Tobias J. Kippenberg.  
“Mode-locking via soliton formation in optical microresonators”
- **Cavity Enhanced Spectroscopy Meeting (CES2013), Naples, Italy, 10-13 June 2013 (invited)**  
Tobias Herr, Victor Brasch, John D. Jost, Christine Y. Wang, Nikita M. Kondratiev, Michael L. Gorodetsky and Tobias J. Kippenberg.  
“Microresonator frequency combs and soliton generation”
- **Space optical clocks meeting (SOC2), Birmingham, United Kingdom, 27-28 May 2013**  
Tobias Herr, Victor Brasch, Klaus Hartinger, Johann Riemensberger, John D. Jost, Christine Y. Wang, Nikita M. Kondratiev, Michael L. Gorodetsky and Tobias J. Kippenberg.  
“Phase noise in microresonator based combs”
- **CLEO/Europe - IQEC, Munich, Germany, 12-16 May 2013**  
Tobias Herr, John D. Jost, Victor Brasch, Christine Y. Wang, Nikita M. Kondratiev,

## Acknowledgements

---

Michael L. Gorodetsky and Tobias J. Kippenberg.

“Spectral broadening of microresonator combs for self-referencing”

- **CLEO/Europe - IQEC, Munich, Germany, 12-16 May 2013**

Tobias Herr, Victor Brasch, John D. Jost, Christine Y. Wang, Nikita M. Kondratiev, Michael L. Gorodetsky and Tobias J. Kippenberg.

“Mode-locking via soliton formation in optical microresonators”

- **CLEO/Europe - IQEC, Munich, Germany, 12-16 May 2013**

Christine Y. Wang, Tobias Herr, Pascal Del’Haye, Albert Schliesser, Johannes Hofer, Ronald Holzwarth, Theodor W. Hänsch, Nathalie Picqué and Tobias J. Kippenberg.

“Low phase noise mid-infrared frequency combs based on microresonators”

- **Quantum assisted readout and sensing meeting (DARPA/QuASAR), Boulder, USA, 5-6 March 2013**

Tobias Herr, Victor Brasch, John D. Jost, Christine Y. Wang, Nikita M. Kondratiev, Michael L. Gorodetsky and Tobias J. Kippenberg.

“Mode-locking via soliton formation in optical microresonators”

In 2012:

- **CLEO/QELS, San Jose, CA, USA, 6-11 May 2012**

Tobias Herr, Klaus Hartinger, J. Riemensberger, Christine Y. Wang, Emanuel Gavartin, Ronald Holzwarth, Michael L. Gorodetsky and Tobias J. Kippenberg.

"Universal Dynamics of Kerr-Frequency Comb Formation in Micro-Resonators"

- **DPG Spring Meeting, Stuttgart, Germany, 12-16 March 2012**

Tobias Herr, Klaus Hartinger, J. Riemensberger, Christine Y. Wang, Emanuel Gavartin, Ronald Holzwarth, Michael L. Gorodetsky and Tobias J. Kippenberg.

"Universal Dynamics of Kerr-Frequency Comb Formation in Micro-Resonators"

- **Quantum assisted readout and sensing meeting (DARPA/QuASAR), Boulder, USA, 23-24 February 2012**

Tobias Herr, Klaus Hartinger, J. Riemensberger, Christine Y. Wang, Emanuel Gavartin, Ronald Holzwarth, Michael L. Gorodetsky and Tobias J. Kippenberg.

"Microresonator based Kerr-frequency combs"

In 2011:

- **CLEO/Europe - IQEC, Munich, Germany, 22-26 May 2011**

Tobias Herr, Christine Y. Wang, Pascal Del’Haye, Klaus Hartinger, Ronald Holzwarth and Tobias J. Kippenberg.

“Frequency Comb Generation in Crystalline MgF<sub>2</sub> Whispering-Gallery Mode Resonators”



- **CLEO/QELS, Baltimore, Maryland, USA, 1-6 May 2011**

Tobias Herr, Christine Y. Wang, Pascal Del'Haye, Klaus Hartinger, Ronald Holzwarth and Tobias J. Kippenberg.

"Frequency Comb Generation in Crystalline MgF<sub>2</sub> Whispering-Gallery Mode Resonators"

- **DPG Spring Meeting, Dresden, 13-18 March 2011**

Tobias Herr, Christine Y. Wang, Pascal Del'Haye, Klaus Hartinger, Ronald Holzwarth and Tobias J. Kippenberg.

"Frequency Comb Generation in Crystalline Whispering-Gallery Mode Resonators"

In 2010:

- **DPG Spring Meeting, Hannover, Germany, 8-12 March 2010**

Pascal Del'Haye, Tobias Herr, Albert Schliesser, Ronald Holzwarth and Tobias J. Kippenberg.

"Octave spanning frequency comb on a chip"



# Contents

<b>Acknowledgements</b>	<b>v</b>
<b>Abstract (English/Deutsch)</b>	<b>ix</b>
<b>List of Publications</b>	<b>xiii</b>
<b>List of Presentations</b>	<b>xv</b>
<b>1 Microresonator based optical frequency combs</b>	<b>1</b>
1.1 Optical frequency combs . . . . .	2
1.1.1 Application of frequency combs . . . . .	3
1.1.2 Generation of optical frequency combs in mode-locked lasers . . . . .	3
1.1.3 Self-referencing and stabilization of optical frequency combs . . . . .	4
1.2 Dielectric nonlinear microresonators . . . . .	6
1.2.1 Basic microresonator characteristics . . . . .	6
1.2.2 Microresonators used in this work . . . . .	12
1.3 Microresonator based optical frequency combs . . . . .	16
1.3.1 Application of microresonator based combs . . . . .	17
1.3.2 Kerr-nonlinearity and nonlinear parametric frequency conversion . . . . .	18
1.3.3 Thermal and Kerr-nonlinearity resonance shift and related concepts . . . . .	22
1.3.4 Frequency comb generation via four-wave mixing . . . . .	26
1.3.5 Competing non-linear processes . . . . .	31
1.3.6 Setup for frequency comb generation . . . . .	33
1.3.7 State-of-the-art in microresonator based frequency combs . . . . .	33
<b>2 Formation dynamics and noise in microresonator based frequency combs</b>	<b>39</b>
2.1 Noise in broadband spectra with many comb lines . . . . .	40
2.1.1 Generation of an octave-spanning spectrum in a SiO <sub>2</sub> toroid . . . . .	40
2.1.2 Characterization of frequency noise in microresonator based combs . . . . .	43
2.1.3 Observation of noise in a SiO <sub>2</sub> toroid . . . . .	44
2.1.4 The universal problem of noise in microresonator based combs . . . . .	46
2.1.5 Linking microresonator based comb formation dynamics and noise . . . . .	47

## Contents

---

2.2	Microresonator based comb formation . . . . .	49
2.2.1	Generation of subcombs . . . . .	49
2.2.2	Commensurability of subcombs . . . . .	50
2.3	Emergence of noise in microresonator based combs . . . . .	56
2.3.1	Multiple and broad RF beatnotes . . . . .	56
2.3.2	Intensity noise at low-frequencies . . . . .	57
2.3.3	Line-by-Line reconstruction of microresonator combs . . . . .	60
2.4	Transition to low noise . . . . .	62
2.4.1	The role of dispersion and resonance width . . . . .	63
2.5	Discussion and conclusion . . . . .	64
<b>3</b>	<b>Mid-infrared frequency combs based on microresonators</b>	<b>67</b>
3.1	The mid-infrared regime . . . . .	67
3.2	Microresonator based mid-infrared combs . . . . .	68
3.2.1	Crystalline magnesium fluoride as a resonator material for the mid-infrared . . . . .	68
3.2.2	Generation of mid-infrared frequency comb . . . . .	70
3.2.3	Phase-noise characterization . . . . .	73
3.2.4	Proof-of-principle direct comb spectroscopy experiment . . . . .	75
3.3	Discussion and conclusion . . . . .	76
<b>4</b>	<b>Temporal soliton formation in microresonators</b>	<b>79</b>
4.1	Temporal dissipative Kerr-cavity solitons . . . . .	80
4.2	Evidence of soliton formation in a microresonator . . . . .	80
4.2.1	Microresonator characteristics . . . . .	81
4.2.2	Kerr-nonlinear and thermal resonance shifts and stability . . . . .	82
4.2.3	Observation of discrete steps in the resonator transmission . . . . .	83
4.3	Theoretical description of temporal dissipative solitons in microresonators . . . . .	85
4.3.1	Numerical simulation . . . . .	85
4.3.2	Analytic description . . . . .	86
4.4	Experimental generation of temporal dissipative solitons in a microresonator . . . . .	89
4.4.1	Laser tuning method . . . . .	89
4.4.2	Stability of the soliton states . . . . .	91
4.4.3	Spectral and temporal characterization . . . . .	92
4.5	Resonator mode structure and soliton formation . . . . .	97
4.5.1	Global mode structure . . . . .	97
4.6	Detailed investigation of selected mode families . . . . .	99
4.7	Spectral broadening and supercontinuum generation . . . . .	102
4.8	Discussion and conclusion . . . . .	106
<b>5</b>	<b>Outlook</b>	<b>109</b>

<b>A</b>	<b>Theory of microresonator based frequency comb generation</b>	<b>111</b>
A.1	Optical coupling to microresonators . . . . .	111
A.2	Frequency comb formation in microresonators . . . . .	113
A.2.1	Nonlinear coupled mode equations . . . . .	113
A.2.2	Three mode system . . . . .	115
A.2.3	Nonlinear resonance shift, effective detuning and optical bistability . . . . .	116
A.2.4	Threshold pump power . . . . .	118
A.2.5	Emergence of the first mode . . . . .	118
A.2.6	Emergence of secondary comb lines . . . . .	119
<b>B</b>	<b>Noise consideration in a SiO<sub>2</sub> toroid</b>	<b>123</b>
<b>C</b>	<b>Theory of temporal dissipative solitons in microresonators</b>	<b>129</b>
C.1	Analytical description of solitons in a microresonators . . . . .	129
C.2	Limit conditions for solitons in microresonators . . . . .	131
C.3	Analytical description of steps in the intracavity power . . . . .	132
C.4	Optical spectrum and temporal width of solitons in a microresonator .	132
C.5	Soliton mode-locking in lasers vs. soliton formation in microresonators	133
<b>D</b>	<b>Experimental methods</b>	<b>135</b>
D.1	Frequency comb calibrated broadband laser scan . . . . .	135
D.1.1	Setup and principle . . . . .	135
D.1.2	Data post-processing . . . . .	136
D.1.3	Limitation of the method . . . . .	139
D.1.4	Measurement of resonator dispersion and comb reconstruction	139
D.2	Measurement of microcavity resonance width . . . . .	141
	<b>Bibliography</b>	<b>142</b>
	<b>Curriculum vitae</b>	<b>159</b>



# 1 Microresonator based optical frequency combs

Microresonator based optical frequency combs represent an alternative approach to conventional frequency comb generation. The high light intensities achievable in high quality factor (Q factor) microresonators in conjunction with the  $\chi^{(3)}$ -Kerr nonlinearity of the resonator material enable efficient nonlinear parametric frequency conversion processes such as four-wave mixing (FWM). When driven by a monochromatic continuous wave (cw) pump laser cascaded FWM can give rise to hundreds of new optical lines that are equidistantly spaced in frequency. Together with the pump laser, these new optical frequencies can constitute a frequency comb.

Microresonator based frequency combs have unique properties that distinguish them from conventional frequency combs. Most prominently, the comb line spacing, which is inversely proportional to the size of the resonator, is much higher when compared to conventional frequency combs. This feature enables novel applications that are difficult to implement with conventional frequency comb technology. The compact, monolithic geometry and demonstrated chip-scale integration of microresonators could allow for a widespread use in applications where robustness, size and cost matter. Microresonator based frequency combs are often referred to as “Kerr-combs”, but also other terms such as “micro-combs” are common.

This introductory chapter provides an overview of microresonator based frequency combs and the most relevant physical and methodological concepts in this context. The first Section 1.1 introduces optical frequency combs and highlights a few of their ubiquitous time and frequency applications. Section 1.2 introduces nonlinear dielectric microresonators (or synonymously microcavities) that enable frequency comb generation via cascaded four-wave mixing. The process of microresonator based frequency comb generation, as well as specific applications and state-of-the-art of microresonator based frequency combs are presented in Section 1.3.

## 1.1 Optical frequency combs

Optical frequency combs<sup>6-11</sup> essentially are spectra of discrete laser lines that are equidistantly spaced in optical frequency and mutually coherent. What may seem unspectacular at first, has revolutionized optical frequency metrology and precision spectroscopy. In 2005, the Nobel Prize in physics was awarded to J. L. Hall and T. W. Hänsch for their work on precision spectroscopy and particularly the invention of frequency combs.

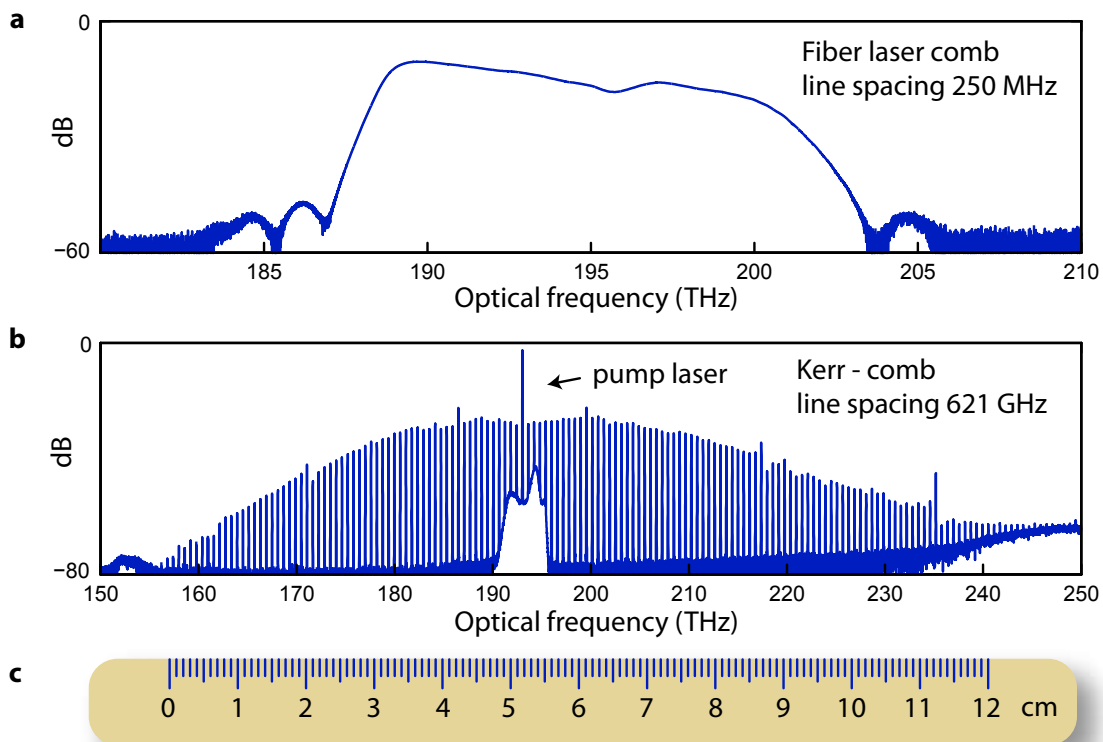


**Figure 1.1: Optical Frequency combs.** Optical Frequency combs are spectra of discrete and equidistant laser lines. **a.** Optical spectrum of a conventional fiber laser based frequency comb (mode-locked erbium fiber laser, amplified and broadened) recorded using an optical spectrum analyzer. The densely spaced lines can not be resolved in this measurement. **b.** Microresonator based “Kerr-comb” generated in a  $\text{Si}_3\text{N}_4$  microresonator, where a pump laser is converted into equidistant sidebands via nonlinear parametric frequency conversion. As the comb line spacing scales inversely with the size of the resonator the line spacing of the microresonator based combs is generally much wider compared to conventional combs. **c.** Frequency combs can be thought of as precise rulers in the optical frequency domain. Like a usual ruler allows to measure distances or length of objects, a frequency comb allows to measure optical frequencies or differences between optical frequencies.



### 1.1.1 Application of frequency combs

As will be detailed in Section 1.1.3 frequency combs provide a link from the optical to the radio-frequency (RF) domain<sup>6,7,10-12</sup> and consequently enable unprecedented precise and absolute measurements of optical frequencies. In this way frequency combs serve as frequency gear-boxes in the most accurate and precise clocks that are based on optical atomic (or even nuclear) transitions.<sup>13-15</sup> Such frequency standards are foreseen to replace the current Cesium-based definition of the second in the future.<sup>16</sup> As absolute optical frequency references, frequency combs are used in precision spectroscopy including the search for minuscule changes in the fundamental physical constants over time.<sup>17-19</sup> In astrophysical spectroscopy frequency combs are enabling tools in the detection of earth-like planets and may allow for the first direct measurement of the universe's expansion rate without relying on a cosmological model.<sup>20-23</sup> More down to Earth, frequency combs enable novel spectroscopy techniques<sup>24-30</sup> from ultra-violet<sup>31-34</sup> to mid-infrared wavelength.<sup>24</sup> Moreover, frequency combs can be used for remote sensing<sup>35</sup> and rapid absolute measurements of distance.<sup>36</sup> Optical frequency combs also bear significant potential in multiplying the capacity of current telecommunication networks,<sup>37</sup> where each comb line can serve as an individual telecommunication channel. In the RF domain optical frequency combs serve as a source of low noise signals resulting from the beating between the comb lines.<sup>38</sup> Likewise important are time domain applications of frequency combs where the equidistant frequency comb spectrum can correspond to a train of ultra-short optical pulses,<sup>39-41</sup> when all line phases are synchronized. These pulses enable analysis of chemical reaction pathways on femto-second time scales<sup>42</sup> (Nobel Prize in Chemistry 1999, A. H. Zewail) and find use in medical applications such as corneal surgery.<sup>43</sup> Moreover, line-by-line phase and intensity adjustments enable the synthesis of complex optical waveforms.<sup>44</sup>

### 1.1.2 Generation of optical frequency combs in mode-locked lasers

Optical frequency combs are conventionally generated in passively mode-locked lasers<sup>39-41,45</sup> where an ultra-short optical pulse is propagating inside the laser cavity with a roundtrip time of  $T_R$ . A mode-locked laser typically comprises a cavity containing a pumped gain medium and a saturable absorber (or equivalent element). The saturable absorber is in many cases responsible for pulse shaping and always required for stable operation of the system.<sup>46-52</sup> The light out-coupled from the laser cavity forms a train of optical pulses that are each separated in time by  $T_R$  from the previous pulse. From one pulse to the other the electric field acquires a so called carrier-envelope phase  $\Delta\phi_0$  with respect to the pulse envelope in the rotating carrier frame (cf. Figure 1.2a).

The optical spectrum that corresponds to the pulse train can be found via Fourier-transformation: The pulse train of equidistant pulses in the time domain corresponds to spectral lines that are equidistant in the frequency domain forming a comb (cf. Figure 1.2b). The pulse repetition rate  $f_{\text{rep}} = T_{\text{R}}^{-1}$  is equal to the frequency spacing of the comb lines. All optical frequencies  $\nu_m$  defining the comb can thus be written as an integer  $m$  multiple of the repetition rate  $f_{\text{rep}}$  plus an offset frequency  $f_0$ :

$$\nu_m = m \cdot f_{\text{rep}} + f_0 \quad (1.1)$$

The offset frequency  $f_0$  can be interpreted as the virtual first comb line when extending the grid of comb lines towards zero frequency. It is related to the difference of the carrier-envelope phase  $\Delta\phi_0$  between subsequent pulses via  $f_0 = f_{\text{rep}} \Delta\phi_0 / (2\pi)$ .<sup>10</sup> As a consequence,  $f_0$  is usually referred to as carrier envelope offset frequency.

For typical conventional frequency comb systems  $f_{\text{rep}}$  is on the order of 10 MHz up to several GHz.<sup>53–56</sup>

### 1.1.3 Self-referencing and stabilization of optical frequency combs

Opposed to optical frequencies on the order of several hundreds of THz, the two frequencies  $f_{\text{rep}}$  and  $f_0$ , which fully define the comb are in the RF domain. Once detected these RF signals can be very precisely measured using electronic RF counters. The absolute precision of the optical frequency measurement is equal to the absolute precision of the RF counting and a coherent RF-to-optical link is established via eq. (1.1). The relative precision of the optical frequencies is enhanced by several orders of magnitude over the RF measurement. The measurement of  $f_{\text{rep}}$  is straightforward. Detecting the comb spectrum on a sufficiently fast photodetector will result in an RF signal at the frequency of  $f_{\text{rep}}$ , which can be understood as a coherent beating between all pairs of adjacent comb lines. The measurement of  $f_0$  is more challenging. The most common method, the so called  $f$ - $2f$ -scheme (cf. Figure 1.2c),<sup>6,7,10–12</sup> requires an octave spanning spectrum, that is a spectrum that spans more than a factor of two in optical frequency. Here, the lower part of the spectrum is sent through a nonlinear crystal for second-harmonic and sum frequency generation (SHG and SFG), which transfers the original comb spectrum  $\nu_n = f_0 + n f_{\text{rep}}$  to approximately doubled optical frequency  $\nu^m \text{ at } m\text{SHG/SFG}_m = 2f_0 + m f_{\text{rep}}$ . Combining the doubled spectrum with the high frequency portion of the original spectrum creates a beatnote with frequency  $f_0$  (cf. Figure 1.2). The requirement of octave spectral span may be relaxed to, for example, two thirds of an octave, when employing a  $2f$ - $3f$ -scheme that works in analogous fashion. Indeed, the practical criterion whether a spectrum can be called for example octave-spanning or not, is usually linked to the ability of generating sufficient power in the doubled comb component to allow detection and locking of the

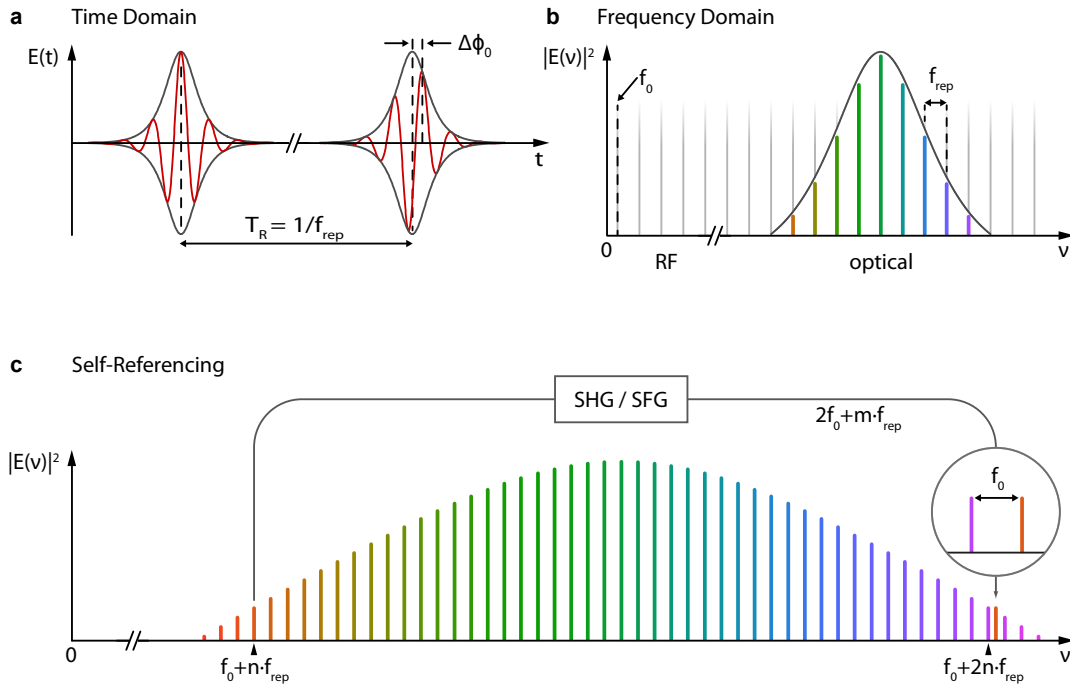


**Figure 1.2: Frequency combs from a pulse train and self-referencing:** **a.** Pulse train as generated in a mode-locked laser. The pulses are separated by the laser cavity roundtrip time  $T_R$ , which corresponds to a pulse repetition rate of  $f_{rep}$ . The red line indicates the electric field strength  $E(t)$  and the dark grey line marks the pulse envelope. From one pulse to the other the electric field is phase-shifted with respect to the pulse envelope by the carrier-envelope offset phase  $\Delta\phi_0$ . **b.** In the frequency domain the pulse train in (a) corresponds to a frequency comb spectrum where the equidistant lines are spaced by the pulse repetition rate frequency  $f_{rep}$ . The carrier envelope offset frequency  $f_0$ , that is the frequency of the virtual first comb line, is related to  $\Delta\phi_0$  via  $f_0 = f_{rep} \Delta\phi / (2\pi)$ . **c.** A common method to achieve self-referencing of a frequency comb is the  $f$ - $2f$  scheme. This scheme can be applied in octave spanning spectra, that is spectra that span at least a factor of two in optical frequency. While the original spectrum of the mode-locked lasers is typically much narrower than an octave, the ultra-short pulses in combination with external nonlinear broadening have enabled octave spanning spectra.<sup>6-8,57-59</sup> In the  $f$ - $2f$  scheme a lower frequency portion of the comb  $f_0 + n \cdot f_{rep}$  is transferred to the approximately doubled optical frequency  $2f_0 + m \cdot f_{rep}$  via second harmonic and sum frequency generation (SHG and SFG) and combined with the high frequency portion of the original comb component. The difference frequency between the doubled comb and the original high frequency comb components is equal to  $f_0$  and can be detected as a beatnote at frequency  $f_0$ .

$f_0$  beatnote.<sup>11</sup> This criterion may be met even with the relevant lines of the frequency comb being 40 dB below the spectral peak intensity.<sup>11</sup> If  $f_{\text{rep}}$  and  $f_0$  can be measured for a comb spectrum the comb may be called self-referenced as it provides (based on an underlying RF standard) a self-contained, absolute optical frequency reference. Important for many applications is a frequency stable comb spectrum. This can be achieved by continuously monitoring and stabilizing  $f_{\text{rep}}$  and  $f_0$  by feeding back onto the laser system. To this end, at least two laser parameters, such as pump current and cavity length, need to be controlled to stabilize the two independent parameters  $f_{\text{rep}}$  and  $f_0$ . However, not all applications require a fully self-referenced and stabilized comb.

### 1.2 Dielectric nonlinear microresonators

All microresonators in the context of frequency comb generation are dielectric microresonators<sup>60</sup> where the optical mode is confined inside a dielectric material with a higher refractive index  $n$  compared to its surrounding material by total internal reflection. The light is propagating on a closed trajectory along the circumference of the resonator. Even though very similar, one can distinguish between whispering gallery mode resonators<sup>60–64</sup> and waveguide resonators.<sup>65–67</sup> In the first case the light is kept on a circular trajectory along the circumference of the resonator. In the second case the light is confined and guided along a not necessarily circular waveguide geometry. Figure 1.3 illustrates both types of resonators. There is a wide variety of microresonator types used for frequency comb generation and related research. This variety includes crystalline resonators,<sup>64,68,69</sup> fused silica microtoroids<sup>70–72</sup> CMOS compatible high-index silica-glass<sup>73</sup> and  $\text{Si}_3\text{N}_4$  waveguide resonators,<sup>67,74,75</sup> as well as, compact fiber cavities<sup>76</sup> and microspheres.<sup>77</sup> Figure 1.4 shows a selection of microresonators that can be used for comb generation. In the present work, three different microresonator platforms have been used. These systems are fused silica microtoroids, crystalline magnesium fluoride resonators and planar silicon nitride resonators. Before these three systems will be introduced in Section 1.2.2, the basic characteristics and properties of dielectric microresonators are summarized in the next Section 1.2.1.

#### 1.2.1 Basic microresonator characteristics

This section introduces the basic resonator characteristics and symbols that will be used throughout this thesis:

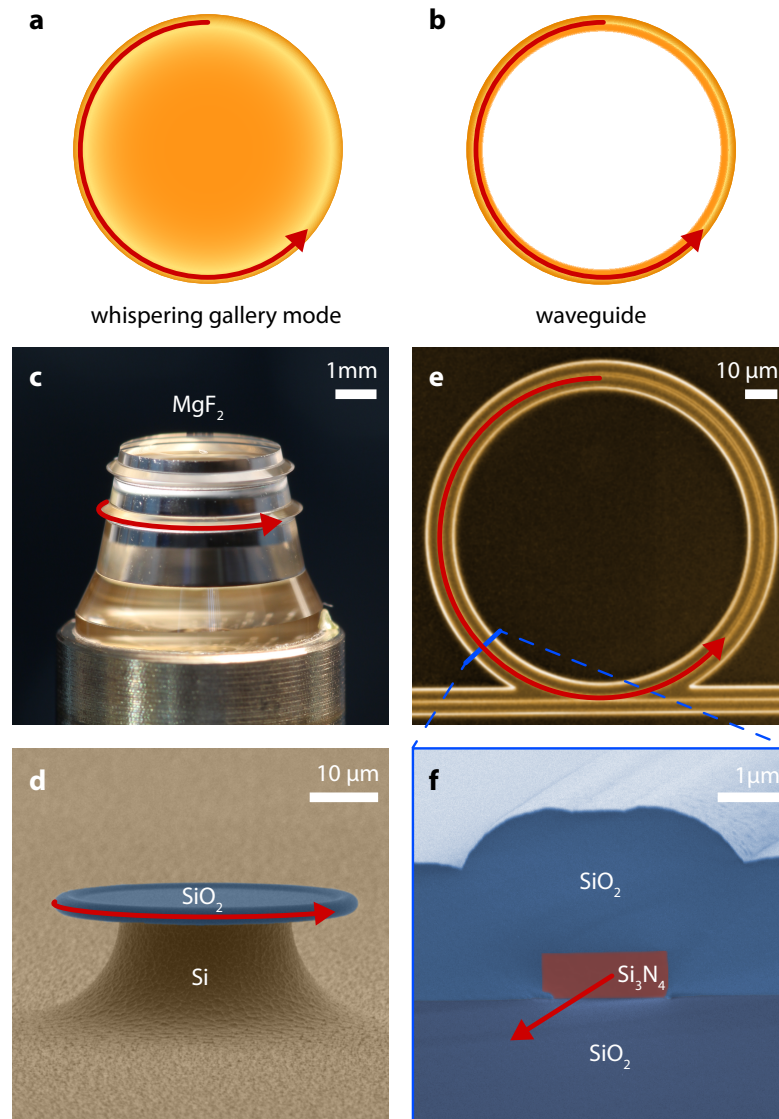


**Figure 1.3: Dielectric microresonators** defined by a material of higher refractive index  $n_0$  compared to the surrounding material. The light trajectory is indicated by red arrows. **a.** Whispering gallery mode resonator: The optical mode is guided inside the outer circumference of the resonator. **b.** Waveguide resonator: The mode is confined to a high refractive index waveguide. **c.** Example of a whispering gallery mode resonator made of magnesium fluoride ( $\text{MgF}_2$ ). The monolithic sample holds two resonators with different circumference (the red arrow indicates the light trajectory in the lower resonator). **d.** Example of a fused silica ( $\text{SiO}_2$ ) toroidal microresonator on top of a silicon ( $\text{Si}$ ) pedestal. **e.** Example of a waveguide resonator made of silicon nitride ( $\text{Si}_3\text{N}_4$ ). The straight waveguide at the bottom does not form part of the resonator and is used to couple light in and out of the resonator. **f.** Cross-section of a resonator waveguide similar to (c) showing the  $\text{SiO}_2$  substrate and cladding surrounding the  $\text{Si}_3\text{N}_4$  waveguide.

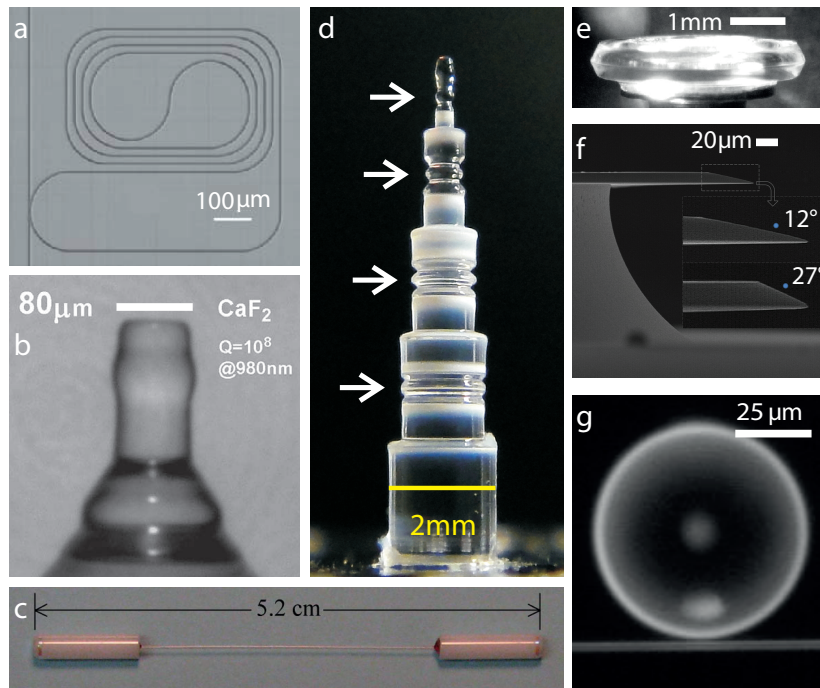


**Figure 1.4: Variety of microresonators for comb generation.** **a**  $\text{Si}_3\text{N}_4$  waveguide resonator. The resonator geometry does not need to be circular.<sup>78</sup> **b** Crystalline  $\text{CaF}_2$  resonator with a diameter of only  $80 \mu\text{m}$ .<sup>64</sup> **c** Compact highly nonlinear fiber cavity with reflective ends.<sup>76</sup> **d** Fused silica resonators (white arrows) that can be fabricated within a few minutes using  $\text{CO}_2$  laser machining.<sup>79</sup> **e**  $\text{MgF}_2$  resonator with a sharp edge to influence dispersion.<sup>80</sup> **f** Fused silica disk resonator with controllable wedge angle that can be fabricated with diameters reaching the centimeter-scale.<sup>81</sup> **g** Fused silica microsphere with a diameter of  $70 \mu\text{m}$  fabricated by melting the tip of a standard single-mode fiber<sup>82</sup>

### Resonance frequencies

The resonance frequencies  $\omega_m$  of an optical resonator are related to the light roundtrip time  $T_R = nL/c$ , where  $n$  denotes the refractive index of the resonator,  $L$  the roundtrip length of the light inside the resonator and  $c$  the speed of light:

$$\omega_m = m 2\pi T_R^{-1} \quad (1.2)$$

Here, the mode number  $m$  is used to index the resonance frequencies  $\omega_m$  of one mode family. Note that due to material and geometrical dispersion the refractive index  $n_0$  as well as the roundtrip length  $L$  are generally dependent on the frequency of  $\omega_m$ . The difference between two adjacent resonances of the same mode family is called free spectral range (FSR) and is equal to the inverse cavity roundtrip time:

$$\text{FSR} = T_R^{-1} \quad (1.3)$$

For frequency comb generation a particular mode with high mode number on the order of  $m \sim 10^2$  to  $10^4$  is excited by an external cw pump laser (cf. Section 1.3.4). It is therefore convenient to switch from the absolute mode number  $m$  to the relative mode number  $\mu$  defined as  $\mu = 0$  for the externally pumped mode.

### Microresonator dispersion

The dispersion of a microresonator is determined by the combined effect of material dispersion and geometrical dispersion.<sup>80,83,84</sup> The material dispersion describes the frequency dependence of the refractive index  $n_0$ . Effects due to the geometric mode profile inside the resonator are called geometrical dispersion. These geometric effects include a mode profile dependent roundtrip length  $L$  and an effectively reduced refractive index due to the evanescent component of the optical mode experiencing a lower refractive index outside of the resonator material. The total microresonator dispersion can be measured as the deviation  $\Delta_\omega(\mu)$  of the resonance frequencies from equidistance. With the above definition of the relative mode number  $\mu$  the resonance frequencies  $\omega_\mu$  in the spectral region of the pump laser frequency  $\omega_p \approx \omega_0$  can be written as<sup>3</sup>

$$\omega_\mu = \omega_0 + D_1 \mu + \frac{1}{2} D_2 \mu^2 + \frac{1}{6} D_3 \mu^3 + \dots \quad (1.4)$$

The FSR at the expansion frequency corresponds to  $D_1/2\pi$  and the parameters  $D_2$  and  $D_3$  describe second and third order dispersion. The parameter  $D_2$  corresponds to the difference between the two FSRs adjacent to the mode  $\omega_0$ . For  $D_2 > 0$  (and  $D_2 \gg D_i$ ,  $i = 3, 4, \dots$ ) the dispersion is called anomalous (normal in case of  $D_2 < 0$ ). Consequently, the deviation  $\Delta_\omega(\mu)$  of the resonance frequencies from equidistance

can be defined as

$$\Delta_\omega(\mu) = \omega_\mu - \omega_0 - D_1 \mu = \frac{1}{2} D_2 \mu^2 + \frac{1}{6} D_3 \mu^3 + \dots \quad (1.5)$$

The dispersion parameter  $D_2$  is directly related to the group velocity dispersion  $\beta_2$  (GVD)<sup>85</sup>:

$$\beta_2 = -\frac{n D_2}{c D_1^2} \quad (1.6)$$

The dispersion of a microresonator has decisive influence on the frequency comb generation (cf. Section 1.3.4). In particular, the bandwidth of the generated spectra and the noise properties of the combs (cf. Chapter 2), as well as the possibility of soliton pulse formation inside the resonator (cf. Chapter 4) are affected by the resonator's dispersion.

### Optical resonance width

Each optical resonance with frequency  $\omega_\mu$  has a certain (line)width  $\kappa$  given by the cavity decay rate. The cavity decay rate  $\kappa = \kappa_0 + \kappa_{\text{ext}}$  includes the internal loss rate  $\kappa_0$  and the coupling rate to the external waveguide  $\kappa_{\text{ext}}$  (cf. Section 1.3.6). The internal loss rate  $\kappa_0$  combines various resonator loss mechanisms such as absorption inside the resonator bulk and surrounding material, scattering losses due to surface and material imperfections and bending losses. Moreover, losses due to phonon-photon coupling and non-linear parametric frequency conversion may contribute. The parameter  $\eta = \kappa_{\text{ext}}/\kappa$  is called coupling efficiency. Experimentally the coupling rate  $\kappa_{\text{ext}}$  can be adjusted by changing the distance between coupling waveguide and resonator, which affects the overlap of evanescent resonator and waveguide modes. The combined value of  $\kappa$  describes the decay of the energy stored in the resonator  $E_{\text{cav}}$  according to

$$E_{\text{cav}}(t) = E_{\text{cav}}(0) e^{-\kappa t}. \quad (1.7)$$

Depending on the ratio of  $\kappa_0$  to  $\kappa_{\text{ext}}$  three coupling regimes can be distinguished. These are undercoupled ( $\kappa_0 > \kappa_{\text{ext}}$ ), overcoupled ( $\kappa_0 < \kappa_{\text{ext}}$ ), and critically coupled ( $\kappa_0 = \kappa_{\text{ext}}$ ). The optical linewidth can be measured as detailed in Appendix D.2.

### Quality factor

The quality factor  $Q$  of a resonator is defined as  $2\pi$  times the ratio of energy stored in the resonator  $E_{\text{cav}}$  to energy dissipated per oscillation cycle  $E_{\text{diss}}$ . In the case of a



weakly damped oscillator the quality factor can be written as

$$Q = 2\pi \frac{E_{\text{cav}}}{E_{\text{diss}}} = \omega \tau. \quad (1.8)$$

where  $\omega$  denotes the resonance frequency and  $\tau = 1/\kappa$  is the cavity lifetime.

### Finesse and circulating intracavity power

The finesse  $F$  of a resonator is defined as the ratio of FSR to resonance width:

$$F = \frac{\text{FSR}}{\kappa/2\pi} \quad (1.9)$$

The finesse relates the pump power  $P_{\text{in}}$  in the coupling waveguide to the power circulating inside the resonator  $P_{\text{cav}}$ . For an on-resonant pump laser and critical coupling the intracavity power is maximal

$$P_{\text{cav}} = \frac{F}{\pi} P_{\text{in}}. \quad (1.10)$$

The general result for non-critical coupling and detuned pump laser is given in Appendix A.1.

### Nonlinear refractive index $n_2$

The nonlinear refractive index  $n_2$  quantifies the change of the effective refractive index  $n$  experienced by a light field in a Kerr-nonlinear medium depending on the light field's intensity  $I$ :

$$n = n_0 + n_2 I \quad (1.11)$$

Here  $n_0$  denotes the material refractive index. The nonlinear refractive index  $n_2$  is directly related and proportional to the  $\chi^{(3)}$ -nonlinearity, which is responsible for parametric frequency conversion and comb generation in microresonators (cf. Section 1.3.2).

### Effective mode area $A_{\text{eff}}$ and effective mode volume $V_{\text{eff}}$

Microresonator based frequency comb generation relies on efficient non-linear frequency conversion. The latter requires high light intensities  $\sim |E|^2$  (electric field  $E$ ) inside the microresonator, which in turn requires a high finesse  $F$  and a small effective mode area  $A_{\text{eff}}$ . The latter is determined by the mode profile orthogonal to the

propagation direction of the light:

$$A_{\text{eff}} = \frac{(\int |E|^2 dA)^2}{\int |E|^4 dA}, \quad (1.12)$$

where the integration is done over the plane orthogonal to the propagation direction of the light. Based on  $A_{\text{eff}}$  the effective mode volume  $V_{\text{eff}} = A_{\text{eff}} L$  can be defined, where  $L$  is the roundtrip length of the cavity.

### 1.2.2 Microresonators used in this work

During the course of this work three different microresonator platforms have been used. These are described below:

#### Fused silica microtoroids

High- $Q$ , toroidal fused silica microresonators (microtoroids),<sup>70</sup> as shown in Figure 1.3d), are the first systems in which Kerr-frequency comb generation has been observed.<sup>72,86</sup> Fused silica toroidal microresonators are fabricated from a fused silica ( $\text{SiO}_2$ ) layer on a silicon (Si) substrate. First, fused silica disks are defined, etched and undercut. Then, a  $\text{CO}_2$ -laser is used to heat and melt the outer rim of the fused silica disk. This surface tension assisted "reflow" process creates a toroidal microresonator with a smooth surface that does not suffer from the surface roughness remaining after the previous etching steps. The fabrication process is illustrated in Figure 1.5 and described elsewhere<sup>70</sup> in detail. The high  $Q$ -factors in combination with the small effective mode area  $A_{\text{eff}}$  allow for efficient non-linear frequency conversion (cf. Table 1.1). The transparency window of fused silica limits the operation wavelength of the combs to the near-infrared region. Light can be evanescently coupled to these resonators by a tapered fiber.<sup>87</sup>

#### Magnesium fluoride whispering gallery mode resonators

Crystalline whispering gallery mode resonators<sup>68</sup> have been developed with record high microresonator  $Q$ -factor<sup>88,89</sup> and frequency comb generation<sup>90</sup> has been demonstrated in a calcium fluoride ( $\text{CaF}_2$ ) resonator shortly after the first observation in a fused silica microtoroid.<sup>72</sup> In this work crystalline magnesium fluoride ( $\text{MgF}_2$ ) microresonators are used.<sup>2,91,92</sup>  $\text{MgF}_2$  microresonators are fabricated from a cylindrical blank with millimeter-scale dimensions. The blanks are epoxy-glued to metal posts that allow mounting the crystal into an air bearing spindle, where the resonator fabrication takes place. In a first preforming step the resonator is defined by creating an axial symmetric protrusion in the rotating resonator using diamond abrasive films or

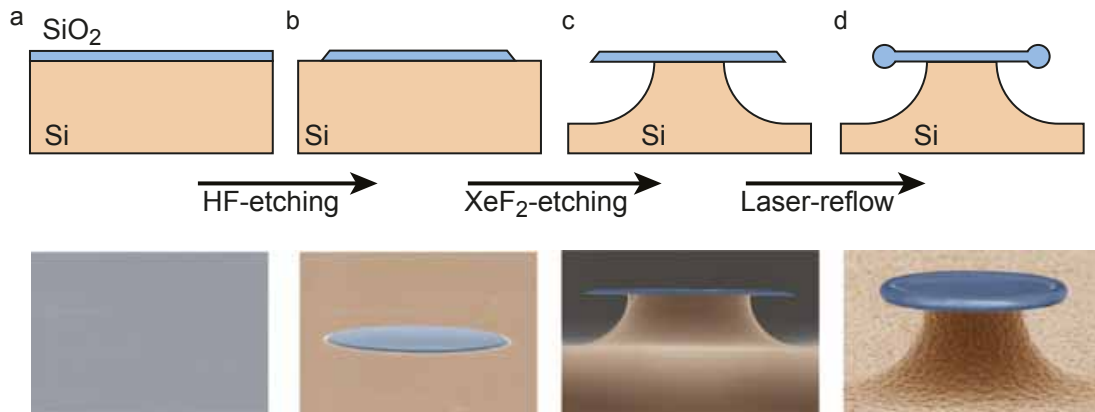


**Figure 1.5: Fabrication of a fused silica microtoroid.** **a.** Using photolithography circular disks of photoresist are defined on an oxidized silicon wafer. **b.** Hydro-fluoric (HF) acid is used to remove the fused silica ( $\text{SiO}_2$ ) not protected by the photoresist. **c.** Xenon-fluoride ( $\text{XeF}_2$ ) is used to undercut the  $\text{SiO}_2$  disks by selectively etching Si. **d.** A  $\text{CO}_2$  laser is used to melt the outer edge of the  $\text{SiO}_2$  disk such that a toroidal microresonator forms from the melted material due to surface tension (Figure kindly provided by P. Del’Haye<sup>86</sup>).

diamond turning<sup>a</sup>. The resulting preform usually has a surface roughness on the level of a few micron. Subsequent polishing steps using diamond particles with decreasing grain size (down to 30 nm) result in low surface roughness of the resonator and high  $Q$ . Figure 1.6 illustrates the fabrication process. Despite their comparatively low nonlinearity  $n_2$  and large mode-area  $A_{\text{eff}}$ , the high quality factors of  $\text{MgF}_2$  resonators allow for efficient frequency conversion with sub-mW threshold pump powers (cf. Table 1.1). Notably, the transparency of magnesium fluoride extends far into the mid-infrared wavelength region. Light can be evanescently coupled to these resonators e.g. by a tapered fiber<sup>87</sup> or a coupling prism.<sup>93,94</sup>

### Silicon nitride waveguide resonators

High- $Q$  silicon nitride ( $\text{Si}_3\text{N}_4$ ) waveguide resonators have recently been developed<sup>67</sup> and used for frequency comb generation.<sup>3,74,75</sup>  $\text{Si}_3\text{N}_4$  waveguide resonators<sup>4,67,74,75</sup> are fabricated<sup>b</sup> in a CMOS-compatible process, which makes this type of resonator suitable for mass-scale production and on-chip integration in photonic-circuitry. The height of the planar resonator geometry is given by the thickness of a  $\text{Si}_3\text{N}_4$  layer that is deposited onto a  $\text{SiO}_2$  substrate. The lateral geometry of the resonators is defined via electron-beam lithography, which allows for precise and reproducible resonator designs. The full chip is protected by a  $\text{SiO}_2$  cladding protecting the system against environmental influences such as dust or humidity. The quality factors of

<sup>a</sup>The diamond turning has been carried out by LT Ultra Precision Technology GmbH.

<sup>b</sup>The  $\text{Si}_3\text{N}_4$  resonators used in this work have been fabricated by K. Hartinger, J. Riemensberger and V. Brasch

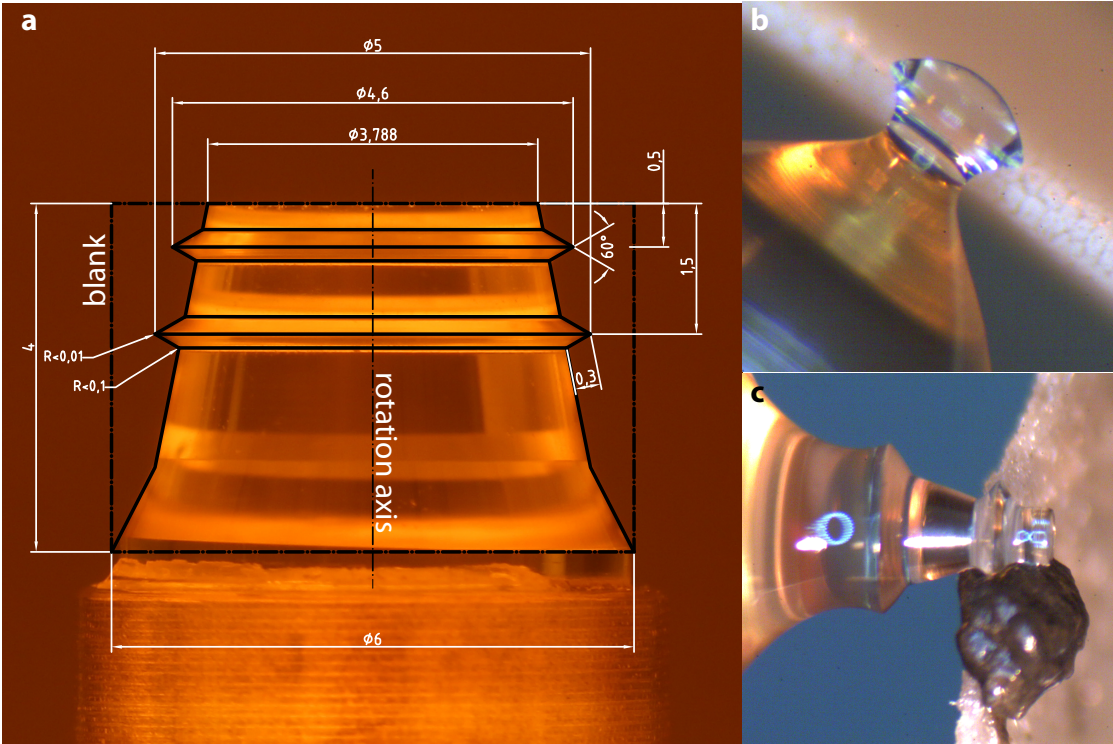


**Figure 1.6: Fabrication of crystalline magnesium-fluoride microresonators.** **a.** Diamond turned magnesium fluoride resonator before the final polishing step. The sample holds two resonators. Superimposed is the technical drawing (length in units of mm) used for the diamond turning process. The original cylindrical magnesium fluoride blank is indicated by the black dash-dotted line. The black thin dash-dotted vertical line in the center indicates the rotation axis when mounted to the air bearing spindle for fabrication. **b.** Manually shaped resonator and abrasive diamond film (in the background). **c.** Diamond turned resonator rotating in diamond particle paste to remove residual cracks originating from the diamond turning process.

## 1.2. Dielectric nonlinear microresonators

silicon nitride waveguide resonators are currently much lower compared to the the magnesium fluoride or fused silica resonators. This, however, is compensated for by the more than ten times higher nonlinear refractive index  $n_2$  and the very small mode-area  $A_{\text{eff}}$  in the square micron range (cf. Table 1.1). The waveguide that couples light in and out of the resonator is an integrated on-chip  $\text{Si}_3\text{N}_4$  bus-waveguide. Light can be injected and extracted from the bus waveguide using e.g. inverse tapers<sup>95</sup> in combination with lensed fibers<sup>96</sup> or by directly pig-tailing the chip with a standard optical fiber.<sup>97</sup>

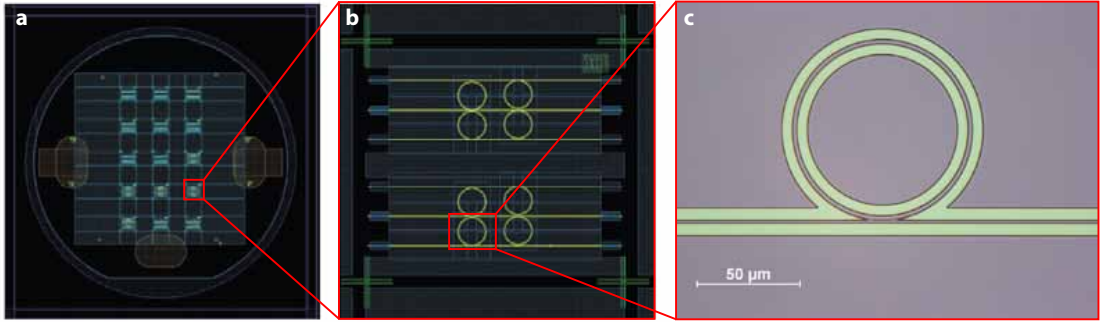


**Figure 1.7: Fabrication of a planar silicon nitride microresonator.** a.,b. Digital wafer and chip layout used for e-beam lithography. c. Optical microscope image of a microresonator during fabrication.

Resonator Type:	Crystalline $\text{MgF}_2$	Fused $\text{SiO}_2$ Toroid	$\text{Si}_3\text{N}_4$ waveguide
$Q$	$10^8$ - $10^9$	$10^7$	$10^6$
FSR (GHz)	10-200	80-1000	10-1000
$n_0$	1.37(o), 1.38(e)	1.44	1.98
$n_2$ ( $10^{-20}\text{m}^2\text{W}^{-1}$ )	0.9	2.2	25
$A_{\text{eff}}$ ( $\mu\text{m}^2$ )	30-100	$\sim 3$	$\sim 1$
Transparency ( $\mu\text{m}$ )	0.13-7.7	0.21-2.8	-
$1/L \cdot dL/dT$ ( $10^{-6}\text{K}^{-1}$ )	$\sim 10$	0.55	$\sim 2$
$1/n \cdot dn/dT$ ( $10^{-6}\text{K}^{-1}$ )	0.09(o), 0.03(e)	10.5	30
Coupling method	tapered fiber	tapered fiber	integrated waveguide

**Table 1.1: Comparison of different microresonators used in this work.** The compared quantities are quality factor  $Q$ , free spectral range (FSR), refractive index  $n_0$  (o: ordinary ray; e: extraordinary ray), non-linear refractive index  $n_2$ , effective mode-area  $A_{\text{eff}}$ , transparency window, relative thermal expansion and relative thermal refractive index change.<sup>74,98-102</sup> Moreover, the coupling method used in this work is indicated.

### 1.3 Microresonator based optical frequency combs

Microresonator based frequency combs<sup>72,103</sup> represent an entirely novel approach towards optical frequency comb generation. As opposed to conventional frequency combs, microresonator based frequency combs do not rely on mode-locked lasers but on nonlinear optical frequency conversion inside microresonators. These microresonators confine light into small volumes with spatial dimensions down to the micron scale. If a microresonator is made of a nonlinear medium the strong spatial light confinement enables efficient nonlinear optical frequency conversion<sup>104</sup> such as parametric oscillations<sup>105,106</sup>, four-wave mixing,<sup>68,71,77</sup> Raman<sup>82,107,108</sup> and Brillouin lasing,<sup>81,109,110</sup> frequency doubling<sup>111</sup> and tripling.<sup>112</sup> Relevant for frequency comb generation is four-wave mixing, a non-linear optical process where four electromagnetic fields inside a Kerr-nonlinear medium are coupled phase-coherently via the parametric  $\chi^{(3)}$ -nonlinearity.

Microresonator combs however do not rely on mode-locked lasers and their time domain output is not generally pulsed. Nevertheless and despite being inadequate the term “(pulse) repetition rate” is often used to refer to the mode spacing of microresonator based combs.

It is important to realize that a microresonator based comb generator, despite being driven by a laser, is not itself a laser. The microresonator can be seen as a passive device that merely converts the monochromatic cw pump light into other frequency components via nonlinear four-wave mixing. The frequency conversion may be described in terms of the parametric gain (cf. Section 1.3.2). Notably different from a laser gain, the parametric gain is phase and frequency selective and depends on the light fields present in the microresonator.

After highlighting some of the application of microresonator based combs (Section 1.3.1), the following sections introduce the physical background and setup for microresonator based comb generation. Following on a general discussion on nonlinear parametric processes in Section 1.3.2, the thermal and nonlinear optical effects on the resonance frequency will be discussed in Section 1.3.3. The latter is important for stable operation of the generated comb spectra and particularly enables a passive locking technique termed “thermal (self-)locking”.<sup>113</sup> Section 1.3.4 explains how the non-linear process of four-wave mixing can result in the generation of a frequency comb and is followed by a discussion on competing nonlinear frequency conversion mechanisms in Section 1.3.5. The generic setup for frequency comb generation is described in Section 1.3.6. A short overview of the state-of-the-art of the emerging microresonator comb technology is given in Section 1.3.7.

### 1.3.1 Application of microresonator based combs

Compared to conventional mode-locked laser combs, microresonators based combs are naturally characterized by a much wider mode-spacing, ranging from multi-GHz to THz. Figure 1.8 illustrates the different parameter regimes covered by conventional and microresonator based comb generators. In some ‘conventional’, mode-locked laser based combs higher repetition rates up to a ten GHz have been achieved.<sup>114,115</sup> These or even higher repetition rates, however, are difficult to reach as this implies shrinking the laser cavity including the gain medium and the saturable absorber that is required for stable mode-locking. Notably, repetition rates exceeding 100 GHz and higher<sup>116</sup> have been demonstrated in solid-state laser systems employing semiconductor saturable absorber mirrors (SESAMs)<sup>50</sup>; here, however, the spectral span is currently very limited to a few manometers only. In the past harmonic mode-locking,<sup>117</sup> that is multiple pulses propagating inside the laser cavity, has been employed to achieve high repetition rates. This approach, however, remains technically challenging.<sup>118</sup> Another way of achieving widely spaced combs is mode-filtering of a narrow spaced comb.<sup>20–23</sup> Mode-filtering, however, leads to a reduction of optical power and the non-perfect suppression of unwanted comb lines effectively leads to an apparent shift of the wanted comb line if the spectral resolution is insufficient to resolve the narrowly spaced structure.

Microresonator based comb generators provide a natural way of achieving combs with mode spacing in the multi-GHz to THz regime. In that sense, microresonator based frequency combs are complementary to conventional combs and can complete the available technology when a wide comb line spacing, high power per comb line or compactness is key.<sup>103</sup> A CMOS-compatible fabrication process enables potential mass-scale and low cost fabrication. The latter is required for widespread applications outside research laboratories in e.g. medical spectroscopy applications<sup>28</sup> and telecommunications.<sup>119,120</sup>

In proof of principle experiments Kerr-combs have already been demonstrated in applications where the wide comb line spacing is essential.<sup>103</sup> These applications include line-by-line pulse shaping and optical waveform synthesis,<sup>44,97,121</sup> low phase noise microwave generation,<sup>38,68,79,90,122–125</sup> a miniature rubidium based optical clock,<sup>126</sup> high-capacity telecommunications<sup>120</sup> mid-infrared direct comb spectroscopy<sup>2</sup> (Chapter 3) and high-repetition rate ultra-short pulse generation<sup>1,127</sup> (Chapter 4).

Further envisioned applications<sup>103</sup> include astronomical spectrometer calibration for the search of exo-planets and direct measurement of the universe’s expansion.<sup>20–23</sup> Compact chip-scale dual comb spectrometers<sup>24,29,128</sup> and direct frequency comb spectroscopy<sup>25,26,30</sup> could lead to widespread use of microresonator comb enabled precision spectrometers. Moreover, chip-scale microresonator based combs could

provide a compact, energy efficient and vibration insensitive gear-box required for mobile and space optical clocks.<sup>103, 129</sup>

### 1.3.2 Kerr-nonlinearity and nonlinear parametric frequency conversion

The following discussion on non-linear parametric processes follows the presentation given by R.W. Boyd.<sup>135</sup> Non-linear optical processes can often be described by means of the time dependent polarization  $P(z, t)$  of the non-linear optical medium in response to an optical field  $E(z, t)$  (we restrict ourselves to one spatial coordinate  $z$ ):

$$P(z, t) = \epsilon_0 (\chi^{(1)} E(z, t) + \chi^{(2)} E^2(z, t) + \chi^{(3)} E^3(z, t) + \dots) = \epsilon_0 \chi_{\text{eff}} E(z, t) \quad (1.13)$$

Here  $\epsilon_0$  is the vacuum permittivity and  $\chi^{(1)}$ ,  $\chi^{(2)}$  and  $\chi^{(3)}$  denote the linear as well as second and third order non-linear optical susceptibilities<sup>c</sup>. We note that the effective susceptibility  $\chi_{\text{eff}}$  relates to the effective refractive index  $n$  via

$$n = \sqrt{1 + \chi_{\text{eff}}}. \quad (1.14)$$

All materials considered in this work are inversion symmetric, which implies a vanishing  $\chi^{(2)}$  (other even terms vanish as well). The non-linear contribution  $P_{\text{NL}}(t)$  to the polarization can thus be approximated by

$$P_{\text{NL}}(z, t) = \epsilon_0 \chi^{(3)} E^3(z, t). \quad (1.15)$$

This  $\chi^{(3)}$ -nonlinearity<sup>d</sup> is often referred to as parametric Kerr-nonlinearity. The Kerr-nonlinearity is responsible for self- and cross-phase modulation and enables parametric frequency conversion processes. In these parametric frequency conversion processes the quantum state of the medium remains unchanged and consequently the total energy of the involved photons is conserved.

We introduce a complex electric field composed of three mutually different frequency components and propagating through a nonlinear medium in the  $z$ -direction  $E(z, t) = E_1 e^{i(k_1 z - \omega_1 t)} + E_2 e^{i(k_2 z - \omega_2 t)} + E_3 e^{i(k_3 z - \omega_3 t)} + \text{c.c.}$ . The optical frequencies of the field are  $\omega_{1,2,3}$  and  $k_{1,2,3}$  are the wave-vectors. Next, we insert  $E(z, t)$  into eq. 1.15 and express the nonlinear polarization in discrete frequency components  $\omega_n$

$$P_{\text{NL}}(z, t) = \sum_n P_{\text{NL}}(\omega_n) e^{i(k_n z - \omega_n t)}. \quad (1.16)$$

---

<sup>c</sup>In a vector formulation, i.e.  $E(t) \rightarrow \vec{E}(t)$  and  $P(t) \rightarrow \vec{P}(t)$ ,  $\chi^{(i)}$  becomes a  $(i+1)$ -rank tensor.

<sup>d</sup>Different physical effects with different response time to the electric field contribute to the  $\chi^{(3)}$ -nonlinearity.<sup>135</sup> In the context of frequency comb generation the  $\chi^{(3)}$ -nonlinear effects is due to electronic polarization of the medium, which can be considered instantaneous (response time  $< 10^{-15}$  s). On longer time scales other effects, such as, molecular orientation and electrostriction, may contribute to the  $\chi^{(3)}$ -nonlinearity.



### 1.3. Microresonator based optical frequency combs

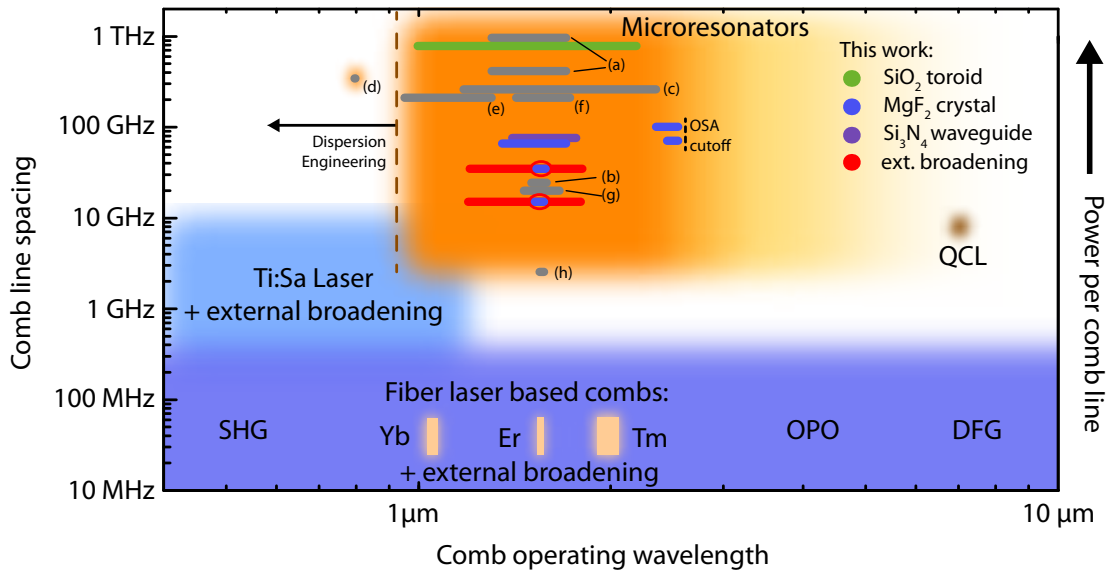


**Figure 1.8: Comparison of frequency comb technology** in terms of comb operating wavelength and comb line spacing. **Fiber laser based combs:** At comb line spacings up to few hundreds of MHz mode-locked fiber laser based systems cover the wavelength regime ranging from visible to mid-infrared. These systems rely on a primary comb generated in the gain bandwidth of ytterbium (Yb), erbium (Er) or thulium (Tm) doped fibers and are then externally broadened in nonlinear fibers. Second harmonic generation (SHG) and frequency down-conversion via optical parametric oscillation (OPO) or difference frequency generation (DFG) transfers the comb to shorter and longer wavelength regimes. **Ti:Sa laser:** Higher comb line spacings, up to 10 GHz, have been demonstrated in mode-locked titanium-sapphire lasers which in most cases are also externally broadened. **QCL:** Recently, a new approach to mid-infrared frequency comb generation at high comb line spacing was demonstrated based on a quantum cascade laser (QCL).<sup>130</sup> **Microresonator based combs** access in a natural way the regime of comb line spacings above several GHz and high power per comb line. Direct frequency comb generation is possible over a wide wavelength range and independent of broadband laser gain media. The mid-infrared region remains largely unexplored but experiments suggest that microresonator based combs can work far in the mid-infrared regime. On the short wavelength side the current limitation is given by the onset of normal dispersion (cf. Section 1.3.4). A **Selection of demonstrated microresonator based combs** is represented by the horizontal bars. Pertaining to this work the color indicates the used resonator platform. Green: First octave spanning spectrum achieved in a microresonator<sup>5</sup>; Blue bars (rightmost): Combs exploring the potential of direct mid-infrared comb generation<sup>2</sup>; Blue and purple bar (center): Two complementary systems that allowed for a platform independent understanding of comb formation dynamics. Blue/red (two lowermost): Mode-locked soliton states allowing for external spectral broadening (red). The references to other work are (shown in gray): [a] First microresonator based combs<sup>72</sup> (in SiO<sub>2</sub>), [b] First combs in crystalline CaF<sub>2</sub>,<sup>90</sup> [c] Octave spanning spectrum in Si<sub>3</sub>N<sub>4</sub>,<sup>131</sup> [d] Short wavelength comb using higher order transverse modes in CaF<sub>2</sub>,<sup>85,132</sup> [e] Dispersion engineered comb in Si<sub>3</sub>N<sub>4</sub>,<sup>133</sup> [f] Mode-locked Si<sub>3</sub>N<sub>4</sub> comb, [g] Si<sub>3</sub>N<sub>4</sub> based combs with 20 GHz line spacing,<sup>78</sup> [h] Comb in large fused silica disks with a line spacing of 2.6 GHz.<sup>134</sup>

For the complex polarization amplitudes  $P_{\text{NL}}(\omega_n)$  we find several frequency components that can be subdivided into different physical processes<sup>135</sup> as listed below. We only list the expressions with positive frequency  $\omega_n$  and the mutually different indices  $k, l, m = 1, 2, 3$  refer to the frequency components of the electric field  $E(z, t)$ . The wave-vector  $k_{k,l,m,n}$  always corresponds to the wave of frequency  $\omega_{k,l,m,n}$  with the same index.

### Intensity dependent refractive index, self- and cross-phase modulation

$$P_{\text{NL}}(\omega_n = \omega_k) e^{ik_k z} = \epsilon_0 \chi^{(3)} \underbrace{(3E_k E_k^*)}_{\text{SPM}} + \underbrace{(6E_l E_l^* + 6E_m E_m^*)}_{\text{XPM}} E_k e^{ik_k z} \quad (1.17)$$

When a light field is propagating in a non-linear medium it will experience an intensity dependent refractive index. This effect is called self-phase modulation (SPM). Moreover, when two light fields are co-propagating in a non-linear medium the light fields will mutually alter the effective refractive index they experience. This effect is called cross-phase modulation (XPM). In eq. 1.17 the light field  $E_k$  undergoes SPM and XPM by the fields  $E_l, E_m$ . Note that no new light frequencies are generated. Defining the light intensities  $I_{k,l,m} = \frac{1}{2} n_0 \epsilon_0 c |E_{k,l,m}|^2$  and using eq. 1.14 we find an expression for the effective refractive index experienced by the light field  $E_k$ :

$$n = n_0 + n_2 I_k + 2n_2 (I_l + I_m), \quad (1.18)$$

where  $n_0$  denotes the (linear) refractive index and

$$n_2 = \frac{3}{2n_0^2 \epsilon_0 c} \chi^{(3)} \quad (1.19)$$

the non-linear refractive index, which is often used as a measure of the third order  $\chi^{(3)}$ -nonlinearity. From eq. 1.18 we see that for a given intensity the effect of cross-phase modulation is twice as strong as the effect of self-phase modulation.

### Third harmonic generation

$$P_{\text{NL}}(\omega_n = 3\omega_k) e^{ik_n z} = \epsilon_0 \chi^{(3)} E_k^3 e^{i3k_k z} \quad (1.20)$$

Typically, third harmonic generation is achieved by frequency doubling and subsequent sum frequency generation in  $\chi^{(2)}$ -nonlinear media. The coupling of four light fields via the  $\chi^{(3)}$  allows for the direct generation of frequency tripled light. Whether this process can occur efficiently in microresonators depends on the resonance spec-

trum of the resonator, that is whether the tripled frequency is supported by a cavity resonance or not.

#### Triple component sum frequency generation

$$P_{\text{NL}}(\omega_n = 2\omega_k + \omega_l) e^{ik_n z} = 3\epsilon_0 \chi^{(3)} E_k^2 E_l e^{i(2k_k + k_l)z} \quad (1.21)$$

$$P_{\text{NL}}(\omega_n = \omega_k + \omega_l + \omega_m) e^{ik_n z} = 6\epsilon_0 \chi^{(3)} E_k E_l E_m e^{i(k_k + k_l + k_m)z} \quad (1.22)$$

Triple component sum frequency generation is the generalization of third harmonic generation in a  $\chi^{(3)}$ -nonlinear medium. The different numeric pre-factors are due to the different numbers of possible permutations.

#### Four-wave mixing

$$P_{\text{NL}}(\omega_n = \omega_k + \omega_l - \omega_m) e^{ik_n z} = 6\epsilon_0 \chi^{(3)} E_k E_l E_m^* e^{i(k_k + k_l - k_m)z} \quad (\text{non-degenerate}) \quad (1.23)$$

$$P_{\text{NL}}(\omega_n = 2\omega_k - \omega_l) e^{ik_n z} = 3\epsilon_0 \chi^{(3)} E_k^2 E_l^* e^{i(2k_k - k_l)z} \quad (\text{degenerate}) \quad (1.24)$$

Four wave-mixing (FWM) is the process responsible for frequency comb generation in a microresonator. The different numeric pre-factors are due to the different numbers of possible permutations. In a photon picture,<sup>135,136</sup> FWM can be interpreted as the annihilation of two photons. In the above non-degenerate case two photons of frequency  $\omega_k$  and  $\omega_l$  are annihilated and of two photons of frequency  $\omega_m$  and  $\omega_n$  are created respecting energy conservation  $\omega_k + \omega_l = \omega_m + \omega_n$ . The above case of degenerate FWM corresponds to the annihilation of two photons of frequency  $\omega_k$  and the creation of two photons with respective frequency  $\omega_l$  and  $\omega_n$ , where now  $2\omega_k = \omega_l + \omega_n$ . A similar description is possible for the other parametric processes, such as third harmonic generation, and illustrated in Figure 1.9).

#### Phase-matching

In all parametric frequency conversion processes the nonlinear polarization  $P_{\text{NL}}(z, t)$  acts as a source for the wave with frequency  $\omega_n$ . For efficient frequency conversion the source and the already generated new wave  $\omega_n$  need to interfere constructively. This is the case if the involved waves are phase-matched. In the above case of FWM

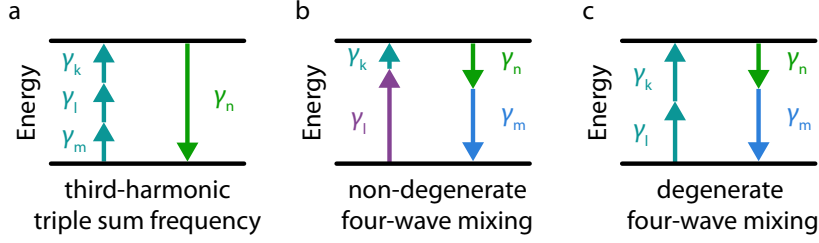


**Figure 1.9: Energy schemes of  $\chi^{(3)}$ -nonlinear parametric processes** illustrating the annihilation (upwards pointing arrows) and creation (downward pointing arrows) of photons ( $\gamma_{k,l,m,n}$ ). The energies of the photons  $\gamma$  correspond to the length of the arrows. **a.** Third harmonic generation and triple sum frequency **b.** Non-degenerate four-wave mixing **c.** Degenerate four-wave mixing.

this requires:

$$k_n = k_k + k_l - k_m \quad (\text{non-degenerate}) \quad (1.25)$$

$$k_n = 2k_k - k_l \quad (\text{degenerate}) \quad (1.26)$$

In Section 1.3.4 we will explain how four-wave mixing can give rise to the generation of broadband frequency comb spectra and how this process is intrinsically phase matched in a microresonator. Before, however, the important effect of thermal and Kerr-nonlinear resonance shifts and related concepts will be introduced in the next Section 1.3.3.

### 1.3.3 Thermal and Kerr-nonlinear resonance shift and related concepts

The thermal (and Kerr-nonlinear) locking<sup>113</sup> of a microresonator to the pump laser is an important experimental technique in the context of microresonator frequency combs. It enables the passive locking of a microresonator resonance to the pump laser. This locking technique relies on the fact that the effective resonance frequency  $\omega_0^{\text{eff}}$  depends on the circulating intracavity power  $P_{\text{cav}}$  and the resulting temperature change  $\Delta T$  of the material due to absorptive heating. This dependence of the effective resonance frequency  $\omega_0^{\text{eff}}$  on  $P_{\text{cav}}$  and the induced temperature change  $\Delta T$  is also responsible for a characteristic triangular resonance shape, a so called thermal triangle, observed when a high power laser is scanned over a high-Q resonance of the microresonator in the direction of decreasing optical frequency.

#### Effective resonance frequency

When a high power pump laser is coupled and tuned into the resonance of a microresonator the effective resonance frequency  $\omega_0^{\text{eff}}$  will shift away from the original, so called

cold resonance frequency  $\omega_0$ . This shift is due to thermal expansion ( $\alpha_L = 1/L \cdot dL/dT$ ), thermally induced refractive index change ( $\alpha_n = 1/n \cdot dn/dT$ ) and SPM:

$$\omega_0^{\text{eff}} = \omega_0 \left( 1 - \frac{1}{L} \frac{dL}{dT} \Delta T - \frac{1}{n_0} \frac{dn_0}{dT} \Delta T - \frac{1}{n} \frac{n_2 P_{\text{cav}}}{A_{\text{eff}}} \right) \quad (1.27)$$

Here,  $\omega_0$  denotes the cold resonance frequency. For all materials considered here the thermal expansion  $\alpha_L$ , the relative thermal refractive index change  $\alpha_n$  and  $n_2$  are positive, implying that all three effects lead to an decrease of the optical resonance frequency when light is coupled to the resonator.

The high power pump laser does not only shift the resonance frequency  $\omega_0 \rightarrow \omega_0^{\text{eff}}$  but all resonance frequencies  $\omega_\mu \rightarrow \omega_\mu^{\text{eff}}$ . The thermal effects will result in a slightly smaller FSR when the temperature increases due to the positive coefficients  $\alpha_n$  and  $\alpha_L$ . The associated differential thermal resonance shift between the resonances  $\omega_\mu^{\text{eff}}$  is small, yet important for stabilizing the comb spacing<sup>123</sup> as detailed in Section 1.3.4. The Kerr-nonlinear shift of the modes  $\omega_\mu^{\text{eff}}$  ( $\mu \neq 0$ ) is mostly due to XPM by the strong pump laser and twice as large SPM for the pumped mode  $\omega_0^{\text{eff}}$ . This leads to a notable differential shift of the effective resonance frequencies  $\omega_{\mu \neq 0}^{\text{eff}}$  with respect to  $\omega_0^{\text{eff}}$  as illustrated in Figure 1.10. To describe the physics of microresonator based combs,

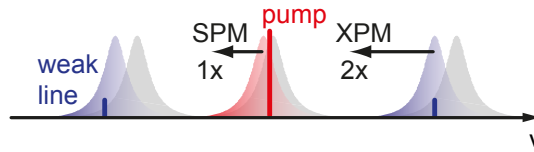


**Figure 1.10: Differential nonlinear resonance shift** due to self- and cross-phase modulation (SPM and XPM). The nonlinear shifts are dominated by the pump laser that acts on itself via SPM. Weak comb lines in other resonances experience a twice as large effect via XPM. The difference between the two effects leads to a differential shift of the effective resonance frequencies.

thermal resonance shifts can usually be ignored, as they are slow on the time scales the comb generation takes place. Moreover, as discussed above, thermal effects shift all resonance frequencies simultaneously with little differential shift. For experimental comb generation thermal effects are, however, very important. One example is the thermal (and Kerr-nonlinear) self-locking described hereafter.

#### Thermal and Kerr-nonlinear self-locking

For frequency comb generation in a microresonator a pump laser  $\omega_p$  is used to drive the microresonators close to its effective resonance frequency  $\omega_0^{\text{eff}}$  at a certain effec-

tive detuning<sup>e</sup>  $\zeta_0^{\text{eff}} = 2(\omega_0^{\text{eff}} - \omega_p)/\kappa$ . In the presence of thermal effects this detuning is stable when the pump laser is effectively blue detuned ( $\zeta_0^{\text{eff}} < 0$ ) but unstable if effectively red detuned ( $\zeta_0^{\text{eff}} > 0$ )<sup>113</sup> unless very far red detuned. To understand this we consider the stable, blue detuned case. Here, a small fluctuation  $\delta\zeta_0^{\text{eff}} > 0$  will result in the pump laser  $\omega_p$  moving closer to the effective resonance frequency  $\omega_{\text{eff}}^0$ . As a direct consequence the intracavity power  $P_{\text{cav}}$  will rise and lead to an increase in absorptive heating. In accordance with eq. 1.27 the effective resonance frequency  $\omega_{\text{eff}}^0$  will decrease, counteract the small fluctuation of  $\delta\zeta_0^{\text{eff}}$  and thus stabilize the effective detuning  $\zeta_0^{\text{eff}}$ . An analogous reasoning applies to the case where  $\delta\zeta_0^{\text{eff}} < 0$ . Assuming a fixed pump laser frequency, the microresonator effectively self-locks itself on this frequency. The thermal self-stability in the case of a blue detuned pump laser is called “thermal lock”. A destabilizing mechanism will be the result when the laser is red detuned unless very far red detuned.

Besides the thermal effects, an additional resonance shift arises from the Kerr-non-linearity of the system, which can be described in terms of the Kerr-optical bistability (cf. Appendix A.2.3). As the Kerr-effect via SPM always leads to a reduction of the resonance frequency for an increased intracavity power, the Kerr-effect contributes to the self-stability described above.

Thermal self-locking of the effective resonance frequency  $\omega_0^{\text{eff}}$  to the pump laser  $\omega_p$  is not only convenient for the experimenter, but important to frequency comb generation in microresonators. Here, the pump laser frequency already defines a comb line that should remain fixed and hence cannot be used to follow the cavity resonance frequency. Thus it is the resonance of the microresonator that needs to stay locked to the fixed pump laser frequency.

### Thermal triangle

When scanning a low power probe laser over a resonance of a microresonator a Lorentzian resonance dip is observed (cf. Figure 1.11 and Appendix A.1) in the transmission through the coupling waveguide. When repeating the same experiment with a high power pump laser, an almost triangular resonance shape, a so called “thermal triangle”, is observed (cf. Figure 1.11) when the scan is performed in the direction of decreasing optical frequency. This phenomenon can be understood as an effect of thermal (and Kerr-nonlinear) locking of the cavity to the pump laser. When the pump laser approaches the resonances the resonator heats up and the resonance frequency shifts towards lower frequencies, that is in the direction of the laser scan. When the scan is performed slow enough (compared to the thermal time constants of the systems) the resonator can be thought of being thermally locked to the res-

---

<sup>e</sup>For consistency throughout this text we have normalized the detuning to  $\kappa/2$ .

onator, where, however, the increasing necessary resonance shift requires that the pump laser approaches the point of effective zero detuning  $\zeta^{\text{eff}} = 0$  (where the power in the cavity is maximized). At effective zero detuning the pump laser will transit from the effectively blue detuned to the effectively red detuned regime. Here, due to cool-down, the effective resonance frequency suddenly increases and approaches its original cold value  $\omega_0^{\text{eff}} = \omega_0$ . In the transmission signal this manifests itself as an almost instantaneous increase to full transmission<sup>f</sup>.

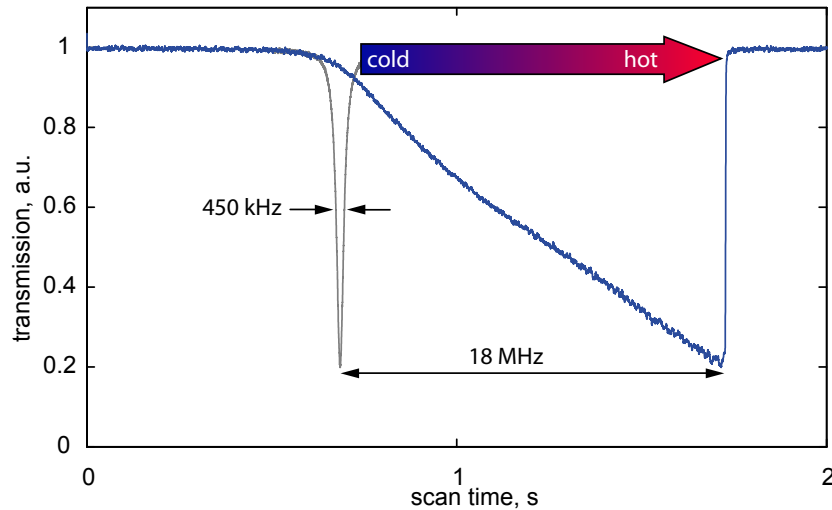


**Figure 1.11: Thermal triangle:** The gray trace shows a measured transmission signal when scanning a low power probe laser with decreasing optical frequency over a resonance of MgF<sub>2</sub> resonator. Self-phase modulation and temperature change of the resonator are negligible. The trace follows a Lorentzian lines shape of width  $\kappa/2\pi = 450$  kHz. When the same experiment is repeated with higher pump power the transmission trace strongly deviates from the low power case (blue trace; normalized to the gray trace). Due to absorptive heating (indicated by the blue-to-red shaded arrow) the effective resonance frequency shifts in the scan direction towards smaller optical frequencies. A triangular resonance shape, a so called thermal triangle, is observed. The width of the triangle exceeds the width of the cold resonance by far. Note that part of the resonance shift arises from the Kerr-effect.

#### Thermal instability

So far we have implicitly assumed that the coefficients  $\alpha_L$ ,  $\alpha_n$  and  $n_2$  are positive. Indeed this is an essential prerequisite for the thermal and Kerr-nonlinear locking technique. If one of the three  $\alpha_L$ ,  $\alpha_n$  or  $n_2$  were to be negative it would act as a destabilizing effect in the described locking mechanism. As all three effects act on three

<sup>f</sup>The thermal triangle can also be discussed in terms of a thermal bistability of the resonator.<sup>113</sup>

different time scales<sup>g</sup> they can not compensate for each other and lead to unstable and oscillatory behavior, where the effective resonance frequency is periodically changing. Figure 1.12a shows the effect of thermal instability due opposite signs of  $\alpha_L > 0$  and  $\alpha_n < 0$  in a  $\text{CaF}_2$  microresonator<sup>h</sup>. A similar effect has been reported and analyzed in polydimethylsiloxane coated silica microresonators.<sup>137</sup>

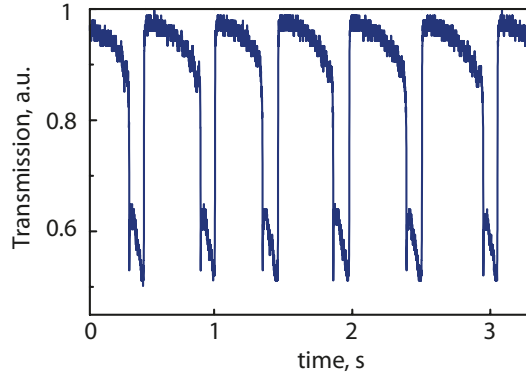


**Figure 1.12: Thermal instability observed in a  $\text{CaF}_2$  microresonator.** Experimentally observed oscillatory behavior in the laser transmission in a  $\text{CaF}_2$  resonator ( $Q \approx 10^8$ , radius 2 mm) while the pump laser frequency is kept constant.

### 1.3.4 Frequency comb generation via four-wave mixing

Cascaded four-wave mixing can convert a monochromatic, cw pump laser into equidistant optical lines constituting a frequency comb. For efficient resonant build-up and parametric amplification the comb line frequencies need to be close to the (effective) resonance frequencies of the resonator. As a consequence the FSR of the resonator corresponds approximately to the spacing of the comb lines. It is however important to note that the equidistance of the comb lines is a result of the energy conserving nature of the four-wave mixing process and does not rely on equidistant resonance frequencies. This implies that comb lines may be slightly offset from the center frequency of the resonances.

In the following we refer to the comb line  $m$  as the comb line being supported by the cavity mode with the same mode number. Referring, as an example, to the above case of non-degenerate FWM (eq. 1.23). The energy conserving nature of the FWM processes implies that the comb lines  $m_k, m_l, m_m$  and  $m_n$  involved in the FWM process obey  $m_k + m_l = m_m + m_n$ . As the comb lines need to be close to resonant with the

<sup>g</sup>The thermal expansions depends on the temperature profile of the full resonator geometry, the thermally induced refractive index change depends on temperature of the mode volume and the self-phase modulation instantaneously depends on the intensity inside the cavity.

<sup>h</sup>The  $\text{CaF}_2$  resonator was fabricated by Johannes Hofer.



cavity the wavelength of the comb line  $m$  is  $\lambda_m \approx L/m$ , where  $L$  is the roundtrip length of the resonator. The wave-vectors of a comb line can thus be written as

$$k_m = \frac{2\pi}{\lambda_m} \approx \frac{2\pi}{L} m, \quad (1.28)$$

Inserting this result into the phase-matching condition (eq. 1.25) shows that the phase matching condition  $k_n = k_k + k_l - k_m$  is intrinsically achieved in the resonator. For convenience we may replace the mode number  $m$  by the relative mode number  $\mu$  without changing the result.

The process of frequency comb generation in a microresonator via FWM commences with an initial degenerate FWM step and then proceeds by cascaded FWM. The process is illustrated in Figure 1.13 and explained below.

#### Degenerate four-wave mixing

The pump laser with frequency  $\omega_p$  is tuned into a cavity resonance with relative mode number  $\mu = 0$  (by definition). To enable thermal locking (cf. Section 1.3.3) the pump laser is tuned in the direction of decreasing optical frequency and kept effectively blue detuned as shown in Figure 1.13a. With the pump laser frequency approaching the resonance the intracavity power keeps increasing and approaches the parametric threshold power  $P_{\text{cav}}^{\text{th}}$  derived in Appendix A.2.4 and given by

$$P_{\text{cav}}^{\text{th}} = \frac{\kappa n_0^3 A_{\text{eff}}}{2\omega_0 n_2}. \quad (1.29)$$

For the resonators considered here this yields an intracavity threshold power on the order of a few W equivalent to intracavity threshold intensities  $I_{\text{cav}}^{\text{th}} = P_{\text{cav}}^{\text{th}}/A_{\text{eff}}$  ranging from several MW/cm<sup>2</sup> to GW/cm<sup>2</sup>. The threshold pump power, that is the external laser power required to pump the resonators, is much lower due to the resonant enhancement of the cavity and given by (cf. Appendix A.2.4):

$$P_{\text{in}}^{\text{th}} = \frac{\kappa^2 n_0^2 V_{\text{eff}}}{8\eta\omega_0 c n_2} \quad (1.30)$$

Once the intracavity power is high enough the parametric threshold is exceeded and frequency conversion via degenerate FWM sets in. In this first degenerate four-wave mixing step two sidebands, seeded by vacuum fluctuations, are generated symmetrically to the pump laser in the cavity resonances with relative mode indices  $\pm\mu_{\text{th}}$ . Due to the energy conserving nature of degenerate FWM, the frequency symmetry around the pump laser is exact. In terms of optical frequency the newly generated sidebands are separated from the pump laser by  $\Delta$  as illustrated in Figure 1.13b where,

for simplicity, we have assumed that  $\mu_{\text{th}} = 1$ . In general, the value of  $\mu_{\text{th}}$  depends on the dispersion  $D_2$ , the cavity linewidth  $\kappa$  and the pump power  $P_{\text{in}}$ . It is worth emphasizing that the pump frequency  $\omega_p$  is close to but not exactly resonant with the resonator. Similarly the comb lines generated are close to but not necessarily equal to the effective resonance frequencies of their respective cavity modes.

### Requirement of anomalous resonator dispersion

For efficient power build-up of the first sidebands the degenerate FWM requires the effective resonance frequencies of the modes  $\pm\mu_{\text{th}}$  to be approximately symmetric with respect to the pump laser frequency  $\omega_p$ . This symmetry, however, is impeded by the differential resonance shift between pumped resonance and the other resonances via SPM and XPM, respectively (cf. Section 1.3.3). Moreover, the pump laser is blue detuned from the pumped resonance and further increases the asymmetry. This asymmetry can be compensated by an anomalous resonator dispersion (FSR increases with mode number). Thus, the latter is an important requirement for FWM based Kerr-comb generation. In some cases an effective anomalous dispersion may also be created in a small spectral window by coupling to higher order modes<sup>138</sup> (as observed in Section 4.5)<sup>i</sup>.

### Cascaded four-wave mixing

Once the first new comb lines are generated in the degenerate FWM step, these new light frequencies can themselves act as additional pump or seed laser and create more comb lines via degenerate and non-degenerate FWM. Eventually this results in a vast cascade of FWM processes that can give rise to a  $\Delta$ -spaced frequency comb. As before the exact preservation of the frequency spacing  $\Delta$  is a consequence of energy conservation in FWM processes. The bandwidth growth of the four-wave mixing cascade is typically limited by the resonator dispersion, which results in a growing mismatch between resonance frequency and the equidistant  $\Delta$ -spaced comb lines. Effects of non-linear mode-pulling (via SPM and XPM) in combination with spectral intensity variations in the resonator can, however, effectively alter the mode structure and pull more resonance into suitable frequency positions (similar to the first degenerate FWM step described above where the SPM, XPM and dispersion compensated for one another). A more detailed and quantitative understanding of frequency comb generation in a microresonator will be presented in Chapter 2, where we will see that the value of  $\mu_{\text{th}}$ , which may be large, has a decisive influence on the noise properties and frequency comb nature of the generated spectra.

---

<sup>i</sup>Theoretical work suggests that the generation of Kerr-combs in the normal dispersion regime may be possible.<sup>139</sup> This, however, has so far not been demonstrated experimentally.

### 1.3. Microresonator based optical frequency combs

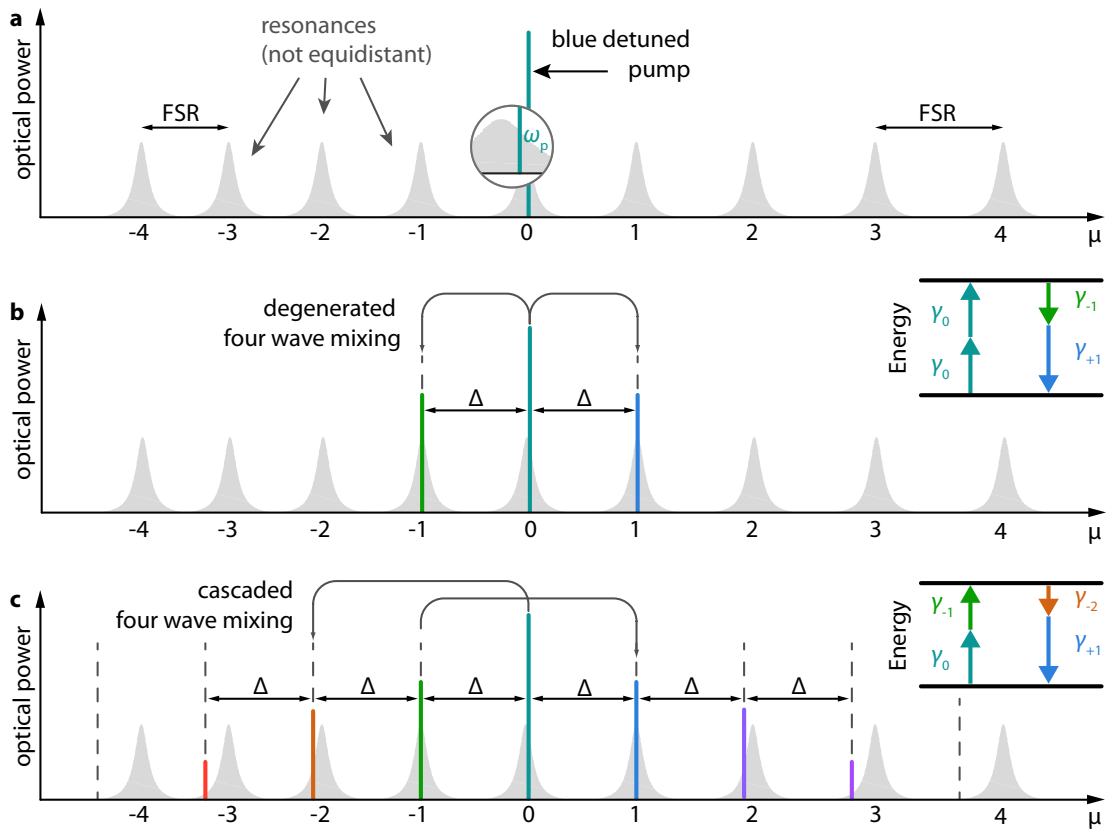


**Figure 1.13: Frequency comb generation via four-wave mixing in a microresonator. a.**

The microresonator modes with relative mode number  $\mu$  are illustrated by solid gray Lorentzians. Due to dispersion the resonance frequencies are not exactly equidistant which leads to varying free-spectral ranges. Here the case of anomalous dispersion is shown, where the FSR increases with mode number (compare the two marked FSRs). For frequency comb generation a blue detuned pump laser  $\omega_p$  is coupled to one of the resonances (relative mode number  $\mu = 0$ ). **b.** Symmetric  $\Delta$ -spaced sidebands are generated symmetrically around the pump laser in a degenerate four-wave mixing process. The inset illustrates the annihilation of two pump photons  $\gamma_0$  and the creation of two photons  $\gamma_{\pm 1}$  in the resonator modes adjacent to the pump. **c.** Cascaded four-wave mixing generates a  $\Delta$ -spaced frequency comb spectrum where the bandwidth is limited by the mismatch between equidistant,  $\Delta$ -spaced comb lines and non-equidistant resonance positions. The inset illustrates the annihilation of a pump photon  $\gamma_0$  and a sideband photon  $\gamma_{-1}$ , as well as the creation of two photons  $\gamma_{-2}$  and  $\gamma_{+1}$ .

### Time domain output of microresonator based frequency combs

The process of (cascaded) FWM that leads to the formation of the comb is phase sensitive (cf. eq. 1.23 and 1.24) and can consequently, in a steady state, results in constant mutual phase relations between comb lines. These phase relations depend on the comb state<sup>j</sup> and result in a periodic but not pulsed intracavity waveform. Pulses may be formed external to the resonator by individually manipulating the phase of each comb line such that a pulse forms.<sup>97,124</sup> In Chapter 4 we present soliton formation as a mechanism that allows to generate pulsed waveforms directly in a microresonator.

### Stabilization of microresonator based frequency combs

Microresonator combs can routinely be stabilized.<sup>79,123,125</sup> Like in conventional combs this requires that the two parameters, comb line spacing and comb offset frequency can be controlled independently. As the pump laser already constitutes a comb line the offset control corresponds to controlling the pump laser frequency (where the thermal lock, Section 1.3.3 ensures that the resonator stays locked to the pump laser frequency). The line spacing of the comb can be controlled by actuating the FSR of the resonator. One all-optical method<sup>123,125</sup> relies on the fact that small changes in the pump power modify the FSR via thermorefractive index change, thermal expansion and Kerr-effect (cf. Section 1.3.3). Another method employs mechanical stress<sup>79</sup> induced by a piezo mechanical actuator to alter the shape and circumference of the resonator. Prerequisite to controlling the comb parameters is their detection and measurement (unless individual comb lines are referenced to external optical frequency standards). This limits the comb line spacing to frequencies of currently below  $\sim 100$  GHz, where sufficiently fast detectors are available. The detection of the offset frequency is more challenging as it requires that two different harmonics of the comb spectrum have a spectral overlap. Practically, an octave or at least two thirds of an octave spanning spectrum is required. In Chapter 2 we present an octave spanning spectrum directly generated in a microresonator, in Chapter 4 we will harness ultra-short soliton pulses generated in a microresonator for external nonlinear spectral broadening of the comb spectrum to well beyond two thirds of an octave.

All combs in this work are operated in a free-running mode, that is without active control of line spacing or offset frequency. While these combs could in principle be stabilized with the methods described above, the focus of this work is on the physical mechanism of microresonator based comb generation.

---

<sup>j</sup>It is to date not clear whether the phase relation are entirely random (but constant) or if the non-linear system has an attractor that causes identical phase relations for identical experimentally controllable parameters.

### 1.3.5 Competing non-linear processes

FWM mixing is not the only relevant nonlinear optical process that can occur in a  $\chi^{(3)}$ -nonlinear microresonator. As discussed above (cf. Section 1.3.2) other parametric processes such as third harmonic generation and triple sum frequency generation are possible and have been observed (see references given above). Typically these processes are not within the comb bandwidth and are not of interest for the present case. In addition stimulated Brillouin- and stimulated Raman-scattering are efficient nonlinear processes that can compete with FWM. Both processes are inelastic photon-phonon scattering processes in the resonator material. Different from FWM, these inelastic scattering processes do not conserve the photonic energy, which is a requirement for equidistant comb spectra.

#### Stimulated Raman Scattering

Stimulated Raman scattering<sup>135</sup> (SRS) is an inelastic scattering process where photons of the pump field  $\omega_p$  are scattered off optical phonons  $\Omega_R$  (molecular vibration) inside the material. In the stimulated process the scattered light field has an altered frequency of

$$\omega_R = \omega_p - \Omega_R. \quad (1.31)$$

The Raman shift  $\Omega_R$  of dielectrics is typically on the order of 10 THz. SRS can be understood in terms of a model, where it is assumed that the molecular vibration can be described by a damped harmonic oscillator with resonance frequency  $\Omega_R$ . Further it is assumed that the polarizability of the molecules depends on the internuclear separation. Consequently an oscillating molecule will lead to a modulation of the refractive index with frequency  $\Omega_R$ . It can be shown that the refractive index modulation with frequency  $\Omega_R$  leads to an amplification of the field with  $\omega_R$ , which in combination with the pump field  $\omega_p$  drives the molecular oscillation.<sup>135</sup> The SRS threshold power for the case of a critically coupled microresonator can be estimated to

$$P_{\text{in}}^{\text{th,SRS}} \approx \frac{\kappa^2 n_0^2 V_{\text{eff}}}{4g_R c^2}, \quad (1.32)$$

where  $g_R$  denotes Raman gain.<sup>82, 107, 108</sup> The maximum FWM gain is only a factor of two higher than the maximal Raman gain.<sup>107</sup> Particularly when pumping in the normal dispersion regime, where the initial degenerate FWM process is suppressed SRS can be observed. Microresonator based Raman-lasing has been demonstrated<sup>82, 107, 108</sup> and a transition between FWM and SRS regimes as function of pump laser detuning has been reported.<sup>71</sup>

SRS is not an energy conserving process. Consequently, if SRS takes part in the comb formation as a frequency defining process (i.e. a line is first generated by an SRS process) it can lead to non-equidistant optical lines and prevent comb generation. Due to the broadband gain bandwidth, SRS may however serve as an additional gain mechanism transferring energy from the pump to comb lines that have initially been generated by FWM. In this case the equidistance of the lines is guaranteed by FWM and the SRS serves as an additional amplification process.

### **Stimulated Brillouin scattering**

Stimulated Brillouin scattering (SBS)<sup>135</sup> is an inelastic scattering process where photons of the pump field  $\omega_p$  are scattered off acoustic phonons  $\Omega_B$  inside the material. In a 1-dimensional geometry, corresponding to the microresonator case, the scattered light field has a reduced frequency of

$$\omega_B = \omega_p - \Omega_B. \quad (1.33)$$

The beating between  $\omega_p$  and  $\omega_B$  can then via electrostriction<sup>k</sup> drive the scattering acoustic mode. This further enhances back-scattering, which leads to a positive feedback mechanism. The SBS threshold power<sup>109</sup> for the case of a critically coupled microresonator can be estimated to

$$P_{\text{in}}^{\text{th,SBS}} \approx \frac{\kappa^2 n_0^2 V_{\text{eff}}}{4g_B c^2}, \quad (1.34)$$

where  $g_B$  denotes the Brillouin gain. Compared to SRS  $g_B$  is approximately two orders of magnitude larger than  $g_R$ .<sup>109</sup> Thus compared to FWM and SRS, SBS has a much lower threshold. Based on this alone one would expect SBS to be the dominating process in nonlinear microresonators. Indeed, SBS has been observed in microresonators and has been used for the implementation of low threshold microresonator based Brillouin-lasers.<sup>81, 109, 110, 140</sup> Here the the ‘acoustic’ frequency  $\Omega_B$  is typically on the order of 10 GHz. However, for SBS to be relevant in a microresonator, it is required that the frequency  $\omega_B$  is supported by a cavity resonance. The bandwidth of the Brillouin gain is determined by the decay rate of the phonons and typically below 100 MHz. Due to this narrow spectral gain window and the high finesse  $F$  of a microresonator, it is extremely rare that this condition is fulfilled unintentionally. Thus, despite being a high gain non-linear process, it is not relevant in the case of microresonator based frequency comb generation.

---

<sup>k</sup>material compression in the prescience of an electrical field that relates to the non-instantaneous part of the  $\chi^{(3)}$ -nonlinearity

### 1.3.6 Setup for frequency comb generation

The generic setup for frequency comb generation is shown in Figure 1.14. Here a tunable monochromatic pump laser is evanescently coupled to the microresonator via a tapered single-mode fiber or an integrated on-chip waveguide. To enable thermal locking (cf. 1.3.3) the pump laser is tuned towards a microresonator resonance with decreasing optical frequency. This leads to a build-up of intracavity power and a frequency comb spectrum may be generated as it is described above in Section 1.3.4. The coupling waveguide also serves to extract the generated comb spectrum from the resonator. During comb generation the optical spectrum, the transmission through the resonator and the RF beatnote generated by the mutual beating between the comb lines are monitored. Once thermalized the system can stay thermally locked over many hours without any adjustments to the pump laser. Figure 1.15 shows the optical spectrum of a microresonator based comb and the corresponding RF beatnote.

Depending on the experiment additional components and methods are employed. These will be described in their specific context in the Chapters 2, 3 and 4.

### 1.3.7 State-of-the-art in microresonator based frequency combs

Only discovered<sup>72</sup> in 2007, microresonator based frequency combs are far from maturity. The state-of-the-art of this dynamic field has rapidly evolved over the last years:

- **Equidistance and phase-stability:** The verification of the equidistance of the comb lines on a level comparable with conventional frequency comb technology has been demonstrated.<sup>72, 75, 79, 124, 125</sup> Moreover, the long-term relative phase stability among the comb lines has been shown.<sup>97, 124</sup>
- **Full stabilization:** Techniques to stabilize microresonator frequency combs have been developed, using all optical heating or mechanical actuation on the microresonator in order to modify its FSR, which in turn allows stabilizing the comb line spacing.<sup>79, 123–125</sup> Note that the offset frequency of microresonator based combs is easily controllable by the pump laser frequency, which defines one of the comb lines.
- **Variety of resonator platforms:** A variety of different resonator types has been developed including CMOS-compatible resonator platforms (see Section 1.2.1). The development of new resonators includes efforts of engineering the dispersion properties.<sup>4, 5, 80, 133</sup>
- **Extension of the spectral coverage into the visible:** So far, the requirement of anomalous dispersion limits microresonator combs to optical wavelength longer

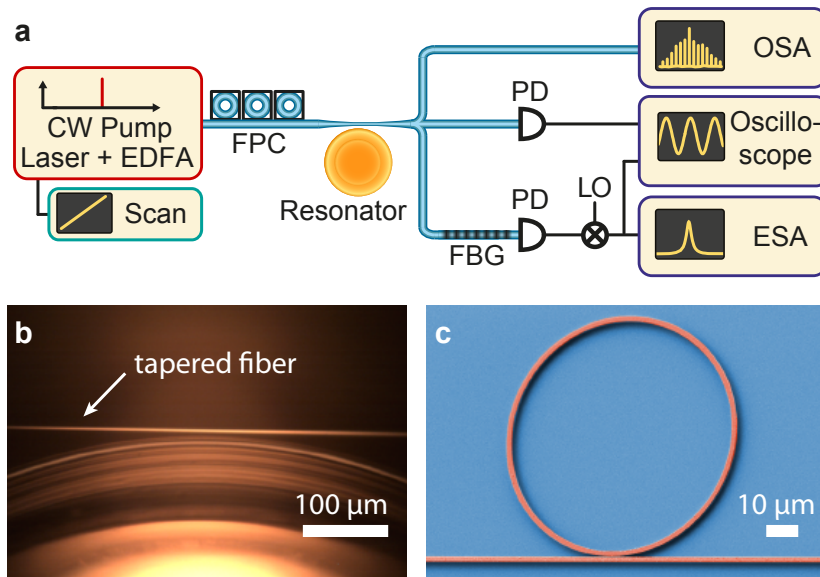


**Figure 1.14: Generic setup for frequency comb generation.** **a.** The main components of the setup are a pump laser, a microresonator and electronics for monitoring the generated frequency combs. All optical links are fiber based (light blue lines). The pump laser is a tunable near-infrared cw laser source around 1550 nm wavelength. Its optical power is adjustable ranging from 1 mW up to several W. The higher power levels are achieved by using an erbium-doped fiber amplifier (EDFA). The pump is evanescently coupled from the coupling waveguide into the microresonator after polarization optimization for maximal coupling efficiency to the resonance using a fiber polarization controller (FPC). The evanescent coupling is achieved using a tapered fiber with adjustable distance to the resonator or a chip-integrated waveguide at a predefined distance to the resonator. The generated comb spectrum is coupled out in the same way and then send to an optical spectrum analyzer (OSA), to a photodetector (PD) to monitor the transmission through the coupling waveguide and to a fast photo-detector to detect the RF beatnote between neighboring comb lines. The detected RF beatnote is monitored on an electronic spectrum analyzer (ESA). Note that prior to the RF beatnote detection the pump light is filtered out using a fiber-Bragg grating (FBG). Depending on the frequency of the RF beatnote it is necessary to down-convert it to frequencies measurable with the available RF equipment. The down-conversion is achieved using a harmonic mixer in combination with an RF local oscillator (LO). **b.** Optical microscope image showing the tapered fiber used to couple light into and out of a  $\text{MgF}_2$  resonator (lower half of the image, top view). A similar configuration is used to couple light to fused silica microtoroids. **c.** Scanning electron microscope image showing a  $\text{Si}_3\text{N}_4$  resonator and integrated coupling waveguide (red) on the  $\text{SiO}_2$  substrate (blue). The image was taken before adding the protective cladding. The coupling to the resonator is achieved by the fixed on-chip coupling waveguide. The optical fiber-to-chip coupling is achieved using lensed fibers.



### 1.3. Microresonator based optical frequency combs

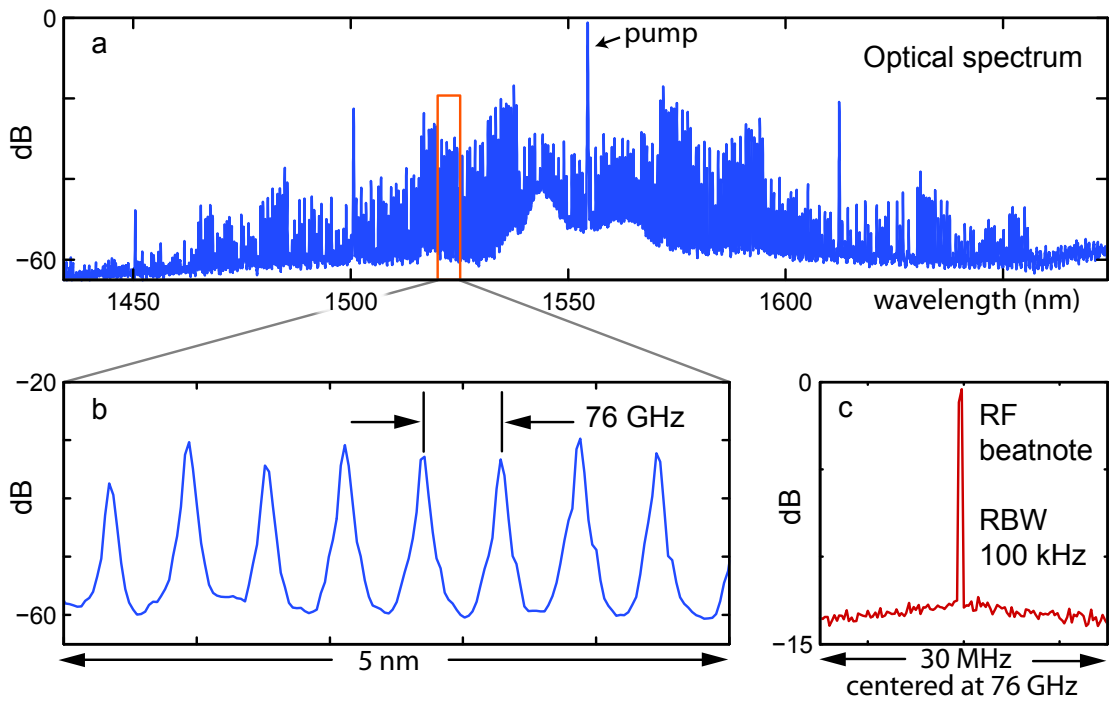


**Figure 1.15: Optical spectrum and RF beatnote of a microresonator based frequency comb** **a.** Optical spectrum generated in a  $\text{Si}_3\text{N}_4$  microresonator with a FSR of 76 GHz. **b.** Zoom into the optical spectrum (c) resolving individual comb lines. The apparent width of the comb lines is given by the resolution limitation of the optical spectrum analyzer. **c.** RF beatnote resulting from the beating between neighboring comb lines. Note that the rather low signal-to noise ratio of below 15 dB results from the RF cutoff of the photodetector (3-dB cutoff at 45 GHz).

than 1  $\mu\text{m}$ . Dispersion engineering is expected to move this frontier towards shorter wavelength. Though inherently limited to a few comb lines only, FWM between higher order transverse modes provide a way to operate microresonator based combs independently of material dispersion.<sup>85,132</sup>

- **Extension of the spectral coverage into the mid-infrared:** The mid-infrared regime is highly important for molecular spectroscopy applications in research and technology. In Chapter 3 we explore the potential of microresonator based comb in the mid-infrared.<sup>2</sup>
- **Wide range of comb line spacings:** Comb line spacings ranging from few GHz to THz frequencies have been demonstrated as illustrated in Figure 1.8. Narrow comb line spacings are challenging as the finesse of the microresonator decreases. Large comb line spacings ( $> 100$  GHz) can not easily be detected (and hence stabilized), with currently available detectors. Recently, an approach to detecting comb line spacing frequencies beyond the bandwidth of available detectors has been demonstrated.<sup>125</sup>
- **Theoretical description:** Theoretical advances in the field of Kerr-combs include an analytic understanding on threshold and dynamics of comb formation<sup>3,71,141</sup> (see also Chapter 2), as well as, the introduction of coupled mode equations to the field of Kerr-combs.<sup>142–144</sup> This approach can be employed to realistically describe and simulate the spatio-temporal dynamics of Kerr-comb.<sup>1,145,146</sup> More recently the mean-field model, well established in fiber based systems, has been successfully used to describe stable comb states and the achievable comb bandwidth.<sup>147,148</sup>
- **Understanding of the comb formation dynamics:** So far only the general principle of comb generation in nonlinear microresonators was understood. The rich nonlinear dynamics of these systems, however, remained largely unexplored. This work contributes a first detailed understanding of the comb formation dynamics in the spectral domain. The latter particularly includes the explanation of noise phenomena and transition to low noise operating regimes (Chapter 2).<sup>3</sup> More recently, parametric seeding experiments have been used to deliberately influence the comb formation.<sup>149</sup>
- **Mode-locking:** While frequency comb generation has been demonstrated in a variety of microresonator platforms it was so far not possible to achieve intrinsic phase and intensity adjustment of the comb lines, such that pulses are formed inside the microresonator. It was not clear if mode-locking can be achieved in microresonator based combs. This work demonstrates that mode-locking can be achieved via soliton formation and provides a solid theoretical understanding of this process (Chapter 4). A pulsed time domain output has very recently

also been observed in independent research<sup>127</sup> and may as well be explained by soliton formation. Whether other mode-locking mechanism besides soliton formation exist is subject of future research.

- **Self-referencing:** So far microresonator based combs can not be self-referenced and full stabilization is only possible by referring to external absolute frequency standards. Specifically, it is so far not possible to detect the offset frequency  $f_0$  of microresonator based combs. The latter is challenging as it requires a broadband comb spectrum (such that different frequency harmonics of the spectrum overlap spectrally). This work demonstrates that in principle octave spanning spectra, as required for  $f-2f$  self-referencing, can be generated directly in a microresonator (Chapter 2).<sup>5</sup> More recently, octave spanning spectra were also demonstrated in  $\text{Si}_3\text{N}_4$  microresonators.<sup>131</sup> It remains, however, challenging to achieve octave spanning spectra while maintaining low noise performance. An alternative way towards broadband spectra for self-referencing can be based on external spectral broadening as it is usually done for conventional frequency combs. External broadening, however, requires ultra-short optical pulses not generally provided by microresonators. The direct ultra-short pulse generation in microresonators, may provide a viable route to self-referencing (Chapter 4).

Microresonator based frequency combs have rapidly evolved within half a decade since their discovery. While the technology is still far from maturity and open scientific questions remain, the achieved advances are encouraging and motivate further research and development.



## 2 Formation dynamics and noise in microresonator based frequency combs

The starting point of this chapter is the first generation of an octave-spanning optical frequency comb directly from a microresonator. The comb spectrum covers the wavelength range from 990 nm to 2170 nm and is attained from a continuous wave laser coupled to a fused silica microresonator, without relying on additional external broadening. The ability to derive octave spanning spectra from microresonator comb generators represents a key step towards  $f$ - $2f$ -self-referencing and broadband frequency comb application of microresonator-based optical frequency combs.

In the octave spanning spectrum we observe unexpectedly and for the first time significant frequency noise in the comb lines. Follow-up experiments characterizing noise in other microresonator systems show that frequency noise is a general problem severely limiting the microresonator based comb technology. These noise phenomena can not be understood within the so far developed theory of microresonator based comb formation. This understanding, however, is crucial to mature the microresonator based comb technology. This chapter describes, how based on observations in  $\text{SiO}_2$  toroids, crystalline  $\text{MgF}_2$  and planar  $\text{Si}_3\text{N}_4$  microresonators, a detailed understanding of the formation of dynamics of microresonator based combs is developed. This understanding explains the observed noise phenomena and allows to identify low noise operating regimes.

Section 2.1 describes how frequency noise, observed for the first time in an octave spanning spectrum, emerges as a universal problem in microresonator based combs. The noise problem is then linked to the formation dynamics of the microresonator frequency combs, which is investigated in Section 2.2. Section 2.3 explains in detail how the formation dynamics of a comb determines its noise properties. In Section 2.4 low noise regimes and the transition to low noise operation is investigated.

### 2.1 Noise in broadband spectra with many comb lines

The possibility of generating broadband spectra directly in a microresonator is an advantage of microresonator based combs over mode-locked laser based combs. In a microresonator the achievable bandwidth is not limited by the width of the laser gain medium but rather by the dispersion of the microresonator, which is responsible for an offset between the cavity resonances and the comb modes. After the successful demonstration of frequency comb generation in SiO<sub>2</sub> toroids with spectra comprising 30-60 comb lines<sup>72, 123</sup> it is the next plausible step to fully exploit the potential of this platform towards broader spectra. In Section 2.1.1 it is shown that indeed broadband, octave spanning spectra can be generated directly in a microresonator, if the dispersion is optimized.

However, along with the remarkable generation of an octave spanning spectrum comes the first and surprising observation of comb linewidth broadening, which is reported in Section 2.1.2 and 2.1.3. This constitutes the first observation of significant noise in a microresonator based comb. It is found that the comb lines exhibit a linewidth of 70 MHz, that is, much wider than the linewidth of the used pump laser (300 kHz, shortterm). In Section 2.1.4 we will see that broad comb lines, and more generally frequency noise, appears to be a general problem encountered in the generation of microresonator based combs. In Section 2.1.5 it is proposed that the observed noise does not arise from conventional noise processes but from the frequency comb formation dynamics itself. The understanding of the connection between microresonator based comb formation and noise will then be in the focus for the remainder of this Chapter.

#### 2.1.1 Generation of an octave-spanning spectrum in a SiO<sub>2</sub> toroid

##### Toroidal microresonator and dispersion engineering

The dispersion of a microresonator (together with the nonlinear resonance shifts) determines the mismatch between equidistant comb lines and effective resonance frequencies. Ideally this mismatch is small over a wide wavelength range, such that the resonator supports broadband spectra. For the generation of the octave spanning spectrum, a fused silica microtoroid is used. The geometry of a microresonator is an important contributor to the resonator dispersion (cf. Section 1.2.1) and thus critical for its potential for broad comb generation. In order to optimize the dispersion, different microresonator geometries were simulated using finite element methods.<sup>150</sup> The simulations take the bulk material and the geometric dispersion into account. The different simulated geometries are defined by a fixed outer diameter of 80  $\mu\text{m}$  and different toroid cross-section diameters (cf. Figure 2.1, inset). Based on these simulations

## 2.1. Noise in broadband spectra with many comb lines

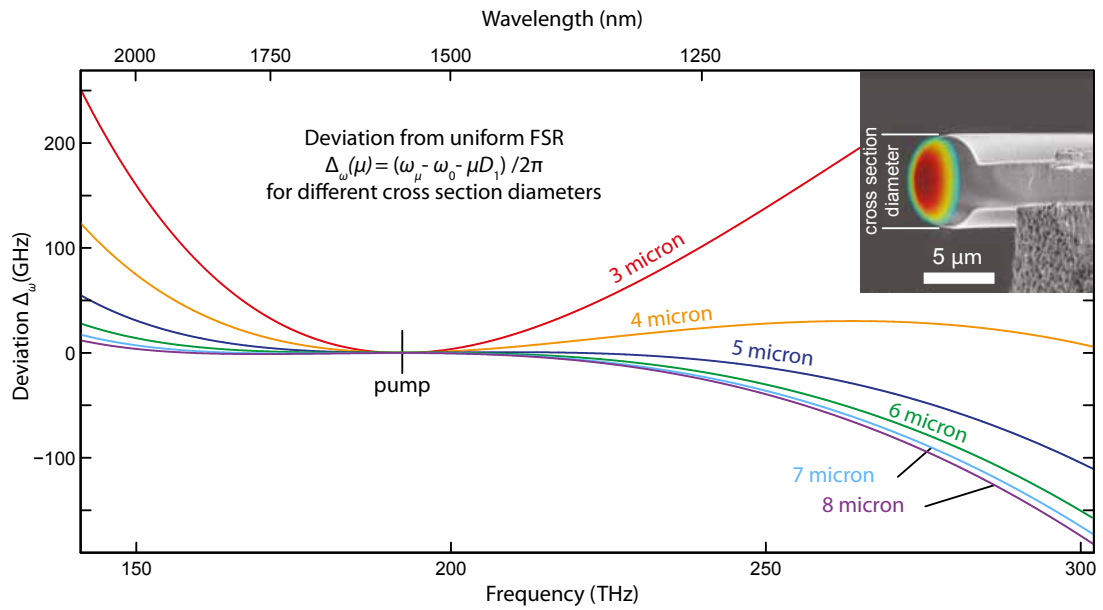


**Figure 2.1: Simulation of dispersion in a microtoroid.** The curves show the dispersion induced deviation between the simulated resonance frequencies and the frequencies that would have been expected for a FSR that is spectrally uniform and defined at the pump frequency. The different curves correspond to different resonator geometries that are characterized by a common radius  $R = 80 \mu\text{m}$  and a varying cross section diameter (see inset) as specified in the graph. Flatter curves imply less spectral variation in the FSR. Convex (concave) curves correspond to anomalous (normal) dispersion. Note that the continuous curves interpolate between the discrete simulated resonance values. The inset shows the mode profile of an optical mode at approximately 1560 nm with an effective mode area of  $A_{\text{eff}} = 4 \mu\text{m}^2$ .

the deviation of the cold resonance frequencies  $\omega_\mu$  from an equidistant frequency grid is derived. Mathematically this deviation is given by  $\Delta_\omega(\mu) = (\omega_\mu - \omega_0 - \mu D_1) / 2\pi$ , where  $\omega_0$  is the frequency of the pumped resonance and the parameter  $D_1 / 2\pi$  corresponds to the FSR at the pump frequency (cf. Section 1.2.1). The simulations (Figure 2.1) show that the size of the cross section diameter (which is controllable in the fabrication process) has considerable influence on the dispersion or equivalently the deviation  $\Delta_\omega(\mu)$  from a uniform resonance frequency grid. A close to uniform FSR is beneficial for broad comb generation as the mismatch between equidistant comb modes and microresonator modes is smaller over a given wavelength range. Based on the simulations a cross section diameter close to 6 micron is found to be ideal in terms of uniformity of the FSR. Note that the dispersion remains slightly anomalous (as required, cf. Section 1.3.4; convex curve in Figure 2.1) at the pump frequency if the cross section diameter is not chosen too large. Even for a dispersion optimized geometry the mismatch in the wings of an octave spanning comb exceeds several thousands of cavity resonance width. Owing to the Kerr-nonlinearity and the associated differential resonance shifts (cf. Section 1.3.3), this mismatch can be overcome and previously unexpected broad comb spectra can emerge.

### Generation of an octave spanning spectrum

For octave spanning frequency comb generation we employ a high-Q fused silica, toroidal microresonator. The toroid has, as in the dispersion simulation, a diameter of 80  $\mu\text{m}$  corresponding to a FSR of 850 GHz and a cross section diameter of 5.6  $\mu\text{m}$ . Its pumped resonance has a width of approximately 1 MHz. The experimental setup (also see Figure 1.14) consists of an external cavity diode laser (ECDL) that is amplified by an erbium doped fiber amplifier (EDFA) to an output power of up to 2.5 W. The amplified light is coupled into the high-Q microresonator mode using a tapered optical fiber.<sup>87</sup> Owing to the high power coupled into the resonator, the optical modes experience a significant thermal frequency shift as a result of light absorption in the microresonator. This shift can be as high as 1 THz corresponding to a temperature change<sup>5</sup> of  $\Delta T = 800$  K. A sufficiently large sweeping range of the diode laser is required to optimize the coupling. Once the coupling between tapered fiber and microresonator is optimized, the laser is manually tuned into a resonance from high to low frequencies, which results in thermal locking<sup>113</sup> (cf. Section 1.3.3) of the microresonator mode to the pump laser. The optical frequency comb generated in the microresonator is monitored by two optical spectrum analyzers, which are required to cover the full spectrum. Figure 2.2a shows that when pumping with 2.5 W of optical power at 1560 nm, a spectrum spanning more than one octave (from 990 nm to 2170 nm), is directly generated within the monolithic microresonator and output coupled into the tapered fiber. The more narrowly spaced modes on the low frequency side of the spectrum are artifacts from the IR-B spectrum analyzer and correspond to the second order



## 2.1. Noise in broadband spectra with many comb lines

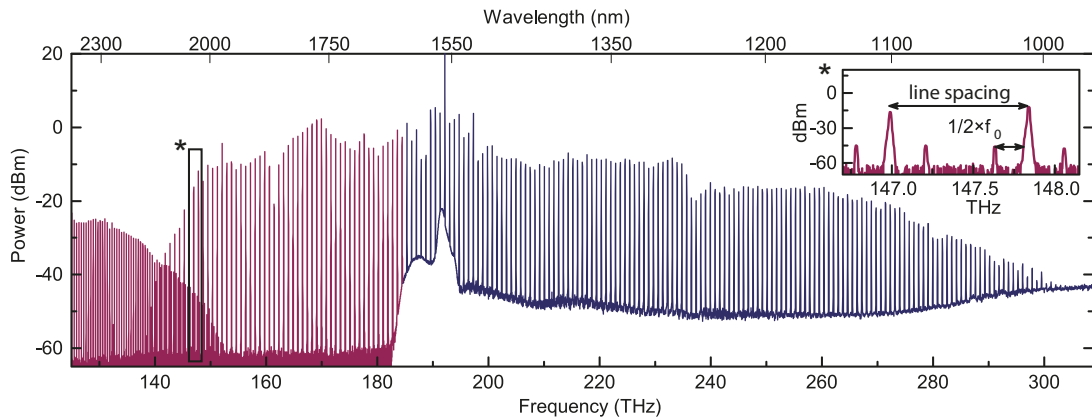


**Figure 2.2: Octave spanning frequency comb generation in a microresonator.** Octave spanning optical frequency comb, directly generated from a cw laser in an 80- $\mu\text{m}$ -diameter microresonator (comb line spacing  $f = 850$  GHz). Two different optical spectrum analyzers are been used (blue and purple) to record the full spectrum. The denser lines on the low frequency side are a replica of the high frequency end of the spectrum at half the frequency due to the grating spectrometer's second order diffraction. This artifact allows to determine the carrier envelope offset frequency (approx.  $f_0 = 160$  GHz) directly from the optical spectrum within the resolution of the spectrum analyzer (inset).

diffraction of the high frequency part of the spectrum (at 1  $\mu\text{m}$ ). Note that the comb's carrier envelope offset frequency  $f_0$  (which can be determined by the difference between first and second order diffraction, cf. inset Figure 1b) and mode spacing frequency are too high to be directly detected with a photodiode and stabilized with an  $f$ - $2f$  interferometer.

### 2.1.2 Characterization of frequency noise in microresonator based combs

While important, spectral span is not the only relevant criterion of a comb spectrum. Equally important is the frequency noise characteristics of the generated comb spectrum. We can distinguish frequency noise in individual comb lines (width of comb lines), frequency noise in the comb line spacing and frequency noise in the offset frequency. The latter is given by the pump laser frequency noise (cavity filtered, cf. Appendix B) and low compared to the other relevant forms of noise considered in this work. Frequency noise in an individual comb line can be measured by measuring the heterodyne beatnote between an external narrow linewidth laser (optical local oscillator) and the comb line. The effort of using an additional laser comes with the benefit of a high sensitivity due to the strong local oscillator. Frequency noise in the comb line spacing can be measured by detecting the RF beatnote, resulting from the beating between neighboring comb lines. Frequency noise in an individual comb line (a broad comb linewidth) and frequency noise in the comb line spacing (a broad RF

beatnote) are usually considered equivalent. On the one hand strong fluctuations in the comb line spacing, imply broad individual comb lines. On the other hand, broad comb lines, imply a not sharply defined comb line spacing. This rule applies with the one caveat of common frequency noise. If all comb lines fluctuate in a synchronized fashion (corresponding to a translation of the full comb) this would still result in a narrow, low noise RF beat note (corresponding to the still perfectly stable comb line spacing). All noise phenomena considered in this work are much broader in frequency than any fluctuation of the pump laser. As the latter constitutes a comb line, the special case of common frequency noise is not of relevance in the present context. In the following we will use the term ‘noise’ to refer to any frequency noise present in the comb.

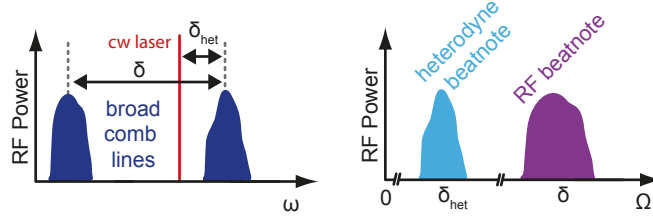


**Figure 2.3: Heterodyne and RF beatnote.** Optical frequency comb lines (dark blue) broadened by frequency noise. The noise induced broadening can be detected in the electronic domain either by recording a heterodyne beatnote (light blue) with a narrow cw laser (red) at the heterodyne beatnote frequency  $\delta_{\text{het}}$ , or if feasible by detecting the RF beatnote (beating between adjacent comb lines; purple) at a frequency of  $\delta/2\pi \approx \text{FSR}$ .

### 2.1.3 Observation of noise in a SiO<sub>2</sub> toroid

To access the noise properties of the generated octave spanning spectrum a fiber laser (1050 nm wavelength, < 50 kHz linewidth) is employed to record a beat note with a comb line in the blue wing of the comb (see Figure 2.4g for setup). This corresponds to the measurement of the linewidth of an individual comb line (the RF beatnote at almost THz frequency is too high to be detected). Surprisingly, the observed beatnote has a linewidth of  $\Delta f \approx 70$  MHz (resolution bandwidth 3 MHz), which is significantly broader than both, the linewidth of the employed pump laser (300 kHz shortterm) and the width of the cavity resonance (approx. 1 MHz). In particular, the measured comb linewidth is much broader than the linewidth observed earlier in similar spectra with fewer comb lines.<sup>72,123</sup> The measurement is shown in Figure 2.4a,b. Further measurements (in other comb states; Figure 2.4c-f) reveal that the width of the measured beat note exhibits a complex dependence on both, pump power and detuning of the laser with respect to the cavity resonance. It is observed that small changes in the detuning can lead to rather narrow or strongly broadened

beat notes, while the width and shape of the optical comb is almost the same.<sup>a</sup>

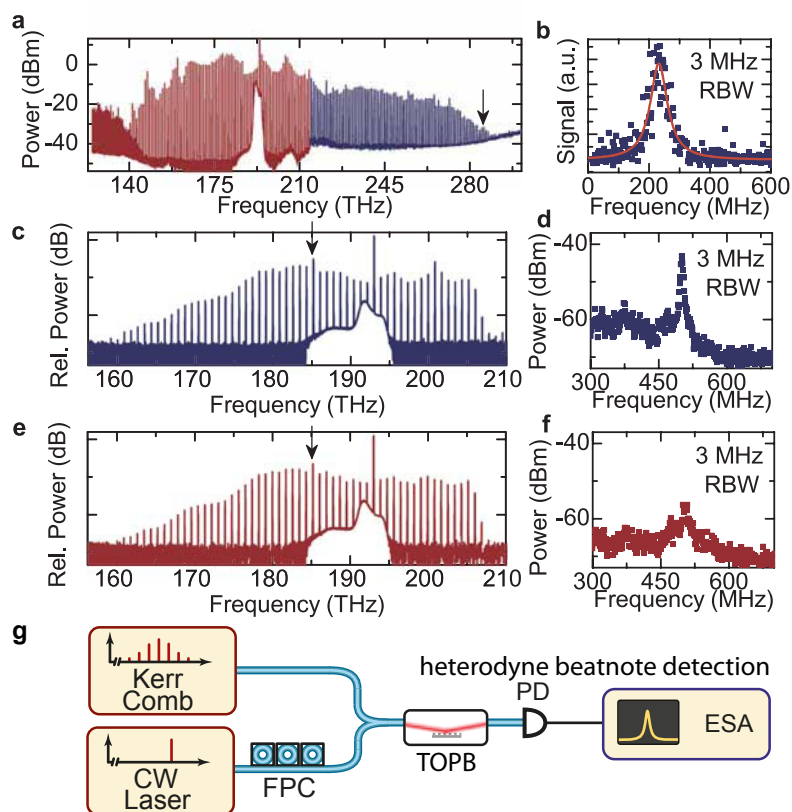


**Figure 2.4: Linewidth measurement of frequency comb modes.** **a,b.** Octave spanning comb and corresponding radio frequency beatnote with a fiber laser at 1050 nm (arrow in spectrum). **c,d.** Comb in a different resonator with rather narrow beatnote. **e,f.** The comb in (c,d) shows a transition to a broader beatnote when the pump laser detuning is changed. The beat notes in (d,f) have been generated with an additional external cavity diode laser at the positions of the arrows in the optical spectra in (c,e). **g.** Experimental setup for the heterodyne beatnote detection using an additional cw laser (FPC: fiber polarization controller; TOBP: Tunable optical bandpass filter to increase the signal-to-noise ratio; PD: Photodetector; ESA: Electronic spectrum analyzer).

### Potential noise mechanisms

A multitude of physical processes can in principle account or contribute to the observation of noise. These processes include line broadening frequency noise mechanisms, such as thermorefractive noise, thermoelastic noise, thermal Brownian motion, ponderomotive noise, photothermal noise, laser phase noise and effects related to self-/cross phase modulation.<sup>5, 151–153</sup> Frequency noise, and particularly, multiple RF

<sup>a</sup>This observation can be explained by  $\delta$ - $\Delta$ -matching described in Section 2.4.

beatnotes can also be generated by optomechanical oscillations resulting from the radiation pressure induced coupling between optical and mechanical modes,<sup>154–156</sup> as well as, by thermal oscillations of the resonator.<sup>157</sup> In Appendix B these noise processes are discussed for the case of the octave spanning spectrum in a microtoroid. There it is described that from the above noise processes all processes except the self-/cross phase modulational noise and radiation pressure driven mechanical effects can be excluded. The possibility of the self-/cross phase modulational noise, which could result from a high phase noise diode laser pump, as well as the mechanical effects, which are known to occur in the free-standing toroidal structure motivated the development of crystalline  $\text{MgF}_2$  microresonator for comb generation during the course of this work. It was then hoped, that a low noise fiber pump laser (which can not be employed in toroids due to the comparably large thermal shift exceed the typical fiber laser tuning range) and the more embedded mode volume would eliminate the noise processes. However, as it will be explained in the next section, this was not the case.

### 2.1.4 The universal problem of noise in microresonator based combs

While it was hoped that crystalline  $\text{MgF}_2$  microresonator would be less prone to noise (cf. previous section) the phenomenology prevails similar to the case of the  $\text{SiO}_2$  toroid in the form of broad RF beatnotes. The same holds true for  $\text{Si}_3\text{N}_4$  resonators, which, due to the embedding oxide layer, are not susceptible to mechanical vibrations (cf. Figure 2.5). Similar observations are made in other recent work aiming at higher number of comb lines to either increase spectral span or to achieve measurable lower repetition rates (below 100 GHz). Here noise is reported in the form of linewidth broadening<sup>5</sup> as described in the previous Section 2.1.3, in the form of multiple RF beatnotes<sup>124</sup> and in the form of low-frequency noise observed in the resonator transmission.<sup>131</sup> Moreover, recent complementary time domain studies using  $\text{Si}_3\text{N}_4$  waveguide resonators have revealed distinct paths to comb formation resulting in either highly or partially coherent behaviour.<sup>97</sup> This indicates that the problem of noise is not limited to broadband spectra in fused silica microresonators, but commonly observed in essentially all recent experiments with high numbers of comb lines. The observed noise phenomena are severely limiting the applicability of microresonator based combs. Understanding and remedy of this limitation is not only an open scientific question, but indeed crucial for bringing this new technology to maturity.

## 2.1. Noise in broadband spectra with many comb lines

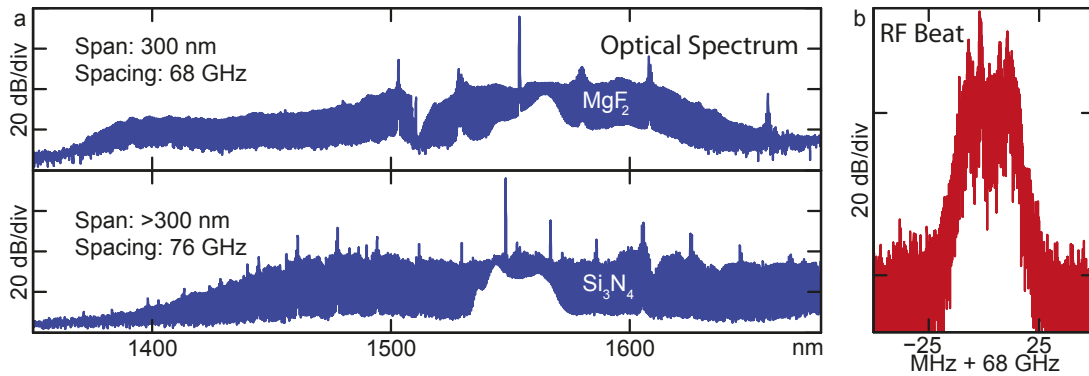


**Figure 2.5: Frequency noise in MgF<sub>2</sub> and Si<sub>3</sub>N<sub>4</sub> resonators.** a. Optical spectra generated in crystalline MgF<sub>2</sub> (pump power 500 mW) and Si<sub>3</sub>N<sub>4</sub> waveguide microresonators (pump power 3 W). Both spectra exhibit broad RF beatnotes, shown here for the MgF<sub>2</sub> resonator (resolution bandwidth 300 kHz).

### 2.1.5 Linking microresonator based comb formation dynamics and noise

To shed light on the origin of the frequency noise, we investigate the RF beatnote (in a MgF<sub>2</sub> system) and the heterodyne beatnote (in a Si<sub>3</sub>N<sub>4</sub> system) at different stages during comb formation. The results, shown in Figure 2.6, reveal an intriguing behaviour in both systems: The broad beatnote, visible in the lowermost data sets, emerges from a number of multiple narrow beatnotes, whose number is increasing as more power is coupled to the resonator. We observe, that both, intensity and frequency of these beatnotes can change continuously or discontinuously when the laser detuning is varied. This result *unifies* the observation of broad and multiple beatnotes made individually in earlier work.<sup>5,124</sup> The phenomenology prevails, both, in the crystalline MgF<sub>2</sub> and Si<sub>3</sub>N<sub>4</sub> systems despite their vastly different geometries and material characteristics showing the universality of the noise phenomenon. Figure 2.7 illustrates the complexity of the underlying physics. The observed beatnotes can be narrow or broad, embedded in an unresolved noise pedestal, and generally show a rich structure. By interpreting broad and multiple beatnotes as identical phenomena, pure line broadening phase noise mechanisms (such as self-/cross phase modulation) can be excluded as the principal reason for the observations. While crystalline resonators support mechanical radial breathing modes,<sup>69</sup> as well as surface acoustic modes,<sup>156,158</sup> which could give rise to multiple, modulation beatnotes and chaotic opto-mechanical oscillations,<sup>159</sup> the on-chip geometry of the Si<sub>3</sub>N<sub>4</sub> system (which has no free boundaries due to the embedding oxide) renders mechanical oscillations implausible.

Other, so far not discussed, potential noise mechanism include Stimulated Raman Scattering (SRS) and multi-mode effects between different mode families. SRS may

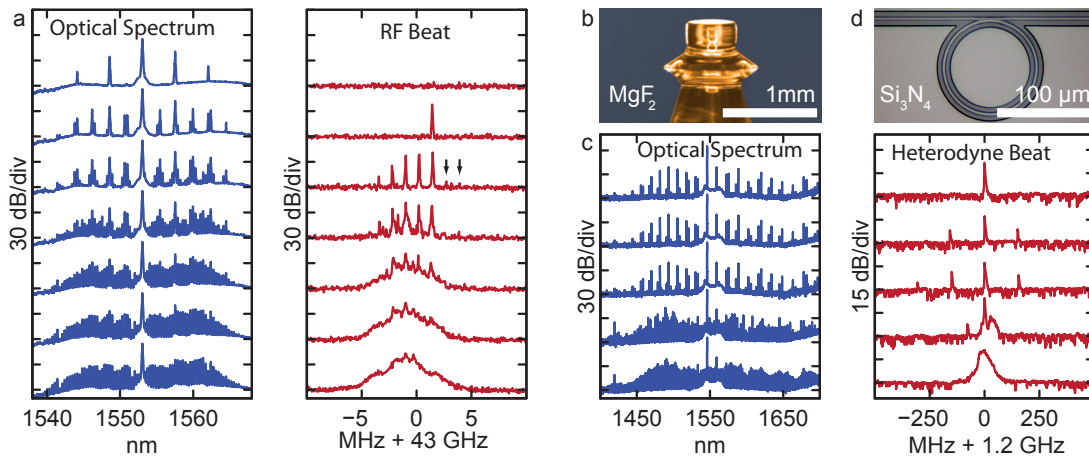


**Figure 2.6: Multiple and broad RF and heterodyne beatnotes.** **a.** Evolution of the optical frequency comb (blue, pump power 50 mW) in a  $\text{MgF}_2$  microresonator (FSR 43 GHz) and the RF beatnote (red, RBW 100 kHz) while tuning the pump laser into resonance. Arrows indicate smaller peaks. **b.** Photograph of a  $\text{MgF}_2$  microresonator similar to the one used in the measurement. **c.** As in (a) but for a  $\text{Si}_3\text{N}_4$  (FSR 200 GHz) microresonator. The measurement of the RF beatnote is replaced by an equivalent heterodyne beatnote measurement between a comb line and an external cw laser. **d.** Microscope picture of a  $\text{Si}_3\text{N}_4$  microresonator similar to the one used in the measurement.

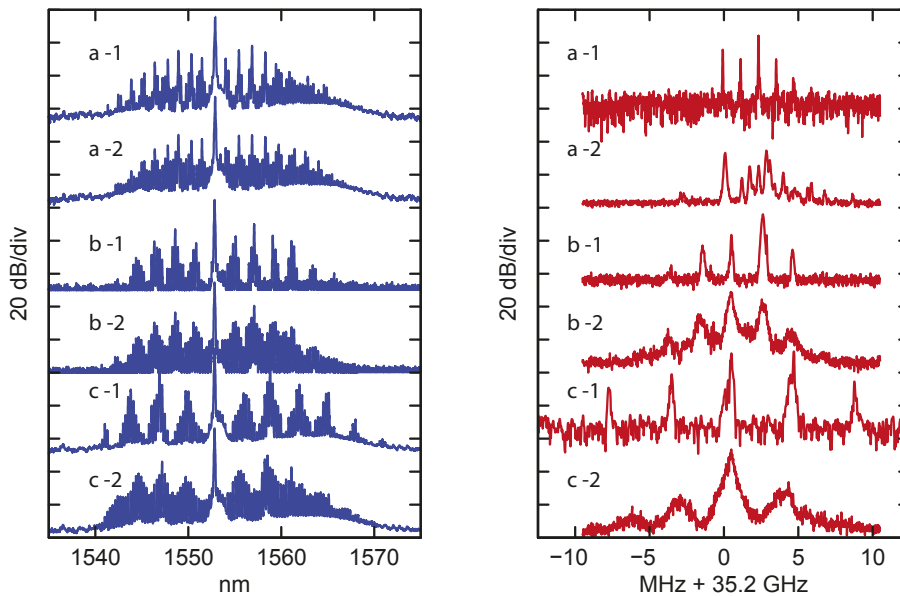


**Figure 2.7: Optical spectrum and RF beatnote.** Optical microresonator based comb spectra (blue) and corresponding RF beat notes (red) generated in a 35 GHz FSR  $\text{MgF}_2$  resonator by pumping different mode families (pump power 50 to 200 mW). Each comb (a,b,c) is shown in an early state of its evolution (a,b,c-1) and after increasing the intra-cavity power (reducing the detuning) (a,b,c-2).

result in ill-positioned comb lines, but seems unlikely given the symmetry of the spectra generated in the  $\text{MgF}_2$  resonator (Figure 2.7). Moreover, the comb span is much smaller than the expected Raman-shift of approximately 10 THz (80 nm). While multi-mode effects between different mode families in crystalline resonators have been reported,<sup>85</sup> these are unlikely as the general interaction between different mode families (with generally different FSRs) via FWM is suppressed by the requirement of phase matching (cf. Section 1.3.4).<sup>71</sup> Multi-mode interactions are even more unlikely in  $\text{Si}_3\text{N}_4$  resonators that are intrinsically close to single mode.

We suggest, that the cause for the broad and multiple beatnotes lies in the dynamics of microresonator based comb formation itself.

## 2.2 Microresonator based comb formation

In the previous Section 2.1 it is suggested that the comb formation process itself is responsible for the observed noise phenomena in microresonator based frequency combs. In the present Section we therefore study in detail the formation of microresonator based combs.

To generate a comb the pump laser is tuned into a resonance with a decreasing optical frequency to enable the thermal locking (cf. 1.3.3). The more the pump laser frequency approaches the (effective) resonance frequency, the higher the intracavity power and the parametric gain (cf. Appendix A.2.4). Figure 2.8 explains schematically the initial states of microresonator based comb formation. The first comb lines are generated in a degenerate FWM process symmetrically to the pump frequency  $\omega_p$ , as soon as the parametric gain overcomes the loss of the cavity (cf. Figure 2.8a). It has been observed, that the first lines can oscillate either in the resonator mode directly adjacent to the pump or at a multiple of this spectral distance.<sup>5,44,73,90,160</sup> This can be understood within the framework of nonlinear coupled mode equations<sup>3,142-145</sup> as detailed later on and in appendix A.2.5. In a simplified picture the sidebands are generated where dispersion  $D_2$ , nonlinear mode-shifts and pump laser detuning compensate each other.

### 2.2.1 Generation of subcombs

In the following, we distinguish two scenarios of comb formation and refer to these scenarios as *multiple* mode spaced (MMS) and *natively* mode spaced (NMS) combs:

### MMS combs:

In MMS combs the first parametric sidebands are generated at a frequency spacing  $\Delta$ , corresponding to a *multiple* mode number difference ( $|\mu| > 1$ ), away from the pump (cf. Fig 2.8a and Appendix A.2.5). Cascaded FWM transfers the initial spacing  $\Delta$  to order sidebands. The initial spacing  $\Delta$  is preserved and reproduced between all emerging lines, due to the conservation of energy in parametric FWM processes.<sup>72, 135</sup> We refer to all these initial sidebands spaced by  $\Delta$  as *primary* comb lines. At a later stage of the comb evolution (i.e. reduced detuning and increased circulating power) *secondary* lines are generated adjacent the primary lines via degenerate or non-degenerate FWM processes (cf. Figure 2.8b), resulting in natively  $\delta$ -spaced lines in neighboring resonator modes ( $\delta/2\pi \approx \text{FSR}$ ). The formation of lines in a second degenerate process can be understood in terms of parametric gain lobes that are broad enough to allow neighboring modes to be populated (cf. Appendix A.2.4). It is worth emphasizing that despite generally not uniform FSRs (resonator property) all subcombs have the same native spacing  $\delta$  (comb property), which will become clear later. The spectrally separated subcombs initiated in these processes grow via non-degenerate FWM when the power coupled to the cavity is further increased, and eventually merge to form a gap-free spectrum of lines (cf. Figure 2.8c). Note that the non-degenerate FWM process may also yield lines in between two previously existing strong lines (cf. Figure 2.9a,b and Appendix A.2.6). Combs of MMS type with this spectral evolution have so far been observed in systems possessing a smaller FSR (10 – 100 GHz) or high pump power ( $\gtrsim 1$  W).<sup>5, 5, 44, 73, 90</sup>

### NMS combs:

In NMS combs the first parametric sidebands are generated in the modes  $\mu = +1, -1$  adjacent to the pump.<sup>71, 72</sup> As such NMS combs are a special case of MMS combs where  $\Delta = \delta$  and non-degenerate cascaded FWM leads to the generation of a frequency comb spectrum growing outwards from the pump. No subcombs are generated in the NNS scenario. MMS combs can be interpreted as NMS with correspondingly higher FSR as long as only the primary lines exist.

### 2.2.2 Commensurability of subcombs

In the following we will investigate the properties of MMS combs to understand if and how their formation mechanism affects the width and number of the RF beatnotes. To do so, we perform a multi-heterodyne experiment between subcombs in the MMS scenario (in a  $\text{MgF}_2$  resonator with a FSR of 35 GHz) and a conventional stabilized mode-locked fiber laser comb of 250 MHz repetition rate. This method allows to accurately determine the spacing between select microresonator based comb lines



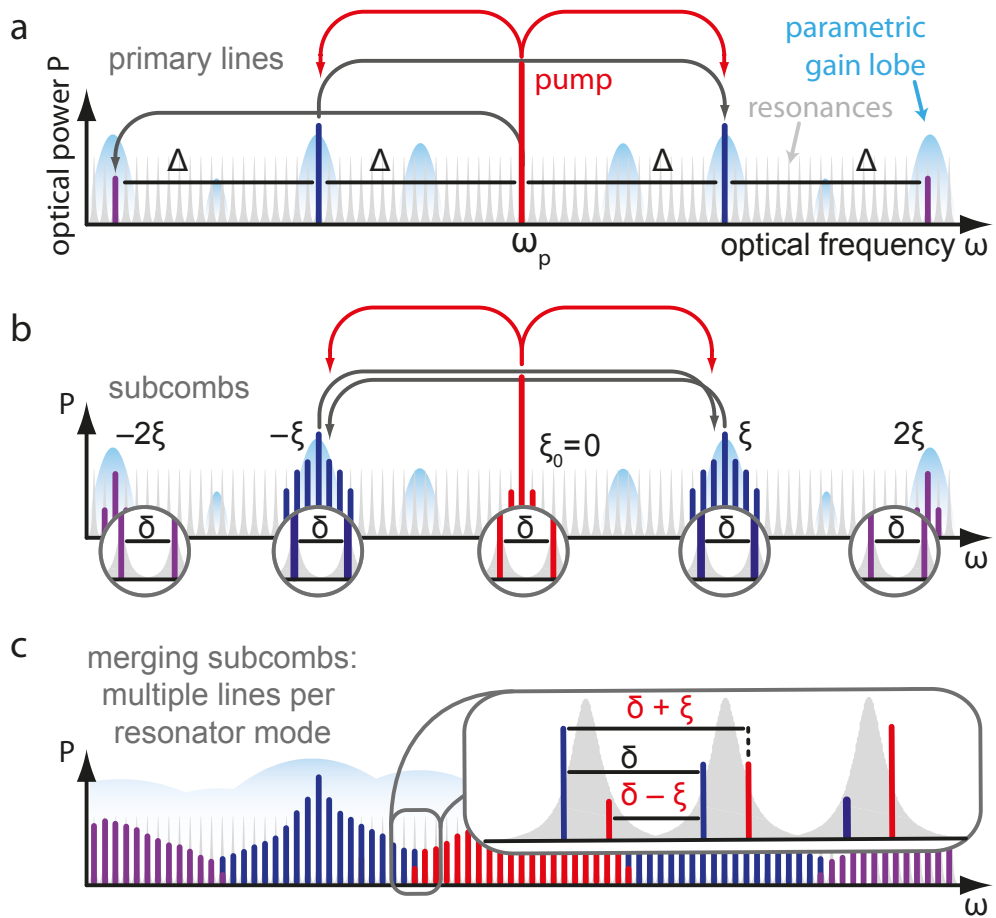


**Figure 2.8: Microresonator based comb formation via subcombs.** **a.** Generation of primary  $\Delta$ -spaced sidebands via four-wave mixing. **b.** Secondary lines around the primary lines form subcombs with a native spacing  $\delta$ . The spacing  $\Delta$  is not generally an integer multiple of  $\delta$ , i.e. the subcombs possess different offset frequencies  $0, \pm\xi, \pm2\xi, \dots$  **c.** The subcombs merge into a gap-free spectrum. Due to the different comb offset frequencies, this can result in multiple comb lines in individual resonance.

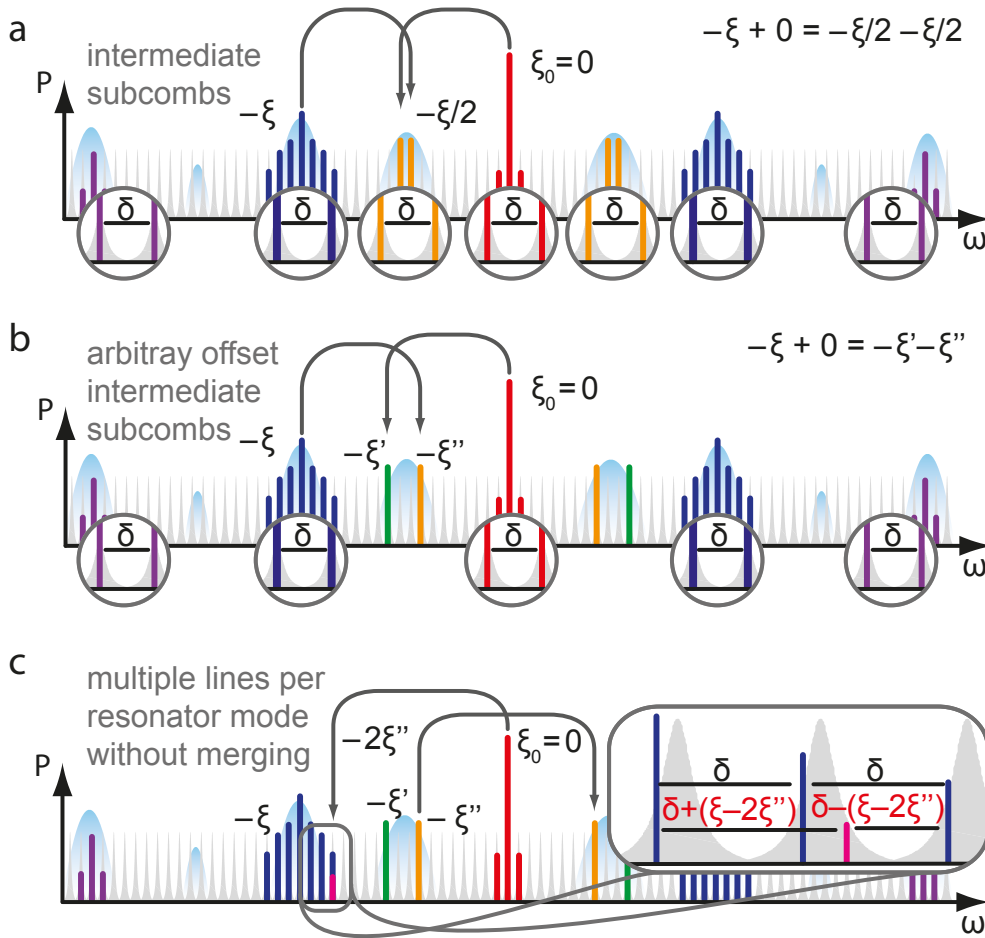


**Figure 2.9: Intermediate subcombs.** **a.** Natively spaced secondary comb lines may also emerge in between primary lines at an averaged offset frequency (indicated for the yellow lines with averaged offset  $-\xi/2$ ). **b.** Non-natively spaced secondary comb lines may be generated in between primary lines with arbitrary offsets  $-\xi'$  and  $-\xi''$ . **c.** As a result of state (b) multiple lines per resonator mode can appear already in sparse combs before the spectral gaps are closed.

(cf. Figure 2.10). In the multi-heterodyne experiment we address the vital question of the commensurability of primary and secondary comb lines. More precisely, it is tested whether the primary spacing  $\Delta$  is an integer multiple of the native spacing  $\delta$ , i.e. whether the generated optical spectrum forms an intermittent but consistent frequency comb, whose gaps can be filled by increasing the coupled power and extending the existing subcombs.

### Description of the multi-heterodyne experiment

A narrow linewidth, 1553 nm cw fiber laser is amplified by an erbium doped fiber amplifier (amplified spontaneous emission filtered) to 80 mW of power and sent to the MgF<sub>2</sub> resonator for microresonator based comb generation. The pump laser is offset locked to 20 MHz below a line of a 250 MHz repetition rate fiber laser comb. The performance of the lock is verified by an RF counter. The resonator is thermally locked to the pump laser and before each measurement the system is given sufficient time to thermalize. After comb generation the generated spectrum is split into several beams. One beam is sent to an optical spectrum analyzer for detection of the optical microresonator based comb spectrum, a second one is sent to a fast 45 GHz bandwidth photo-diode for detection of the RF beatnote between natively spaced neighboring comb lines. The electronic signal generated in the fast photodetector- is down-mixed using the third harmonic of a local RF oscillator at 11.7 GHz and sent to an electronic spectrum analyzer and another frequency counter. Note that, prior to the RF beatnote detection, the pump was attenuated by approx. 30 dB using a narrow (only affecting the pump laser line) fiber-Bragg grating in transmission. Finally, another fraction of the Kerr-comb power is combined with the spectrum of the fiber-laser comb. Two tunable optical bandpass filters (bandwidth 0.8 nm) are used to filter out two narrow spectral region of the combined comb spectra at the position of the primary Kerr-comb lines. The two filtered spectral portions are sent to two photodetectors for detection of the multi-heterodyne beatnote between the two combs (which typically exceed a signal-to-noise ratio of 20 dB in 300 kHz). The beatnotes frequencies are determined by frequency counters with a gate time of 0.1 s. The heterodyne beatnotes, in combination with the offset lock of the pump, allows to accurately determine the frequency difference between primary comb lines and pump frequency. Hereto we have assumed that the microresonator based comb lines do not deviate by more than 250 MHz from their positions expected based on the FSR of the resonator. The sign ambiguity in the beatnote signal (which only depends on the absolute value of the frequency difference between the comb lines) is resolved by varying the repetition rate of the fiber-laser comb in a controlled manner. All RF counters are synchronized by a common trigger signal.

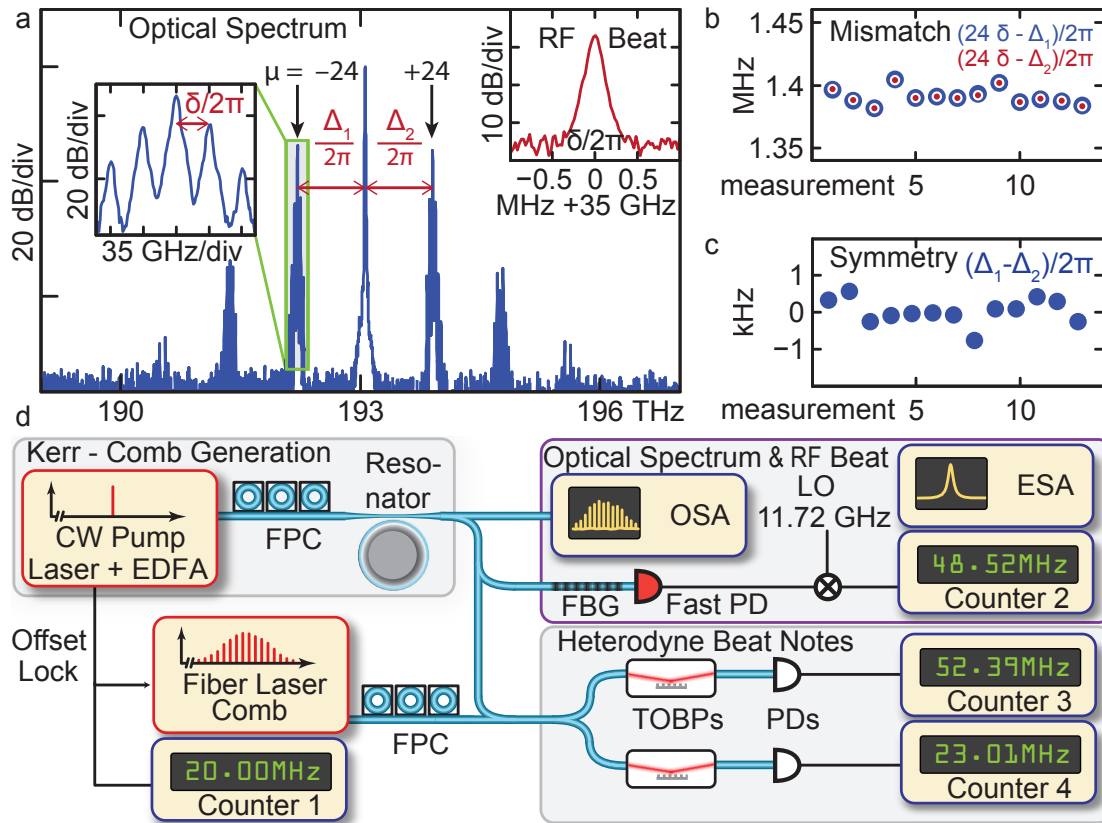


**Figure 2.10: Commensurability of the subcombs:** **a.** Optical microresonator based comb spectra generated in a 35 GHz FSR  $\text{MgF}_2$  resonator (pump power 80 mW, resonance width 1 MHz, pump laser offset locked to a fiber laser comb, primary spacing  $\Delta$  corresponds to 24 free spectral ranges). The secondary comb lines around the primary lines are spaced by the native spacing  $\delta$ . The resulting radio frequency (RF) beatnote consists of a single and narrow signal (cf. right inset, 35 dB in a resolution bandwidth of 300 kHz, pump attenuated by FBG prior to detection). Heterodyne beatnotes are generated between the innermost primary microresonator based comb lines and a conventional 250 MHz fiber laser comb. Frequency counting of all beatnotes allows for precise determination of the frequency distances  $\delta$ ,  $\Delta_1$  and  $\Delta_2$ . **b.** The spacing  $\Delta_1$  and  $\Delta_2$  are not integer multiples of  $\delta$ , but show a mismatch of 1.4 MHz. The open blue and the red circles correspond to redundant measurements of the mismatch. The perfect agreement between both measurements rules out potential systematic errors in the frequency counting. The different mismatches observed in different measurements are due to drifts of the free running system. **c.** Difference of  $\Delta_1$  and  $\Delta_2$  as indicated in **a.** No deviation from the symmetry of the primary comb lines with respect to the pump is detected. **d.** Experimental setup. EDFA: Erbium doped fiber amplifier; FPC: Fiber polarization controller; OSA: Optical spectrum analyzer; ESA: Electronic spectrum analyzer; FBG: fiber Bragg grating (attenuates the pump by 30 dB); LO: Local RF Oscillator; PD: Photodiode; TOBP: Tunable Optical Bandpass Filter.

### Commensurability of subcombs

As a striking result of the multi-heterodyne experiment we find that the subcombs are not commensurate. Specifically, a mismatch of  $(\mu \cdot \delta - \Delta)/2\pi \approx 1.4$  MHz, ( $\mu = 24$ ) between the actual position of the primary comb line and the expected position is observed, assuming a comb line grid with spacing  $\delta$  centered on the pump laser frequency. The experimental results are shown in Figure 2.10. The observed mismatch exceeds the precision of the measurement by far. The redundancy in performing this measurement with a pair of symmetric primary comb lines rules out artifacts in the frequency counting such as cycle slips that would lead to an incorrectly detected mismatch. Importantly, the RF beatnote resulting from the mutual beating between neighboring natively  $\delta$ -spaced comb lines is found well-defined and unique over the full spectral width of the optical spectrum (cf. right inset in Figure 2.10a). Based on these observations, we conclude that the optical spectrum consists of multiple, equidistant combs indexed  $i$ , composed of lines indexed  $n$ , at optical frequencies  $\omega_n^{(i)}$  separated by the same spacing  $\delta$ :

$$\omega_n^{(i)} = \omega_p + \xi_i + n \cdot \delta, \quad n = 0, \pm 1, \pm 2, \dots \quad (2.1)$$

These equidistant subcombs possess non-commensurate offset frequencies  $\xi_j \neq \xi_i + n \cdot \delta$ ,  $j \neq i$  as illustrated in Figure 2.8b. Whenever isolated lines (i.e. not in the direct vicinity of existing lines) are generated (cf. Figure 2.9b,c), new subcombs with new offsets are defined, which then can grow as described above. While the process shown in Figure 2.9b results in arbitrarily offset subcombs, processes similar to Figure 2.9a, result in a set of subcombs with equal relative offset differences  $\Delta\xi$  to their respective nearest-neighbor subcomb.

Even though all subcombs are spectrally separated and reside at spectral positions with different resonator FSR, their individual spacings  $\delta$  are equal, resulting in a single narrow overall RF beatnote (cf. Figure 2.10). This observation becomes clear when switching from a frequency to a time domain picture. Here, FWM can be interpreted as a time dependent modulation of the effective refractive index of the resonator affecting all modes equally (assuming similar mode profiles). Thereby, once generated, the spacing  $\delta$  implies a time domain modulation of the refractive index with beatnote frequency  $\delta$ . This modulation will add modulational sidebands to already existing optical lines (regardless of their spectral position) and the modulational sidebands (orange) can then act as seeds for FWM (cf. Figure 2.11). A similar seeding process, induced by an externally modulated pump laser, has very recently been used to influence the dynamics of microresonator based combs.<sup>149</sup>

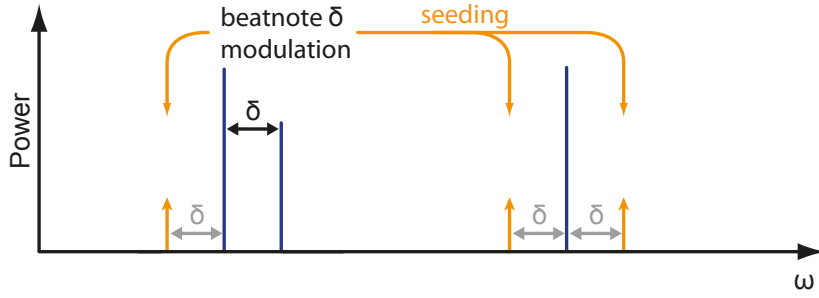


**Figure 2.11: Spectrally separated subcombs with equal spacing** can be understood as a result of the time domain modulation of the refractive index, which is experienced by all optical lines regardless of their spectral position. Once a particular spacing  $\delta$  is realized at one spectral position (here between the two blue lines), this creates modulational sidebands acting as a seed for FWM around other already existing comb lines.

### 2.3 Emergence of noise in microresonator based combs

In the previous section we revealed that the formation of microresonator combs proceeds via the initial formation of subcombs that merge into a spectrally gap free spectrum. Indeed this merging is directly related to the emergence of noise. Here, a critical point is reached, when the bandwidth growth of the subcombs closes their spectral separation and leads to an overlap (Figure 2.8c). Due to the typically incommensurate subcombs, individual resonator modes are populated by multiple lines with slightly different optical frequencies. In the following it is explained, how the interaction of subcombs can create multiple and broad RF beatnotes, as well as, intensity noise at low frequencies.

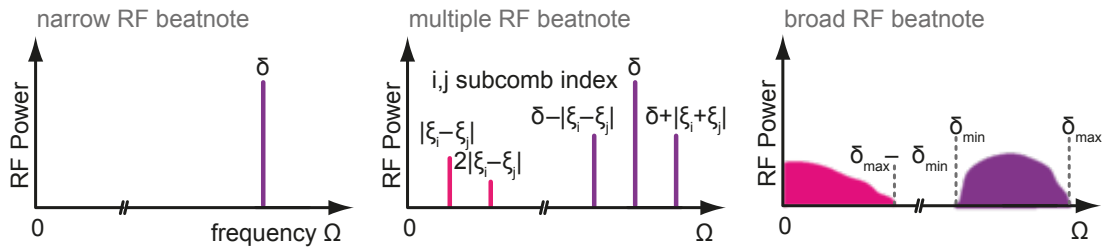


**Figure 2.12: RF beatnote and low-frequency intensity noise.** Single, multiple and broad RF beatnotes and the corresponding low-frequency signals observed as intensity noise in the generated combs.

#### 2.3.1 Multiple and broad RF beatnotes

When monitoring the RF beatnote on an electronic spectrum analyzer during comb formation, sidebands appear around  $\delta$  with frequencies  $\delta_{\pm}^i = \delta \pm \Delta\xi_i$  where  $\Delta\xi_i =$

$\xi_{i+1} - \xi_i$  is the offset difference between the two merging combs. This can be seen schematically in Figure 2.12 or experimentally in Figure 2.6a (third data set from top). Once these *new* RF beatnotes are generated, they can spread throughout the optical comb spectrum, effectively leading to multiple lines within individual resonator modes and correspondingly even more RF beatnotes  $\delta_{\pm}^{i,j} = \delta \pm \Delta\xi_{i,j}$  with  $\Delta\xi_{i,j} = \xi_i - \xi_j$ . Eventually this results in a broad RF beatnote as indicated in Figure 2.12 and experimentally observed in Figure 2.6a. We emphasize that the emergence of noise is not a consequence of large spectral comb span. Note that not all possible side beatnotes  $\delta_{\pm}^{i,j} = \delta \pm \Delta\xi_{i,j}$  may be generated as the finite cavity bandwidth will suppress lines far off the resonance frequencies. Further note, that multiple beatnotes can be observed even before spectral gaps close when FWM processes similar to Figure 2.9b,c, occur. This is experimentally evidenced in Figure 2.13 showing a comb generated in a MgF<sub>2</sub> resonator exhibiting multiple beat notes even though the subcombs have not yet merged. These beat notes can be measured locally at any spectral position as a result of a global refractive index modulation. As already explained above, this modulation allows to transfer a newly arising beat note spacing to all spectral positions throughout the comb (with varying relative intensities). The described pathways to multiple and broad RF beatnotes are absent in NMS combs, which is in agreement with previous experimental observation.<sup>72, 161</sup>

#### 2.3.2 Intensity noise at low-frequencies

The subcomb hypothesis can also explain a further, hereto unexplained phenomenon observed in MMS combs (corresponding to comb states shown in Figure 2.8c or Figure 2.9c). If the low frequency electronic spectrum of the transmitted light is recorded, intensity noise features (i.e. with frequency  $\Omega \ll \delta$ ) appear, whose emergence coincides with the generation of the frequency comb. Indeed, while the spacings  $\delta$ ,  $\delta_{\pm}^i$ , and  $\delta_{\pm}^{i,j}$  are close to the FSR of the resonator and therefore require dedicated RF equipment for their detection, this phenomenon finds its equivalent in the lower RF regime, where the frequencies  $\Delta\xi_i$  and  $\Delta\xi_{i,j}$  can readily be measured at much lower frequency  $\Delta\xi_i, \xi_{i,j} \ll \delta, \delta_{\pm}^i, \delta_{\pm}^{i,j}$  in the comb spectrum. This is schematically shown in Figure 2.12. In particular, broad RF beatnotes at frequencies corresponding to the native spacing  $\delta$  will coexist with a broad signal at low frequencies close to DC as it has been reported first in broadband spectra generated in Si<sub>3</sub>N<sub>4</sub>.<sup>131</sup> The correspondence between microresonator based comb formation induced comb frequency noise and intensity noise at low frequencies provides a sensitive and easy access to noise analysis of microresonator based combs. An experimental example of this correspondence is shown in Figure 2.14.

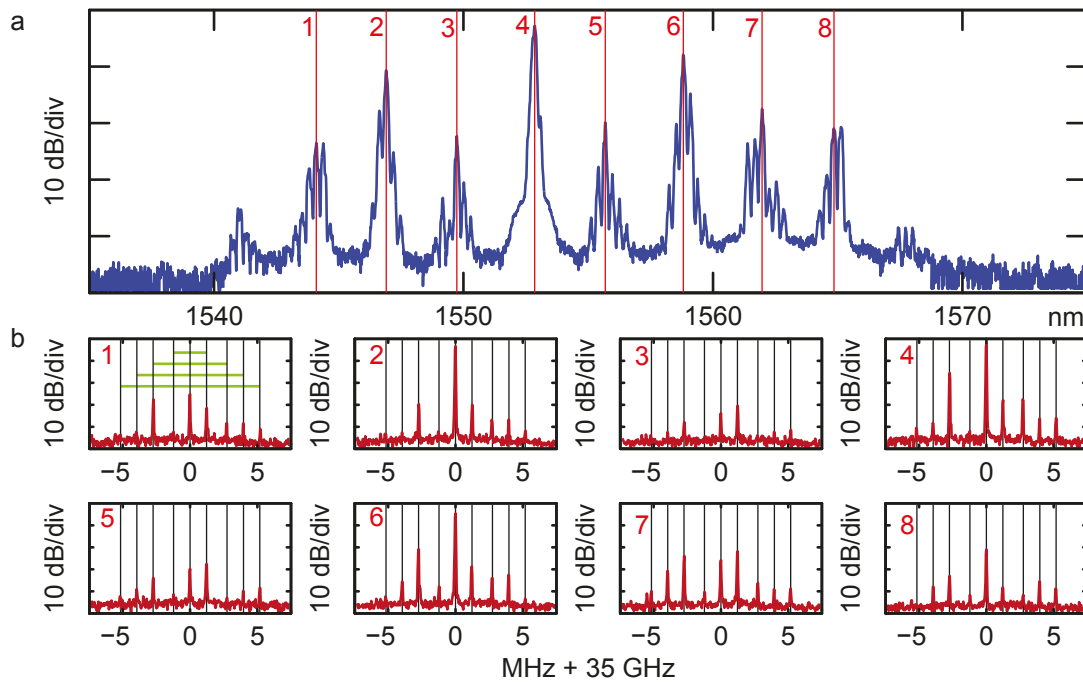


**Figure 2.13: Multiple beat notes in sparse combs:** **a.** Optical frequency comb spectrum generated in a  $\text{MgF}_2$  resonator (far detuned, pump power 100 mW, FSR 35 GHz). The vertical lines mark eight different positions where a narrow tunable bandpass filter was placed to filter out 0.8 nm of the comb spectrum (corresponding to three resonator modes). **b.** RF beat note measured at the filtered portion of the spectrum in (a) using a fast photodetector and resolution bandwidth of  $\text{RBW} = 300$  kHz. The black vertical and green horizontal lines serve as guides to the eye illustrating the non-equidistant but symmetric (with respect to the central peak) spacing of the RF peaks. The latter is expected when all possible RF beatnote frequencies are observable (cf. Section 2.3.1).



### 2.3. Emergence of noise in microresonator based combs

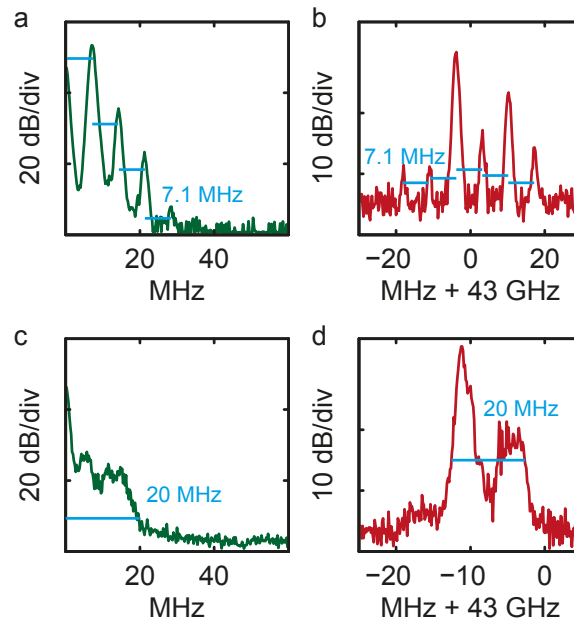


**Figure 2.14: RF beatnote and low-frequency intensity noise signal.** **a.** Low-frequency intensity noise spectrum of a comb in a 43 GHz FSR  $\text{MgF}_2$  resonator. **b.** RF beatnote between neighboring comb lines recorded using a resolution bandwidth of 300 kHz. **c,d.** Same as (a,b) for a different comb state. The blue lines illustrate the strong correspondence between RF beatnote and low-frequency intensity noise.

### 2.3.3 Line-by-Line reconstruction of microresonator combs

To obtain further experimental proof of the subcomb hypothesis, we perform a broadband spectroscopic reconstruction of the generated comb with close to MHz-resolution over a span of approximately 6 THz. This novel method allows a line-by-line reconstruction of the microresonator based comb, that is, measuring the relative frequencies of the microresonator based comb lines.

#### Description of the microresonator based comb reconstruction experiment

Frequency comb assisted diode laser spectroscopy enables broadband precision spectroscopy of cavity resonances<sup>84</sup> (cf. Appendix D.1). Here, this approach is developed further in order to spectrally reconstruct microresonator based comb spectra (cf. Figure 2.15f for setup). To this end a diode laser, scanning over a frequency interval of approx. 6 THz (from 1545 nm towards longer wavelengths) is split into three beams, two of which serve for frequency calibration of the laser scan. This calibration is based on the detection of the bandpass-filtered heterodyne beatnote between the scanning laser and a mode-locked fiber laser comb (250 MHz repetition rate) based on which frequency calibration markers are derived as detailed in Appendix D.1. The third diode laser beam is used to probe the microresonator comb spectrum by generating and recording RF markers at the respective frequencies. The markers are generated by filtering the heterodyne beatnote between microresonator based comb and scanning laser using a 1.9 MHz low-pass filter. Whenever the scanning laser moves over a microresonator based comb line an electric signal passes the filter and is recorded simultaneously to the scan calibration signal. This allows to determine the relative frequencies of the the microresonator based comb lines. Details of the method are provided in Appendix D.1.

#### Reconstruction of subcombs

An exemplary fraction of raw data showing that more than one comb line can exist in a single cavity resonance is shown in Figure 2.15a. While this is predicted by the above theory of merging subcombs, it is surprising from the perspective of the previous picture of Kerr comb formation. Moreover, the comb reconstruction in Figure 2.15c indeed reveals individual subcombs, with different offset frequencies  $\xi$ , but identical comb line spacing. The equal comb line spacing is further evidenced by the narrow and well-defined RF beatnote in Figure 2.15d. Note that multiple beatnotes are not observed in this case as the overlap between the individual subcombs is too small and the signal is dominated by the more powerful, not overlapping lines of the subcomb. The intensity noise, however, provides a more sensitive method, which is capable of detecting the beating between the slightly overlapping subcombs (cf. Figure 2.15e).

### 2.3. Emergence of noise in microresonator based combs

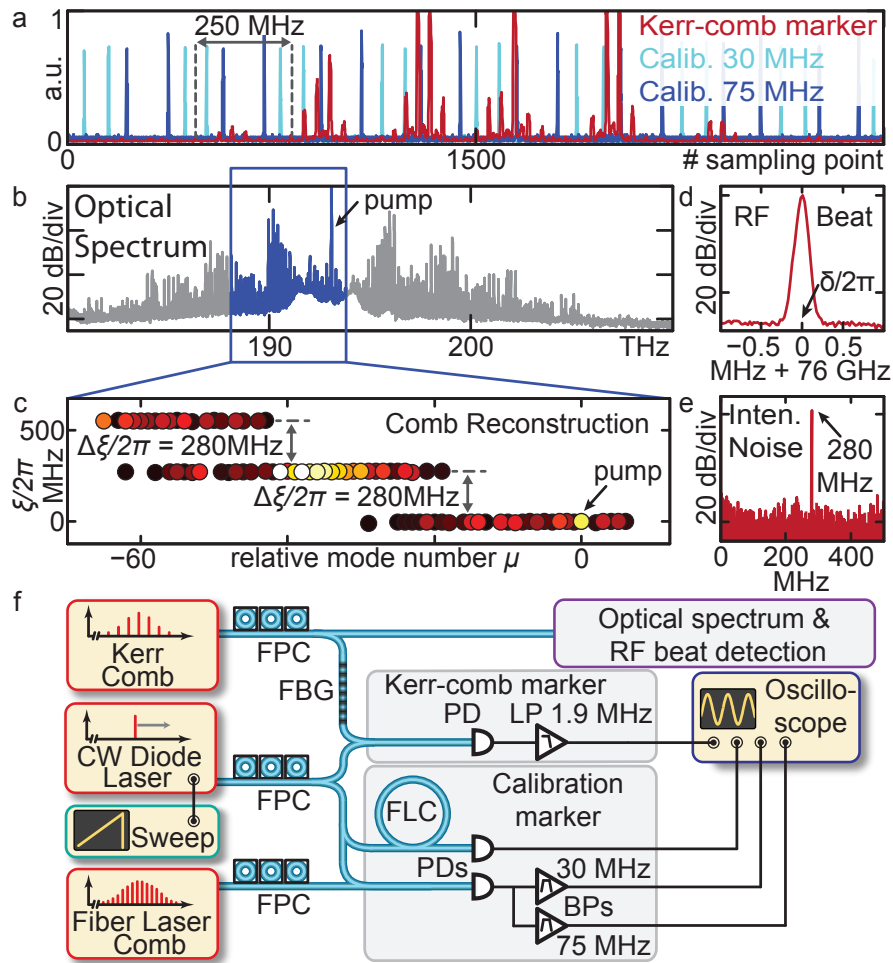


**Figure 2.15: Line-by-line reconstruction of microresonator combs.** **a.** Fraction of raw data showing frequency calibration (light/dark blue) and Kerr comb marker (red). For details see Appendix D.1). The data correspond to a 2 GHz wide scan resolving multiple comb lines generated in a single resonance of a 76 GHz FSR  $\text{Si}_3\text{N}_4$  resonator (pump power 5 W, resonance width 200 MHz). The high intensity lines are clipped due to the limited dynamic range of the recording oscilloscope. **b.** Optical spectrum of a microresonator based comb (same resonator as in (a) but different pump laser detuning). The blue colored 6 THz wide section corresponds to the scanned reconstruction range. **c.** Visualization of the reconstructed microresonator based comb showing the offset  $\xi$  of the comb lines versus their relative mode numbers  $\mu$  (lighter colors correspond to higher comb line power). Three subcombs are visible with relative offsets differences of  $\Delta\xi/2\pi = 280$  MHz. All spacings  $\delta$  within the individual subcombs are equal. **d.** RF beatnote of the comb in (b) (resolution bandwidth RBW = 100 kHz) corresponding to  $\delta/2\pi = 76$  GHz. **e.** Intensity noise spectrum with a peak at 280 MHz resulting from the beating between the offset subcombs (RBW = 100 kHz). **f.** Setup for microresonator based comb reconstruction. FLC = fiber Loop Cavity, LP/BP = Low-/Band-Pass filter, for other abbreviations see Figure 2.10d, for details concerning the setup see Appendix D.1.

### Reconstruction of a sparse yet noisy comb

In Section 2.3.1 it was discussed that noise can emerge before spectral gaps in the comb spectrum close. This can occur via FWM processes similar to the one described in Figure 2.9b,c. The result of a comb reconstruction experiment in a  $\text{Si}_3\text{N}_4$  resonator is shown in Figure 2.16, where the subcombs have not yet merged, but a broad (approx. 0.2 GHz width) peak appears in the recorded intensity noise spectrum at a frequency of 1.4 GHz. The microresonator based comb reconstruction reveals that this noise arises from groups of optical lines spaced by approximately 1.4 GHz. The broad nature of the intensity noise peak finds its correspondence in the broad (in the direction of offset) reconstructed groups of lines. Here, the comb reconstruction resolves numerous, densely spaced multiple lines per cavity resonance in each of the broad line groups, explaining the width of the observed peak.

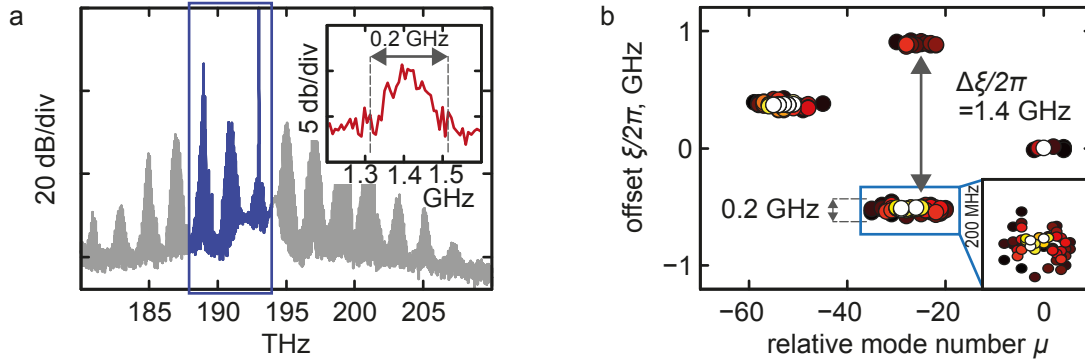


**Figure 2.16: Multiple beat notes in sparse combs.** **a.** Optical frequency comb spectrum generated in a 76 GHz FSR  $\text{Si}_3\text{N}_4$  resonator. The inset shows a broad peak at 1.4 GHz observed in the intensity noise of the comb (pump power 3 W, RBW = 100 kHz). **b.** microresonator based comb reconstruction showing multiple subcombs two of which populate the same cavity resonances. A closer look (cf. inset) reveals even more lines populating single cavity resonances with much smaller separation.

## 2.4 Transition to low noise

In a second comb reconstruction experiment we observe a transition from a spectrum composed of multiple and offset subcombs to one that exhibits only a single comb over the full reconstruction range (cf. Figure 2.17) when reducing the pump laser detuning (which affects the subcomb offsets and the comb line spacing). The fact that the intensity noise vanishes suggests that the full spectrum forms a consistent frequency comb. This observation could explain a similar behavior of an intensity noise drop observed recently in a  $\text{Si}_3\text{N}_4$  system.<sup>131</sup> The detected RF beatnote is for both comb states well-defined and narrow, however, the signal-to-noise ratio increases

from 20 dB to almost 60 dB in the second state. We attribute this transition to a  $\delta$ - $\Delta$ -matching where commensurability between the spacings  $\delta$  and  $\Delta$  is achieved by appropriate choice of laser power and detuning, which affect comb offset and spacing in a distinct manner.<sup>5,131</sup> Reducing the laser detuning further results in the re-appearance of intensity noise peaks and eventually broad noise signatures. Note that this transition is not possible in all comb states. For example, a similar transition could not be achieved for the comb in Figure 2.15, where the offset  $\Delta\xi/2\pi = 280$  MHz is significantly larger than  $\Delta\xi/2\pi = 66$  MHz in the case of Figure 2.17.

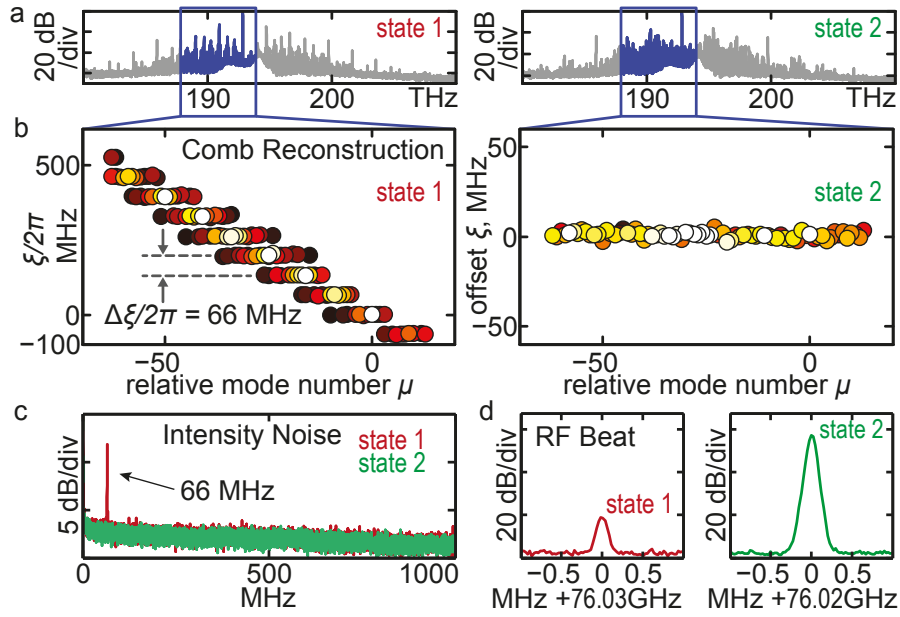


**Figure 2.17: Subcomb transition to low noise in microresonator based combs:** **a.** Optical spectra of two microresonator comb states 1,2 (pump power 6 W) in a  $\text{Si}_3\text{N}_4$  resonator with FSR of 76 GHz. State 2 evolves from state 1 when further reducing the detuning of the pump laser. **b.** A transition is observed from multiple subcombs to a single comb over the bandwidth of the microresonator based comb reconstruction. In state 1 all subcombs have the same mode spacing, but have different offsets  $\xi$ , which differ by a constant relative amount of  $\Delta\xi/2\pi = 66$  MHz. **c.** In the transmission from state 1 to state 2 the intensity noise peak resulting from the beating between overlapping offset subcombs disappears (resolution bandwidth RBW = 300 kHz). **d.** The RF beatnote shifts by approx. 10 MHz (due to the increase of intracavity power) and the signal-to-noise ratio increases (RBW = 100 kHz).

### 2.4.1 The role of dispersion and resonance width

In the following we show, that the ratio  $\kappa/D_2$  of resonance width to dispersion (at the pump wavelength) is closely linked to the question, whether a comb evolves along the NMS or MMS pathway. To estimate under which conditions the intrinsically low noise NMS combs can be achieved, we determine the distance in terms of mode

number between pump and first sideband by solving the nonlinear coupled mode equations<sup>3,142–145</sup> and deriving the parametric gain for the initial degenerate FWM process. We particularly include the detuning of the pump laser, as well as the detuning of the generated sidebands with respect to the cavity resonances. For a constant launched pump power  $P_{\text{in}}$  and tuning the pump laser into resonance from the higher frequency side, the circulating power inside the cavity increases. The first sidebands with mode numbers  $\pm\mu_{\text{th}}$  are generated when the parametric threshold is reached, i.e. when the gain overcomes the cavity decay rate  $\kappa$ :

$$\mu_{\text{th}} \simeq \sqrt{\frac{\kappa}{D_2} \left( \sqrt{\frac{8\eta P_{\text{in}} c n_2 \omega_p}{\kappa^2 n_0^2 V_{\text{eff}}}} - 1 + 1 \right)} \quad (2.2)$$

Here,  $\eta$  denotes the coupling strength ( $\eta = 1/2$  for critical coupling),  $\omega_p$  the pump frequency,  $n_2$  the nonlinear index, and  $V_{\text{eff}}$  the effective nonlinear mode volume. The derivation of this result given in Appendix A.2.5.

The primary mode spacing observed for the 35 GHz FSR MgF<sub>2</sub> resonator in Figure 2.10a ( $\eta = 0.5$ ,  $\omega_p/2\pi = 193$  THz,  $n_2 = 0.9 \times 10^{-20} \text{m}^2\text{W}^{-1}$ ,  $n_0 = 1.37$ ,  $V_{\text{eff}} = 6.2 \times 10^{-13} \text{m}^3$ ,  $\kappa/2\pi = 1$  MHz,  $P_{\text{in}} = 0.1$  W) corresponds to a dispersion of  $D_2/2\pi = 11$  kHz, which is consistent with the measured dispersion of  $D_2/2\pi \approx 10$  kHz. The method<sup>84</sup> used to measure dispersion is detailed in Appendix D.1.

The smallest possible  $\mu_{\text{th,min}}$  is achieved if the threshold is reached with the pump laser being exactly resonant with the cavity. This can either approximately be achieved by carefully setting the pump power  $P_{\text{in}}$  or by applying injection locking to the pump laser.<sup>162</sup> In this ideal case the previous equation simplifies to

$$\mu_{\text{th,min}} = \sqrt{\frac{\kappa}{D_2}}. \quad (2.3)$$

The above derivation assumes that  $D_2$  dominates over higher order dispersion terms. This is not the case in the direct vicinity of the zero dispersion point. Here, a similar analysis following the one above but including higher order terms is required.

## 2.5 Discussion and conclusion

The main findings presented in this chapter can be summarized as follows:

- **Octave spanning comb generation:** The generation of an octave spanning spectrum directly in a microresonator was shown for the first time. Note that a similar result was achieved more recently in a Si<sub>3</sub>N<sub>4</sub> resonator by Okawachi et al.<sup>131</sup> These results illustrate the potential microresonator based systems have for

broadband comb generation far beyond the gain width of laser based systems.

- **Observation of noise:** The octave spanning spectrum and follow-up experiments led to the first observation and characterization of noise phenomena in microresonator based combs.
- **In depth understanding of comb formation:** Precision frequency metrology experiments and theoretical analysis enable a detailed understanding of comb formation dynamics far beyond the previous understanding.
- **Explanation of noise phenomena:** Our experimental observations and theoretical analysis fully explain the observation of broad<sup>5</sup> and multiple beatnotes,<sup>124</sup> intensity noise, sudden drops of this noise for certain comb states,<sup>131</sup> and loss of coherence in time domain experiments.<sup>44</sup>
- **Intrinsically low-noise regime:** In addition, our study identifies  $\sqrt{\kappa/D_2}$  as one important figure of merit for the design of low noise microresonator based comb generators (where  $D_2 > 0$  describes anomalous dispersion). For intrinsically low-noise microresonator based combs (i.e. emerging symmetrically in steps corresponding to single FSRs around the pump laser) the ratio  $\kappa/D_2$  should be close to unity, which can either be achieved by reducing the cavity decay rate or by increasing the anomalous dispersion  $D_2$ . Note that  $\sqrt{\kappa/D_2} \approx 1$  and low noise has been achieved in experimental systems.<sup>2,72</sup>
- **Transition to low-noise regimes:** The condition  $\mu_{\text{th}} \sim 1$  is not a strict one in order to achieve low noise. A detuning dependent transition from multiple subcombs to a broadband, single comb (cf. Figure 2.17) can occur in some combs, which we attribute to  $\delta$ - $\Delta$ -matching. Here, by adjusting the relative offset between different subcombs, a consistent single comb forms. This is likely to occur much easier the closer the initial sidebands are spaced and the smaller the relative offset differences between the subcombs are.

The role of dispersion is important, both, for broadband as well as low noise comb generation: A rather ‘flat’ dispersion (reducing the mismatch between cavity and comb modes) is generally advantageous for broadband spectra. The generation of an octave spanning spectrum, however, shows, that a huge mismatch of thousands of cavity linewidths can be overcome by nonlinear differential frequency shifts. Besides broadband comb generation, these nonlinear effects also allow to operate in the strongly anomalous dispersion regime (with the cost of reduced bandwidth) where  $\sqrt{\kappa/D_2} \approx 1$ . This regime is characterized by intrinsic low phase noise comb generation.

The dispersion  $D_2$  can be influenced by increasing the free spectral range of the resonator, as  $D_2$  can be interpreted as the material and geometrical dispersion of

the resonator integrated over the frequency interval of one FSR. This explains, why systems with large FSR are advantageous to generate low noise combs. Another way of dispersion engineering, particularly relevant to  $\text{Si}_3\text{N}_4$  resonators and related systems is dispersion engineering via geometrical and material modification, such as atomic layer deposition,<sup>4</sup> of the resonators. Moreover, in crystalline  $\text{MgF}_2$  resonators, where many mode families exist the choice of mode family used for comb generation significantly influences the dispersion parameter  $D_2$  (cf. Section 4.5). The specific use of avoided modal crossings in resonators<sup>146,163</sup> may provide an elegant way of achieving locally strongly anomalous dispersion at the pump wavelength. In this manner narrowly spaced primary sidebands and low frequency noise is achieved while an elsewhere moderate dispersion may facilitate broadband comb generation. Lastly, the dispersion  $D_2$  also depends on the pump wavelength. This is particularly important for the mid-infrared regime where in  $\text{MgF}_2$ , due to material properties, the dispersion is strongly anomalous. Indeed we will show in the next Chapter 3 that low noise comb generation is easily possible in the mid-infrared wavelength region<sup>2</sup> as opposed to operating the same resonators in the near-infrared where  $D_2$  is smaller.



## 3 Mid-infrared frequency combs based on microresonators

The mid-infrared spectral range (2 to 20  $\mu\text{m}$ ) is of particular importance for chemistry, biology and physics as many molecules exhibit strong ro-vibrational transitions. Here, optical frequency combs are creating new opportunities for advanced spectroscopy. In this chapter we demonstrate a novel approach to generating mid-infrared frequency combs based on microresonators. As the parametric gain responsible for comb generation is not bound to the availability of laser gain media the broadband comb spectra can be generated directly in the mid-infrared. Specifically, we generate comb spectra spanning 200 nm ( $\approx 10$  THz) around the pump wavelength of 2.45  $\mu\text{m}$ . With its distinguishing features of compactness, efficient conversion, large mode spacing and high power per comb line, this novel frequency comb source holds promise for new approaches to molecular spectroscopy even deeper in the mid-infrared.

Section 3.1 introduces the technologically important mid-IR wavelength regime. Microresonator based frequency comb generation in the mid-IR regime is reported in Section 3.2.

### 3.1 The mid-infrared regime

The mid-infrared (mid-IR) spectral range ( $\lambda \sim 2 \mu\text{m}$  to 20  $\mu\text{m}$ ) is known as the “molecular fingerprint” region as many molecules have their highly characteristic, fundamental ro-vibrational transition bands in this part of the electromagnetic spectrum. Broadband mid-IR spectroscopy therefore constitutes a powerful and ubiquitous tool for optical analysis of chemical components that is used in biochemistry, astronomy, pharmaceutical monitoring and material science.<sup>25,27,29,35,164,165</sup> Mid-IR frequency combs have therefore become highly desirable and recent progress in generating such combs by nonlinear frequency conversion<sup>166–168</sup> has given access to this spectral region. Due to its scientific and technological significance, laser technology in the

mid-infrared is an active area of research and development. The advent of a compact and versatile coherent light source in this region came after the invention of quantum cascade lasers (QCLs) in 1994.<sup>169</sup> However, QCLs are intrinsically difficult to be passively mode-locked<sup>170</sup> and only active mode-locking has been unequivocally demonstrated with very narrow span comb of approximately 0.3 THz bandwidth.<sup>171</sup> Recently an electrical injection scheme was used to generate a 3 THz wide comb spectrum based on a QCL.<sup>130</sup> Today, the most common approach to create frequency combs in the mid-IR is to frequency down-convert a near-infrared comb through nonlinear processes, such as optical parametric oscillation<sup>167, 168</sup> or difference frequency generation.<sup>166</sup> Here, we demonstrate a novel route to mid-IR frequency comb generation based on high-Q crystalline magnesium fluoride  $\text{MgF}_2$  microresonators.

## 3.2 Microresonator based mid-infrared combs

Most resonator platforms cannot operate in the mid-IR wavelength regime. In the following we will describe how  $\text{MgF}_2$  microresonators are uniquely suited for the mid-infrared. We will then show that frequency a comb can be generated (similar to the near-infrared) by driving the resonator with a monochromatic mid-IR laser.

### 3.2.1 Crystalline magnesium fluoride as a resonator material for the mid-infrared

Most microresonator platforms cannot operate in the mid-IR regime and the reason for choosing  $\text{MgF}_2$  as the resonator material is threefold:

**Transparency:** The transparency window of many crystalline materials (such as  $\text{CaF}_2$  and  $\text{MgF}_2$ ) extends from the UV ( $\sim 160$  nm) to the mid-infrared ( $\sim 7\mu\text{m}$ ), enabling high-Q ( $> 10^8$ ) in the mid-infrared. This is in stark contrast to fused silica or quartz, which always contain water and suffer from strong absorption above  $2.2\mu\text{m}$ .

**Anomalous Dispersion:** The ability to generate optical frequency combs via cascaded FWM in the presence of self- and cross-phase modulation of the pump requires the dispersion at the pump frequency to be anomalous (cf. Section 1.3.4), i.e. a free spectral range (FSR) of the cavity that reduces with increasing wavelength. We assess the dispersion properties by carrying out fully vectorial finite-element simulations<sup>150, 172</sup> including material and geometrical effects. Figure 1c shows the dispersion (cf. Section 1.2.1) properties of a  $700\mu\text{m}$ -diameter  $\text{MgF}_2$  crystalline resonator, revealing a GVD that is anomalous over the full mid-infrared transparency range. In contrast to previous work in crystalline (and other) resonators, the present experiments operate in the strongly anomalous dispersion regime. We emphasize that this dispersion regime – far from the zero dispersion point which is at about  $1.55\mu\text{m}$  – has previously been considered as unfavorable for Kerr-comb generation.<sup>72, 74, 90</sup> Here we experimentally

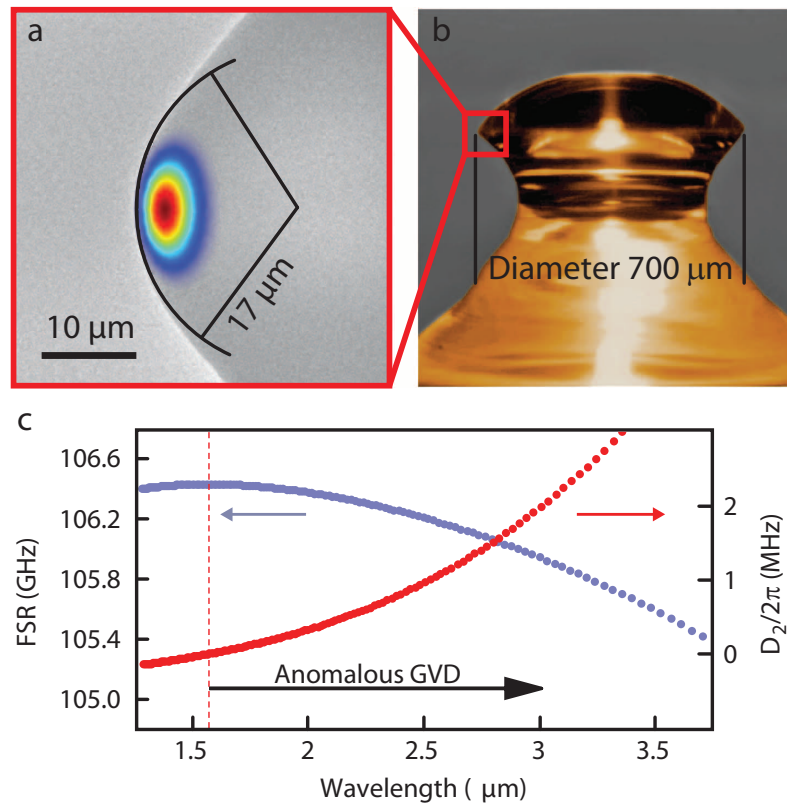


**Figure 3.1: Mid-IR Dispersion of a  $\text{MgF}_2$  microresonator.** **a.** Finite element simulation of the optical intensity profile of the fundamental WGM at wavelength of  $2.45 \mu\text{m}$  superimposed on a scanning electron microscope image of a  $700 \mu\text{m}$  diameter resonator. The radius of curvature of the resonator protrusion, which confines the mode in the azimuthal direction, is  $17 \mu\text{m}$ . **b.** Optical microscope image of a resonator. **c.** The figure shows the simulated FSR for fundamental modes (blue curve) and the difference of the FSR between adjacent modes (red curve) as a function of the wavelength for the resonator in panel (a). The dispersion is increasingly anomalous with longer wavelength above the zero dispersion wavelength of approximately  $1.6 \mu\text{m}$ .

demonstrate that the strong anomalous dispersion does not prevent broadband Kerr-comb generation in the highly interesting mid-infrared regime, which is attributed to the strong nonlinear frequency pulling by self- and cross-phase modulation exceeding the amount of cavity dispersion. Moreover, as detailed in the previous Chapter 2, sufficiently high anomalous dispersion is one way of achieving low noise operation of the comb. The dispersion requirement renders other materials, such as  $\text{Si}_3\text{N}_4$  waveguide resonators which are used successfully at shorter wavelength for Kerr-comb generation, unfavorable as their dispersion is normal in the mid-infrared.<sup>131</sup>

**Positive thermo-refractive coefficient:** The sign of the temperature coefficient of the refractive index ( $dn/dT$ ) and the thermal expansion coefficient  $\alpha$  are both positive in  $\text{MgF}_2$  (for temperatures close to room temperature) which allows the cavity mode to be thermally locked to the pump laser frequency<sup>113</sup> (Section 1.3.3) and enables the stabilization of the repetition rate and offset frequency of microresonator based frequency combs.<sup>123, 125</sup> On the contrary, materials with opposite signs of  $dn/dT$  and  $\alpha$ , such as  $\text{CaF}_2$ , suffer from large thermal oscillatory instabilities and thus require active locking (or injection locking) schemes (cf. Section 1.3.3).

#### 3.2.2 Generation of mid-infrared frequency comb

The setup for mid-IR comb generation is shown in Figure 3.2. Following the generic design (cf. Section 1.3.6) it comprises a mid-IR pump laser, a tapered fiber as an in- and out-coupling waveguide, a  $\text{MgF}_2$  resonator as well as diagnostic devices.

##### Resonator characterization

Tapered optical coupling fibers made of fused silica were used for characterization of the resonators at  $1.55 \mu\text{m}$ . For pre-characterization, the linewidth of the resonances was measured as described in Appendix D.2 at a wavelength of  $1.55 \mu\text{m}$  yielding  $\kappa/2\pi \approx 500 \text{ kHz}$ . A scanning electron microscope was used to measure the transverse radius of curvature of the resonator to be  $17 \mu\text{m}$  (cf. Figure 3.1a). The effective mode area  $A_{\text{eff}}$  of the resonator, as well as, its dispersion were determined in a fully vectorial finite element simulation (Figure 3.1c). An effective mode area of  $A_{\text{eff}} = 60 \mu\text{m}^2$  was found. The dispersion parameter  $D_2$  (cf. Section 1.2.1) is on the order of the resonator's linewidth  $\kappa$ , that is  $\kappa/D_2 \sim 1$ . Based on the findings in Chapter 2 we can expect low noise performance of  $\text{MgF}_2$  resonators in the mid-IR regime.

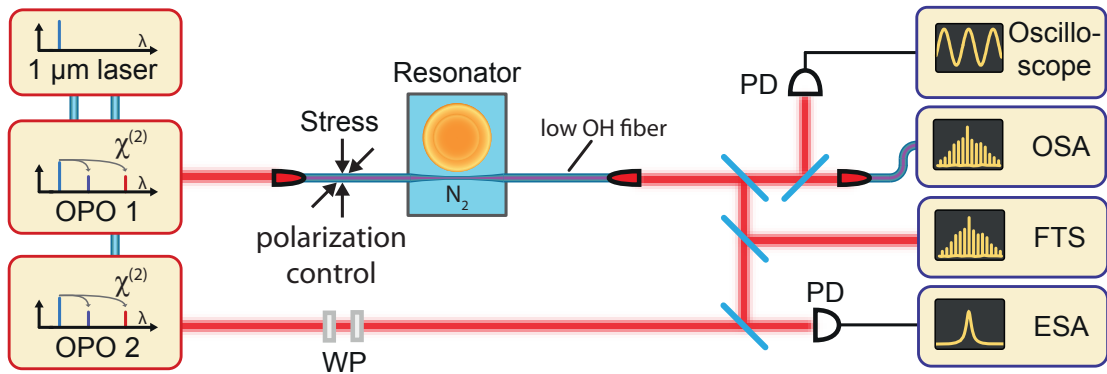


**Figure 3.2: Setup for mid-IR frequency comb generation.** The experimental setup includes two cw mid-IR optical parametric oscillators (OPO 1 and OPO 2) that are pumped at a wavelength of  $1\ \mu\text{m}$ . OPO 1 serves as the pump laser for comb generation. It is coupled into a low-OH silica fiber. Stress and fiber bending is used to optimize the polarization. The coupling to the resonator is achieved via a tapered section in the fiber and monitored by observing the transmitted power on an oscilloscope (PD: photodetector). An electronic spectrum analyzer (ESA) is used to record the low-frequency noise in the transmitted intensity. The generated frequency comb is detected using an optical spectrum analyser (OSA) with a cut-off wavelength of  $2.5\ \mu\text{m}$  and a Fourier transform spectrometer (FTS) with much smaller dynamic range. OPO 2 is used to record heterodyne beatnotes with the generated comb lines. The polarization of OPO 2 light is adjusted using waveplates (WP). The heterodyne beatnotes can also be monitored on the ESA. To avoid attenuation of light the full setup (with the only exception of the tapered coupling fiber and a short fiber length to couple light into the OSA) is implemented using free-space optics. The resonator is kept in a dry nitrogen ( $\text{N}_2$ ) atmosphere to reduce light absorption by water.

### OPO pump laser

The employed pump laser is the idler beam of a commercial high-power single-frequency, cw optical parametric oscillator (OPO). The pump of the OPO is a 15 W ytterbium-doped fiber laser operating at 1064 nm, and the OPO is a four mirror ring resonant cavity using a temperature-controlled MgO-PPLN crystal as the nonlinear element. The idler beam is tuneable from 2.4 to 3.2  $\mu\text{m}$  with up to 3 W of output power, corresponding to a signal beam at a wavelength of 1.9 to 1.6  $\mu\text{m}$ . The idler beam can be fine-tuned by piezoelectric tuning of the pump fiber laser. Both the idler and the signal beams have specified linewidths of less than 1 MHz. The idler beam of the OPO was coupled into the tapered-fiber by an AR-coated aspherical ZnSe lens. A coupling efficiency of more than 60% was obtained.

### Coupling light to the microresonator

Optical power levels of 200 mW to 1 W were coupled into the resonators by employing a tapered fiber made of low-OH fused silica ( 3.4 dB/m at  $\lambda=2.5 \mu\text{m}$ ), which is single-mode at 2.5  $\mu\text{m}$ . The resonator and tapered fiber are embedded in a dry nitrogen purged environment, as water vapor is highly absorptive in the mid-infrared (prior exposure to air, however, does not result in accumulation of water layers as  $\text{MgF}_2$  crystals are hydrophobic). To keep the fiber length short no paddle-type fiber polarization controller is used. Instead, the polarization is controlled by stress and bending induced birefringence in the fiber.

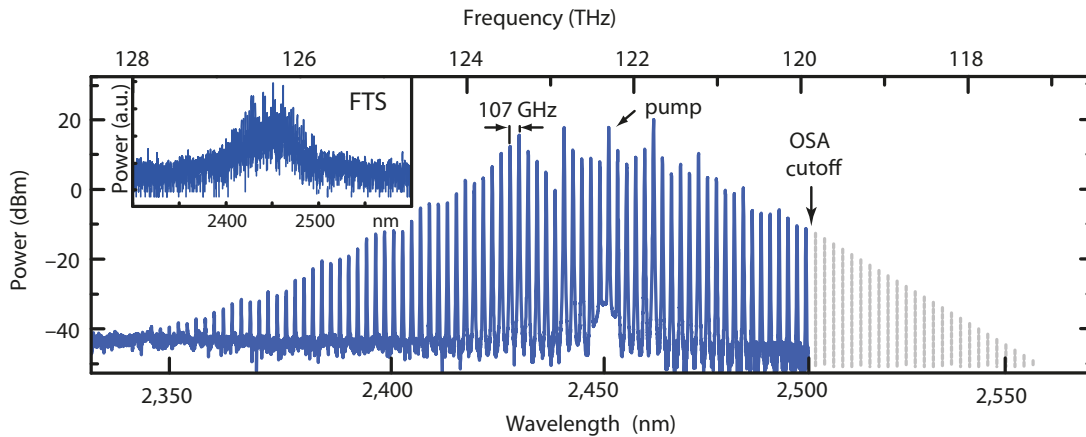


**Figure 3.3: Mid-infrared frequency comb.** Optical spectrum with a line spacing of 107 GHz centered at 2.45  $\mu\text{m}$  as recorded by with an optical spectrum analyzer. The comb is generated from by pumping a 700  $\mu\text{m}$  diameter  $\text{MgF}_2$  resonator with  $\approx 0.6$  W of optical power. The grey vertical lines indicate frequency components which are expected to exist based on symmetry around the pump. The inset shows the spectrum taken with a Fourier transform spectrometer (FTS) revealing the overall symmetry of the spectrum.

### Generated mid-infrared combs

The output spectra were recorded by an optical spectrum analyzer (OSA) with cut-off wavelength at  $2.5 \mu\text{m}$ . Figure 3.3 shows the optical frequency comb spectrum derived from the  $700 \mu\text{m}$ -diameter resonator pumped with approximately 600 mW of laser power at  $\lambda=2.45 \mu\text{m}$ . We observed more than 100 modes spaced by 107 GHz (corresponding to a span of over 200 nm), which corresponds to the FSR of the resonator. The power per comb line ranges from a few microwatt up to several milliwatt, significantly higher than current state-of-the-art down-converted mid-infrared combs.<sup>167, 168</sup>

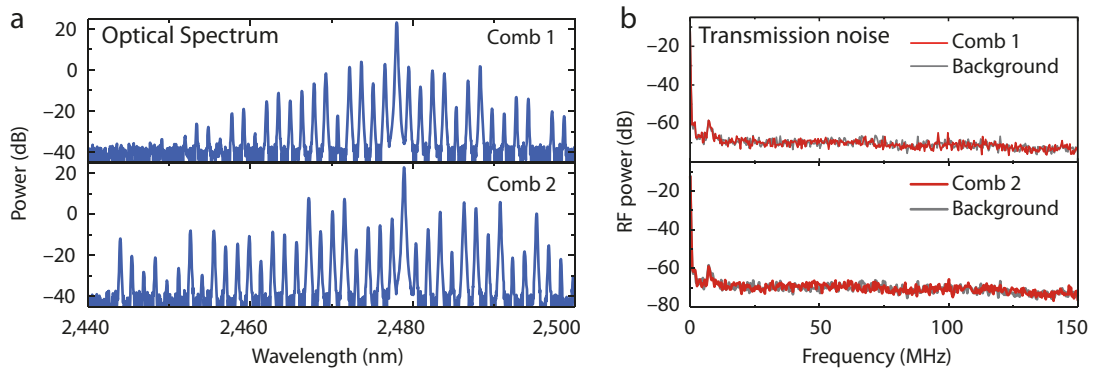


**Figure 3.4: Low-frequency intensity noise a.** Two comb spectra derived from a 1 mm diameter resonator with a line spacing of 70 GHz. (b) Low-frequency intensity noise spectra of the two combs. No evidence for noise above the detector background is found. This indicates that the two combs have low phase noise

### 3.2.3 Phase-noise characterization

A key requirement of an optical frequency comb is low frequency and intensity noise. In Chapter 2 it was shown that a high anomalous dispersion parameter  $D_2$  on the order of the cavity decay rate  $\kappa$  is one way of achieving low phase noise operation of the comb. This regime is realized in  $\text{MgF}_2$  resonators pumped at mid-IR wavelength implying that low-phase operation can be expected. This is in contrast to the observation that none of the employed resonators used in this chapter showed a low noise behavior in the shorter wavelength regime at  $1.5 \mu\text{m}$  (see also Section 2.1.4).

As ultra-fast mid-infrared detectors capable of detecting the comb line spacing of tens of GHz frequencies are not yet commercially available we investigate the noise characteristics of the generated mid-infrared combs in two alternative ways. First, by measuring the intensity noise (cf. Section 2.3.2), and second, by performing a cw heterodyne beatnote measurement (cf. Section 2.1.2), between a second cw OPO and

a single comb component. In both measurements a detector with a bandwidth of 100 MHz is used:

**Low frequency intensity noise:**

Figure 3.4a shows the two comb spectra derived from a 1-mm-diameter resonator with a line spacing of 70 GHz. Their respective intensity noise spectra are shown in Figure 3.4b along with the detector background noise. No additional noise is observed, implying the low noise performance of the generated comb.

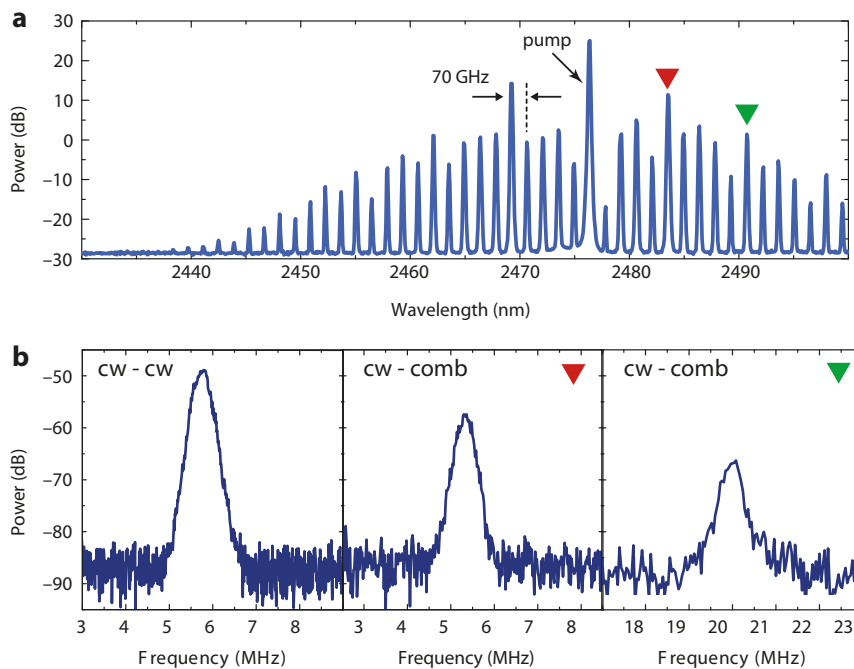


**Figure 3.5: Heterodyne beatnote of the mid-infrared frequency comb modes with an external cw laser:** **a.** Frequency comb spectrum with a line spacing of 70 GHz (1 mm diameter resonator) used for the beatnote measurement. **b.** Beatnote between the cw laser and the pump (left), and beatnotes between the cw laser and the comb modes (middle and right; marked by the red/green triangle in (a), respectively). All beatnotes have a FWHM of approximately 300 kHz, corresponding to the resolution bandwidth used in the measurement. No other peaks are observed in a measurement with a larger frequency span. Beatnotes between the cw laser and other comb modes show the same linewidth.

**Heterodyne beatnote:**

The results of the CW heterodyne beatnote measurement are shown in Figure 3.5. A second OPO (OPO 2 in Figure 3.2), similar to the pump laser source, is used as an



external cw laser in the beatnote measurement. Figure 3.5b shows the comb spectrum investigated, which was derived from the same resonator as in Figure 3.4. After measuring the beatnote of the cw laser with the narrow-linewidth pump (Figure 3.5b, left), the beatnotes between the cw laser and different comb modes are recorded (Figure 3.5b, middle/right). All beatnotes exhibit the same linewidth corresponding to the employed resolution bandwidth of 300 kHz. Importantly, neither additional linewidth broadening of the comb modes relative to the pump nor multiple beatnotes are observed in this measurement, showing that the comb lines exhibit a similar linewidth as the cw pump laser.

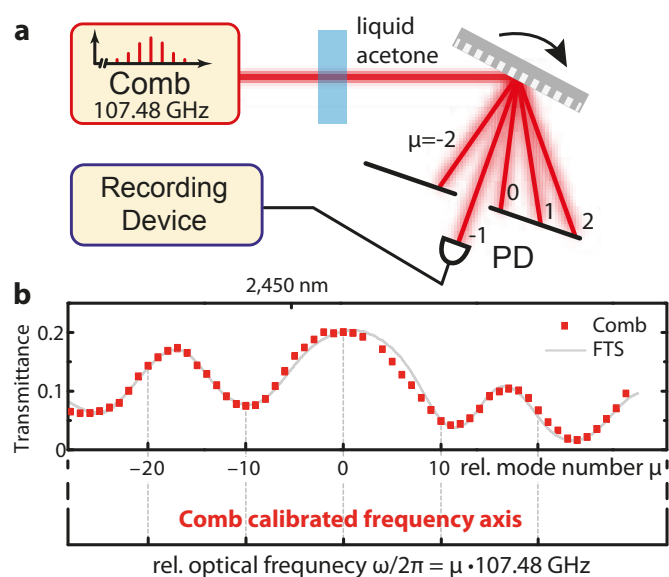


**Figure 3.6: Direct comb spectroscopy a.** Setup of a proof-of-principle direct comb spectroscopy experiment. A microresonator comb with a comb line spacing of 107.48 GHz, is sent through a 0.5 mm thick layer of liquid acetone. The wide comb spacing allows to resolve individual comb lines after dispersing the comb spectrum on a diffraction grating. **b.** The line-by-line transmittance (fraction of light passing through the acetone sample) is recorded. Each data point (red squares) corresponds to a comb line. As the comb lines are resolved each data point is assigned a relative comb line number with respect to the pump laser. As the frequency spacing between the comb lines is known this translates into a comb calibrated relative frequency axis. To validate the results the measurement is also performed with a white light source and a Fourier transform spectrometer (FTS).

### 3.2.4 Proof-of-principle direct comb spectroscopy experiment

Frequency combs have recently demonstrated potential for advances in molecular spectroscopy.<sup>173, 174</sup> To demonstrate that the high power per comb line and the wide mode spacing is well suited for the recording of broadband vibrational spectra in the liquid or solid phase, we performed a proof-of-principle direct comb absorption

spectroscopy experiment<sup>25</sup> of a 0.5 mm thick layer of liquid acetone using the comb in Figure 3.3 as light source and recording the attenuated spectra with the OSA. Note that if a white light source is used for spectroscopy, a wavelength-calibrated detector system, such as an OSA is required, whereas with a frequency comb source the calibration is contained in the known frequencies of the comb modes, and only a detector that can resolve the individual comb components is required. The direct comb spectroscopy experiment does not rely on the wavelength calibration of the OSA. The result is shown in Figure 3.6 and validated by an independent measurement of the same acetone sample employing a conventional white light source and a Fourier transform spectrometer (FTS). The discrepancy between the FTS and the comb measurements comes from the fact that the power in the resonator has not been stabilized in this experiment, so the comb line intensities fluctuate on a few seconds time scale required for data taking. In future experiments employing a mid-infrared disperser and detector array, we expect microresonator-based combs to be suitable light sources for direct molecular fingerprinting, which would drastically reduce the acquisition time and increase sensitivity. Therefore, new opportunities for real-time spectroscopic investigation and optimization of chemical reactions may come into reach, including industrial real-time process control of e.g. pharmaceutical products.

### 3.3 Discussion and conclusion

The main findings presented in this chapter can be summarized as follows:

- **Mid-IR frequency combs:** It is demonstrated that microresonator based frequency combs can be generated at mid-IR wavelength. The presented mid-IR combs operate in the highly anomalous dispersion regime. This regime was previously considered unfavorable. Our observation therefore reveals an unexpected potential of microresonator based combs for mid-IR applications.
- **Low noise operation:** As predicted in Chapter 2 the high dispersion resulting in  $\sqrt{\kappa/D_2} \sim 1$  leads to an intrinsic low noise behavior. With the same resonators this has not been achieved at shorter, near-infrared wavelengths where the anomalous dispersion is lower.

As shown in the simulation in Figure 3.1, the magnitude of  $D_2$  is increasing monotonically for wavelengths above  $1.55 \mu\text{m}$  in  $\text{MgF}_2$  resonators (anomalous dispersion). Consequently, low phase noise Kerr combs can be expected across the entire mid-IR region (within the transparency window of the resonator material).

In the present work, the choice of the pump wavelength of  $\lambda = 2.45 \mu\text{m}$  originates from the current limitation of the available optical spectrum analyzer and the strongly

increasing coupling fiber absorption beyond  $2.5\ \mu\text{m}$ . While the first reason is not a limiting factor of the system itself, the fiber absorption may be circumvented by employing e.g. a coupling prism<sup>94</sup> or tapered chalcogenide fibers<sup>175</sup> instead.

Pertaining to the advantages of crystalline microresonator based mid-infrared frequency comb generators, we note that the native mode spacing in the range of 10-110 GHz is a unique feature. Indeed, a growing number of emerging applications requires combs with large line spacing, such as astronomical spectrometer calibration, arbitrary optical waveform synthesis and spectroscopy. Line-by-line pulse shaping of individual comb lines<sup>97</sup> may prove beneficial to coherent control of chemical reactions. Moreover, the ability to separate the individual modes of the mid-infrared Kerr comb with a single grating onto a one-dimensional array in the image plane of the spectrometer enables direct fingerprinting of molecular absorption.<sup>25</sup> The high power per comb line increases the sensitive of the spectrometer and the comb property allows cavity enhanced spectroscopy.<sup>176,177</sup>

In summary, a crystalline microresonator-based optical frequency comb in the mid-infrared ‘molecular fingerprint’ region is demonstrated for the first time. The comb is generated directly in the mid-IR wavelength range from a monochromatic cw pump laser. A broadband laser gain medium is not required. Future integration of the microresonators with mid-infrared QCLs could open the path to novel simple and compact mid-infrared comb generators. Furthermore, the choice of the microresonator material is not limited to dielectric crystals. As many semiconductors such as silicon (Si), germanium (Ge) and indium phosphide (InP) are Kerr-nonlinear and exhibit a wide transparency windows in the mid-infrared, a whole class of on-chip molecular spectrometers based on this approach is conceivable.



## 4 Temporal soliton formation in microresonators

**This chapter reports on the stable formation of temporal dissipative solitons in a continuously driven nonlinear microresonator. These soliton light pulses are spontaneously generated in the presence of anomalous dispersion when the initially blue detuned driving laser is tuned through the effective zero detuning of a high-Q resonance. This regime of laser detuning has not been used for microresonator based frequency combs so far, as it is not stable in the absence of solitons. Once generated the solitons propagate stably (until the driving laser is switched off) inside the microresonator with a roundtrip time corresponding to the inverse free-spectral range. The number of solitons in the microresonator can be controlled by the pump laser detuning. The results are in excellent agreement with numerical simulations and soliton theory.**

**In the time domain temporal dissipative solitons in a microresonator enable the conversion of a continuous wave laser into a train of femto-second pulses in a compact, monolithic device. In the frequency domain, the generated pulse train corresponds to a low noise optical frequency comb, with unprecedentedly smooth spectral envelope. As such the regime of temporal dissipative solitons represents an entirely new way of frequency comb generation in microresonators with great prospects for applications.**

Section 4.1 introduces temporal dissipative cavity solitons. Section 4.2 reports on first experimental evidence of soliton formation in a microresonator, which will be confirmed and interpreted by a theoretical analysis in Section 4.3. In Section 4.4 we demonstrate experimentally the stable generation of temporal dissipative solitons in a microresonator, which allows a detailed temporal and experimental characterization. In Section 4.5 it is investigated how the mode structure of a resonator relates to its potential of supporting temporal dissipative cavity solitons. Section 4.7 describes a proof-of-concept experiment where the ultra-short soliton pulses are used for supercontinuum generation.

### 4.1 Temporal dissipative Kerr-cavity solitons

Temporal dissipative cavity solitons<sup>178, 179</sup> can exist stably in a nonlinear cavity for an infinite amount of time when a continuous wave (cw) pump laser is coupled to the cavity. As solitons these pulses of light propagate inside the cavity without changing their intensity profile. Essentially, temporal dissipative solitons<sup>a</sup> rely on the double-balance between anomalous dispersion and Kerr-nonlinearity on the one hand, and cavity loss and parametric frequency conversion of the pump light in support of the soliton on the other hand.<sup>178–181</sup> Mathematically, the system is described by the Lugiato-Lefever equation<sup>182</sup> (damped, driven nonlinear Schrödinger equation, cf. Appendix C.1), to which temporal dissipative Kerr-cavity solitons<sup>180, 183</sup> on top of a cw field at the pump frequency are stable solutions. It is worth emphasizing that temporal dissipative solitons in lasers are known and studied since the 1990s.<sup>179</sup> While spatial dissipative cavity solitons<sup>183, 184</sup> have been frequently observed in experiments, temporal dissipative cavity solitons have only recently been observed experimentally for the first time in fiber cavities.<sup>181</sup> Here the solitons were induced by external writing pulses coupled to the cavity, which in addition was driven by a cw laser. It is worth emphasizing that the term dissipative *cavity* soliton (temporal and spatial) only refers to the class of solitons found in coherently driven passive nonlinear cavities. Consequently, this does not include dissipative solitons in lasers<sup>179</sup> where the system is pumped incoherently. As lasers essentially comprise a cavity this nomenclature of cavity solitons is misleading.

### 4.2 Evidence of soliton formation in a microresonator

In the context of the pioneering fiber cavity experiments that led to the first observation of dissipative temporal cavity solitons in 2010,<sup>181</sup> it has been suggested that these solitons may also be supported by nonlinear optical microresonators, such as the ones used for comb generation. The relation between possible soliton formation and microresonator based combs, however, remains so far unexplored. It is particularly unclear if and how a transition between the generally not pulsed intracavity waveform in a typical comb state (cf. Section 1.3.4) and a soliton state could occur. The following Section will explore and reveal the possibility of temporal dissipative soliton formation in a MgF<sub>2</sub> microresonator.

---

<sup>a</sup>The concept of dissipative solitons is not limited to optics but exists in a wide range of non-conservative systems.<sup>178</sup>

## 4.2. Evidence of soliton formation in a microresonator

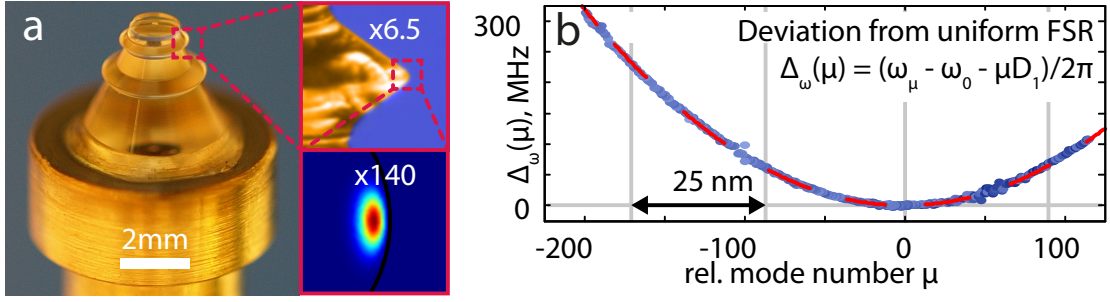


**Figure 4.1: Crystalline MgF<sub>2</sub> microresonator and dispersion.** **a.** MgF<sub>2</sub> crystal carrying two whispering-gallery-mode microresonators of different size (the smaller one with an FSR of 35.2 GHz is used). The smaller panels show a magnified view of the resonator and the simulated optical mode profile. **b.** Second order anomalous dispersion (FSR increases with mode number) of the microresonator with 35.2 GHz FSR shown as the deviation  $\Delta_\omega(\mu) = \frac{1}{2}D_2\mu^2 + \frac{1}{6}D_3\mu^3 \dots$  of the measured resonance frequencies (blue dots)  $\omega_\mu$  from an equidistant frequency grid  $\omega_0 + \mu D_1$  (horizontal grey line), where  $\mu$  denotes the relative mode number and  $D_1/2\pi$  corresponds to the FSR at the frequency  $\omega_0$ . The resonator's anomalous dispersion is accurately described by  $D_2/2\pi = 16$  kHz (red dashed line) and higher order terms neglected. The grey vertical lines mark spectral intervals of 25 nm width ( $\mu = 0$  corresponds to 1553 nm).

### 4.2.1 Microresonator characteristics

Nonlinear microresonators, as used for microresonator based combs, fulfill the basic requirements for temporal dissipative cavity solitons, namely Kerr-nonlinearity, anomalous dispersion, parametric gain and cavity loss. Here, we use a MgF<sub>2</sub> microresonator with an FSR of 35.2 GHz (cf. Figure 4.1a). The critically coupled resonance width is 450 kHz. The dispersion of the resonator was determined using the method described in Appendix D.1 and found to be accurately described by  $D_2/2\pi = 16$  kHz (anomalous dispersion if  $D_2 > 0$ ) without higher order terms such as  $D_3$  (cf. Section 1.2.1). This corresponds to a GVD of  $\beta_2 = -9.39$  ps<sup>2</sup>km<sup>-1</sup>. The microresonator dispersion causes the resonance frequencies to deviate from an equidistant frequency grid, that can be defined by the FSR around the pumped resonance frequency  $\omega_0$ . The frequency deviation  $\Delta_\omega(\mu) = D_2\mu^2$  increases quadratically with increasing relative mode number  $\mu$  with respect to the pumped mode frequency (cf. Figure 4.1b). Based on finite element simulations<sup>150,172</sup> the effective mode area can be estimated to  $A_{\text{eff}} = 90 \times 10^{-12}$  m<sup>2</sup> (cf. Figure 4.1a). The latter corresponds to an estimated nonlinear parameter of  $\gamma = \frac{\omega_p}{c} \frac{n_2}{A_{\text{eff}}} = 4.1 \times 10^{-4}$  m<sup>-1</sup>W<sup>-1</sup>.

Before we commence our search for solitons in microresonators Section 4.2.2 discusses the optical bistability and additional thermal effects in the resonator that will be important in the remainder of this chapter.

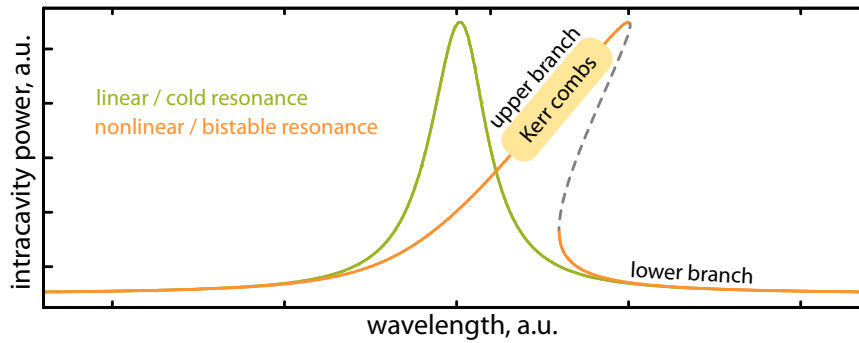


**Figure 4.2: Bistable intracavity power as function of laser detuning.** The green line indicates the Lorentzian resonance shape for the case of a linear cavity or low pump power. The orange line illustrates the bistability resulting from the thermal and/or Kerr-nonlinear resonance shift of a microresonator at high pump power. Microresonator based combs (Kerr-combs) operate on the upper branch characterized by high average intracavity power.

#### 4.2.2 Kerr-nonlinear and thermal resonance shifts and stability

In the case of strongly driven Kerr-nonlinear microresonators, the intracavity field as function of the pump laser detuning cannot be described by a Lorentzian resonance shape (cf. Figure 4.2). Instead, the resonance is asymmetrically shifted towards longer wavelength (lower frequencies) by thermal effects and by the Kerr-nonlinearity when the intracavity power increases.

The thermal resonance shift occurs on a much slower time scale (thermal relaxation time) compared to the quasi-instantaneous Kerr-shift. The combined Kerr-nonlinear and thermal resonance shifts manifest themselves in a non-Lorentzian, triangular resonance shape when the pump laser is scanned with decreasing optical frequency over the resonance (cf. Figure 4.3a, inset).<sup>61, 113, 185</sup> These resonance shifts also result in a bistable behavior, that is, two possible stable solutions (so called 'upper branch' and 'lower branch') for the intracavity power can exist for a particular pump laser detuning (cf. Figure 4.2). A mathematical description for the example of the Kerr-optical bistability is contained in Appendix A.2.3. The solution with higher intracavity power is realized when the cavity is effectively blue detuned (pump frequency higher than the shifted resonance frequency). This detuning regime is self-stable as a result of a negative feedback between fluctuations in the effective detuning and resulting resonance shift.<sup>113</sup> The self-stability is exploited in microresonator based frequency comb generation where the pump laser is operated effectively blue detuned (cf. Section 1.3.3). Stable, effectively red detuned operation is only possible for a large effective red detuning, but usually not considered due to low intracavity power levels.<sup>113</sup>



### 4.2.3 Observation of discrete steps in the resonator transmission

In search of solitons in microresonators we scan a pump laser (fiber laser, wavelength 1553 nm, linewidth 10 kHz, coupled pump power 5 mW) with decreasing optical frequency  $\omega_p$  over a high-Q resonance of the crystalline MgF<sub>2</sub> resonator. This approach is motivated as the pump laser detuning is known to be a critical parameter for the existence of Kerr-cavity solitons.<sup>180, 181, 186</sup> Figure 4.3b shows the evolution of the optical spectrum during the laser scan. Reducing the laser-cavity detuning leads to a build-up of intra-cavity power and once a critical power threshold is reached widely spaced primary comb modes are generated by FWM, followed by secondary modes filling in the spectral gaps as frequently observed<sup>3, 80, 97</sup> in FWM based microresonator combs and described in Chapter 2. While performing the scan, the RF signal (electronically down-mixed to 20 MHz) that results from the beating between neighboring comb lines is sampled and Fourier-transformed. The Fourier-transformed, sampled RF signal is contained in Figure 4.3c. A necessary signature of stable soliton formation is a low-noise, narrow RF signal, resulting from the repetitive out-coupling of a soliton pulse. Indeed, we observe a transition from a broad, noisy RF signal to a single, low-noise RF beatnote for a particular laser detuning. This transition coincides with the beginning of a series of discrete steps in the transmission (Figure 4.3a), which deviates markedly from the expected thermal triangle (inset in Figure 4.3a). The RF beatnote remains narrow throughout all steps. Note that observations similar to the discrete transmission steps have been made in a  $\chi^{(2)}$  nonlinear microwave resonator and connected to soliton formation.<sup>187</sup>

#### Effective pump laser detuning

To determine the effective pump laser detuning, we derive and record a Pound-Drever-Hall (PDH) error signal<sup>188</sup> while scanning over the resonance. A characteristic feature of the PDH error signal is the change of sign when the laser is tuned through the (effective) zero detuning.

Strikingly, the first step, that is, the transition to low noise, coincides with the zero crossing of the PDH signal, which marks the effective zero detuning frequency. This observation implies that the occurrence of the steps coincides with the transition from the upper branch regime (generally used for microresonator based combs) to the lower branch regime. Note that in the fiber cavity experiment that observed temporal dissipative cavity solitons for the first time,<sup>181</sup> the driving laser was stabilized on the lower branch.

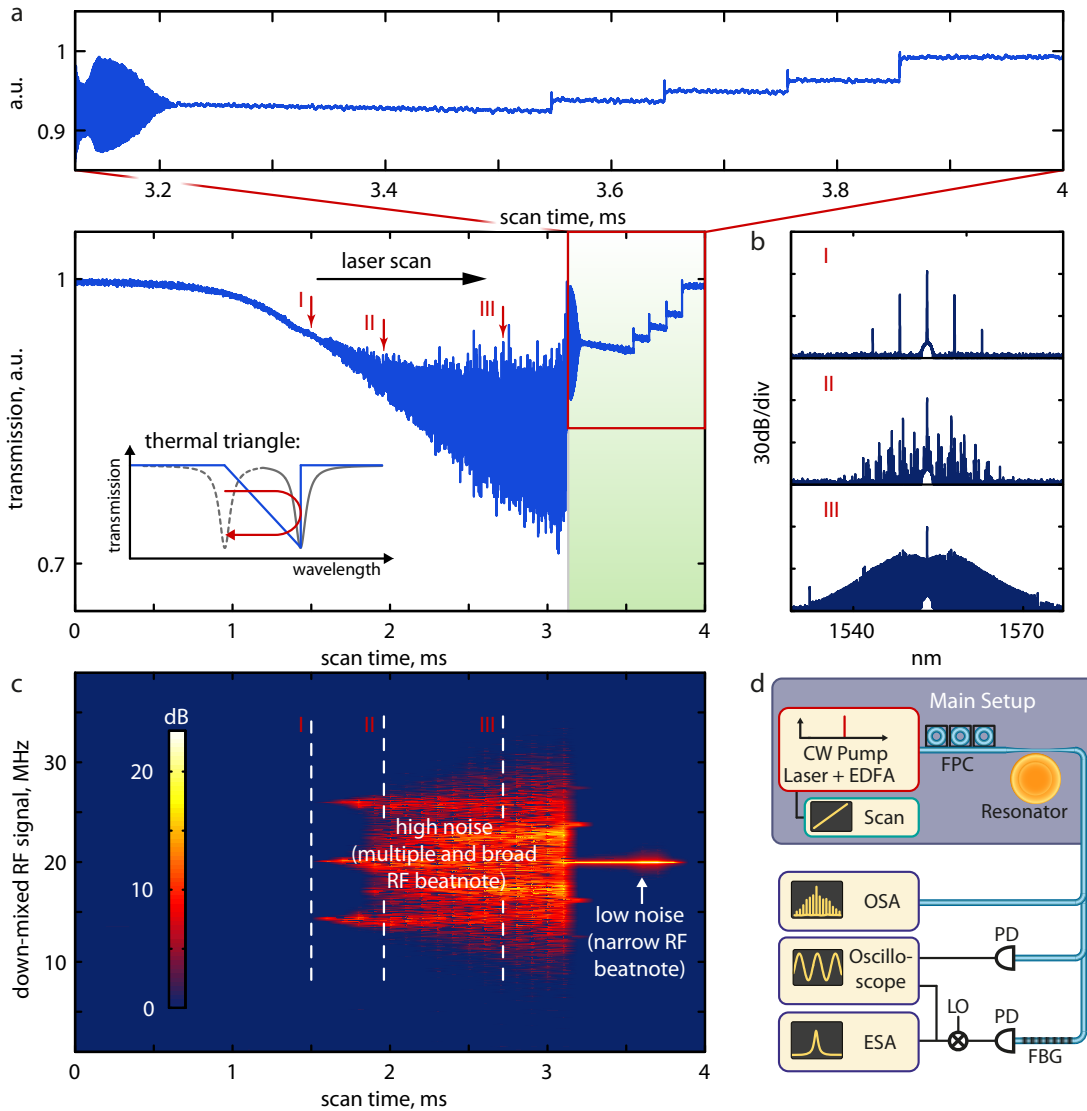


**Figure 4.3: Transmission and beatnote** **a.** Transmission observed when scanning a laser over a high-Q Kerr-nonlinear resonance in a  $\text{MgF}_2$  resonator (coupled pump power 5 mW). The transmission signal deviates from the expected thermal triangle (cf. inset) in the form of discrete steps (green shading). **b.** Evolution of the optical power spectrum for three different positions in the scan; the spectrum (II) and in particular the mesa shaped one (III) exhibit a high-noise RF beat signal. **c.** Down-mixed RF beat signal. **d.** Experimental main setup composed of pump laser and resonator followed by an optical spectrum analyzer (OSA), an oscilloscope to record the transmission and to sample the down-mixed beatnote (via the third harmonic of a local oscillator LO at 11.7 GHz), and an electrical spectrum analyzer (ESA) to monitor the beatnote. Before beatnote detection the pump is filtered out by a narrow-band fiber-Bragg grating (FBG) in transmission; FPC: Fiber polarization controller, EDFA: erbium-doped fiber amplifier, PD: photodetector.

### 4.3. Theoretical description of temporal dissipative solitons in microresonators

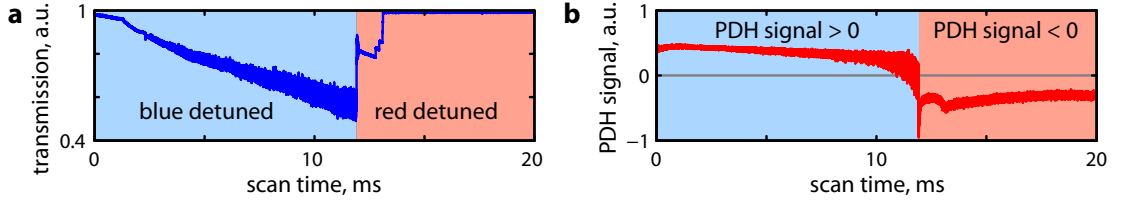


**Figure 4.4: Pound-Drever-Hall (PDH) error signal.** **a.** Transmission signal including the characteristic steps. **b.** PDH error signal for the same laser scan as in (a). The chosen PDH modulation frequency is  $\Omega_{\text{PDH}} = 60$  MHz. Effective blue/red detunings are shaded blue/red.

### 4.3 Theoretical description of temporal dissipative solitons in microresonators

To understand the intriguing observations of discrete steps in the transmission, and the possible connection to soliton-formation we carry out numerical simulations based on the coupled mode-equations approach.<sup>142</sup> These are presented in Section 4.3.1. In Section 4.3.2 the numerical results are compared to and interpreted using an analytical description of temporal dissipative cavity solitons.

#### 4.3.1 Numerical simulation

The numerical simulations are based on the coupled mode equations (eqs. A.17 in Appendix A.2.1).<sup>71, 141, 142, 144, 189, 190</sup> Note that the coupled mode equations are equivalent to the Lugiato-Lefever equation when third and higher order dispersion can be neglected,<sup>191</sup> which is the case in the present microresonator (cf. Figure 4.1b). The coupled mode equations are propagated in time using an adaptive step-size Runge-Kutta integrator. Random vacuum field fluctuation are introduced to seed the initial degenerate FWM. The computation time grows cubically with the number of modes taken into account. If  $2K$  sidebands and the pump are considered, then the total number of nonlinear terms in all  $2K + 1$  equations is  $\frac{1}{3}(K + 1)(8K^2 + 7K + 3)$ .

#### Simulated physical system

The simulated system corresponds to a typical  $\text{MgF}_2$  microresonator with a FSR of 35.2 GHz and dispersion  $D_2 = 10$  kHz,  $D_3/2\pi = -130$  Hz and a quality factor of  $Q = 2 \times 10^8$ . The remaining resonator parameters are refractive and nonlinear indices as well as the effective mode-area  $A_{\text{eff}} = 90 \mu\text{m}^2$  (obtained from finite element simulations, cf. Figure 4.1). We neglect effects of non-unity mode-overlap, interactions with other mode families, any particularities of the resonator geometry and thermal effects. The coupled pump power is set to  $P_{\text{in}} = 100$  mW at a pump frequency of  $\omega_p/2\pi = 193$  THz.

### Simulated scans over a high-Q resonance

Results of simulated laser scans including 101 optical modes are shown in Figure 4.5. The blue curve in Figure 4.5a shows the simulated intracavity power as function of the normalized detuning  $\zeta_o = 2(\omega_0 - \omega_p)/\kappa$  of the pump laser  $\omega_p$  from the cold resonance frequency. Note that the intracavity power is equivalent to the experimental transmission trace in Figure 4.3a when mirrored horizontally (an increased transmission corresponds to a drop in intracavity power). Due to the nonlinear Kerr-shift of the resonance frequency, the effective detuning between pump laser and resonance is smaller than  $\zeta_o$ . Remarkably, the step features are very well reproduced, implying that the simulation includes all relevant physical mechanisms. In agreement with the experiment the number and height of steps fluctuate in repeated numerical scans. Numerically tracing out all possible comb evolutions yields the orange curves in Figure 4.5a. The first part of the evolution of the optical spectrum, shown in Figure 4.5b follows the typical pathway for FWM based comb formation (Chapter 2). Later on, with each step in the transmission, the optical spectrum becomes less modulated until it eventually reaches a perfectly smooth envelope state (frame XI).

### Pulses in the time domain

To reveal the potential underlying soliton formation we investigate the time dependent waveform in Figure 4.5c by phase-coherently adding the individual simulated optical modes. Indeed, the first step in the intracavity power (frame V) corresponds to a transition to a state where multiple pulses inside the cavity exist. Further steps are associated with a step-wise reduction of the number of pulses propagating in the resonator. The separation between multiple pulses in the resonator is random.

#### 4.3.2 Analytic description

To confirm the soliton nature of the simulated pulses we perform an accurate simulation of 501 modes (cf. Figure 4.5d-f) and analyze a state of five pulses (A state with a different number of pulses could have been chosen as well). We compare the numerical simulation with an approximate analytical solution of the Lugiato-Lefever equation.<sup>182</sup> For multiple solitons the analytical solution<sup>180</sup> (cf. Appendix C.1) has the form

$$\Psi(\phi) \simeq C_1 + C_2 \cdot \sum_{j=1}^N \operatorname{sech} \left( \sqrt{\frac{2(\omega_0 - \omega_p)}{D_2}} (\phi - \phi_j) \right), \quad (4.1)$$

### 4.3. Theoretical description of temporal dissipative solitons in microresonators

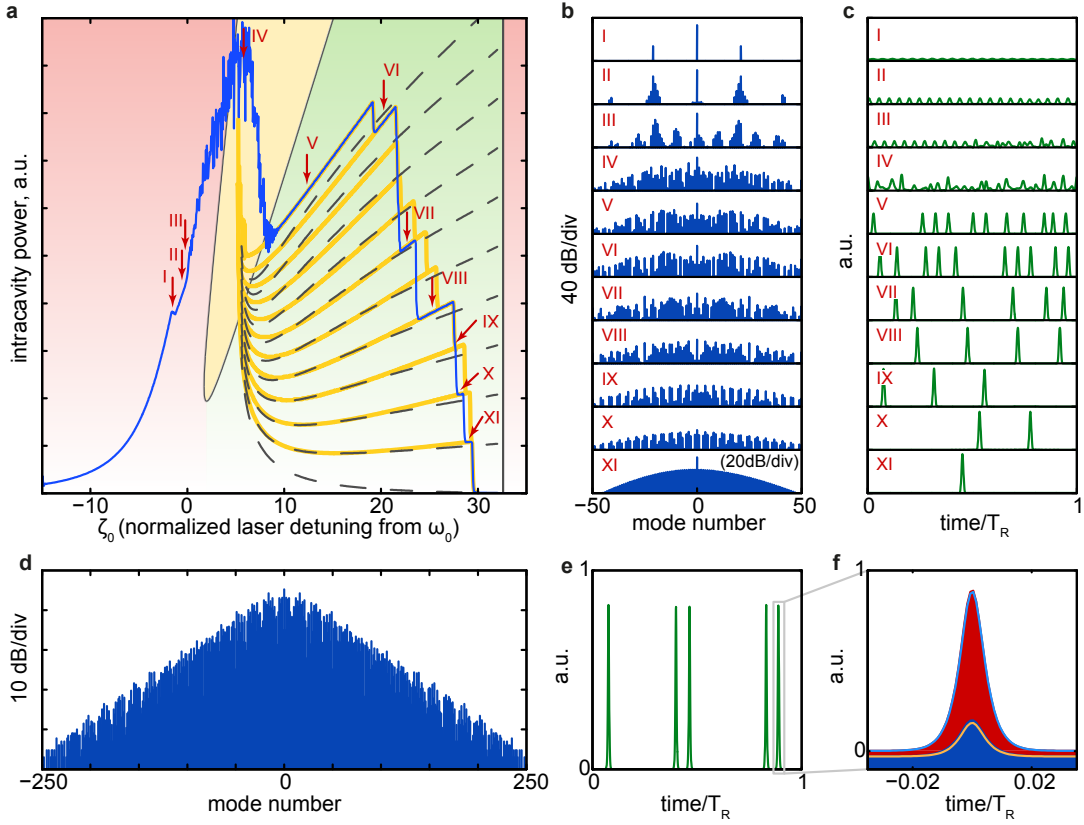


**Figure 4.5: Numerical Simulations of dissipative temporal soliton formation in a microresonator.** **a.** Intracavity power (blue, corresponding to the transmission signal in Figure 4.3a when mirrored horizontally) during a simulated laser scan (101 simulated modes) over a resonance in a  $\text{MgF}_2$  resonator. The step features are clearly visible. The orange lines trace out all possible states of the system during the scan. The dashed lines show an analytical description of the steps. The green area corresponds to the area where solitons exist, the yellow area allows for solitons with a time variable, oscillating envelope; no solitons can exist in the red area. **b/c.** Optical spectrum and intracavity intensity for different positions I-XI in the laser scan. **d.** Optical spectrum obtained when simulating 501 modes and stopping the simulated laser scan in the soliton-regime. **e.** Intracavity intensity for the comb state in (d) showing 5 solitons. **f.** Zoom into one of the soliton states showing the numerical results for the field real (red solid) and imaginary part (dark blue solid). The respective analytical soliton solutions are shown as light blue and orange lines.

where  $\Psi$  denotes the complex field amplitude,  $\phi \in [0...2\pi)$  the angular coordinate inside the resonator,  $\phi_j$  the angular coordinate of the  $j$ th soliton,  $\omega_p$  the pump frequency, and  $N$  is the number of solitons. The complex numbers  $C_1$  and  $C_2$  are fully determined by the resonator parameters and the pump conditions and the ratio  $|C_2|^2/|C_1|^2$  of soliton peak power to cw background can typically exceed several hundreds (cf. Appendix C.1). Indeed, the close to perfect match between analytical solution and numerical result shows that the pulses forming in the microresonator are stable temporal cavity solitons. These solitons emerge from the modulated intra-cavity waveform, which may explain their spontaneous formation as opposed to fiber cavities where stimulating writing pulses are required.<sup>181</sup>

### **Soliton pulse duration and optical spectrum**

In Appendix C.1 the minimal temporal width (FWHM) of the soliton pulse is derived based on equation 4.1

$$\Delta t_{\min}^{\text{FWHM}} \approx 2\sqrt{\frac{-\beta_2}{\gamma F P_{\text{in}}}}, \quad (4.2)$$

where  $F$  is the cavity's finesse,  $P_{\text{in}}$  the coupled pump power,  $\beta_2$  the GVD and  $\gamma$  the nonlinear parameter of the system (cf. Section 4.2.1).

The optical spectrum can be found as the Fourier-transform of the temporal soliton pulse, which results in a sech-shape spectral envelope. The widths (FWHM)  $\Delta t$  of the temporal pulse and the width (FWHM)  $\Delta\omega$  of the optical spectrum are related via the time-bandwidth product of TBP=  $\Delta t\Delta\omega \approx 0.315$  (see Appendix C.1 for a derivation).

Note that in the case of  $N$  multiple solitons inside the cavity the observed more structured optical spectrum  $\Psi_N$  ( $\Psi$  denotes the field amplitude) results from interference of single soliton spectra  $\Psi_j(\mu)$ , where the relative phases of these spectra are determined by the positions  $\phi_j$  of individual solitons:  $\Psi_N(\mu) = \Psi(\mu) \sum_{j=1}^N e^{i\mu\phi_j}$ . The line-to-line variations can be high, however, the overall averaged spectrum still follows the single soliton shape and is proportional to  $\sqrt{N}\Psi(\mu)$ .

### **Limit conditions for temporal dissipative solitons in a microresonator**

Having shown the soliton nature of the pulses in a combined numerical and analytical analysis, we can interpret the blue and orange curves in Figure 4.5a based on general limits<sup>186</sup> applying to solitons as solutions of the Lugiato-Lefever equation. Adopting these criteria for the present case we identify three main regions in Figure 3a, colored red, yellow and green (for details see Appendix C.1). Solitons with a constant temporal

#### 4.4. Experimental generation of temporal dissipative solitons in a microresonator

---

envelope can only exist in the green area. While the yellow area still allows for solitons with a time varying, oscillating envelope<sup>146</sup> (“breather solitons”), solitons can not exist in the red area. Note that in the red area on the left, the system may undergo chaotic Hopf-bifurcations.<sup>186</sup> The correspondence of these analytical limits with the numerical results is remarkable.

##### Analytical description of the steps in intracavity power

For different numbers of solitons we can derive the total power inside the resonator by averaging the respective analytic soliton solution (eq. 4.1) over one cavity roundtrip time (for details see Appendix C.1). The result is shown as dark gray dashed lines in Figure 4.5a, and is in excellent agreement with the numerically observed steps (to account for the limitation due to the low mode number of simulated modes an additional correction factor of order unity is applied). The intracavity power changes discontinuously with the number of solitons present in the cavity.

#### 4.4 Experimental generation of temporal dissipative solitons in a microresonator

To experimentally investigate soliton states, we develop a method that allows to reliably tune into the desired soliton state. This method relies on tuning the laser with an appropriately chosen tuning speed into the soliton state and is described in the next section. In Section 4.4.2 we will discuss the remarkable stability of the solitons, which allows a detailed spectral and temporal characterization in Section 4.4.3.

##### 4.4.1 Laser tuning method

In Section 4.2.3 (Figure 4.4), it was shown that the the first transmission step, that is the transition to solitons coincides with a transition of the pump laser from the effectively blue detuned to the effectively red detuned regime. Experimentally the soliton states in the MgF<sub>2</sub> resonator can not be stably reached by slowly (manually) tuning into the soliton state. The obstacle lies in the temperature drop the resonator experiences when transiting from effective blue detuning (high intracavity power) to effective red detuning (lower intracavity power). This sudden temperature drop leads to a blue-shift of the resonance frequency and a loss of the soliton state. On the other hand, when tuning very quickly into the soliton state the resonator is still cold and its subsequent heating will again lead to a loss of the soliton state.

We solve this problem by tuning into the soliton state with an ideal, intermediate tuning speed, such that the resonator reaches the soliton state in a thermal equilib-

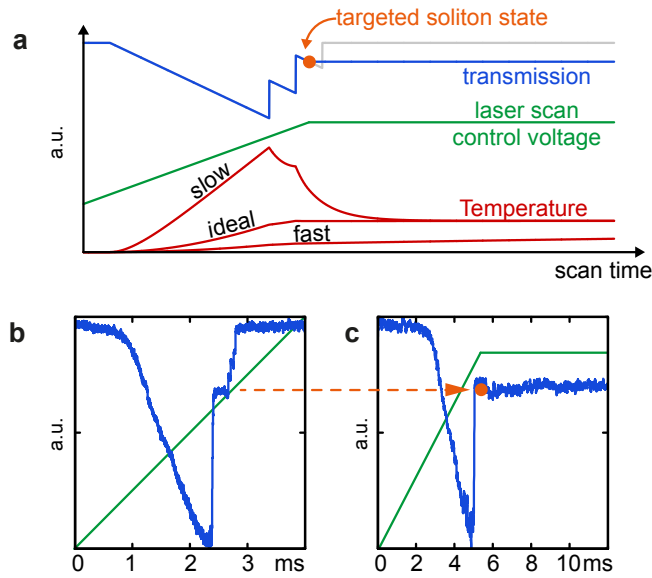


**Figure 4.6: Laser tuning method to achieve soliton states.** **a.** Illustration of the laser tuning method, where a laser frequency scan (green) is performed that stops when the targeted comb state, marked by a orange dot in the corresponding transmission signal (the grey line illustrates the signal that would have been observed if the scan had been continued). The system remains stably in this state when the appropriate scan speed is chosen. In this ideal scenario the temperature (which starts increasing as soon as light is coupled to the resonator) reaches the steady-state equilibrium temperature of the targeted state when the system has reached this state via laser detuning. If the laser scan is performed too slow (fast) then the resulting temperature will be too high (low) and destabilize the system. **b.** Experimental laser scan over a resonance, showing a pronounced step followed by multiple smaller steps. **c.** Demonstration of the adaptive scanning method. The laser scan is stopped after the transition to the soliton regime. The appropriate choice of scan speed allows the system to operate stably in a soliton state. The coupled pump power is 30 mW.

rium, that is, neither too hot nor too cold. This method is illustrated in Figure 4.6. Practically this is achieved by programming an electronic laser frequency ramp signal defined by the three parameters laser tuning speed, and laser start and end wavelength. This signal is used to control the piezo tuning of the fiber laser. The laser frequency ramp is performed in the direction of decreasing optical frequency from the effectively blue detuned regime into the effectively red detuned regime (as done in the first laser scan experiment at the beginning of the chapter, Figure 4.3). Once found for a particular resonator, the scan parameters do not need to be changed and allow reliable generation of soliton states at the push of a button. In contrast to fiber cavity experiments, the soliton pulses form spontaneously without the need for external stimulation. The number of solitons formed can be controlled by the pump laser detuning. The generated solitons remain stable for hours until the pump laser is switched off without the need for active feedback on neither the resonator nor the pump laser. The stability of the soliton states is discussed in the next section.



#### 4.4. Experimental generation of temporal dissipative solitons in a microresonator

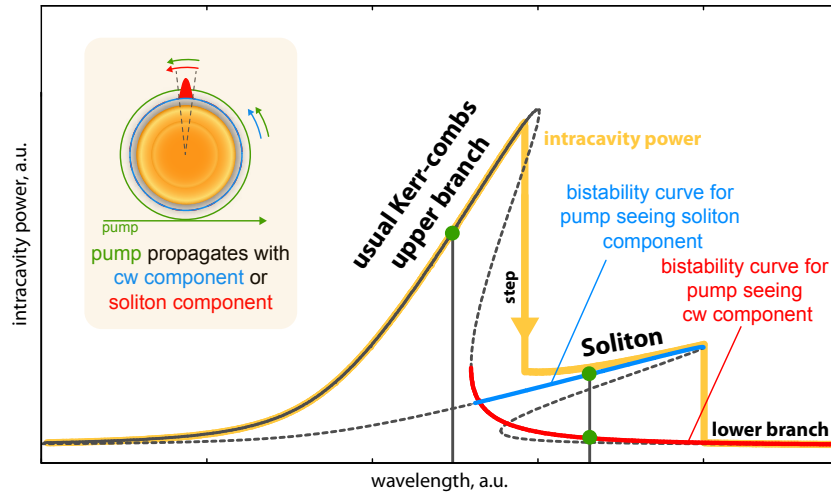


**Figure 4.7: Stability of soliton states:** Considering only the Kerr-nonlinear resonance shift the intracavity power can be described by bistability curves where the upper branch solution corresponds to high and the lower branch solution to low intracavity power. When tuning into the resonance with decreasing optical frequency (increasing wavelength) the intracavity power is described by the upper branch of the Kerr-bistability curve. After the transition to a soliton state the major fraction of the pump light is described by the lower branch bistability curve (red). The fraction of the pump light that propagates with the soliton inside the microresonator (cf. inset) experiences a larger phase shift and is effectively blue detuned on the upper branch of another bistability curve (blue). The extend of the 'soliton bistability curve' towards longer wavelength depends on the peak power of the solitons (i.e. the maximal nonlinear phase shift), the relative height of the curve depends on the relative fraction of the pump light that is affected by the high peak power soliton. The overall intracavity power can be inferred by adding the bistability curves resulting in the yellow curve.

#### 4.4.2 Stability of the soliton states

As it was shown in Figure 4.4 and discussed in the Section 4.4.1 the soliton states are achieved when the pump laser is tuned into the effectively red detuned regime. As moreover observed in Section 4.4.1 the generated solitons remain stable without any active external feedback applied to the system. This is remarkable and indeed surprising as operating in the effectively red detuned regime is usually considered unstable (unless far red detuned, which however does not permit high intracavity power)<sup>113,185</sup> (cf. Section 1.3.3). In the following we will qualitatively explain that the self-stability of the system can be attributed to the presence of solitons. In the case of a pulsed intracavity waveform different fractions of the pump light experience different Kerr-nonlinear phase shifts during one roundtrip. The small spatial fraction of the pump light that propagates overlapping with the high intensity soliton inside the resonator, experiences a much larger phase shift compared to the light propagating with the weak cw background field. While the main fraction of the pump light is effectively

far red detuned (and dominating the PDH signal<sup>b</sup>, Figure 4.4), the small fraction overlapping with the soliton inside the resonator is effectively blue detuned permitting high soliton power. The blue detuned soliton component is evidenced by the series of steps that correspond to a set of small triangular resonances, which are characteristic for blue detuning (one triangle per realized soliton state as shown in Fig. 4.3a and Figure 4.5). Thus, considering the Kerr-nonlinear resonance shift, a soliton state can be interpreted as a superposition of two stable solutions,<sup>113</sup> effective blue (high power solitons) and far red detuned (low power cw background), realized at the same time. Figure 4.7 illustrates the situation in terms of two Kerr-nonlinear bistability curves applying to the pump light that co-propagates with either the high power soliton or the weak cw background. In addition to the quasi-instantaneous Kerr-effect the thermal resonance shifts are important. As opposed to the Kerr-effect, the thermal resonance shift is slow compared to the cavity roundtrip time and only depends on the averaged intracavity power. In the microresonator the detuning dependent change of the averaged intracavity power is dominated by the effectively blue detuned soliton component as opposed to the effectively red detuned cw component (cf. Figure 4.3a and Figure 4.5a). This implies that with respect to the slow thermal effect the resonator behaves as being effectively blue detuned and is thus self-stable.<sup>113</sup>

### 4.4.3 Spectral and temporal characterization

Having access to stable operation of soliton states, we experimentally investigate their RF beatnotes, their optical spectra and their temporal characteristics. For temporal characterization we employ frequency-resolved optical gating<sup>192</sup> (FROG) and a single shot waveform sampling method.

We note that in all temporal characterization experiments no spectral filtering, phase or intensity adjustment (except for pump suppression) is applied. The gain window ( $\geq 4$  THz) of the optical amplifier used before temporal characterization supports more than 100 comb modes.

#### Frequency resolved optical gating

Frequency resolved optical<sup>192</sup> gating (FROG) corresponds to a second-harmonic generation (SHG) autocorrelation experiment, where the frequency-doubled light is spectrally resolved (Setup shown in Figure 4.10b). In contrast to SHG intensity autocorrelation, the FROG method allows reliable identification of ultra-short pulses. In a FROG

---

<sup>b</sup>We note that while the intracavity power in the soliton state is dominated by the soliton component, the PDH signal in Figure 4.4 is dominated by the large fraction of the pump light that is effectively red detuned. Experimentally this can be seen by the only small changes to the PDH signal in the red detuned regime when transmission steps occur.

#### 4.4. Experimental generation of temporal dissipative solitons in a microresonator

---

measurement a short pulse is not only identified by a sharp signal confined to a narrow interferometer delay range (as it is the case in an SHG intensity auto-correlation measurement), but must also exhibit the necessary spectral width as required by the time-bandwidth product (TBP). Prior to the FROG experiment the optical spectra are sent through a fiber-Bragg grating for pump suppression ( $-30$  dB) and are subsequently amplified to 50 mW. Dispersion compensating fiber (Thorlabs DCF3, DCF38) is used for dispersion compensation. In the FROG setup (cf. Fig 4d) the generated optical pulses are interferometrically split and recombined with a variable delay in a nonlinear BBO crystal (critically phase matched). The recombination of the beams inside the crystal occurs at a small angle. Consequently second harmonic generation (SHG) in the symmetric forward direction (the other directions are blocked) occurs only when the optical pulses in the two arms of the interferometer overlap temporally in the BBO crystal. The generated SHG light is spectrally resolved and recorded as a function of delay by a grating based line-CCD spectrometer, which yields a FROG trace. Each FROG trace consists of nearly 1000 spectra with individual exposure times of 800 ms, that is 800 s recording time for one FROG trace. Both FROG hardware and software were home-build and implemented in the course of this thesis. The possible delay range of more than 100 ps allows for cross-correlating consecutive pulses as shown in Figure 4.8b and 4.9b,d.

##### Spectral and temporal characterization

Employing the FROG method we observe, in full consistency with the numerical simulations, single and multiple pulse states as shown in Figure 4.8 and Figure 4.9. The single pulse state is characterized by a smooth spectral envelope, without spectral gaps. This envelope follows a  $\text{sech}^2$ -shape (3 dB bandwidth 1.6 THz) as expected from the Fourier transform of a  $\text{sech}$ -shaped soliton pulse. Based on the TBP for  $\text{sech}$ -shaped pulses of 0.315 (cf. Section 4.3.2) the expected pulse duration is 197 fs. The observed low phase noise RF beatnote is resolution bandwidth limited to 1 kHz and its signal-to-noise ratio exceeds 60 dB. The FROG trace shows a train of pulses well separated by the cavity roundtrip time of  $T_R = 28.4$  ps, corresponding to the FSR of 35.2 GHz. The multi-pulse states (here shown for the case of two and five pulses), show a more structured optical spectrum. This structure reflects the number and distribution of pulses in the cavity (cf. Section 4.3.2). The RF beat note generated in the multi-pulse states is of similar quality as in the single pulse state. Moreover, the FROG measurement allows for a full reconstruction (neglecting a time direction ambiguity) of intensity and phase of the pulses (cf. Figure 4.10a). The N-by-N ( $N=63$ ) FROG trace of the single pulse state (cf. Figure 4.8) is analyzed using a principal component generalized projection algorithm,<sup>193</sup> after background subtraction as well as noise removal via Fourier-filtering. The FROG reconstruction error is

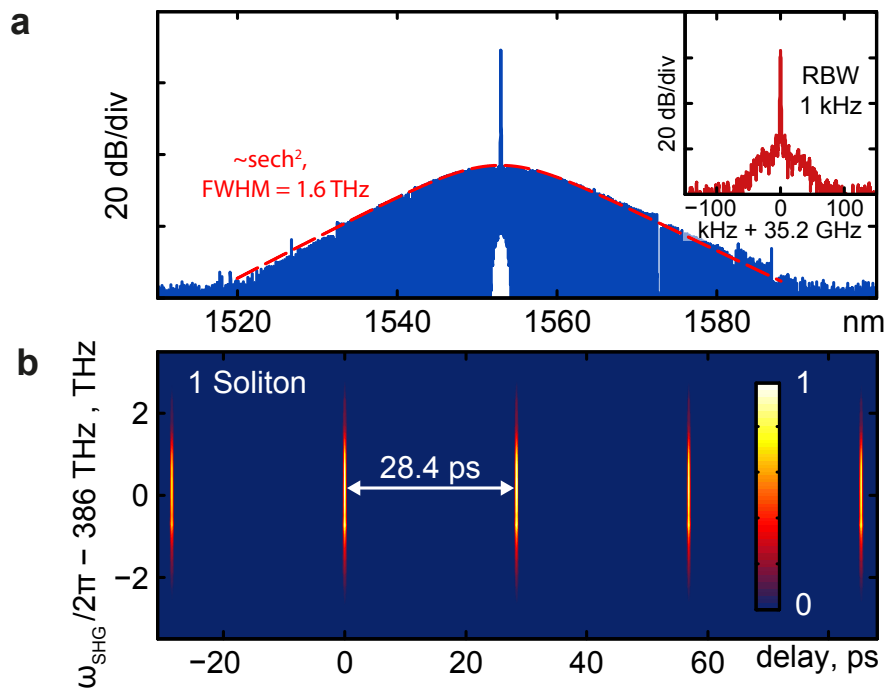


**Figure 4.8: Spectral and temporal characterization of a single soliton state.** **a.** Optical spectrum of a single soliton state. The insets show the RF beatnote, which is resolution bandwidth limited to 1 kHz width. The red line in the optical spectrum indicates the spectral  $\text{sech}^2$  intensity envelope expected for soliton pulses with a 3 dB bandwidth of 1.6 THz. **b.** FROG traces of the comb states in (a) corresponding to single pulses. The FROG setup is shown in Figure 4.10. The coupled pump power is 30 mW.

#### 4.4. Experimental generation of temporal dissipative solitons in a microresonator

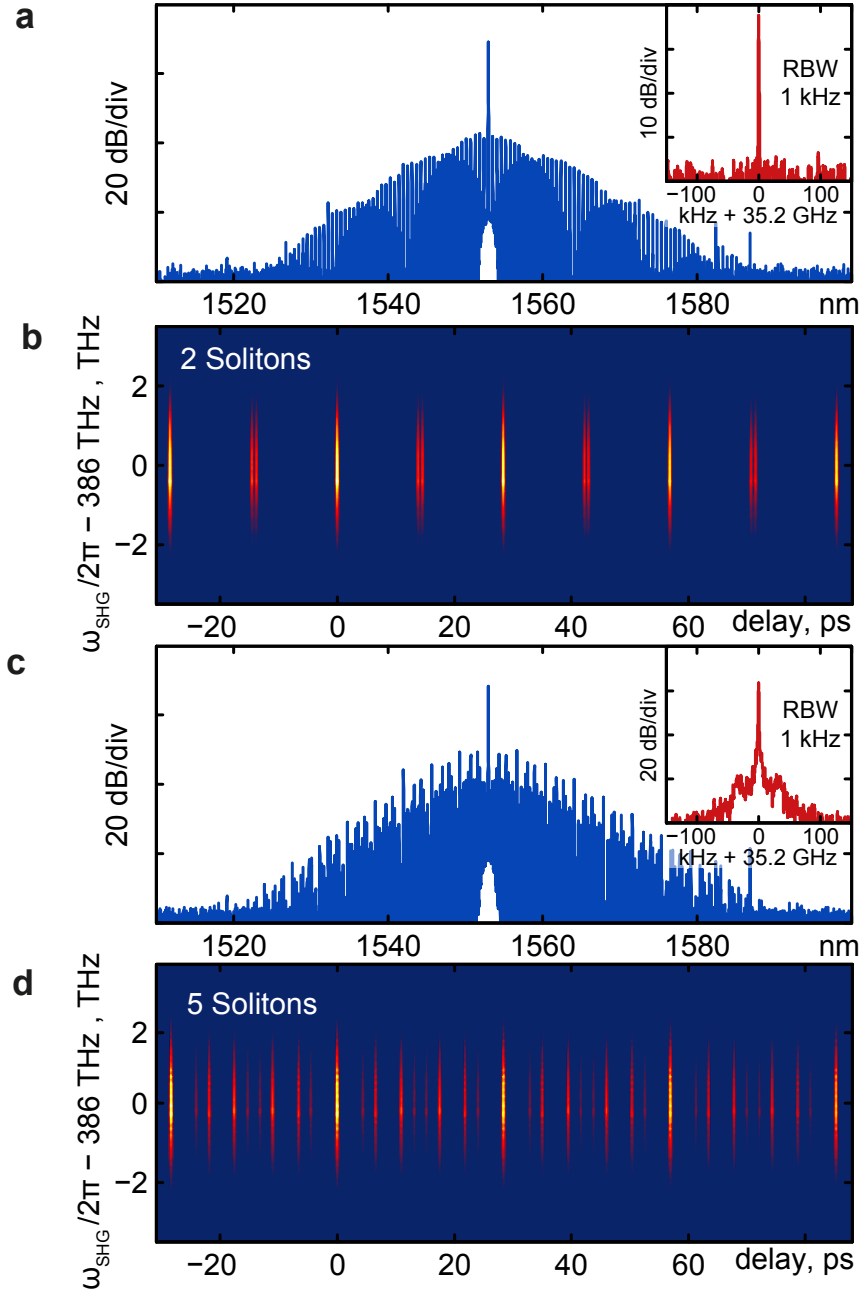


**Figure 4.9: Spectral and temporal characterization of a multiple soliton states.** **a,c.** Optical spectra of two selected comb states with two (a) and five (c) solitons, respectively. The insets show the RF beatnotes, which is resolution bandwidth limited to 1 kHz in both cases. Soliton interference leads to a more structured spectrum when compared to the single soliton state in Figure 4.8. **b,d.** FROG traces of the comb states in (a) and (v), respectively. Color coding and coupled pump power same as in Figure 4.8.

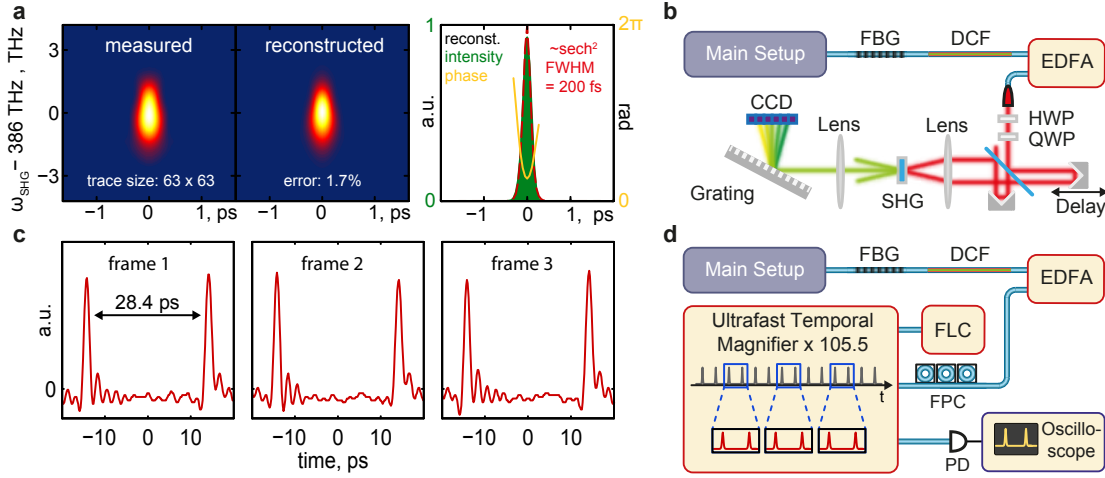


**Figure 4.10: Temporal characterization of ultra-short pulses.** **a.** Higher resolution experimental FROG trace of a single soliton pulse (left). The reconstruction converges to a FROG error of  $\epsilon = 1.7\%$  in good agreement with the experimental trace (middle). The reconstruction (right) of intensity and phase yields an estimated pulse duration of 200 fs (FWHM). **b.** Setup of the FROG experiment. **c.** Sampled optical intensity of the microresonator output over a duration of 40 ps. The three measurements (frame 1,2,3) are separated from one another by a duration of 4 ns corresponding to approx. 140 round-trip times  $T_R$  ( $T_R = 28.4$  ps). **d.** Setup of the intensity sampling experiment including the PicoLuz LLC Temporal Magnifier and a 4 GHz sampling oscilloscope. FBG: fiber-Bragg grating (in transmission), DCF: dispersion compensating fiber, EDFA: erbium-doped fiber amplifier, SHG: second harmonic generation, FLC: fiber laser comb (250MHz rep. rate), PD: photodetector, FPC: fiber polarization controller, HWP: half-wave-plate, QWP: quarter-wave-plate.

defined as  $\epsilon = \frac{1}{N} \sqrt{\sum_{i,j} (M_{ij}^{\text{meas}} - M_{ij}^{\text{reco}})^2}$ , where  $M_{ij}^{\text{meas}}$  and  $M_{ij}^{\text{reco}}$  denote the elements of the  $N \times N$  matrices representing the measured and reconstructed FROG traces. The reconstructed intensity profile is consistent with the expected  $\text{sech}^2$ -shape for solitons and the reconstructed temporal width of 200 fs (FWHM) is in agreement with the bandwidth of the optical spectrum and the expectation based on eq. 4.2 (FROG reconstruction error  $\epsilon = 1.7\%$ ).

### Single shot waveform sampling

To further corroborate the presented results an independent intensity sampling method is applied to a single soliton state. The high repetition rate prohibits a direct sampling, which would require hundreds of GHz bandwidth in detection and recording. This limitation can be overcome by stretching the optical waveform in time using a commercial ‘Ultrafast Temporal Magnifier’,<sup>194</sup> using the time lens effect time lens.<sup>195</sup> Here, analogous to a regular optical lens that imposes a quadratic spatial phase on a beam of light, a quadratic phase is imposed on the optical signal in the

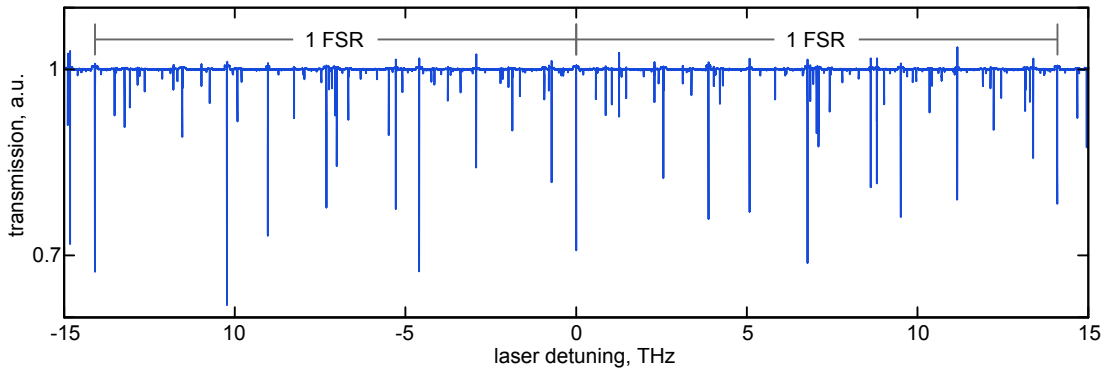


**Figure 4.11: Resonator transmission spectrum** obtained in a frequency comb calibrated laser scan over two FSR of a 14 GHz crystalline  $\text{MgF}_2$  resonator. The upward spikes (values  $> 1$ ) result from cavity-ringdown.

time domain. Similar to the regular lens, this leads to a temporal magnification that is a distortionless stretching in the time domain<sup>c</sup>. The setup is shown in Figure 4.10d. While the time resolution of about 2.5 ps does not allow for determining the duration of the pulse, this single-shot method, as opposed to auto-correlation-type experiments, does not rely on averaging. The results in Figure 4e clearly show optical pulses separated by  $T_R$ , with constant pulse amplitudes, as expected for solitons.

## 4.5 Resonator mode structure and soliton formation

In this section we investigate how the mode structure of the resonator affects its potential of supporting temporal dissipative cavity solitons. This is not only an interesting scientific question but essential to reliably reproduce soliton formation in other resonators and different resonator platforms.

### 4.5.1 Global mode structure

The mode structure, that is the ensemble of mode families and their respective dispersion, is critical to support temporal dissipative cavity solitons. To characterize the full mode spectrum and the dispersion of all relevant modes we perform a broadband high-resolution spectroscopy experiment.<sup>84</sup> A frequency comb calibrated diode laser scan (cf. Appendix D.1) is used to record the low power resonator transmission over a bandwidth exceeding 8 THz. The achieved spectral resolution is on the order of a few MHz. A  $\text{MgF}_2$  resonator with a FSR of 14.1 GHz is employed for this investigation. An exemplary fraction of the laser scan is shown in Figure 4.11.

<sup>c</sup>We thank A. Gaeta and R. Salem for providing the Ultrafast Temporal Magnifier (PicoLuz LLC) for our experiment.

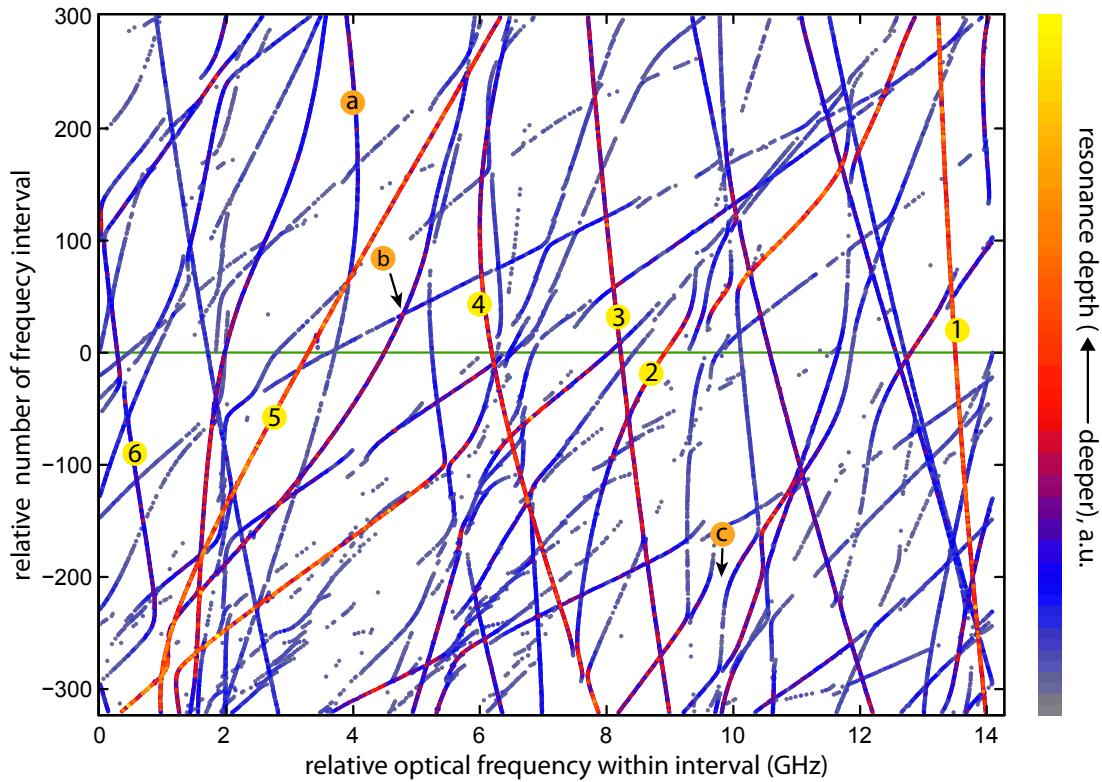


**Figure 4.12: Mode structure of 14.1 GHz crystalline MgF<sub>2</sub> resonator.** In this 2-dimensional representation of the mode structure, mode families are represented by their resonance frequencies forming lines. Different FSRs correspond to different (linear) slopes. Dispersion causes the lines to bend. A leftward curvature (when moving upwards in the graph) corresponds to normal dispersion (e.g. label a). A rightward curvature corresponds to anomalous dispersion (e.g. label 4). The different FSR of different mode families leads to crossings (label b) and avoided crossing (label c). The labels 1 to 6 indicate modes that show significant FWM when pumped at higher power. The green line marks the frequency interval of the pump laser used for soliton experiments at 1553 nm wavelength.

To visualize the data we choose a 2-dimensional representation of the data where the laser scan is divided into intervals of a length of approximately 1 FSR. The scan data is then arranged such that the relative frequency within such intervals is on the horizontal axis, and consecutive intervals are arranged at consecutive vertical positions. A peak-detection algorithm is used to mark the resonance frequencies. The result is shown in Figure 4.12 revealing the rich mode structure of the resonator. Mode families with different FSR that cross other mode families or that bend due to avoided mode crossings can be seen. Moreover, at the same optical frequency mode families can exhibit anomalous or normal dispersion.



## 4.6 Detailed investigation of selected mode families

Our goal is to identify which mode families support temporal dissipative cavity solitons. To this end we repeat the laser scan over only one FSR at much higher pump power (30 mW coupled, fiber laser with 10 kHz linewidth) and record the intensity of the light generated at frequencies different from the pump frequency (a fiber-Bragg grating is used to filter out the pump frequency). In this measurement six mode families are identified that show significant nonlinear frequency conversion. The latter is required, both, for microresonator based frequency comb generation as well as soliton formation. We will restrict our analysis to these six mode families as they are guaranteed to possess a high enough nonlinearity. The respective thermal triangles observed in the transmission signal along with the power of the light converted to frequency different from the pump is shown in Figure 4.13. Interestingly, only two mode families (1 and 4) exhibit the steps in the transmission that are characteristic for soliton formation (Note that the signal of the converted light reveals the steps more clearly than the transmission signal as it does not suffer from the large background of the not coupled pump light).

Next, we employ the data shown in Figure 4.12 to specifically assess the dispersion properties of the six mode families. Hereto, we extract for each mode family its dispersion in terms of its deviation  $\Delta_\omega(\mu)$  (cf. Section 1.2.1) from an uniform FSR as it was done above for another MgF<sub>2</sub> resonator in Figure 4.1b.

**Mode family 1**, supports solitons and is characterized with an almost purely second order anomalous dispersion described fully by  $D_2/2\pi = 1.9$  kHz (as the mode family used for soliton generation in the resonator with 35 GHz FSR, cf. Figure 4.1). **Mode family 4** also supports solitons but, in addition to a  $D_2/2\pi = 21$  kHz term, the dispersion is characterized by a third order contribution  $D_3/2\pi = 90$  Hz. Both mode families, 3 and 4, are affected by avoided modal crossing at relative mode numbers of  $\mu \approx -300$ . These avoided crossing, which lead to local shift of the resonance frequencies, do not prevent soliton generation. It is interesting to note that the values of  $D_2$  of the mode families 3 and 4 differ by more than a factor of ten. Their linewidth  $\kappa$  differs by almost a factor of four (as indicated in Figure 4.14).

**Mode families 2, 3, 5 and 6** do not show any evidence of soliton formation despite a high optical Q (linewidth similar or narrower compared to mode families 1 and 2). This can be explained either by a not general anomalous dispersion (mode family 2) or by avoided modal crossings occurring close to the pump frequency (mode families 3, 5, 6) where the soliton has its highest spectral intensity and therefore is most fragile against imperfections in the mode structure.

In summary, we can identify an anomalous dispersion dominated by  $D_2 > 0$  as a major

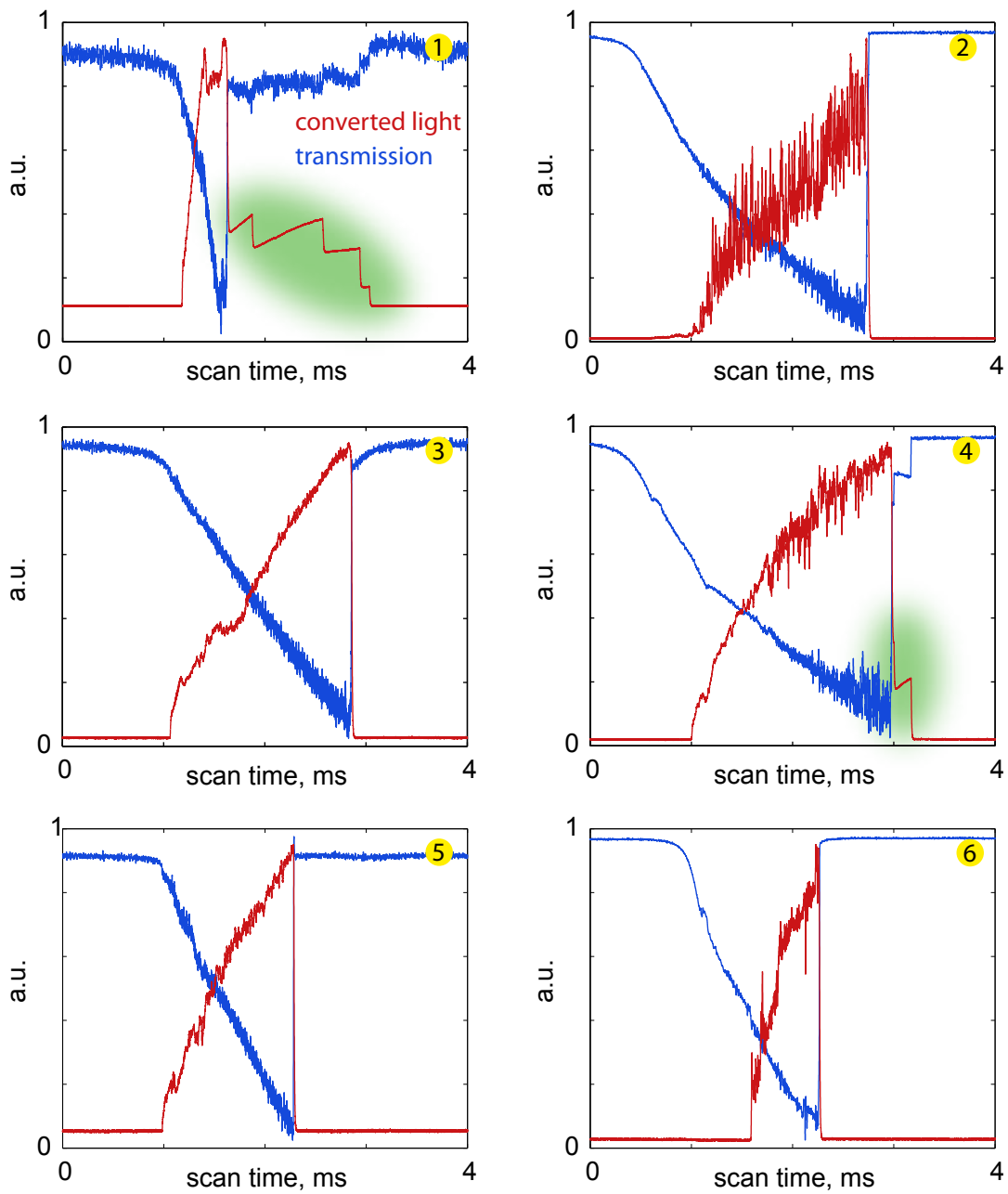


**Figure 4.13: Transmission and frequency conversion signal for six selected modes.** The panels contain the transmission signal (blue) as well as the signal resulting from detecting the intensity of frequency converted (red). All modes exhibit significant frequency conversion, but only two modes (1 and 4) show the step structure characteristic for soliton formation.

#### 4.6. Detailed investigation of selected mode families

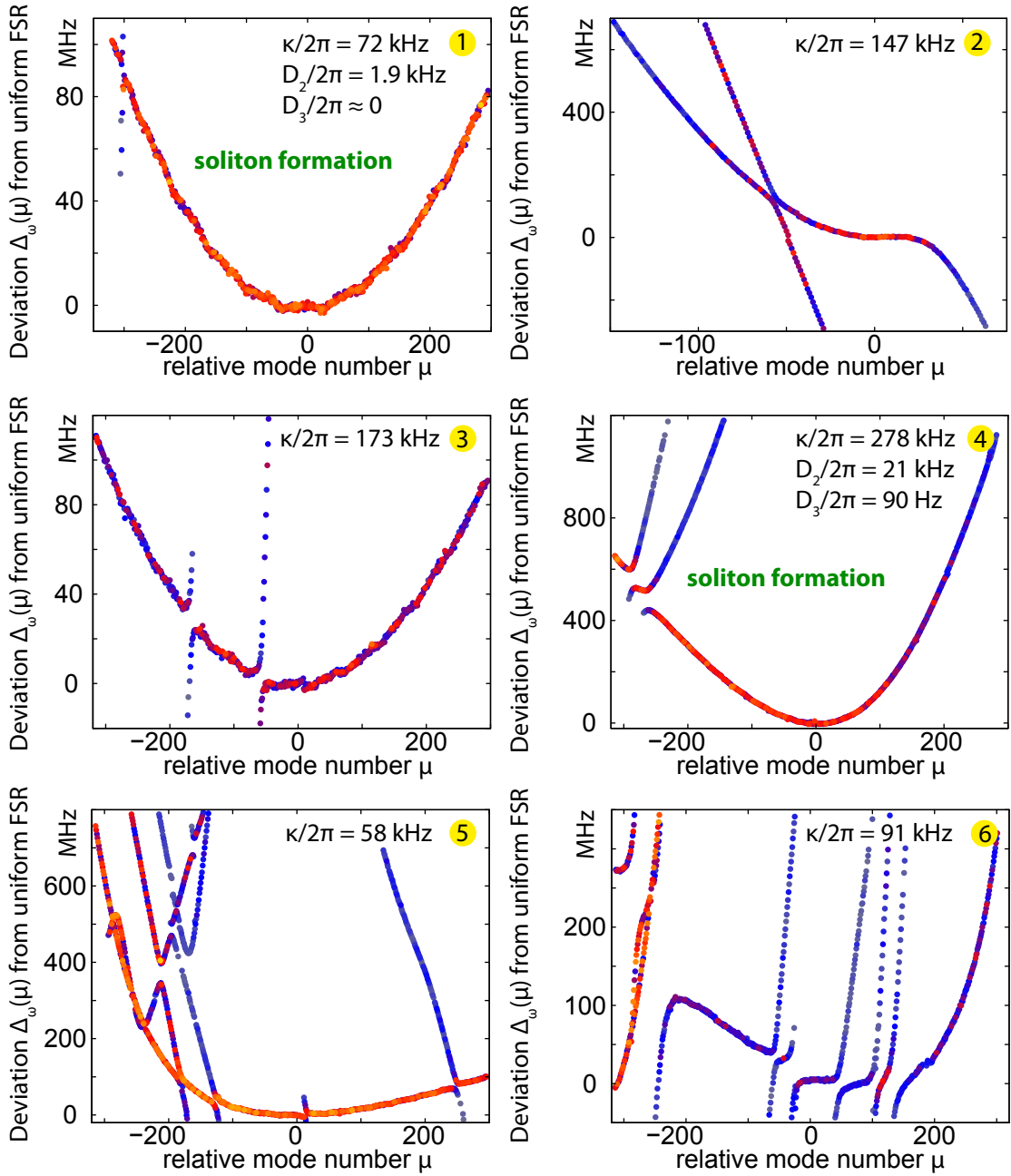


**Figure 4.14: Dispersion of six selected mode families.** The panels show the dispersion as the deviation  $\Delta_\omega(\mu)$  from a uniform FSR (cf. Section 1.2.1). The color code indicates the resonance depth and is the same as in Figure 4.12. The linewidth  $\kappa$  of the mode family (at the pump frequency,  $\mu = 0$ ) is indicated. If applicable the dispersion parameters  $D_2$  and  $D_3$  are included in the panels. Mode family 1 is almost perfectly characterized by  $D_2$  only. Mode family 4 requires an additional  $D_3$  term. Both mode families are slightly affected by modal crossings far away ( $\mu \approx -300$ ) from the pumped mode  $\mu = 0$ . Mode family 2 only shows anomalous dispersion (convex curve) close to the pump and negative relative mode numbers  $\mu$ . The remaining mode families 3, 5 and 6 are heavily affected by modal crossings, some of which are in the vicinity of the pumped mode  $\mu = 0$ .

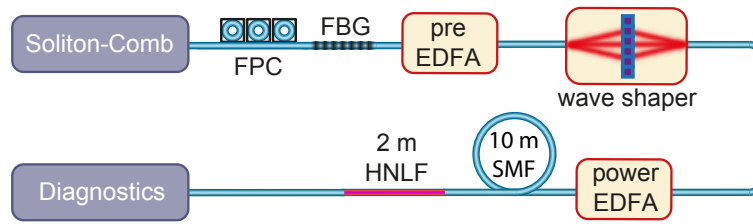


**Figure 4.15: Setup for spectral broadening.** The ultra-short pulses generated in a soliton state ('soliton-comb') are first amplified (pre-EDFA) to approximately 10 mW of power after pump attenuation through a narrow-band fiber-Bragg grating (FBG). A wave-shaper is used to chirp the pulses prior to amplification to several watts of average optical power (power EDFA). The pulses are re-compressed in a 10 m length of single mode fiber (SMF) spliced to a highly nonlinear fiber (HNLF). The resulting spectrum is sent to an optical spectrum analyzer and a fast photodetector for RF beatnote detection. FPC: fiber polarization controller, EDFA: erbium doped fiber amplifier.

requirement for temporal dissipative soliton formation in microresonators. This soliton formation remains robust against a contribution of higher order dispersion terms (such as  $D_3$ ) as long as the anomalous dispersion characteristics is not generally altered. Avoided modal crossings, or more general, spectrally local deviations from the ideal dispersion do not prevent soliton formation as long as they are not situated too close to the pump frequency.

#### 4.7 Spectral broadening and supercontinuum generation

An essential prerequisite for an RF-to-optical link is self-referencing (cf. Section 1.1.3), which can be achieved via e.g.  $f-2f$  or  $2f-3f$  interferometry.<sup>10,12</sup> Necessary for these self-referencing schemes is a minimal optical comb bandwidth of an octave ( $f-2f$ ) or two thirds of an octave ( $2f-3f$ ). So far however, self-referencing of microresonator combs has not been possible as no system was capable of generating sufficiently broad spectra while maintaining the low noise level required for metrology application. Our discovery of soliton formation in microresonators and the generation of ultra-short optical pulses enables spectral broadening using techniques that have been developed for conventional mode-locked lasers.<sup>58</sup> Here we demonstrate in a first proof-of-concept experiment external broadening of a microresonator soliton based frequency comb to a broadband spectrum. The experimental setup is shown in Figure 4.15. The pulses are pre-chirped using a commercial 4f-waveshaper. Here a dispersion that corresponds to the opposite of several meters of standard single mode fiber (SMF28) is applied. The pre-chirped pulse train is then amplified to approximately 3.2 W average power. The pre-chirp is compensated after the amplification by an appropriate length ( $\sim 10$  m) of SMF28 fiber, which is spliced to a 2 m length of highly-nonlinear fiber (HNLF).

#### 4.7. Spectral broadening and supercontinuum generation

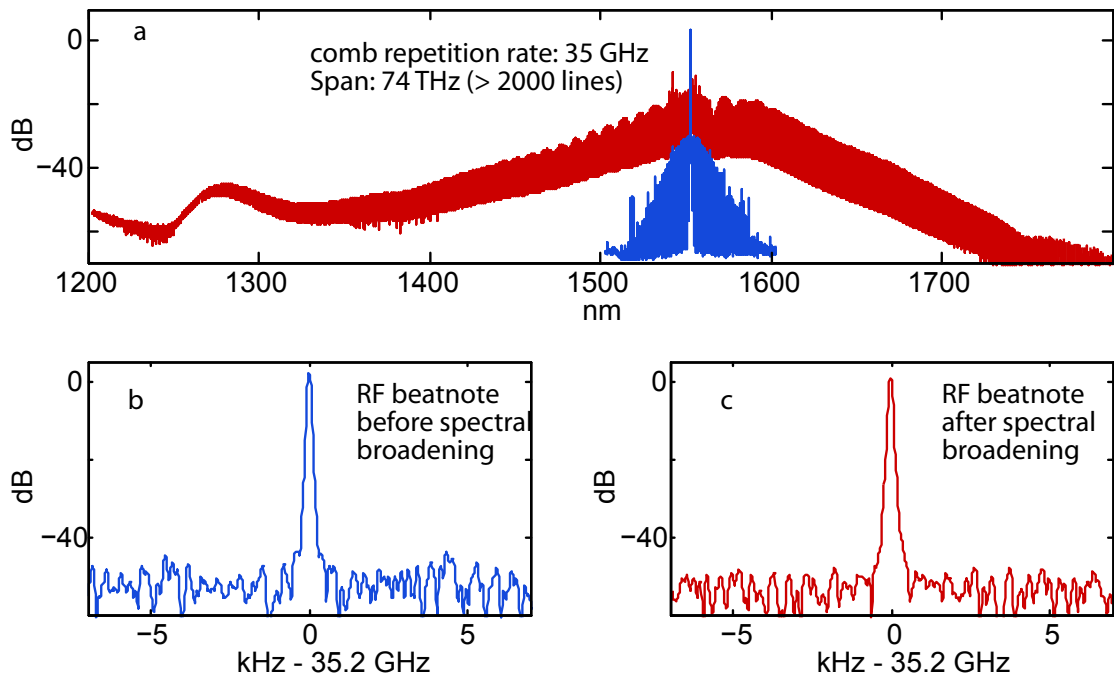


**Figure 4.16: External broadening of ultra-short pulses from a microresonator:** **a** Optical single soliton spectrum (blue) generated in a 35.2 GHz  $\text{MgF}_2$  resonator with 450 kHz resonance width. The spectrum is amplified and broadened to a supercontinuum (red) in a highly-nonlinear fiber. **b,c** Radio-frequency (RF) repetition rate beat note observed when detecting the optical spectra on a fast photo-detector before and after spectral broadening (res. bandwidth 100 Hz). The coupled pump power is 30 mW.

The experiment is first performed with a  $\text{MgF}_2$  resonator that generates pulses of 200 fs duration at a repetition rate of 35.2 GHz (cf. 4.8). The resulting broadened spectrum extends over almost two thirds of an optical octave (cf. Figure 4.16). To achieve higher pulse peak power and broader spectral width, we next repeat the experiment with a larger  $\text{MgF}_2$  resonator and correspondingly lower pulse repetition rate of only 14.1 GHz. The low noise optical soliton spectrum is shown in Figure 4.17. Based on the spectral envelope the pulse duration in the one soliton state is estimated to 112 fs. The achieved spectral bandwidth in the broadening experiment is well beyond two thirds of an octave as required for self-referencing (Figure 4.18). In none of the two broadening experiments an indication of added noise in the RF beatnote is found. A more careful analysis of coherence<sup>58,196</sup> in the broadened spectrum is beyond the present scope and subject of future work. The presented results show that external broadening techniques can in principle be applied to microresonator based combs and open a viable route towards self-referencing microresonator based combs.

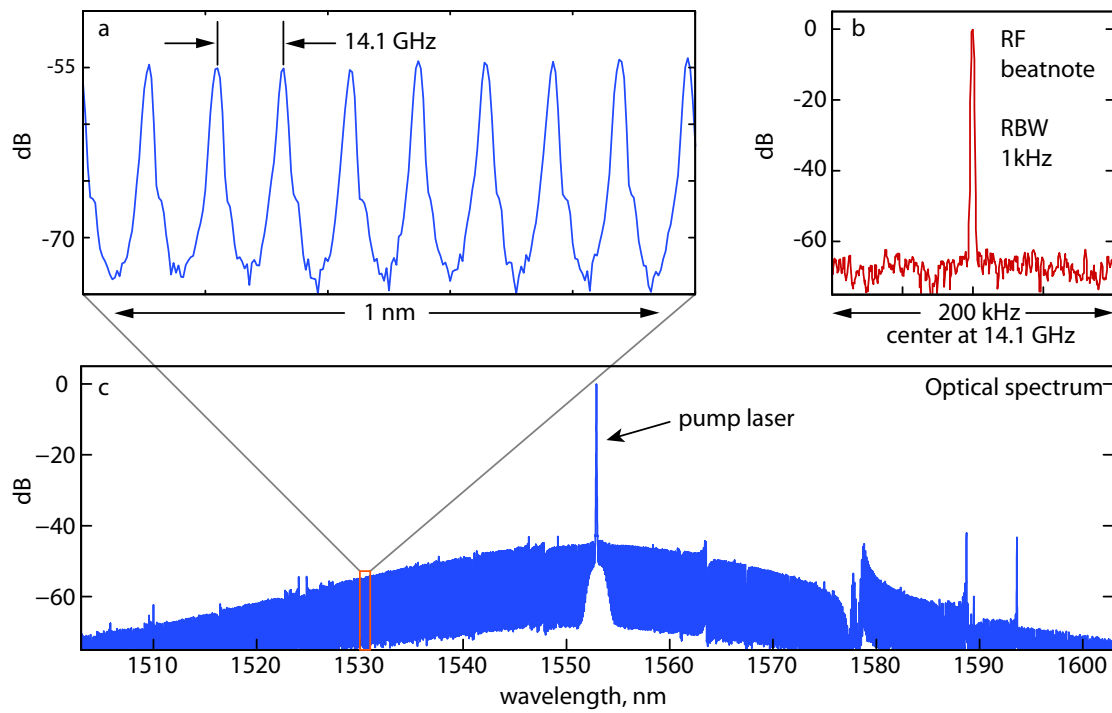


**Figure 4.17: Low noise soliton comb spectrum.** **a.** The optical spectrum is built up of dense optical lines spaced by 14.1 GHz. **b.** The narrow, resolution bandwidth (RBW) limited RF beatnote implies a low noise comb. **c.** The optical intensity envelope is described by a  $\text{sech}^2$ -shape, characteristic for a single soliton state. The artifacts at longer wavelengths are most likely due to avoided modal crossings that can affect the spectrum in far out wings without destroying the soliton. Based on the spectral envelope an estimated pulse duration of 112 fs is found. The coupled pump power is 30 mW.

## 4.7. Spectral broadening and supercontinuum generation

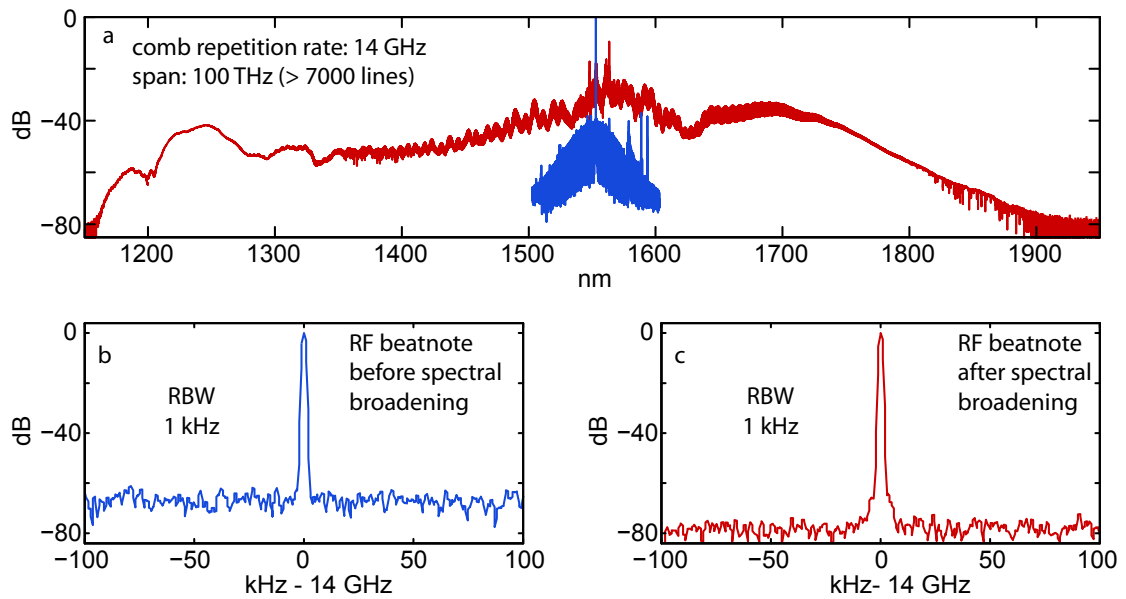


**Figure 4.18: External broadening of ultra-short pulses (estimated 200 fs) from a microresonator:** **a** Optical single soliton spectrum (blue) generated in a 14.1 GHz  $\text{MgF}_2$  resonator with 80 kHz resonance width. The spectrum is amplified and broadened to a supercontinuum (red) in a highly-nonlinear fiber. **b,c** Radio-frequency (RF) repetition rate beat note observed when detecting the optical spectra on a fast photo-detector before and after spectral broadening (res. bandwidth 1 kHz). The coupled pump power is 30 mW. Note that the individual comb lines can no longer be resolved in the broadband spectrum due to the limitation of the optical spectrum analyzer.

### 4.8 Discussion and conclusion

The main findings presented in this chapter can be summarized as follows:

- **Discovery of temporal dissipative soliton formation in microresonators:** Combining experimental, numerical and analytical results, we have discovered spontaneous formation of dissipative temporal cavity solitons in a  $\text{MgF}_2$  microresonator. This marks moreover the first demonstration of direct pulse generation inside a continuously driven microresonator.
- **Laser tuning method to reach stable operation:** A method that allows to reach the stable regime of temporal dissipative solitons is demonstrated. The generated solitons are stable. The number of solitons propagating inside the cavity at the same time is experimentally controllable.
- **Source of ultra-short pulses:** The duration of the soliton pulses depends on the pump power and the dispersion of the resonator. In the present case the optical pulses are in the range from 100 to 200 fs. Given the possibility of dispersion engineering<sup>4,133</sup> in microresonators and the broadband nature of the parametric gain, significantly shorter pulses are conceivable. In contrast to mode-locked lasers the microresonator based approach does neither rely on broadband laser gain media nor on broadband saturable absorbers.
- **A new regime for low noise microresonator based frequency combs:** So far microresonator based combs are operated in a regime qualitatively different from the soliton regime. However, the long-term stability of the solitons allows continuous out-coupling of a train of ultra-short pulses directly from a microresonator. This pulse train corresponds to a low noise frequency comb in the spectral domain. In the single soliton state the spectral envelope is smooth with only low line-to-line power variation. The latter is an important prerequisite for e.g. spectroscopy and telecommunications,<sup>25,119</sup> where the acceptable variation in power between comb lines is limited. Optical spectra comparable to soliton based combs have so far not been generated in microresonators.
- **Spectral broadening and supercontinuum generation:** In a first proof-of-concept experiment we have demonstrated spectral broadening beyond two thirds of an optical octave. Whether the generated supercontinua fulfill stringent coherence criteria as required for self-referencing remains to be shown.

As our results only depend on the generic properties of Kerr-nonlinear microresonators with anomalous dispersion, they apply equally to other microresonator comb platforms. We note that the observations of the step signature is not a spectrally local



particularity but is observed for all resonances of the same mode family that are within the tuning range ( $\pm 0.5$  nm) of the pump laser. Soliton formation, as revealed in our work, may also, at least partially, explain the generation of femto-second pulses in  $\text{Si}_3\text{N}_4$  resonators<sup>127</sup> reported recently. In contrast to mode-locked lasers, which rely on a different gain mechanism, no additional element, such as a saturable absorber is required for stable operation in the microresonator case. A detailed discussion on the difference to mode-locked laser is provided in Appendix C.5. In combination with chip-scale<sup>73,74</sup> integration this opens the route towards compact, stable and low cost ultra-short pulse sources,<sup>179</sup> which can also operate in wavelength regimes (such as the mid-infrared<sup>2</sup>), where broadband laser gain media or saturable absorbers do not exist.

Besides being an exciting scientific observation temporal dissipative cavity soliton generation in microresonators may find use in spectroscopy, optical frequency metrology, microwave photonics, telecommunications and astronomy.



## 5 Outlook

Microresonator based frequency combs have been rapidly evolving over the last years and, with a growing number of researches active in the field, significant advances can be expected over the next years. The results presented in this thesis may help guiding future research and stimulate new ideas:

- **Self-referencing:** Self-referencing requires broadband optical spectra. The demonstration of an octave spanning spectrum (Chapter 2), as well as supercontinuum generation beyond two thirds of an octave show that this is in principle possible (Chapter 4). The understanding of comb formation (Chapter 2) and the related noise processes can help to overcome the obstacle of noise encountered in the first demonstration of an octave spanning spectrum. The demonstration of femto-second pulse generation directly in a microresonator (Chapter 4) links microresonators to conventional frequency comb technology and methods of spectral broadening. Building upon this experience can lead to self-referencing in the near future.
- **Dispersion engineering:** The importance of the dispersion and resonator mode-structure for comb generation and noise characteristics (Chapter 2), as well as soliton formation (Chapter 4) suggests that dispersion engineering will play a key role in the development of future resonator systems. Dispersion engineering, that is influencing the resonator mode spectrum in a controlled way, can take many forms. Besides the material choice of the resonator so far unexplored resonator geometries and combinations of different materials<sup>4</sup> may allow, not only influencing, but truly tailoring a resonator's dispersion.
- **Mid-infrared combs:** The mid-infrared is a very important but difficult to access frequency regime. The demonstration of a low noise frequency comb at mid-infrared wavelengths shows the potential of microresonator technology in this wavelength regime (Chapter 3). Future research may take this approach further

and to longer wavelength. This requires modifications in the laser to resonator coupling, where a replacement of the coupling fiber (such as a coupling prism) has to be found. Directly combining a quantum cascade pump laser with a microresonator may result in compact comb sources over the full transparency window of the resonator. While  $\text{MgF}_2$  resonators are good candidates, other materials, potentially compatible with microfabrication, may emerge.

- **Visible combs:** So far the generation of microresonator based comb at visible wavelength is difficult as here the dispersion is usually normal. The generation of ultra-short pulses (Chapter 4), however, enables efficient frequency conversion in nonlinear crystals. Here sum-frequency and second harmonic generation might allow to transfer microresonator combs into the visible regime with high efficiency.
- **Solitons:** Temporal, dissipative cavity solitons have only recently, in 2010, been observed for the first time in fiber cavities.<sup>181</sup> As such this class of solitons is not well studied experimentally. Here, we have shown the first spontaneous generation of these solitons and the first generation in a microresonator (Chapter 4). On the one hand this provides a unique platform for studying this intriguing phenomenon, on the other hand this may point towards new opportunities for microresonator based combs. For example the generation of dark soliton states in the normal dispersion regime, may allow to generate low noise comb spectra in the normal dispersion regime. The latter would enable generating broadband microresonator combs directly in the visible, as well as using new materials that do not exhibit anomalous dispersion in the relevant spectral region.
- **Mode-locking:** The generation of solitons (Chapter 4) provides one way of mode-locking microresonators, but other methods may exist. The use of a saturable absorber, such as graphene,<sup>197</sup> may lead to mode-locking similar to the case of laser systems.

Microresonator based frequency combs have rapidly evolved within half a decade since their discovery. While the technology is still far from maturity and open scientific questions remain, the achieved advances are encouraging and motivate further research and development. Existing applications<sup>103</sup> include astronomical spectrometer calibration for the search of exo-planets and direct measurement of the universe's expansion.<sup>20-23</sup> Compact chip-scale dual comb spectrometers<sup>24,29,128</sup> and direct frequency comb spectroscopy<sup>25,26,30</sup> could lead to widespread use of microresonator comb enabled precision spectrometers. Moreover, chip-scale microresonator could provide a compact and energy efficient comb source required for mobile applications.

# A Theory of microresonator based frequency comb generation

## A.1 Optical coupling to microresonators

A light field  $\tilde{A} = A(t)e^{-i\omega_0 t}$  at resonance frequency  $\omega_0$  inside a weakly damped resonator can be described in by its rotating frame amplitude  $A$ , which we normalize such that  $|A|^2$  corresponds to the number of photons in the resonator mode. The time evolution of this light field is given by

$$\frac{dA(t)}{dt} = -\frac{\kappa_0}{2}A(t) \quad (\text{A.1})$$

where  $\kappa_0$  denotes the intrinsic cavity decay rate. To maintain a steady intracavity field a driving field (pump laser) is coupled to the resonator:

$$\frac{dA(t)}{dt} = -\frac{\kappa}{2}A(t) + \sqrt{\kappa_{\text{ext}}}s_{\text{in}}(t)e^{-i(\omega_p - \omega_0)t} \quad (\text{A.2})$$

The last phase factor accounts for the fact that the pump frequency  $\omega_p$  may be detuned from the resonance frequency  $\omega_0$ . As the coupling between driving field  $s_{\text{in}}$  and the resonator introduces another loss mechanism the intrinsic cavity decay rate  $\kappa_0$  is replaced by the combined decay rate  $\kappa = \kappa_0 + \kappa_{\text{ext}}$ , where  $\kappa_{\text{ext}}$  denoted the coupling rate. The ratio of  $\eta = \kappa_{\text{ext}}/\kappa$  is called coupling ratio and allows to distinguish three coupling regimes that is undercoupled ( $\kappa_{\text{ext}} < \kappa_0$ ), overcoupled ( $\kappa_{\text{ext}} > \kappa_0$ ) and critically coupled ( $\kappa_{\text{ext}} = \kappa_0$ ).

Applying the phase transformation  $a = A e^{i(\omega_p - \omega_0)t}$  translates eq. (A.2) from the rotating frame of the resonant field  $\omega_0$  into the rotating frame of the driven cavity field defined by the pump frequency  $\omega_p$ :

$$\frac{da(t)}{dt} = -(i(\omega_0 - \omega_p) + \frac{\kappa}{2})a(t) + \sqrt{\kappa_{\text{ext}}}s_{\text{in}}(t) \quad (\text{A.3})$$

## Appendix A. Theory of microresonator based frequency comb generation

---

This allows for the derivation of the steady state intracavity field amplitude  $a$  assuming constant driving conditions  $s_{\text{in}}(t) = s_{\text{in}}$

$$a = \frac{\sqrt{\kappa_{\text{ext}}}}{i(\omega_0 - \omega_p) + (\frac{\kappa}{2})} \cdot s_{\text{in}} \quad (\text{A.4})$$

and the steady state photon number inside the cavity:

$$|a|^2 = \frac{\kappa_{\text{ext}}}{(\omega_0 - \omega_p)^2 + (\frac{\kappa}{2})^2} \cdot |s_{\text{in}}|^2 \quad (\text{A.5})$$

### Coupled resonator transmission

Energy conservation dictates that the photon flux  $|s_{\text{out}}|^2$  equals the difference between incoming photon flux  $|s_{\text{in}}|^2$  and dissipated photons inside the cavity:

$$|s_{\text{out}}|^2 = |s_{\text{in}}|^2 - \kappa_0 |a|^2 = \left(1 - \frac{\kappa_{\text{ext}} \kappa_0}{(\omega_0 - \omega_p)^2 + (\frac{\kappa}{2})^2}\right) \cdot |s_{\text{in}}|^2 \quad (\text{A.6})$$

The transmitted power  $\hbar\omega_p |s_{\text{out}}|^2$  is usually detected on a photo-detector and used for monitoring purposes. The transmission is described by a Lorentzian resonance dip with full width at half maximum (FWHM) of  $\kappa$  and relative depth  $1 - |s_{\text{out}}|^2/|s_{\text{in}}|^2 = \kappa_{\text{ext}} \kappa_0 / \kappa^2$ . Full extinction of the transmission can be achieved under critical coupling conditions  $\kappa_{\text{ext}} = \kappa_0 = \kappa/2$ . In this case the full power launched into the waveguide is dissipated in the resonator.

### Circulating power $P_{\text{cav}}$ and finesse

The circulating power  $P_{\text{cav}}$  inside the cavity can be found by multiplying eq. (A.5) with the photon energy  $\hbar\omega_p$  and division by the roundtrip time  $T_R = 1/\text{FSR}$ :

$$P_{\text{cav}} = \text{FSR} \cdot \frac{\kappa_{\text{ext}}}{(\omega_0 - \omega_p)^2 + (\frac{\kappa}{2})^2} \cdot P_{\text{in}} = 2\eta \cdot \frac{F}{\pi} \cdot \frac{1}{\left(\frac{4(\omega_0 - \omega_p)^2}{\kappa^2}\right) + 1} \cdot P_{\text{in}} \quad (\text{A.7})$$

In the above equation we have introduced the finesse of the resonator as the ratio between FSR and linewidth:

$$F = \frac{\text{FSR}}{\kappa/2\pi} \quad (\text{A.8})$$

The circulating power inside the resonator is proportional to the finesse  $F$  and reaches its maximal value in the case of zero detuning  $\omega_p = \omega_0$  and critical coupling  $\eta = 1/2$ :

$$P_{\text{cav}} = \frac{F}{\pi} \cdot P_{\text{in}} \quad (\text{A.9})$$

## A.2 Frequency comb formation in microresonators

In the following the above formalism will be extended to the case of many nonlinearly coupled optical modes in a resonator with dispersion. These (nonlinear) coupled mode equations<sup>71, 141, 142, 144, 189, 190</sup> allow for analytic derivation of e.g. the threshold pump power and also serve as a basis for numeric simulations used in Chapter 4.

### A.2.1 Nonlinear coupled mode equations

The FWM dynamics in a microresonator can be described using a system of nonlinear coupled mode equations. To this end eq. A.2 needs to be written for all modes with mode number  $\mu$  and extended by a nonlinear coupling term that accounts for the interaction between the modes enabled by the  $\chi^{(3)}$ -nonlinearity. The pump term will only be kept for the mode with relative mode number  $\mu = 0$ .

#### Derivation of the nonlinear coupling term

We start out with the scalar wave equation<sup>135</sup>

$$\frac{1}{R^2} \frac{\partial^2}{\partial \phi^2} E(t, \phi) - \frac{n_0^2}{c^2} \frac{\partial^2}{\partial t^2} E(t, \phi) = \frac{1}{\epsilon_0 c^2} \frac{\partial^2}{\partial t^2} P_{\text{NL}}(t, \phi), \quad (\text{A.10})$$

where the spatial coordinate  $z$  has been replaced by the angular coordinate  $\phi$  to account for the closed geometry of the resonator (without loss of generality a circular resonator with radius  $R$  is assumed). To mathematically describe the nonlinear polarization

$$P_{\text{NL}}(t, \phi) = \epsilon_0 \chi^{(3)} E(t, \phi)^3, \quad (\text{A.11})$$

we expand the electric field in field components at the resonance frequencies  $\omega_\nu$  of the resonator. This approximation is justified by the low losses of high-Q microresonators and the resulting narrow resonances. In the expansion we use the normalised field

## Appendix A. Theory of microresonator based frequency comb generation

amplitudes  $A_\nu$  normalized such that  $|A_\nu|^2$  is the number of photons in the mode  $\nu$ :

$$E(t, \phi) = \frac{1}{2} \sum_\nu \sqrt{\frac{2\hbar\omega_\nu}{n_0^2 \epsilon_0 V_{\text{eff}}}} A_\nu(t) e^{i(\nu\phi - \omega_\nu t)} + c.c. \quad (\text{A.12})$$

$A_\nu(t)$  describes the slowly varying envelope of the field that is changing only on times scales that are much longer than the period  $\omega_\nu^{-1}$  of the carrier frequency. In particular,  $A_\nu(t)$  is assumed to remain approximately constant over one resonator roundtrip. We note that the comb lines do not need to oscillate at the exact same frequency as the resonator modes. A deviation of the comb mode frequency from the resonance frequency  $\omega_\nu$  will be contained in  $A_\nu(t)$ .

Inserting eq. A.12 into eq. A.10 and projecting onto a particular mode  $A_\mu$  i.e. multiplication with  $A_\mu(t)^* e^{-i(\mu\phi - \omega_\mu t)}$  and integration over the spatial coordinate  $\phi$  eventually results in:

$$\frac{\partial A_\mu}{\partial t} = ig \sum_{\mu', \mu'', \mu'''} A_{\mu'} A_{\mu''} A_{\mu'''}^* e^{-i(\omega_{\mu'} + \omega_{\mu''} - \omega_{\mu'''} - \omega_\mu t)} \quad (\text{A.13})$$

In the last step terms with negative frequencies as well as terms of the form  $A_{\mu'} A_{\mu''} A_{\mu'''}^*$  that describe tripe sum frequency and third harmonic generation have been omitted. The nonlinear coupling coefficient

$$g = \frac{\hbar\omega_0^2 c n_2}{n_0^2 V_{\text{eff}}} \quad (\text{A.14})$$

describes the  $\chi^{(3)}$ -nonlinearity of the system with the refractive index  $n_0$ , nonlinear refractive index  $n_2$ , the effective nonlinear cavity volume  $V_{\text{eff}} = A_{\text{eff}}L$  (resonator length  $L$ ), the speed of light  $c$  and  $\hbar$  the Planck constant divided by  $2\pi$ . Physically  $g$  can be interpreted as the per photon frequency shift of the resonance frequency due to the Kerr-nonlinearity (via SPM). The summation is done for all  $\mu', \mu'', \mu'''$  respecting the relation  $\mu = \mu' + \mu'' - \mu'''$ .

### The full coupled mode equation

The full nonlinear coupled mode equations including the pump term as well as the cavity loss are:

$$\begin{aligned} \frac{\partial A_\mu}{\partial t} = & -\frac{\kappa}{2} A_\mu + \delta_{\mu 0} \sqrt{\kappa_{\text{ext}}} s_{\text{in}} e^{-i(\omega_p - \omega_0)t} \\ & + ig \sum_{\mu', \mu'', \mu'''} A_{\mu'} A_{\mu''} A_{\mu'''}^* e^{-i(\omega_{\mu'} + \omega_{\mu''} - \omega_{\mu'''} - \omega_\mu)t} \end{aligned} \quad (\text{A.15})$$



Without loss of generality the initial phase of the pump is set to zero while  $s = \sqrt{P_{\text{in}}/\hbar\omega_0}$  denotes the amplitude of the pump power  $P_{\text{in}}$  coupled to the cavity and  $\delta_{\mu 0}$  is the Kronecker delta. The transmitted power through the coupling waveguide  $s_{\text{out}}$  is described by

$$s_{\text{out}} = s_{\text{in}} - \sqrt{\eta\kappa} \sum A_{\mu} e^{-i(\omega_{\mu} - \omega_p)t}. \quad (\text{A.16})$$

In the above equations it is assumed that neither the resonator to waveguide coupling, nor the nonlinearity or resonator loss depends on the optical wavelength. Moreover, we assume unity mode overlap for all wavelength. Also, particularities of the resonator geometry and interaction with other mode families are not taken into account.

Using the expression for the cold cavity resonance frequencies  $\omega_{\mu} = \omega_0 + D_1\mu + \frac{1}{2}D_2\mu^2$  (cf. eq. 1.4 in Section 1.2.1) the system of equations may be written in a dimensionless way<sup>141</sup>:  $f = \sqrt{8\eta g/\kappa^2}s$ ,  $d_2 = D_2/\kappa$ ,  $\zeta_{\mu} = 2(\omega_{\mu} - \omega_p - \mu D_1)/\kappa = \zeta_0 + d_2\mu^2$ ,  $\tau = \kappa t/2$ . Moreover, the phase transformation  $a_{\mu} = A_{\mu}\sqrt{2g/\kappa}e^{-i(\omega_{\mu} - \omega_p - \mu D_1)t}$  is applied to achieve time-independence of the nonlinear terms:

$$\begin{aligned} \frac{\partial a_{\mu}}{\partial \tau} = & -[1 + i\zeta_{\mu}]a_{\mu} \\ & + i \sum_{\mu' \leq \mu''} (2 - \delta_{\mu'\mu''}) a_{\mu'} a_{\mu''} a_{\mu'+\mu''-\mu}^* + \delta_{0\mu} f \end{aligned} \quad (\text{A.17})$$

In this form all frequencies, detunings and magnitudes are measured in units of half resonance linewidth  $\kappa/2$ . As opposed to the modes  $A_{\mu}$ , the fields  $a_{\mu}$  correspond to an equidistant frequency grid. Note that amplitude and phase modulation implicitly included in the time dependence of  $a_{\mu}$  include frequency deviations from the equidistant grid and in particular noisy comb states with multiple lines per resonance. For the stationary soliton solutions discussed in the main text and later on here, the amplitudes and phases of  $a_{\mu}$  are constant in time when third and higher order dispersion is neglected.

### A.2.2 Three mode system

To determine the parametric threshold and the first oscillating mode it is sufficient to consider a three mode system of  $a_0$ ,  $a_{+\mu}$ , and  $a_{-\mu}^*$ ,<sup>142</sup> i.e. pump as well as two first primary sidebands emerging in the resonator modes indexed  $+\mu$  and  $-\mu$ .

The equation for the pump reads

$$\frac{\partial a_0}{\partial \tau} = -[1 + i\zeta_0 - i|a_0|^2]a_0 + f \quad (\text{A.18})$$

and requiring  $\partial a_0/\partial \tau = 0$  we find for the steady state (as long as no sidebands are

excited):

$$(\zeta_0 - |a_0|^2)^2 |a_0|^2 + |a_0|^2 = f^2. \quad (\text{A.19})$$

The linearised equations describing the sidebands read:

$$\begin{aligned} \frac{\partial a_{+\mu}}{\partial \tau} &= -[1 + i\zeta_\mu - 2i|a_0|^2] a_{+\mu} + i a_0^2 a_{-\mu}^*, \\ \frac{\partial a_{-\mu}^*}{\partial \tau} &= -[1 - i\zeta_\mu + 2i|a_0|^2] a_{-\mu}^* - i a_0^{*2} a_{+\mu}. \end{aligned} \quad (\text{A.20})$$

This system of linear equations can be written in matrix form

$$\begin{pmatrix} \partial a_{+\mu} / \partial \tau \\ \partial a_{-\mu}^* / \partial \tau \end{pmatrix} = \underbrace{\begin{pmatrix} -[1 + i\zeta_\mu - 2i|a_0|^2] & i a_0^2 \\ -i a_0^{*2} & -[1 - i\zeta_\mu + 2i|a_0|^2] \end{pmatrix}}_{=:M} \begin{pmatrix} a_{+\mu} \\ a_{-\mu}^* \end{pmatrix}, \quad (\text{A.21})$$

with the corresponding eigenvalues  $\lambda$  of  $M$ :

$$\lambda = -1 \pm \sqrt{|a_0|^4 - (\zeta_\mu - 2|a_0|^2)^2}. \quad (\text{A.22})$$

### A.2.3 Nonlinear resonance shift, effective detuning and optical bistability

When using eq. A.19 to describe the dependence of the intracavity power  $|a_0|^2$  on the pump laser detuning  $\zeta_0$  we find a Lorentzian resonance shape for small pump powers  $f^2$  (in agreement with eq. A.7). However, when the pump laser power is increased, the resonance shape becomes asymmetric and eventually reaches the bistable regime where two stable values of intracavity power are possible at a given laser detuning. This is visualized in Figure A.1. Which solution is realized depends on the tuning direction of pump laser. When approaching the resonance from higher optical frequencies ( $\zeta_0 < 0$ ) the 'upper branch' solution is realized; in the opposite scan direction the 'lower branch' solution describes the system. Experimentally the transmission trace corresponds to either a triangular resonance shape or an apparently narrowed resonance depending on the laser scan direction. Note that this effect is fully analogous to the thermal triangle described in Section 1.3.3. The pump laser tuning direction used for comb generation from high to low optical frequencies is indicated in Figure A.1. The maximal intracavity power of  $|a_0|^2 = f^2$  is reached for an effective zero detuning (cf. Section 1.3.3) when the pump laser frequency is equal to the effective nonlinearly shifted resonance frequency. Below, in Section A.2.4 we will find  $|a_0| = 1$  as an important threshold value for comb generation. In this context we note that this threshold is always reached as long as  $f^2 \geq 1$  and that the pump laser detuning for reaching the threshold is always  $\zeta_0 \leq 1$ .

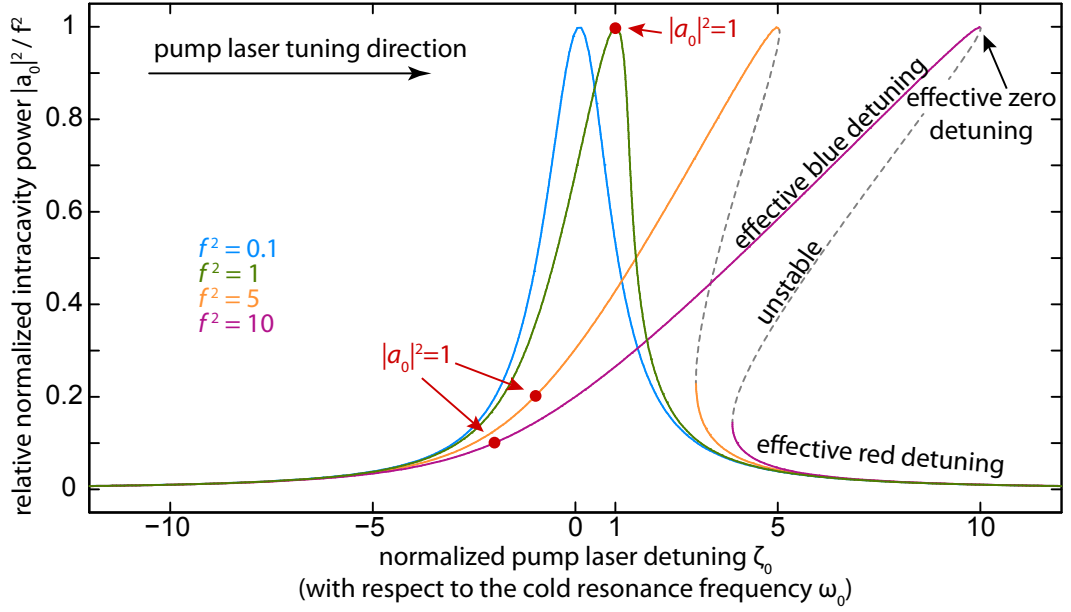


**Figure A.1: Intracavity power vs. pump laser detuning:** The normalized intracavity power  $|a_0|^2/f^2$  is shown as a function of laser detuning  $\zeta_0 = 2(\omega_0 - \omega_p)/\kappa$ . For low pump powers ( $f = 0.1$ ) the intracavity power follows a Lorentzian resonance shape. For higher pump powers the resonance becomes increasingly asymmetric due to the non-linear resonance shift (self-phase modulation). Eventually this leads to bistability, that is, two stable solutions for  $|a_0|^2$  exist for a certain detuning values  $\zeta_0$ . When tuning the pump laser  $\omega_p$  into the resonance from the higher frequency side maximal intracavity power  $|a_0|^2 = f^2$  is reached for an effective zero detuning when the pump laser frequency is equal to the effective nonlinearly shifted resonance frequency. Before (after) this point the pump laser is effectively blue (red) detuned. Tuning the laser beyond effective zero detuning results in a sudden jump to the lower branch solution causing a triangular resonance shape. The value  $|a_0|^2 = 1$  can always be reached for pump powers  $f^2 \geq 1$  and a detuning of  $\zeta_0 \leq 1$ .

### A.2.4 Threshold pump power

The expression  $G = \Re(\lambda + 1)\kappa$  denotes the parametric gain<sup>71</sup> (in not normalized units) of the sidebands  $+\mu$  and  $-\mu$  that are excited if  $G > \kappa$ :

$$G = \sqrt{\kappa^2 |a_0|^4 - 4(\omega_0 - \omega_p + \mu^2 D_2 - \kappa |a_0|^2)^2}, \quad (\text{A.23})$$

An illustration of the parametric gain lobes is shown in Fig. A.2a. To derive the threshold power (minimal pump power  $P_{\text{in}}$  for the generation of sidebands) we consider the maximal gain for the modes  $\pm\mu$  where the second term under the radicand is close to zero. In the presence of (at least locally) anomalous dispersion (corresponding to  $D_2, d_2 > 0$ ) this maximum can be reached approximately for some integer value of  $\mu$  if  $D_2$  is not too large<sup>a</sup>. We thus find that the minimal power required for  $G > \kappa$  in the pump mode is  $|a_0|^2 = 1$ . Interestingly, this threshold power corresponds to a non-linear resonance shift of the pump mode of half a cavity linewidth. In not normalized units the intracavity threshold power can be written as

$$P_{\text{cav}}^{\text{th}} = \frac{\kappa}{2gT_{\text{R}}} = \frac{\kappa n_0^3 A_{\text{eff}}}{2\omega_0 n_2}. \quad (\text{A.24})$$

To derive the threshold pump power, that is the minimal power in the coupling waveguide required to generate sidebands we can simply use assume the case of effective zero detuning where  $|a_0|^2$  becomes maximal (effective nonlinear resonance frequency and laser frequency are both detuned from the cold resonance frequency towards smaller frequency by  $\kappa/2$ ). Mathematically this corresponds to  $\zeta_0 = 1$ . Using  $|a_0|^2 = 1$ ,  $\zeta_0 = 1$  and eq. A.19 we find the threshold pump power required for the generation of parametric sidebands to be  $f^2 = 1$  (also see ref.<sup>141,142</sup>) or equivalently in not normalized units:

$$P_{\text{in}}^{\text{th}} = \frac{\kappa^2 n_0^2 V_{\text{eff}}}{8\eta\omega_0 c n_2} \quad (\text{A.25})$$

### A.2.5 Emergence of the first mode

Here we address the question how distant (in terms of mode number difference) the first parametrically generated modes are with respect to the pump mode. We treat the general case where the pump power  $P_{\text{in}}$  can be higher than  $P_{\text{in}}^{\text{th}}$ . From the steady state eq. (A.19) the laser detuning can be expressed as a function of normalized energy

---

<sup>a</sup> This derivation assumes that the maximum gain can be reached for an integer value of  $\mu$ . For high values of  $D_2$  (typically reached in resonator with large FSR) this assumption may not be true and the gain maximum does not necessarily coincide with an integer value of  $\mu$  (i.e. the spectral maximum of the gain does not coincide with a resonance frequency). In this case the effective threshold power computed below slightly underestimates the true threshold power.

in the pumped mode and the pump power. Here we make use of the fact that for  $P_{\text{in}} \geq P_{\text{in}}^{\text{th}}$  (or equivalently  $f^2 \geq 1$ ) the intracavity threshold power  $|a_0|^2 = 1$  is always reached for a laser detuning  $\zeta_0 \leq 1$  (cf. Section A.2.3):

$$\zeta_0 = |a_0|^2 - \sqrt{f^2/|a_0|^2 - 1}, \quad (\text{A.26})$$

Using this, the definition of  $\zeta_\mu$  and eq. (A.23) at threshold (i.e.  $G = \kappa$ ) we obtain

$$\sqrt{f^2/|a_0|^2 - 1} - d_2 \mu_{\text{th}}^2 + |a_0|^2 - \sqrt{|a_0|^4 - 1} = 0. \quad (\text{A.27})$$

Here, using the threshold power  $|a_0|^2 = 1$ , we find the relative mode number of the first sidebands at threshold

$$\mu_{\text{th}} = \sqrt{\frac{1}{d_2} (\sqrt{f^2 - 1} + 1)}. \quad (\text{A.28})$$

Alternatively, this can be rewritten in SI units:

$$\mu_{\text{th}} = \sqrt{\frac{\kappa}{D_2} \left( \sqrt{\frac{P_{\text{in}}}{P_{\text{th}}} - 1} + 1 \right)} \quad (\text{A.29})$$

The minimum obtainable  $\mu_{\text{th}}$  is reached for  $P_{\text{in}}^{\text{th}} = P_{\text{in}}$  only depends on the ratio of cavity decay  $\kappa$  rate to second order cavity dispersion  $D_2$ :

$$\mu_{\text{th,min}} = \sqrt{\frac{\kappa}{D_2}} \quad (\text{A.30})$$

### A.2.6 Emergence of secondary comb lines

In an analogous way we derive the relative mode numbers of the secondary sidebands  $\mu''$  and  $\mu'''$  that emerge through a non-degenerate FWM process involving the pump  $\mu = 0$  and a strong primary sideband  $\mu'$ . Similar to before, we start from a linearized set of equations:

$$\begin{aligned} \frac{\partial a_{\mu''}}{\partial \tau} &= -[1 + i\zeta_{\mu''} - 2i|a_0|^2 - 2i|a_{\mu'}|^2] a_{\mu''} + 2i a_0 a_{\mu'} a_{\mu''}^*, \\ \frac{\partial a_{\mu''}^*}{\partial \tau} &= -[1 - i\zeta_{\mu''} + 2i|a_0|^2 + 2i|a_{\mu'}|^2] a_{\mu''}^* - 2i a_0^* a_{\mu'}^* a_{\mu''}. \end{aligned} \quad (\text{A.31})$$

## Appendix A. Theory of microresonator based frequency comb generation

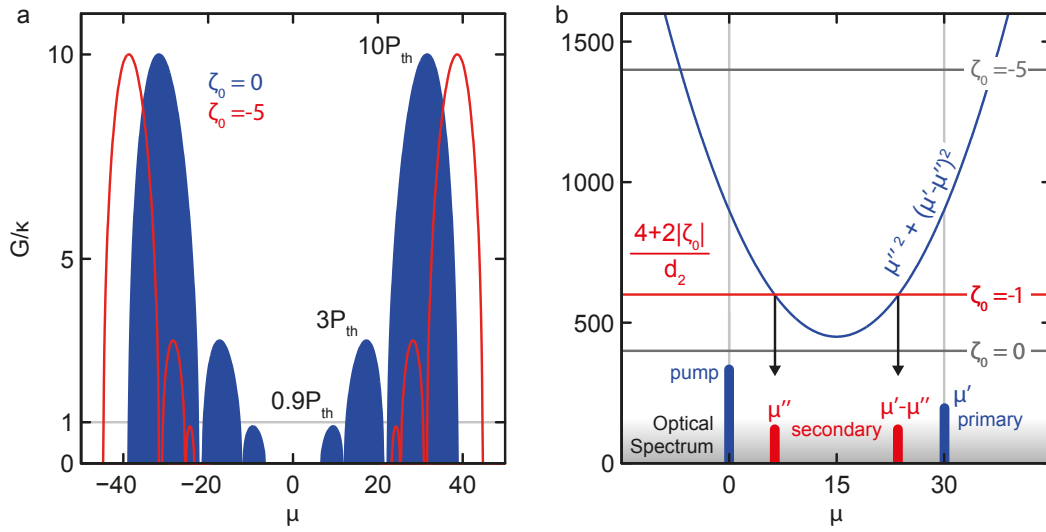


**Figure A.2: Parametric Gain.** **a.** Symmetric degenerate four-wave mixing gain lobes  $G$ , whose position and width depend on the pump laser detuning  $\zeta_0$ , the pump power (here in units of the threshold pump power  $P_{th}$ ) and the dispersion  $D_2$  (here set to  $D_2 = \kappa/100$ ). The grey line corresponds to the cavity decay rate  $\kappa$ , which needs to be exceeded by the gain to allow for growth of parametrically generated primary sidebands. **b.** Position of secondary sidebands generated via non-degenerate FWM of pump  $\mu = 0$  and a primary sideband  $\mu'$ . The secondary sidebands  $\mu''$  and  $\mu'''$  are generated where the red and the blue curve intersect (cf. eq. (A.33)), which depends on the detuning  $\zeta_0$  and in principle can be anywhere inside or outside the interval defined by pump and primary sideband.

where we neglect the influence of other excited lines, in particular the modes symmetric to the pump that are present even in the minimal configuration  $(0, \pm\mu', \pm\mu'', \pm\mu''')$ .

As before, we derive the eigenvalues for the system of equations A.31:

$$\lambda = -1 - \frac{i}{2}(\zeta_{\mu''} - \zeta_{\mu'''}) \pm 2\sqrt{|a_0|^2|a_\mu|^2 - (|a_0|^2 + |a_\mu|^2 - (\zeta_{\mu''} + \zeta_{\mu'''})/4)^2} \quad (\text{A.32})$$

The maximum gain value is reached when the second term in the radicand is zero, that is  $(\zeta_{\mu''} + \zeta_{\mu'''})/4 = |a_0|^2 + |a_\mu|^2$ . In this case, to overcome the cavity decay rate the product of the pump mode power and the power in the sideband needs to be  $2\sqrt{|a_0|^2|a_\mu|^2} > 1$  implying  $|a_0|^2|a_\mu|^2 > 1/4$ . This yields:

$$\mu''^2 + (\mu' - \mu'')^2 = \frac{4(|a_0|^2 + |a_\mu|^2) + 2|\zeta_0|}{d_2} \quad (\text{A.33})$$

Fig. A.2b shows the left- and right-hand side of this expression as a function of relative mode number (For illustrative purposes we have set  $|a_0|^2 + |a_\mu|^2 = 1$ ). The secondary sidebands are generated where the corresponding curves intersect. The location and number of intersection points depend on the pump laser detuning  $\zeta_0$ . From Fig. A.2b it becomes clear that the secondary sidebands can be generated anywhere in between the two primary modes, and in principle also outside of the interval defined by pump and primary sideband.

Fig. A.3 shows typical examples of secondary sideband generation following previous primary sidebands generation. Experimentally a switching between different characteristic comb states (as shown in Fig. A.3a, b and c) may be observed when tuning into resonance.

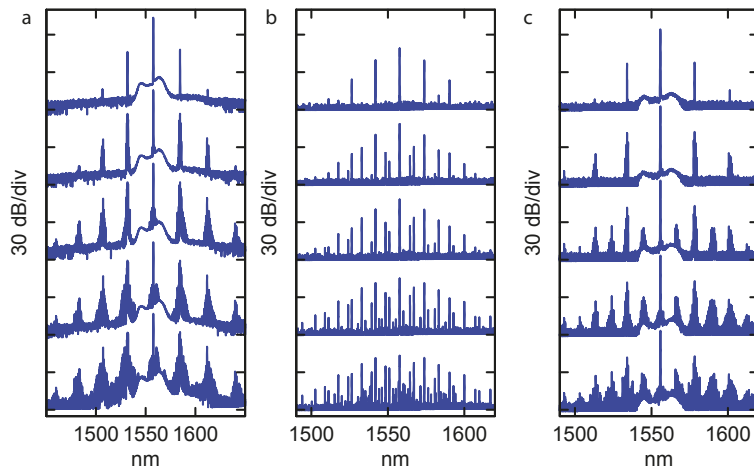


**Figure A.3: Generation of primary and secondary sidebands** following on prior generation of primary sidebands, observed in a 76 GHz FSR  $\text{Si}_3\text{N}_4$  resonator. Secondary sidebands can either be generated **a.** close to the primary sidebands (pump power 2 W), **b.** isolated within the interval between primary lines (pump power 0.8 W), or **(c.)** in a combination of (a) and (b) (pump power 2 W).



## B Noise consideration in a SiO<sub>2</sub> toroid

Chapter 2 presents an octave spanning spectrum generated directly in a fused silica microtoroid. In this spectrum, a broadening of the optical comb lines to  $\approx 70$  MHz is observed. This is much broader than the linewidth of the diode laser used for pumping. Here we will consider noise processes that have been studied in the past in the context of microresonators in order to understand if they can explain the observed noise phenomena in the microtoroid.

Any fluctuation in the parameters of the microresonator or the experimental conditions will affect the frequencies of the comb line. These fluctuations most prominently include changes in the resonance frequencies as well as amplitude and phase noise present in the pump laser and inside the cavity. Thus, a multitude of physical processes can account or contribute to the observation of broad comb lines. These processes include thermorefractive noise, thermoelastic noise, thermal Brownian motion, ponderomotive noise, photothermal noise, laser noise and self-/cross phase modulation.<sup>5, 151–153</sup> Phase noise can also be generated by optomechanical coupling<sup>154–156</sup> of optical and mechanical resonator modes, and by thermal oscillations of the resonator.<sup>157</sup>

Concerning the pump laser, we point out that any intensity noise  $S_{PP}^{\text{in}}(\Omega)$  and phase noise  $S_{\phi\phi}^{\text{in}}(\Omega)$  present in the pump laser transfers into intensity noise  $S_{PP}^{\text{cav}}(\Omega)$  and phase noise  $S_{\phi\phi}^{\text{cav}}(\Omega)$  inside the cavity ( $S_{PP}$  and  $S_{\phi\phi}$  denote the noise spectral densities in units of  $\text{rad}^2/\text{Hz}$  and  $\text{W}^2/\text{Hz}$ ). Using the standard quantum Langevin approach the transfer of noise into the cavity can be calculated.<sup>198</sup> Generally, fluctuations much faster in frequency  $\Omega$  than the optical linewidth  $\kappa$  are filtered out and do not enter the cavity. For a critically coupled cavity and effective zero detuning  $\omega_0^{\text{eff}} - \omega_p = 0$  (cf. Section 1.3.3) the intracavity intensity and phase noise is given by:

$$S_{PP}^{\text{cav}}(\Omega) = \frac{1/T_R^2}{(\kappa/2)^2 + \Omega^2} S_{PP}^{\text{in}}(\Omega) \quad (\text{B.1})$$

$$S_{\phi\phi}^{\text{cav}}(\Omega) = \frac{(\kappa/2)^2}{(\kappa/2)^2 + \Omega^2} S_{\phi\phi}^{\text{in}}(\Omega) \quad (\text{B.2})$$

It can be seen from eqs. B.1 and B.2 that for effective zero detuning there is no conversion between phase and intensity noise. In case of non-zero detuning, however, phase noise is converted to intensity noise and vice versa. For an effective detuning of  $|\omega_0^{\text{eff}} - \omega_p| = \kappa/2$  the response to the pump noise of the critically coupled cavity is:

$$S_{PP}^{\text{cav}}(\Omega) = \frac{(\kappa^2 + \Omega^2)/T_R^2}{\kappa^4 + 4\Omega^4} S_{PP}^{\text{in}}(\Omega) + 4P_{\text{in}}^2 \frac{\Omega^2/T_R^2}{\kappa^4 + 4\Omega^4} S_{\phi\phi}^{\text{in}}(\Omega) \quad (\text{B.3})$$

$$S_{\phi\phi}^{\text{cav}}(\Omega) = \frac{1}{4P_{\text{in}}^2} \frac{\kappa^2\Omega^2}{\kappa^4 + 4\Omega^4} S_{PP}^{\text{in}}(\Omega) + \frac{\kappa^2(\kappa^2 + \Omega^2)}{\kappa^4 + 4\Omega^4} S_{\phi\phi}^{\text{in}} \quad (\text{B.4})$$

Here  $T_R$  is the cavity roundtrip time and  $P_{\text{in}}$  is the power in the coupling waveguide. The conversion from phase noise to noise is particularly relevant for diode pump lasers, such as the one used for octave spanning comb generation. In contrast to their amplitude noise, these lasers have significantly elevated phase noise.<sup>199,200</sup> The value of the root mean square (rms) power fluctuation  $\delta P_{\text{cav}}$  can be found by integrating  $S_{PP}^{\text{cav}}$  over the relevant frequency range according to

$$\delta P_{\text{cav}} = \left( \int S_{PP}^{\text{cav}}(\Omega) \frac{d\Omega}{2\pi} \right)^{1/2}. \quad (\text{B.5})$$

Due to the complex interplay between the various noise mechanism it is difficult to estimate their magnitude quantitatively. The latter is even more difficult in the presence of the thermal and nonlinear lock (cf. Section 1.3.3) that will react on frequency and intensity fluctuation of the pump laser and cavity. Nevertheless, we will qualitatively describe processes that may contribute to the observed linewidth broadening Table B.1 list the parameters of the toroidal fused silica resonator that was employed for comb generation. We keep in mind that a resonance frequency  $\omega_\mu$  is changed by an amount  $\delta\omega_\mu$  when the refractive index  $n$  or the cavity's radius  $R$  experience modifications  $\delta n$  or  $\delta R$ , respectively:

$$-\frac{\delta\omega_\mu}{\omega_\mu} = \frac{\delta n}{n} + \frac{\delta R}{R} \quad (\text{B.6})$$

Parameter	Value
Radius $R$	$40 \mu\text{m}$
Refractive index $n_0$	1.44
Non-linear effective mode area $A_{\text{eff}}$	$4 \mu\text{m}^2$
Non-linear index $n_2$	$2.2 \times 10^{-20} \text{m}^2 \text{W}^{-1}$
Cavity round trip time $T_{\text{R}}$	$2\pi R n / c \approx 1.2 \times 10^{-12} \text{s}$
Optical linewidth $\kappa / (2\pi)$	10 MHz
Pump frequency $\nu_{\text{pump}}$	193 THz
Pump power $P_{\text{in}}$	2 W
Resonator temperature $T$	1000 K
$(1/n)(dn/dT)$	$1 \times 10^{-5} \text{K}^{-1}$
$(1/R)(dR/dT)$	$5.5 \times 10^{-7} \text{K}^{-1}$
Material density $\rho$	$2.2 \text{g/cm}^3$
Specific heat capacity $C$	$700 \text{J kg}^{-1} \text{K}^{-1}$
Effective resonator mass $m_{\text{eff}}$	10 ng
Compressibility $\beta$	$2.7 \times 10^{-11} \text{Pa}^{-1}$

**Table B.1: Toroid and experiment parameters** of a microresonator and experimental conditions for estimating the expected comb frequency noise<sup>98</sup>

### Thermodynamic fluctuations

The thermodynamic fluctuations of a small material volume  $V$  that is coupled to a thermal bath with temperature  $T$  can be expressed as independent root-mean-square fluctuation  $\delta T$  and  $\delta V$  of temperature and volume, respectively.<sup>201</sup> For a microresonator this translates into<sup>153</sup>

$$\delta T = \sqrt{\frac{k_{\text{B}} T^2}{C \rho V_{\text{eff}}}}, \quad (\text{B.7})$$

$$\frac{\delta V_{\text{res}}}{V_{\text{res}}} = \sqrt{\frac{k_{\text{B}} \beta T}{V_{\text{res}}}}, \quad (\text{B.8})$$

where  $V_{\text{eff}}$  is the mode volume and  $V_{\text{res}}$  the resonator volume. Furthermore,  $k_{\text{B}}$  denotes the Boltzmann constant,  $C$  the specific heat capacity,  $\rho$  the material density and  $\beta$  the material compressibility. As these fluctuations are larger for smaller volume they can become significant in microresonators. This is particularly true for fused  $\text{SiO}_2$  toroidal microresonators that can reach high temperatures<sup>5</sup> up to 1000 K in their small mode volumina  $V_{\text{eff}}$ . The temperature fluctuation  $\delta T$  induces, both, modulation of the refractive index  $n$  and the radius  $R$  of the resonator via thermo-refractivity  $dn/dT$  and thermal expansion  $dR/dT$ , respectively. The volume fluctuation affects the radius via  $\delta R/R = 1/3 \cdot \delta V_{\text{res}}/V_{\text{res}}$ . Note that the latter effect is independent of temperature fluctuations and may be interpreted as Brownian motion. From the above expressions

it can be seen that the fluctuation scale only linear and sub-linear with the temperature. Thus the fact that low noise combs with linewidth well below one MHz have been achieved in similar resonator geometries before at room temperature, implies that, even for high temperatures, thermodynamics fluctuations can not explain the observed linewidth broadening. While thermodynamics fluctuations pose a fundamental limit to the frequency stability of microresonators,<sup>153</sup> they are not responsible for the observed linewidth broadening.

**Photothermal effects**

Besides the thermodynamic temperature fluctuations, temperature fluctuations can also be caused by fluctuations in the absorbed power. If  $P_{\text{abs}}$  denotes the power that is absorbed in the cavity, then  $N_{\text{abs}} = P_{\text{abs}} T_{\text{R}} / (\hbar \omega_{\text{p}})$  is the number of absorbed photons. As absorption is a statistical process the fluctuation in the number of photons is given by  $\delta N = \sqrt{N_{\text{abs}}}$ , implying the fluctuation in the absorbed power of  $\delta P_{\text{abs}} = \sqrt{\hbar \omega_{\text{p}} P_{\text{abs}} T_{\text{R}}}$ . The noise  $S_{pp}^{\text{cav}}$  has a much smaller effect as it is drastically diminished by the low absorption coefficient in fused silica. Thus the temperature fluctuations induced by the pump laser can be estimated to

$$\delta T = \frac{\sqrt{\hbar \omega_{\text{p}} P_{\text{abs}} T_{\text{R}}}}{C \rho V} \quad (\text{B.9})$$

Even when setting  $P_{\text{abs}} = P_{\text{in}}$  the temperature fluctuation  $\delta T$  in the photothermal case is two orders of magnitude smaller compared to the case of thermodynamic temperature fluctuation. This implies that photothermal effects are not relevant for the present case.

**Thermal oscillations**

Another effect related to absorption of the pump light in the cavity are thermal oscillation, which can occur as a result of the finite response time of the thermal resonance shift to a change in intracavity power and the finite cavity build-up time.<sup>157, 185</sup> These thermal oscillations, however, require a high material absorption in comparison to scattering induced losses; this criterion is not met in the present high-Q fused silica microtoroid.<sup>157</sup>

---

### Self- and crossphase modulation

The Kerr nonlinearity converts fluctuations in the circulating power  $\delta P_{\text{cav}}$  to variations in the refractive index

$$\delta n = n_0 + n_2 \frac{\delta P_{\text{cav}}}{A_{\text{eff}}}, \quad (\text{B.10})$$

which in turn is responsible for changes in the resonance frequency. It is important to note that the different self- and cross-phase modulational frequency shift on pump mode and other resonator modes will cause a differential frequency shift (cf. Section 1.3.3). In the present case, where a diode laser was used as the pump laser, significant power variations  $\delta P_{\text{cav}}$  may be introduced to the cavity by conversion of the high diode laser phase noise  $S_{\phi\phi}^{\text{in}}(\Omega)$  into cavity intensity noise  $S_{PP}^{\text{cav}}(\Omega)$  according to eq. B.3. Note that for a detuned pump laser the resulting cavity phase noise via the above described mechanism can exceed the pump laser phase noise by several orders of magnitude. Given the phenomenological observation that the comb line broadening depends on the pump laser detuning, self- and cross phase modulation may be responsible for the observed broad comb lines.

### Mechanical oscillations induced by radiation pressure

The high light intensities inside the resonator exert a radiation pressure force on the resonator's boundary. It has been shown that radiation pressure of the photons inside the resonator results in a coupling of optical to mechanical degrees of freedom in microtoroids.<sup>202</sup> Here, a blue detuned pump laser (which is the case for comb generation) can transfer photonic energy into mechanical energy and parametrically drive regenerative mechanical oscillations. These mechanical oscillations act back on the cavity resonance frequencies and could lead to a change of the comb lines frequencies. The threshold power for this so called opto-mechanical parametric instability scales with the effective mass of the mechanical oscillator  $m_{\text{eff}}$  and the mechanical damping rate<sup>202</sup>:

$$P_{\text{mech}}^{\text{th}} \sim m_{\text{eff}}\Gamma. \quad (\text{B.11})$$

While the comb generating toroid is fabricated in a way that ensures highest possible mechanical damping (small undercut, cf. Section 1.2.2) high-Q mechanical modes may still be present. To test the influence of parametric instabilities of the resonator an etched tungsten probe is used to increase the damping rate of mechanical modes. Figure B.1 shows a microscope image of the employed tungsten probe. The probe is moved across the resonator geometry, and in particular, as close to the optical mode as possible without preventing comb generation. In this measurements no

## Appendix B. Noise consideration in a SiO<sub>2</sub> toroid

---

influence on the optical linewidth of comb modes has been observed. While therefore unlikely, parametric instability can not be fully ruled out. Moreover, it has been shown that the radiation pressure induced coupling between optical and mechanical modes can lead to a chaotic quivering of the resonator<sup>159</sup> at high pump powers. Optomechanical effects could therefore contribute to the observed noise, in particular as the frequency noise due to chaotic optomechanical dynamics extends to high Fourier frequency  $> 10$  MHz.<sup>159</sup>

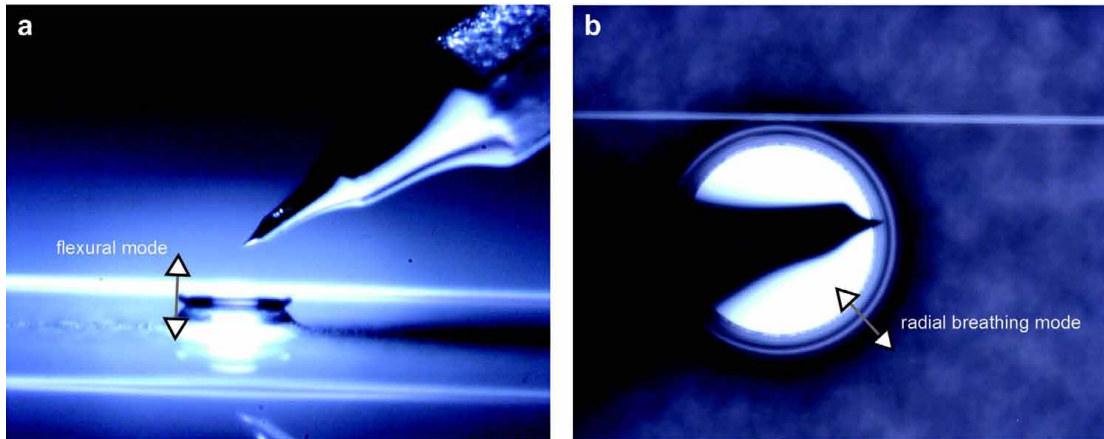


**Figure B.1: Etched tungsten probe** for quenching mechanical oscillations of a micro-toroid. **a.** Side view of the tungsten probe. **b.** Top view of the probe in contact with the resonator close to the toroid rim. The resonator diameter is  $80 \mu\text{m}$ . The mechanical flexural and radial breathing modes are illustrated by arrows in the direction of the mechanical displacement.

# C Theory of temporal dissipative solitons in microresonators

## C.1 Analytical description of solitons in a microresonators

To describe the internal field in a nonlinear microresonator the Nonlinear Schrödinger Equation (NLS) may be used when third and higher order dispersion terms are neglected<sup>191</sup>:

$$\frac{\partial A}{\partial t} - i\frac{1}{2}D_2\frac{\partial^2 A}{\partial \phi^2} - ig|A|^2A = -\left(\frac{\kappa}{2} + i(\omega_0 - \omega_p)\right)A + \sqrt{\frac{\kappa\eta P_{\text{in}}}{\hbar\omega_0}}. \quad (\text{C.1})$$

Here  $A(\phi, t) = \sum_{\mu} A_{\mu} e^{i\mu\phi - i(\omega_{\mu} - \omega_p)t}$  is the slowly varying field amplitude and  $\phi$  is the angular coordinate inside the resonator. This equation may be obtained from the nonlinear equation for the slowly varying amplitude in time domain by using the substitution:

$$\omega_{\mu} = \omega_0 + D_1\mu + \frac{1}{2}D_2\mu^2 = \omega_0 + D_1\mu - \frac{1}{2}D_2\frac{\partial^2}{\partial \phi^2}, \quad (\text{C.2})$$

as  $\sum_{\mu} (i\mu)^n A_{\mu} e^{i\mu\phi - i(\omega_{\mu} - \omega_p)t} = F.T. \left[ \frac{\partial^n}{\partial \phi^n} A(\phi, t) \right]$  (details of analogous derivation for a fiber are given by Boyd<sup>135</sup>).

Transforming eq. (C.1) to its dimensionless form gives:

$$i\frac{\partial \Psi}{\partial \tau} + \frac{1}{2}\frac{\partial^2 \Psi}{\partial \theta^2} + |\Psi|^2\Psi = (-i + \zeta_0)\Psi + if. \quad (\text{C.3})$$

Here  $\theta = \phi\sqrt{\frac{1}{2d_2}}$  is the dimensionless longitudinal coordinate,  $\Psi(\tau, \phi) = \sum A_{\mu}(\tau)e^{i\mu\phi}$  is the waveform, and  $d_2 = D_2/\kappa$  is the dimensionless dispersion. Equation (C.3) is identical to the Lugiato-Lefever equation,<sup>182</sup> where a transversal coordinate is used instead of a longitudinal one in our case. Using the ansatz of a stationary ( $\frac{\partial \Psi}{\partial \tau} = 0$ )

## Appendix C. Theory of temporal dissipative solitons in microresonators

---

soliton on a continuous-wave (cw) background<sup>180</sup> we find an expression for a single soliton

$$\Psi = \Psi_0 + \Psi_1 \simeq \Psi_0 + B e^{i\varphi_0} \operatorname{sech}(B\theta), \quad (\text{C.4})$$

where the real number  $B$  defines both, width and amplitude of the soliton and  $\varphi_0$  defines the phase angle. We note that eq. (C.4) is not an exact solution of eq. (C.3), for which exact soliton solutions are known only in the case of zero losses.<sup>186</sup>

The constant cw background  $\Psi_0$  can be found by inserting  $\Psi_0$  into eq. (C.3) as the lowest branch<sup>186</sup> of the solution of

$$(|\Psi_0|^2 - \zeta_0 + i)\Psi_0 = if, \quad (\text{C.5})$$

which, eventually, results when  $\zeta_0 > \sqrt{3}$  (bistability criterion) and large enough detunings  $f^2 < \frac{2}{27}\zeta_0(\zeta_0^2 + 9)$  in:

$$\begin{aligned} |\Psi_0|^2 &= \frac{2}{3}\zeta_0 - \frac{2}{3}\sqrt{\zeta_0^2 - 3} \cosh\left(\frac{1}{3} \operatorname{arcosh}\left(\frac{2\zeta_0^2 + 18\zeta_0 - 27f^2}{2(\zeta_0^2 - 3)^{2/3}}\right)\right), \\ \Psi_0 &= \frac{if}{|\Psi_0|^2 - \zeta_0 + i} \simeq \frac{f}{\zeta_0^2} - i\frac{f}{\zeta_0}. \end{aligned} \quad (\text{C.6})$$

The soliton component  $\Psi_1$  in eq. (C.4) is approximated by the bright soliton solution of the ordinary NLS (no damping, no driving), which is the limit case for  $\zeta_0 \gg 1$ .

The parameters  $B$  and  $\varphi_0$  can be derived based on general conditions for the soliton attractor,<sup>180</sup> which yields

$$B \simeq \sqrt{2\zeta_0}, \quad (\text{C.7})$$

$$\cos(\varphi_0) \simeq \frac{\sqrt{8\zeta_0}}{\pi f}. \quad (\text{C.8})$$

Based on eqs. (C.6,C.7) we can estimate the ratio  $R$  of soliton peak power to cw pump background:

$$R = \frac{|B|^2}{|\Psi_0|^2} = \frac{2\zeta_0^3}{f^2}. \quad (\text{C.9})$$

For a maximal detuning  $\zeta_0 = \zeta_0^{\max}$  (see eq. (C.13) below) we find:

$$R_{\max} = \frac{\pi^6 f^4}{2^8} = \left(\frac{\pi^3 g \eta P_{\text{in}}}{2\kappa^2 \hbar \omega_0}\right)^2. \quad (\text{C.10})$$



Extending eq. (C.4) to the case of multiple solitons inside the resonator gives

$$\Psi(\phi) \approx \underbrace{\Psi_0}_{C_1} + \underbrace{\left( \frac{4\zeta_0}{\pi f} + i\sqrt{2\zeta_0 - \frac{16\zeta_0^2}{\pi^2 f^2}} \right)}_{C_2} \sum_{j=1}^N \operatorname{sech}\left(\sqrt{\frac{\zeta_0}{d_2}}(\phi - \phi_j)\right). \quad (\text{C.11})$$

It was shown<sup>180</sup> that if a pair of solitons in a train is separated by a distance  $\phi_{j+1} - \phi_j \gtrsim (8/B)\sqrt{2d_2}$  the pair of solitons does not interact. This puts a possible limit  $N_{\max} < \frac{2\pi}{8}\sqrt{\zeta_0/d_2}$  of a maximum number of stationary solitons in the resonator and consequently the maximum number of “steps” in intracavity power and transmission. Assuming that soliton can only emerge for  $\zeta_0 > \sqrt{3}$  (bistability criterion), we find  $N_{\max} \approx \sqrt{\kappa/D_2}$ , which remarkably coincides with the distance between the first generated primary sidebands  $\mu_{\text{th},\min}$  in the process of comb generation.<sup>3</sup>

## C.2 Limit conditions for solitons in microresonators

By substituting  $|h| = |f|/\sqrt{2\zeta_0^3}$ ,  $\gamma = 1/\zeta_0$ ,  $\tilde{\theta} = \sqrt{2\zeta_0}\theta$ ,  $\Psi = \sqrt{2\zeta_0}\tilde{\Psi}$  and changing the phase of the pump, (C.3) is transformed to the damped driven NLS equation for the stationary case:

$$\frac{\partial^2 \tilde{\Psi}}{\partial \tilde{\theta}^2} + 2|\tilde{\Psi}|^2 \tilde{\Psi} - \tilde{\Psi} = -i\gamma \tilde{\Psi} - h, \quad (\text{C.12})$$

which was analyzed for infinite boundary conditions by Barashenkov et al.<sup>186</sup> In particular the condition for the soliton existence  $h > 2\gamma/\pi$  transforms into:

$$\zeta_0^{\max} = \pi^2 f^2 / 8. \quad (\text{C.13})$$

Eq. (C.13) can also be found from the requirement that the right part in equation (C.8) must be smaller than unity. In<sup>186</sup> it was further shown analytically that the boundaries separating the regimes of existence of solitons (as described in the main text) are defined by characteristic curves for  $\tilde{\Psi}_0$  in (C.12). In our case this translates into

$$|\Psi|_{\pm}^2 = \frac{2}{3}\zeta_0 \pm \frac{1}{3}\sqrt{\zeta_0^2 - 3} \quad (\text{C.14})$$

Numerical simulations for our system with periodic boundary conditions show that all these limits remain valid with very good quantitative agreement for a sufficiently large number  $K \gg \frac{2}{\pi}\sqrt{\frac{\zeta_0^{\max}}{d_2}} = f\mu_{\text{th},\min}/\sqrt{2}$  of modes (typically a few hundreds).

### C.3 Analytical description of steps in the intracavity power

The height of steps in the intracavity power can be found by averaging the waveform amplitude (eq. C.11) squared over one roundtrip for different numbers  $N$  of solitons:

$$\begin{aligned} |\overline{\Psi}|^2 &= |\Psi_0|^2 + N \cdot \xi(K) \frac{1}{2\pi} \int_0^{2\pi} (\Psi_1^2 + \Psi_0 \Psi_1^* + \Psi_1 \Psi_0^*) d\phi \\ &= |\Psi_0|^2 + N \sqrt{2d_2} (\Psi_0' \cos \phi_0 + \Psi_0'' \sin \phi_0 + \sqrt{2\zeta_0/\pi}) \simeq \frac{f^2}{\zeta_0^2} + N \xi(K) \frac{2}{\pi} \sqrt{d_2 \zeta_0}. \end{aligned} \quad (\text{C.15})$$

As shown in Fig. 3 in the main manuscript, this approach also describes the laser tuning dependence of the step height. When comparing to the numerical simulations with a rather low mode number, we use a correction factor  $\xi(K)$  of order unity ( $\xi(K) \simeq 1.3$  in the case of 101 simulated modes). For a higher number of simulated modes (e.g. 501) this correction is not required (cf. comment in sec. C.2).

### C.4 Optical spectrum and temporal width of solitons in a microresonator

The optical spectrum  $\Psi(\mu)$  of the soliton has the same hyperbolic secant form as the time domain waveform. Mathematically this corresponds to the Fourier transform of a hyperbolic secant being again a hyperbolic secant:

$$\Psi(\mu) = \text{F.T.} \left[ \sqrt{2\zeta_0} \operatorname{sech} \left( \sqrt{\frac{\zeta_0}{d_2}} \phi \right) \right] = \sqrt{d_2/2} \operatorname{sech} \left( \frac{\pi\mu}{2} \sqrt{\frac{d_2}{\zeta_0}} \right). \quad (\text{C.16})$$

Using the relation for the optical frequency  $\omega = \omega_p + \mu D_1$  and the time  $t = \frac{\phi}{2\pi} T_R = \phi/D_1$  spectral envelopes and the soliton waveform can be rewritten:

$$\Psi(\omega - \omega_p) = \sqrt{d_2/2} \operatorname{sech}((\omega - \omega_p)/\Delta\omega) \quad \text{with} \quad \Delta\omega = \frac{2D_1}{\pi} \sqrt{\frac{\zeta_0}{d_2}}. \quad (\text{C.17})$$

and

$$\Psi(t) = \sqrt{2\zeta_0} \operatorname{sech}(t/\Delta t), \quad \text{with} \quad \Delta t = \frac{1}{D_1} \sqrt{\frac{d_2}{\zeta_0}}. \quad (\text{C.18})$$

## C.5. Soliton mode-locking in lasers vs. soliton formation in microresonators

---

The minimal achievable soliton duration can be found by using  $\zeta_0^{\max}$  (eq. C.13) in the above equation for  $\Delta t$ :

$$\Delta t_{\min} = \frac{1}{\pi D_1} \sqrt{\frac{\kappa D_2 n_0^2 V_{\text{eff}}}{\eta P_{\text{in}} \omega_0 c n_2}}. \quad (\text{C.19})$$

This equation can be recast in terms of the group velocity dispersion  $\beta_2 = \frac{-n_0}{c} D_2 / D_1^2$ , the nonlinear parameter  $\gamma = \frac{\omega}{c} \frac{n_2}{A_{\text{eff}}}$  (for simplicity we assume critical coupling  $\eta = 1/2$  and on resonant pumping):

$$\Delta t_{\min} = \frac{2}{\sqrt{\pi}} \sqrt{\frac{-\beta_2}{\gamma F P_{\text{in}}}}, \quad (\text{C.20})$$

where denotes the finesse  $F = \frac{D_1}{\kappa}$  of the cavity. Note that the values  $\Delta\omega$  and  $\Delta t$  need to be multiplied by a factor of  $2 \operatorname{arccosh}(\sqrt{2}) = 1.763$  to yield the FWHM of the  $\operatorname{sech}^2$ -shaped power spectrum and pulse intensity, respectively.

For the time bandwidth product (TBP) we find  $\Delta t \Delta\omega = 2/\pi$  or, when considering the FWHM of spectral and temporal power (in units of Hz and s),  $\text{TBP} = 0.315$ .

## C.5 Soliton mode-locking in lasers vs. soliton formation in microresonators

This section compares soliton formation in microresonators with soliton mode-locking in lasers where a saturable absorber is necessary for soliton stability:

**Soliton mode-locking in lasers:** Generally mode-locking requires a pulse shaping mechanism, which can be achieved in different ways for example via a fast saturable absorber that forms the circulating intensity inside the laser cavity into a pulse.<sup>45</sup> Here, the shortest achievable pulse duration is limited by the relaxation time of the fast saturable absorber. Another mode-locking mechanism is soliton mode-locking, where the pulse shaping mechanism is provided by the formation of solitons in the presence of negative group velocity dispersion and self-phase modulation via the cavity's non-linearity. This method is widely used and well understood in the context of mode-locked laser and ultra-short optical pulse generation.<sup>51,203</sup> While the pulse shaping does not rely on the effect of a saturable absorber, it has been shown theoretically and experimentally that soliton mode-locked lasers still require a saturable absorber, which ensures the stability of the soliton against the growth of a narrow-bandwidth cw background.<sup>51,203</sup> This cw background arises from the interaction and reshaping of the soliton in the laser cavity and subsequently experiences a larger gain as the soliton, which due to its broadband spectral nature falls into the outer, lower

gain parts of the spectral laser gain window. It is important to note that in the case of soliton mode-locking the relaxation time of the saturable absorber does not limit the achievable pulse duration; it merely ensures the suppression of the continuum on intermediate timescales.<sup>204</sup>

**Soliton formation in microresonators:** Soliton formation in microresonators is similar to soliton mode-locking in lasers. As in the case of a soliton-mode locked laser solitons are formed due to a balance between cavity nonlinearity and self-phase modulation. However, while microresonators are driven by a continuous wave pump laser they are not lasers. The conversion of the continuous pump laser light into other frequency components and the amplification of the newly generated frequency components rely exclusively on the parametric gain due to the Kerr-nonlinearity of the resonator material. The cw pump laser coincides directly with a spectral component of the soliton. Importantly, a saturable absorber is not required for the stability of the solitons as detailed below: Mathematically the coherently driven, damped Kerr-nonlinear microresonator is described by the Lugiato-Lefever equation,<sup>182</sup> which is identical to a damped, driven nonlinear Schrödinger equation. Dissipative temporal cavity solitons, superimposed onto a weak continuous wave background, have been proven to exist as stable mathematical solutions to this equation.<sup>180</sup> Due to the cavity loss, these solitons are dissipative in their nature and their persistence requires a source of energy for replenishment. The latter is provided by continuously and coherently driving the cavity.

The continuous wave background on which the solitons exist in the case of a microresonator is very different from the detrimental cw background in a soliton mode-locked lasers. It is a coherent internal field originating from the pump laser. It is not a narrow bandwidth low intensity cw background pulse produced by perturbation of the soliton. As opposed to a spectrally limited but continuous laser gain medium (continuous in the sense that it can amplify any frequency component within the gain bandwidth) the parametric gain profile is highly frequency selective (as energy conservation needs to be fulfilled in the frequency conversion processes). Moreover, the parametric gain profile depends on the light frequencies and intensities present in the cavity and relies on the phase coherent interaction between all these light frequencies. While it cannot replace a stringent mathematical stability analysis as mentioned above, this illustrates that the growth of a destabilizing cw background is generally not supported in a microresonator. Hence, stable soliton formation in a microresonator does not require a saturable absorber and the solitons are well described by the Lugiato-Lefever equation. This also is in perfect agreement with our experiments, which reveal the generation of stable solitons in optical microresonators.

# D Experimental methods

## D.1 Frequency comb calibrated broadband laser scan

### D.1.1 Setup and principle

Frequency comb calibrated broadband (multi-THz) laser scans<sup>84</sup> are a powerful tool to combine the broadband tuning characteristics of diode lasers and the frequency accuracy of an mode-locked fiber laser comb. In this work frequency comb calibrated laser scans are used for measuring resonator dispersion and for performing the frequency reconstruction of microresonator based combs.

First, it is described how the diode laser scan is calibrated. The experimental setup is shown in Figure D.1. The diode laser light is split into two calibration beams: The

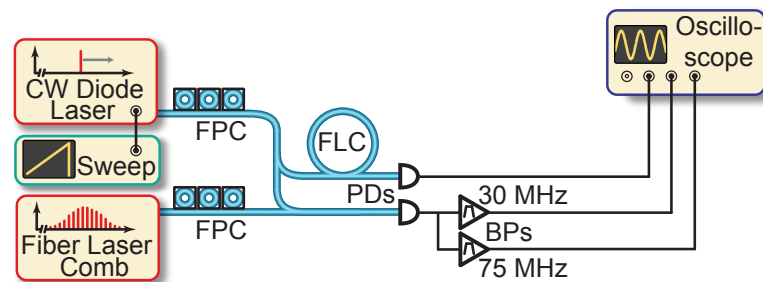


**Figure D.1: Setup for frequency comb calibrated laser scans.** A cw diode laser performs a voltage controlled scan over a multi-THz bandwidth. A fiber loop cavity (FLC) and a fiber laser comb are used to provide a frequency calibration for the laser scan. FPC: Fiber polarization controller; PD: photodetector; BP: Bandpass filter.

**first beam** is combined with the spectrum of a conventional (commercial) mode-locked fiber laser comb (repetition rate  $f_{\text{rep}} = 250$  MHz, see Figure 1.1a for a typical spectrum) resulting in a heterodyne beatnote between the fiber laser comb and the scanning diode laser. Here, we only consider the lowest frequency beatnote  $\leq 125$  MHz

corresponding to the frequency distance between diode laser and nearest comb line. As illustrated in Figure D.2a the heterodyne beatnote (detected by a photodetector) linearly ramps back and forth between zero and  $f_{\text{rep}}/2 = 125$  MHz. Two RF bandpass filters at frequencies 30 MHz and 75 MHz (bandwidth 1 MHz) are used to filter the beatnote signal. This results in electronic marker signals, whenever the scanning diode laser is reaching a frequency that is 30 MHz or 75 MHz above or below the nearest comb line frequency (cf. Figure D.2b). The two electronic marker signals resulting from the filtering at 30 MHz and 75 MHz are recorded simultaneously on separate channels of an oscilloscope (10 million sampling points, peak detect mode). A schematic example of the recorded marker signals as a function of scan time is shown in Figure D.2c. The frequency calibration of the laser scan, that is mapping the time in the scan onto a relative laser frequency detuning is done in a post-processing step. The characteristic pattern of the four electronic markers around each comb line allows to assign a relative detuning to all recorded markers. Interpolating this detuning between adjacent markers allows to assign a relative laser detuning to all times during the scan.

The **second beam** is coupled to a fiber-loop cavity (FLC) with a FSR of  $\sim 10$  MHz and the transmission is recorded simultaneously on another oscilloscope channel. The FLC transmission signal creates a fine ruler of transmission dips that can further increase the accuracy of the laser scan - in particular, when the laser scan velocity is changing between two comb line markers. Note that the signal is inverted to yield peaks instead of dips in the recorded trace. The FSR of the FLC is subject to dispersion and slightly changing over the bandwidth of the laser scan. It can be locally calibrated using the frequency comb markers. A typical calibration data set is shown in Figure D.3. The scan bandwidth is limited by the diode laser range on one side, and by the spectral span of the fiber-laser comb on the other. More than 10000 electronic markers and more than 70000 FLC resonances are recorded in a single scan.

### D.1.2 Data post-processing

First, a peak-detection algorithm is used to find the positions of the comb calibration markers and FLC resonances as illustrated in Figure D.3b and Figure D.3c. The algorithm assumes a minimal separation between adjacent peaks. The detected horizontal peak position is refined by using the mean position of the rising and falling edge at half maximum height.

Second, the consistency of the detected markers is checked. Any deviation from the regular pattern (... , 75 MHz marker, 30 MHz marker, 30 MHz marker, 75 MHz marker, ...) indicates an deviation from a steady and monotonic laser scan (cf. Figure D.4a). It can in addition be tested, whether the number of FLC resonances between two comb

## D.1. Frequency comb calibrated broadband laser scan

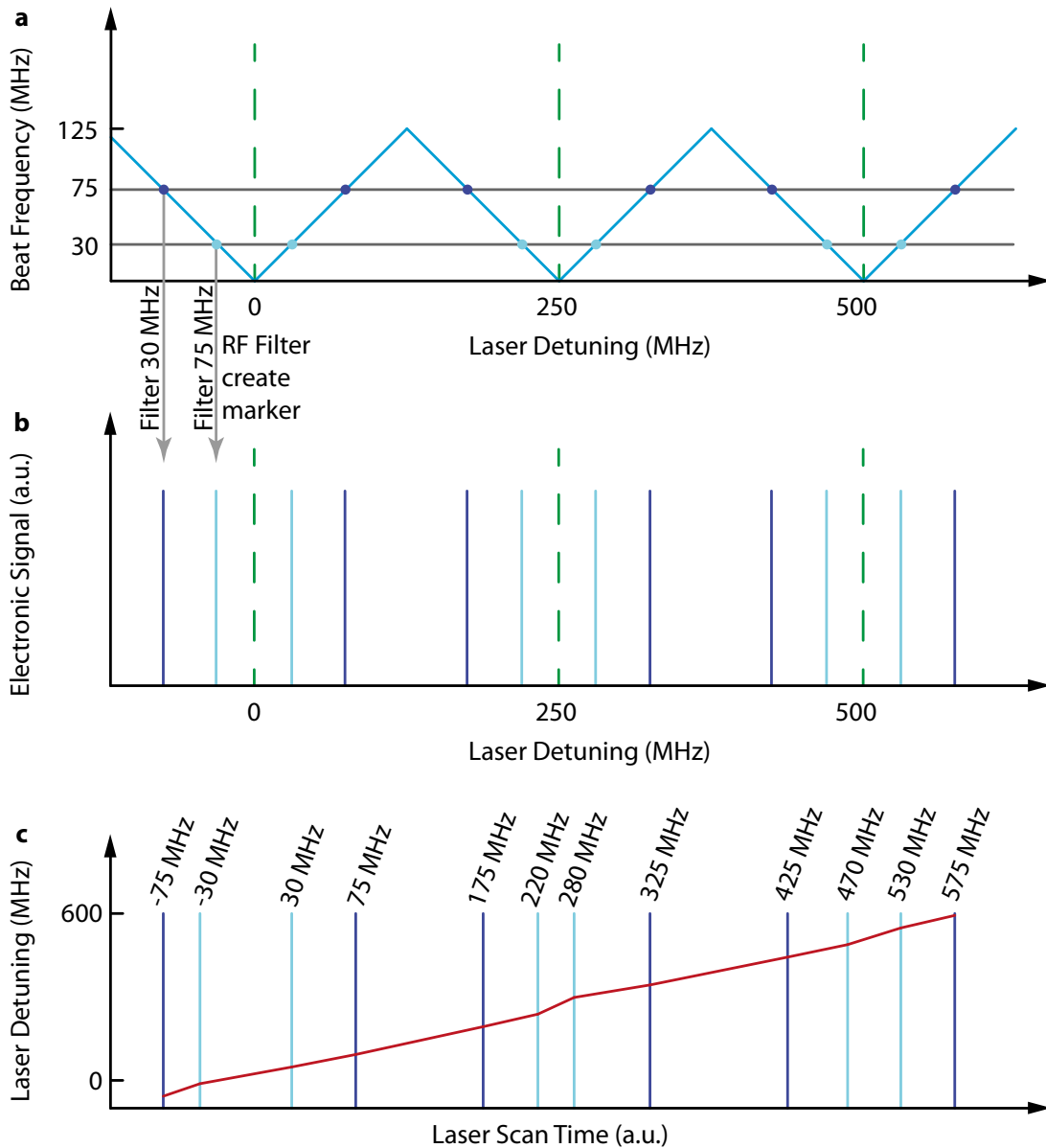


**Figure D.2: Frequency calibration using a frequency comb.** **a.** Heterodyne beatnote frequency (light blue) between diode laser and nearest comb line (dashed green). **b.** The detected and electronically bandpass filtered (at 30 MHz and 75 MHz) heterodyne beatnote yields electronic calibration marker when the laser is frequency offset from a comb line by either 30 MHz or 75 MHz. **c.** Illustration of a typical data set where calibration markers are recorded as a function of scan time. The characteristic pattern of the markers allows to determine their relative laser detuning frequency (labels). Interpolation results in frequency calibration for all any point in time during the scan (red curve).

## Appendix D. Experimental methods

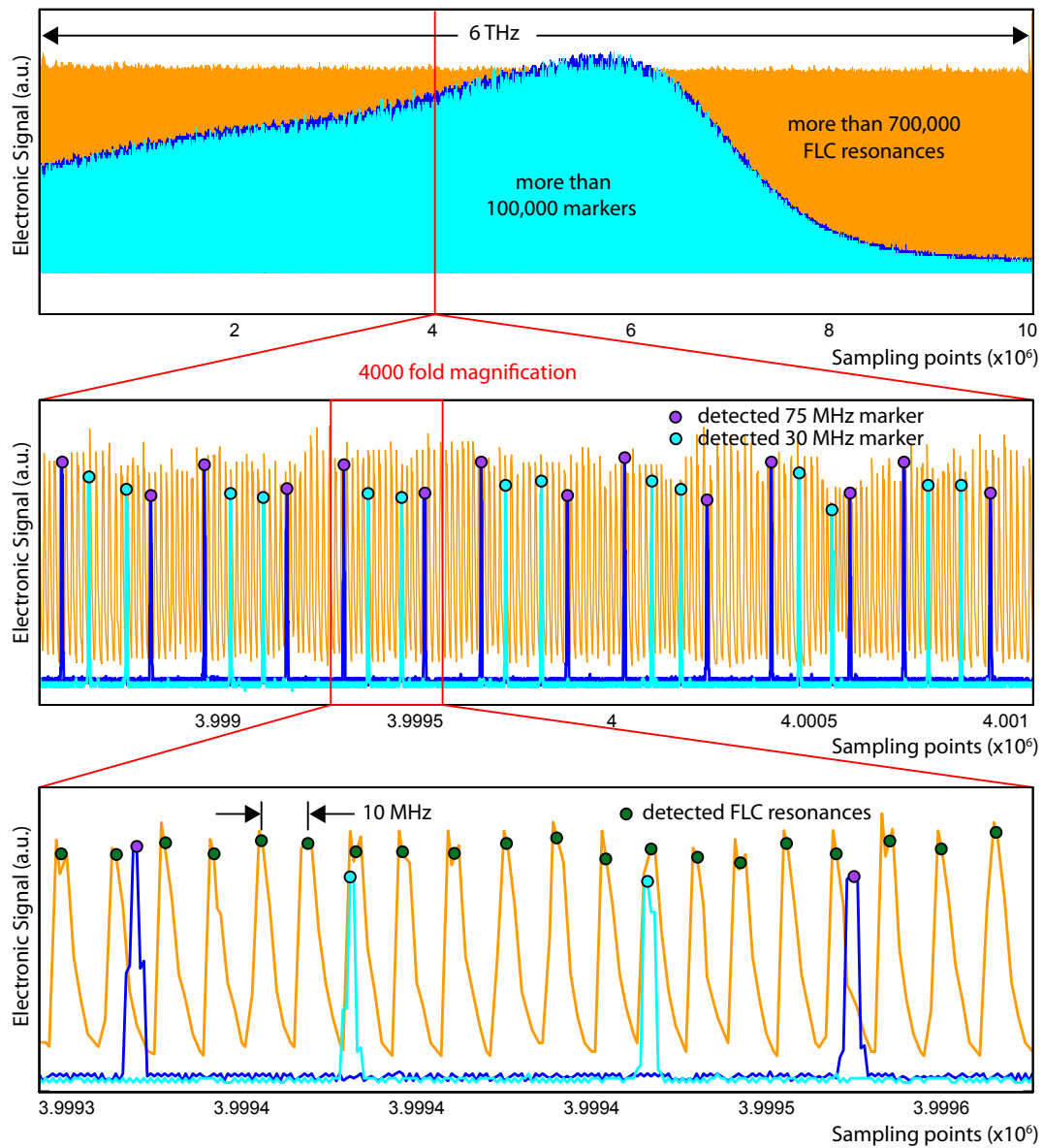


**Figure D.3: Experimental calibration data.** The data comprise two types of comb line markers resulting from the bandpass filtering at 30 MHz (light blue) and 75 MHz (dark blue), as well as, the fiber loop cavity (FLC) transmission (inverted, resonances are peaks). The colored dots mark the automatically detected peaks, which serve as a basis for the frequency calibration.



markers is consistent with the FSR of the FLC (cf. Figure D.4b).

Third, a relative laser detuning is assigned to all markers and via interpolation to all sampling points (corresponding to the time in the scan). The accuracy can be further increased by employing the finer FLC grid.

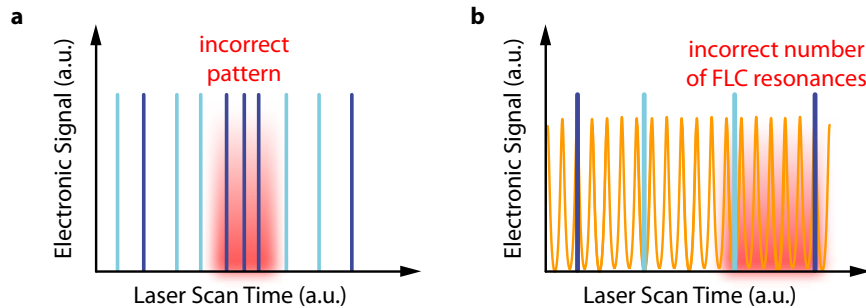


**Figure D.4: Scan error detection.** (same colorcode as in Figure D.3) **a.** Inconsistency in the marker pattern indicating an unsteady or not monotonic laser scan. **b.** The locally calibrated FSR of the fiber loop cavity (FLC) allows a consistency check between comb line markers and may reveal otherwise undetected scan errors on much finer scale than in (a).

### D.1.3 Limitation of the method

In principle the described method allow for sub-MHz resolution over a scan bandwidth of several THz. In broadband scans the precision of the method is limited by the number of available sampling points (note: the peak detect mode reduces the effective number of sampling point by a factor of two) and frequency jitter of the diode laser. The combined effect can be estimated when determining the FSR of the FLC based on individual adjacent peaks of the FLC transmission trace as shown in Figure D.5. A frequency jitter of several MHz is observable. The exact value depends on the diode laser head parameters, namely, temperature and current as well as scan parameters such as wavelength range and scan speed. In terms of spectral scan bandwidth the method is limited by the mode-hop free tuning range of the laser and the spectral coverage of the underlying fiber laser calibration comb.

### D.1.4 Measurement of resonator dispersion and comb reconstruction

#### Measurement of resonator dispersion

For dispersion measurement (requiring knowledge of the relative frequencies of the microcavity resonances) another fraction of the scanning diode laser is used to probe

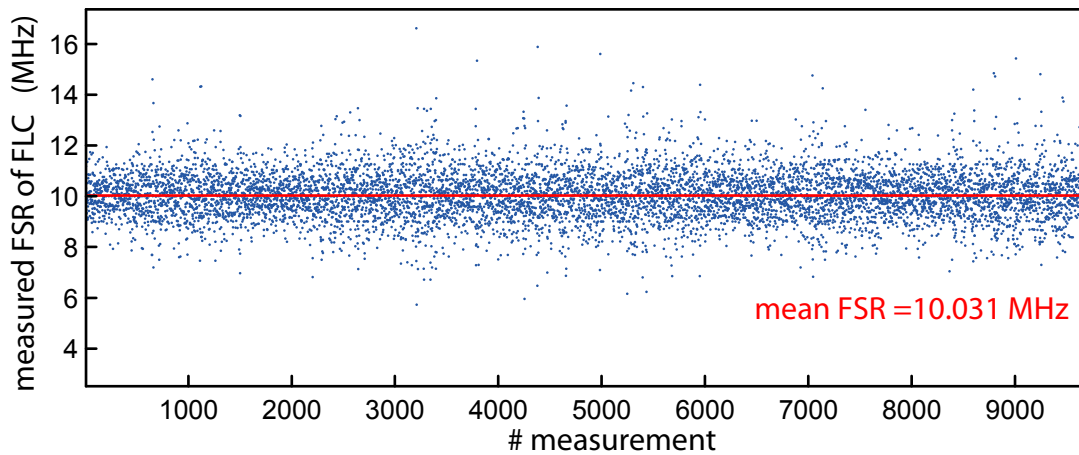


**Figure D.5: Free spectral range of the Fiber loop cavity.** Using only the frequency comb markers as a calibration the difference between adjacent fiber loop cavity (FLC) resonances is determined for approximately 10000 resonances in the central area of the scan. The local FSR is 10.031 MHz. The individual measurements show a few MHz scatter around the mean value which is mainly due to frequency jitter in the scanning diode laser and the limited number of sampling points.

the transmission of the microresonator. The transmission signal is recorded simultaneously with the calibration data during a laser scan on a separate channel of the oscilloscope. The resonances of the microresonator, similar to the FLC resonances, are detected by peak search algorithm and, owing to the calibrated laser scan, assigned a relative frequency. Due to non-linear resonance shifts it is important to only send a minimum required power to the microresonator.

#### Reconstruction of microresonator based combs

In a reconstruction experiment another fraction of the scanning diode laser light is combined with the generated Kerr-comb spectrum. As for the frequency calibration, a heterodyne beatnote is generated and filtered to generate a Kerr-comb line marker. Here, instead of two filters, a single filter is sufficient. A convenient choice is a 1.9 MHz low pass filter creating an electronic signal whenever the laser is within 1.9 MHz of a microresonator comb line.

The Kerr-comb marker signal is recorded simultaneously with the calibration data during a laser scan on a separate channel of the oscilloscope. An example of a typical data set is shown in Figure 2.15a.

## D.2 Measurement of microcavity resonance width

The linewidth of a high-Q optical resonator can be measured by imposing modulation sidebands onto a laser that is scanning over the resonance. Three copies of the Lorentzian-shaped resonance are observed. The separation of the resonances in the scan corresponds to the modulation frequency, which yields a robust self-calibration, that allows to determine the resonance width. To avoid nonlinear resonance shifts it is important to perform the measurement at low power. Moreover, the scan parameters need to be chosen such that a constant scan velocity (in terms of optical frequency) is guaranteed over a sufficiently wide frequency window. Figure D.6 illustrates this method.

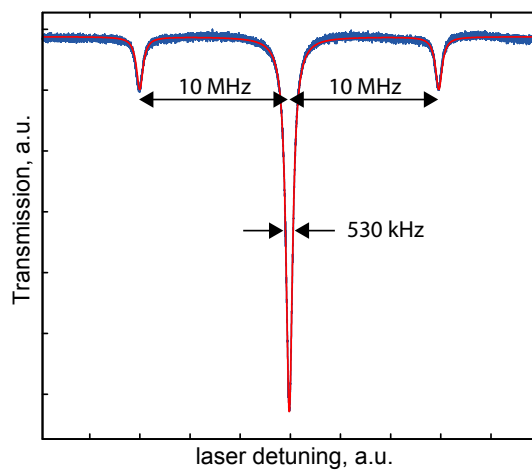


**Figure D.6: Measurement of a microcavity resonance width.** A phase modulated laser is scanned over a cavity resonance yielding the blue trace. The two smaller replica of the resonance are separated from the the main resonance by a distance corresponding to the modulation frequency (here: 10 MHz). The modulation sidebands provide the frequency calibration to determine the full-width at half maximum of the resonance (here: 530 kHz). The red line shows a triple-Lorentzian fit used for data analysis.



## Bibliography

- <sup>1</sup> Herr, T. *et al.* Temporal solitons in optical microresonators. *arXiv* **1211.0733** (2012).
- <sup>2</sup> Wang, C. *et al.* Mid-infrared optical frequency combs at 2.5  $\mu\text{m}$  based on crystalline microresonators. *Nature Communications* **4**, 1345 (2013).
- <sup>3</sup> Herr, T. *et al.* Universal formation dynamics and noise of Kerr-frequency combs in microresonators. *Nature Photonics* **6**, 480–487 (2012).
- <sup>4</sup> Riemensberger, J. *et al.* Dispersion engineering of thick high-Q silicon nitride ring-resonators via atomic layer deposition. *Optics Express* **20**, 770–776 (2012).
- <sup>5</sup> Del’Haye, P. *et al.* Octave spanning tunable frequency comb from a microresonator. *Physical Review Letters* **107**, 063901 (2011).
- <sup>6</sup> Holzwarth, R. *et al.* Optical frequency synthesizer for precision spectroscopy. *Physical Review Letters* **85**, 2264–2267 (2000).
- <sup>7</sup> Jones, D. J. *et al.* Carrier-envelope phase control of femtosecond mode-locked lasers and direct optical frequency synthesis. *Science* **288**, 635–639 (2000).
- <sup>8</sup> Diddams, S. A. *et al.* Direct link between microwave and optical frequencies with a 300 THz femtosecond laser comb. *Physical Review Letters* **84**, 5102–5105 (2000).
- <sup>9</sup> Udem, T., Holzwarth, R. & Hänsch, T. W. Optical frequency metrology. *Nature* **416**, 233–237 (2002).
- <sup>10</sup> Cundiff, S. T. & Ye, J. Colloquium: Femtosecond optical frequency combs. *Reviews of Modern Physics* **75**, 325–342 (2003).
- <sup>11</sup> Ye, J. & Cundiff, S. T. *Femtosecond Optical Frequency Comb: Principle, Operation and Applications* (Springer, 2005).
- <sup>12</sup> Telle, H. R. *et al.* Carrier-envelope offset phase control: A novel concept for absolute optical frequency measurement and ultrashort pulse generation. *Applied Physics B* **69**, 327–332 (1999).

## Bibliography

---

- <sup>13</sup> Diddams, S. A. *et al.* An optical clock based on a single trapped  $^{199}\text{Hg}^+$  ion. *Science* **293**, 825–828 (2001).
- <sup>14</sup> Holzwarth, R., Zimmermann, M., Udem, T. & Hänsch, T. W. Optical Clockworks and the Measurement of Laser Frequencies With a Mode-Locked Frequency Comb. *IEEE Journal of Quantum Electronics* **37**, 1493–1501 (2001).
- <sup>15</sup> Campbell, C. J. *et al.* Single-Ion Nuclear Clock for Metrology at the 19th Decimal Place. *Physical Review Letters* **108**, 120802 (2012).
- <sup>16</sup> Diddams, S. a., Bergquist, J. C., Jefferts, S. R. & Oates, C. W. Standards of time and frequency at the outset of the 21st century. *Science* **306**, 1318–1324 (2004).
- <sup>17</sup> Salumbides, E. *et al.* Improved Laboratory Values of the H2 Lyman and Werner Lines for Constraining Time Variation of the Proton-to-Electron Mass Ratio. *Physical Review Letters* **101**, 223001 (2008).
- <sup>18</sup> Kolachevsky, N. *et al.* Testing the Stability of the Fine Structure Constant in the Laboratory. *Space Science Reviews* **148**, 267–288 (2009).
- <sup>19</sup> van Rooij, R. *et al.* Frequency Metrology in Quantum Degenerate Helium: Direct Measurement of the  $2\ 3S1 \rightarrow 2\ 1S0$  Transition. *Science* **333**, 196–198 (2011).
- <sup>20</sup> Murphy, M. T. *et al.* High-precision wavelength calibration of astronomical spectrographs with laser frequency combs. *Monthly Notices Of The Royal Astronomical Society* **380**, 839–847 (2007).
- <sup>21</sup> Steinmetz, T. *et al.* Laser Frequency Combs for Astronomical Observations. *Science* **321**, 1335–1337 (2008).
- <sup>22</sup> Li, C.-H. *et al.* A laser frequency comb that enables radial velocity measurements with a precision of 1 cm/s. *Nature* **452**, 610–612 (2008).
- <sup>23</sup> Braje, D. A., Kirchner, M. S., Osterman, S., Fortier, T. & Diddams, S. A. Astronomical spectrograph calibration with broad-spectrum frequency combs. *The European Physical Journal D* **48**, 57–66 (2008).
- <sup>24</sup> Keilmann, F., Gohle, C. & Holzwarth, R. Time-domain mid-infrared frequency-comb spectrometer. *Optics Letters* **29**, 1542–1544 (2004).
- <sup>25</sup> Diddams, S. A., Hollberg, L. & Mbele, V. Molecular fingerprinting with the resolved modes of a femtosecond laser frequency comb. *Nature* **445**, 627–630 (2007).
- <sup>26</sup> Stowe, M. C. *et al.* Direct frequency comb spectroscopy. *Advances in atomic molecular and optical physics* **55**, 2–60 (2008).
- <sup>27</sup> Mandon, J., Guelachvili, G. & Picque, N. Fourier transform spectroscopy with a laser frequency comb. *Nature Photonics* **3**, 99–102 (2009).

- <sup>28</sup> Adler, F., Thorpe, M. J., Cossel, K. C. & Ye, J. Cavity-Enhanced Direct Frequency Comb Spectroscopy: Technology and Applications. *ANNUAL REVIEW OF ANALYTICAL CHEMISTRY* **3**, 175–205 (2010).
- <sup>29</sup> Bernhardt, B. *et al.* Cavity-enhanced dual-comb spectroscopy. *Nature Photonics* **4**, 55–57 (2010).
- <sup>30</sup> Cingöz, A. *et al.* Direct frequency comb spectroscopy in the extreme ultraviolet. *Nature* **482**, 68–71 (2012).
- <sup>31</sup> Witte, S., Zinkstok, R. T., Ubachs, W., Hogervorst, W. & Eikema, K. S. E. Deep-ultraviolet quantum interference metrology with ultrashort laser pulses. *Science* **307**, 400–403 (2005).
- <sup>32</sup> Gohle, C. *et al.* A frequency comb in the extreme ultraviolet. *Nature* **436**, 234–237 (2005).
- <sup>33</sup> Jones, J. R., Moll, K. D., Thorpe, M. J. & Ye, J. Phase-Coherent Frequency Combs in the Vacuum Ultraviolet via High-Harmonic Generation inside a Femtosecond Enhancement Cavity. *Physical Review Letters* **94**, 193201 (2005).
- <sup>34</sup> Kandula, D. Z., Gohle, C., Pinkert, T. J., Ubachs, W. & Eikema, K. S. E. Extreme Ultraviolet Frequency Comb Metrology. *Physical Review Letters* **105**, 063001 (2010).
- <sup>35</sup> Schliesser, A., Brehm, M., Keilmann, F. & van der Weide, D. W. Frequency-comb infrared spectrometer for rapid, remote chemical sensing. *Optics Express* **13**, 9029–9038 (2005).
- <sup>36</sup> Coddington, I., Swann, W. C., Nenadovic, L. & Newbury, N. R. Rapid and precise absolute distance measurements. *Nature Photonics* **3**, 351–356 (2009).
- <sup>37</sup> Hillerkuss, D. *et al.* 26 Tbit/s line-rate super-channel transmission utilizing all-optical fast Fourier transform processing. *Nature Photonics* **5**, 364–371 (2011).
- <sup>38</sup> McFerran, J., Ivanov, E. & Bartels, A. Low-noise synthesis of microwave signals from an optical source. *Electronics Letters* **41**, 650–651 (2005).
- <sup>39</sup> Steinmeyer, G., Sutter, D. H., Gallmann, L., Matuschek, N. & Keller, U. Frontiers in Ultrashort Pulse Generation: Pushing the Limits in Linear and Nonlinear Optics. *Science* **286**, 1507–1512 (1999).
- <sup>40</sup> Cundiff, S. T. Phase stabilization of ultrashort optical pulses. *Journal of Physics D* **35**, R43–R59 (2002).
- <sup>41</sup> Keller, U. Recent developments in compact ultrafast lasers. *Nature* **424**, 831–838 (2003).

## Bibliography

---

- <sup>42</sup> Zewail, A. H. Laser Femtochemistry. *Science* **242**, 1645–1653 (1988).
- <sup>43</sup> Loesel, F. H. *et al.* Ultraprecise medical applications with ultrafast lasers: corneal surgery with femtosecond lasers. In Altshuler, G. B. *et al.* (eds.) *Society of Photo-Optical Instrumentation Engineers (SPIE) Conference Series*, vol. 3564 of *Society of Photo-Optical Instrumentation Engineers (SPIE) Conference Series*, 86–93 (1999).
- <sup>44</sup> Weiner, A. M. Ultrafast optical pulse shaping: A tutorial review. *Optics Communications* **284**, 3669–3692 (2011).
- <sup>45</sup> Haus, H. A. Mode-locking of lasers. *IEEE Journal of Quantum Electronics* **6**, 1173–1185 (2000).
- <sup>46</sup> Demaria, A. J., Stetser, D. A. & Heynau, H. Self Mode-Locking of Lasers with Saturable Absorbers. *Applied Physics Letters* **8**, 174–176 (1966).
- <sup>47</sup> Garside, B. K. & Lim, T. K. Laser mode locking using saturable absorbers. *Journal of Applied Physics* **44**, 2335–2342 (1973).
- <sup>48</sup> Brabec, T., Spielmann, C., Curley, P. F. & Krausz, F. Kerr lens mode locking. *Optics Letters* **17**, 1292–1294 (1992).
- <sup>49</sup> Kärtner, F. X. & Keller, U. Stabilization of solitonlike pulses with a slow saturable absorber. *Optics Letters* **20**, 16–18 (1995).
- <sup>50</sup> Keller, U. *et al.* Semiconductor saturable absorber mirrors (SESAM's) for femtosecond to nanosecond pulse generation in solid-state lasers. *IEEE Journal Of Selected Topics In Quantum Electronics* **2**, 435–453 (1996).
- <sup>51</sup> Kärtner, F. X., der Au, J. A. & Keller, U. Mode-locking with slow and fast saturable absorbers-what's the difference? *Selected Topics in Quantum Electronics, IEEE Journal of* **4**, 159–168 (1998).
- <sup>52</sup> Proctor, J. & Kutz, J. N. Nonlinear mode-coupling for passive mode-locking: application of waveguide arrays, dual-core fibers, and/or fiber arrays. *Optics Express* **13**, 8933–8950 (2005).
- <sup>53</sup> Rauschenberger, J., Fortier, T. M., Jones, D. J., Ye, J. & Cundiff, S. T. Control of the frequency comb from a mode-locked Erbium-doped fiber laser. *Optics Express* **10**, 1404–1410 (2002).
- <sup>54</sup> Washburn, B. R. *et al.* Fiber-laser-based frequency comb with a tunable repetition rate. *Optics Express* **12**, 4999–5004 (2004).
- <sup>55</sup> Washburn, B. R. *et al.* Phase-locked, erbium-fiber-laser-based frequency comb in the near infrared. *Optics Letters* **29**, 250–252 (2004).



- <sup>56</sup> Schibli, T. R. *et al.* Frequency metrology with a turnkey all-fiber system. *Optics Letters* **29**, 2467–2469 (2004).
- <sup>57</sup> Ranka, J. K., Windeler, R. S. & Stentz, a. J. Visible continuum generation in air-silica microstructure optical fibers with anomalous dispersion at 800 nm. *Optics Letters* **25**, 25–27 (2000).
- <sup>58</sup> Dudley, J. M. & Coen, S. Supercontinuum generation in photonic crystal fiber. *Reviews of Modern Physics* **78**, 1135–1184 (2006).
- <sup>59</sup> Dudley, J. M. & Taylor, J. R. Ten years of nonlinear optics in photonic crystal fibre. *Nature Photonics* **3**, 85–90 (2009).
- <sup>60</sup> Vahala, K. J. Optical microcavities. *Nature* **424**, 839–846 (2003).
- <sup>61</sup> Braginsky, V. B., Gorodetsky, M. L. & Ilchenko, V. S. Quality-factor and nonlinear properties of optical whispering-gallery modes. *Physics Letters A* **137**, 393–397 (1989).
- <sup>62</sup> Gorodetsky, M. & Fomin, A. E. Geometrical theory of whispering-gallery modes. *IEEE Journal of Selected Topics in Quantum Electronics* **12**, 33–39 (2006).
- <sup>63</sup> Matsko, A. B. & Ilchenko, V. S. Optical Resonators With Whispering-Gallery Modes - Part I: Basics. *IEEE Journal of Selected Topics in Quantum Electronics* **12**, 3–14 (2006).
- <sup>64</sup> Grudinin, I. *et al.* Ultra high Q crystalline microcavities. *Optics Communications* **265**, 33–38 (2006).
- <sup>65</sup> Little, B., Chu, S., Haus, H., Foresi, J. & Laine, J.-P. Microring resonator channel dropping filters. *Journal of Lightwave Technology* **15**, 998–1005 (1997).
- <sup>66</sup> Barwicz, T. *et al.* Microring-resonator-based add-drop filters in SiN: fabrication and analysis. *Optics Express* **12**, 1437–1442 (2004).
- <sup>67</sup> Gondarenko, A., Levy, J. S. & Lipson, M. High confinement micron-scale silicon nitride high Q ring resonator. *Optics Express* **17**, 11366–11370 (2009).
- <sup>68</sup> Savchenkov, A. A. *et al.* Low threshold optical oscillations in a whispering gallery mode CaF<sub>2</sub> resonator. *Physical Review Letters* **93**, 243905 (2004).
- <sup>69</sup> Hofer, J., Schliesser, A. & Kippenberg, T. J. J. Cavity optomechanics with ultrahigh-Q crystalline microresonators. *Physical Reveiw A* **82**, 31804 (2010).
- <sup>70</sup> Armani, D. K., Kippenberg, T. J., Spillane, S. M. & Vahala, K. J. Ultra-high-Q toroid microcavity on a chip. *Nature* **421**, 925–928 (2003).

## Bibliography

---

- <sup>71</sup> Kippenberg, T. J., Spillane, S. M. & Vahala, K. J. Kerr-nonlinearity optical parametric oscillation in an ultrahigh-Q toroid microcavity. *Physical Review Letters* **93**, 83904 (2004).
- <sup>72</sup> Del'Haye, P. *et al.* Optical frequency comb generation from a monolithic microresonator. *Nature* **450**, 1214–1217 (2007).
- <sup>73</sup> Razzari, L. *et al.* CMOS-compatible integrated optical hyper-parametric oscillator. *Nature Photonics* **4**, 41–45 (2010).
- <sup>74</sup> Levy, J. S. *et al.* CMOS-compatible multiple-wavelength oscillator for on-chip optical interconnects. *Nature Photonics* **4**, 37–40 (2010).
- <sup>75</sup> Foster, M. A. *et al.* Silicon-based monolithic optical frequency comb source. *Optics Express* **19**, 14233–14239 (2011).
- <sup>76</sup> Braje, D., Hollberg, L. & Diddams, S. Brillouin-Enhanced Hyperparametric Generation of an Optical Frequency Comb in a Monolithic Highly Nonlinear Fiber Cavity Pumped by a cw Laser. *Physical Review Letters* **102**, 193902 (2009).
- <sup>77</sup> Agha, I. H., Okawach, Y., Foster, M. A., Sharping, J. E. & Gaeta, A. L. Four-wave-mixing parametric oscillations in dispersion-compensated high-Q silica microspheres. *Physical Review A* **76**, 43837 (2007).
- <sup>78</sup> Johnson, A. R. *et al.* Chip-based frequency combs with sub-100 GHz repetition rates. *Optics Letters* **37**, 875–877 (2012).
- <sup>79</sup> Papp, S., Del'Haye, P. & Diddams, S. Mechanical control of a microrod-resonator optical frequency comb. *Physical Review X* **3**, 031003 (2013). 1205.4272.
- <sup>80</sup> Grudinin, I. S., Baumgartel, L. & Yu, N. Frequency comb from a microresonator with engineered spectrum. *Optics Express* **20**, 6604–6609 (2012).
- <sup>81</sup> Lee, H. *et al.* Chemically etched ultrahigh-Q wedge-resonator on a silicon chip. *Nature Photonics* **6**, 369–373 (2012).
- <sup>82</sup> Spillane, S. M., Kippenberg, T. J. & Vahala, K. J. Ultralow-threshold Raman laser using a spherical dielectric microcavity. *Nature* **415**, 621–623 (2002).
- <sup>83</sup> Ilchenko, V. S., Savchenkov, A. A., Matsko, A. B. & Maleki, L. Dispersion compensation in whispering-gallery modes. *Journal of the Optical Society of America A* **20**, 157–162 (2003).
- <sup>84</sup> Del'Haye, P., Arciezt, O., Gorodetsky, M. L., Holzwarth, R. & Kippenberg, T. J. Frequency comb assisted diode laser spectroscopy for measurement of microcavity dispersion. *Nature Photonics* 529–533 (2009).

- <sup>85</sup> Savchenkov, A. A. *et al.* Kerr combs with selectable central frequency. *Nature Photonics* **5**, 293–296 (2011).
- <sup>86</sup> Del’Haye, P. *Optical Frequency Comb Generation in Monolithic Microresonators*. Ph.D. thesis, Ludwig-Maximilians-Universität München (2011).
- <sup>87</sup> Knight, J. C., Cheung, G., Jacques, F. & Birks, T. A. Phase-matched excitation of whispering-gallery-mode resonances by a fiber taper. *Optics Letters* **22**, 1129–1131 (1997).
- <sup>88</sup> Savchenkov, A. A., Ilchenko, V. S., Matsko, A. B. & Maleki, L. Kilohertz optical resonances in dielectric crystal cavities. *Physical Review A* **70**, 51804 (2004).
- <sup>89</sup> Savchenkov, A. A., Matsko, A. B., Ilchenko, V. S. & Maleki, L. Optical resonators with ten million finesse. *Optics Express* **15**, 6768 (2007).
- <sup>90</sup> Savchenkov, A. A. *et al.* Tunable optical frequency comb with a crystalline whispering gallery mode resonator. *Physical Review Letters* **101**, 93902 (2008).
- <sup>91</sup> Herr, T. *et al.* Frequency comb generation in crystalline MgF<sub>2</sub> whispering-gallery mode resonators. *CLEO conference QTuF1* (2011).
- <sup>92</sup> Liang, W. *et al.* Generation of near-infrared frequency combs from a MgF<sub>2</sub> whispering gallery mode resonator. *Optics Letters* **36**, 2290–2292 (2011).
- <sup>93</sup> Gorodetsky, M. L. & Ilchenko, V. S. High-Q optical whispering-gallery microresonators: precession approach for spherical mode analysis and emission patterns with prism couplers. *Optics Communications* **113**, 133–143 (1994).
- <sup>94</sup> Gorodetsky, M. L. & Ilchenko, V. S. Optical microsphere resonators: optimal coupling to high-Q whispering-gallery modes. *Journal of the Optical Society of America B* **16**, 147–154 (1999).
- <sup>95</sup> Almeida, V. R., Panepucci, R. R. & Lipson, M. Nanotaper for compact mode conversion. *Optics Letters* **28**, 1302–1304 (2003).
- <sup>96</sup> Kuwahara, H., Sasaki, M. & Tokoyo, N. Efficient coupling from semiconductor lasers into single-mode fibers with tapered hemispherical ends. *Applied Optics* **19**, 2578–2583 (1980).
- <sup>97</sup> Ferdous, F. *et al.* Spectral line-by-line pulse shaping of on-chip microresonator frequency combs. *Nature Photonics* **5**, 770–776 (2011).
- <sup>98</sup> Weber, M. J. *Handbook of Optical Materials* (CRC Press, Boca Raton, 2003).
- <sup>99</sup> Corning. Magnesium Fluoride MgF<sub>2</sub> Physical and Chemical Properties (2003).

## Bibliography

---

- <sup>100</sup> Milam, D., Weber, M. J. & Glass, A. J. Nonlinear Refractive-index of Fluoride-crystals. *Applied Physics Letters* **31**, 822–825 (1977).
- <sup>101</sup> Retajczyk, T. & Sinha, A. Elastic stiffness and thermal expansion coefficients of various refractory silicides and silicon nitride films. *Thin Solid Films* **70**, 241–247 (1980).
- <sup>102</sup> Hryciw, A. C., Kekatpure, R. D., Yerci, S., Dal Negro, L. & Brongersma, M. L. Thermo-optic tuning of erbium-doped amorphous silicon nitride microdisk resonators. *Applied Physics Letters* **98**, 041102 (2011).
- <sup>103</sup> Kippenberg, T. J., Holzwarth, R. & Diddams, S. A. Microresonator-based optical frequency combs. *Science* **332**, 555 (2011).
- <sup>104</sup> Ilchenko, V. S., Savchenkov, A. A., Matsko, A. B. & Maleki, L. Nonlinear Optics and Crystalline Whispering Gallery Mode Cavities. *Physical Review Letters* **92**, 43903 (2004).
- <sup>105</sup> Savchenkov, A. A., Matsko, A. B., Mohageg, M., Strekalov, D. V. & Maleki, L. Parametric oscillations in a whispering gallery resonator. *Optics Letters* **32**, 157–159 (2007).
- <sup>106</sup> Füst, J. U. *et al.* Low-Threshold Optical Parametric Oscillations in a Whispering Gallery Mode Resonator. *Physical Review Letters* **105**, 263904 (2010).
- <sup>107</sup> Kippenberg, T. J., Spillane, S. M., Armani, D. K. & Vahala, K. J. Ultralow-threshold microcavity Raman laser on a microelectronic chip. *Optics Letters* **29**, 1224–1226 (2004).
- <sup>108</sup> Grudinin, I. S. & Maleki, L. Ultralow-threshold Raman lasing with CaF<sub>2</sub> resonators. *Optics Letters* **32**, 166–168 (2007).
- <sup>109</sup> Grudinin, I. S., Matsko, A. B. & Maleki, L. Brillouin Lasing with a CaF<sub>2</sub> Whispering Gallery Mode Resonator. *Physical Review Letters* **102**, 43902 (2009).
- <sup>110</sup> Li, J., Lee, H., Chen, T. & Vahala, K. J. Characterization of a high coherence , Brillouin microcavity laser on silicon. *Optics Express* **20**, 369–373 (2012).
- <sup>111</sup> Füst, J. U. *et al.* Naturally Phase-Matched Second-Harmonic Generation in a Whispering-Gallery-Mode Resonator. *Physical Review Letters* **104**, 153901 (2010).
- <sup>112</sup> Carmon, T. & Vahala, K. J. Visible continuous emission from a silica microphotonic device by third-harmonic generation. *Nature Physics* **3**, 430–435 (2007).
- <sup>113</sup> Carmon, T., Yang, L. & Vahala, K. J. Dynamical thermal behavior and thermal selfstability of microcavities. *Optics Express* **12**, 4742–4750 (2004).

- <sup>114</sup> Fortier, T. M., Bartels, A. & Diddams, S. A. Octave-spanning Ti:sapphire laser with a repetition rate > 1 GHz for optical frequency measurements and comparisons. *Optics Letters* **31**, 1011–1013 (2006).
- <sup>115</sup> Bartels, A., Heinecke, D. & Diddams, S. A. 10-GHz Self-Referenced Optical Frequency Comb. *Science* **326**, 681 (2009).
- <sup>116</sup> Oehler, A. E., Südmeyer, T., Weingarten, K. J. & Keller, U. 100 GHz passively mode-locked Er:Yb:glass laser at 1.5  $\mu\text{m}$  with 1.6 ps pulses. *Optics Express* **16**, 21930–21935 (2008).
- <sup>117</sup> Becker, M. F., Kuizenga, D. & Siegman, A. Harmonic Mode Locking of the Nd:YAG Laser. *IEEE Journal of Quantum Electronics* **8**, 687–693 (1972).
- <sup>118</sup> Pottiez, O. *et al.* Supermode Noise of Harmonically Mode-Locked Erbium Fiber Lasers With Composite Cavity. *IEEE Journal of Quantum Electronics* **38**, 252–259 (2002).
- <sup>119</sup> Pfeifle, J. *et al.* Microresonator-Based Optical Frequency Combs for High-Bitrate WDM Data Transmission. In *Optical Fiber Communication Conference, OWIC.4* (Optical Society of America, 2012).
- <sup>120</sup> Pfeifle, J. *et al.* Coherent data transmission with microresonator Kerr frequency combs. *arXiv* **1307.1037** (2013).
- <sup>121</sup> Jiang, Z., Huang, C. B., Leaird, D. E. & Weiner, A. M. Optical arbitrary waveform processing of more than 100 spectral comb lines. *Nature Photonics* **1**, 463–467 (2007).
- <sup>122</sup> Savchenkov, A. A., Rubiola, E., Matsko, A. B., Ilchenko, V. S. & Maleki, L. Phase noise of whispering gallery photonic hyper-parametric microwave oscillators. *Optics Express* **16**, 4130–4144 (2008).
- <sup>123</sup> Del’Haye, P., Arcizet, O., Schliesser, A., Holzwarth, R. & Kippenberg, T. J. Full Stabilization of a Microresonator-Based Optical Frequency Comb. *Physical Review Letters* **101**, 53903 (2008).
- <sup>124</sup> Papp, S. B. & Diddams, S. A. Spectral and temporal characterization of a fused-quartz-microresonator optical frequency comb. *Physical Review A* **84**, 53833 (2011).
- <sup>125</sup> Del’Haye, P., Papp, S. B. & Diddams, S. a. Hybrid Electro-Optically Modulated Microcombs. *Physical Review Letters* **109**, 263901 (2012).
- <sup>126</sup> Savchenkov, A. *et al.* Miniature Optical Atomic Clock: Stabilization of a Kerr Comb Oscillator. *arXiv* **1301.3198** (2013).

## Bibliography

---

- <sup>127</sup> Saha, K. *et al.* Modelocking and Femtosecond Pulse Generation in Chip-Based Frequency Combs. *Optics Express* **21**, 1335–1343 (2013).
- <sup>128</sup> Ideguchi, T., Poisson, A., Guelachvili, G., Hänsch, T. W. & Picqué, N. Adaptive real-time dual-comb spectroscopy. *Optics Letters* **37**, 4847–4849 (2012).
- <sup>129</sup> Schiller, S. *et al.* The Space Optical Clocks Project: Development of high-performance transportable and breadboard optical clocks and advanced subsystems. *arXiv* **1206.3765** (2012).
- <sup>130</sup> Hugi, A., Villares, G., Blaser, S., Liu, H. C. & Faist, J. Mid-infrared frequency comb based on a quantum cascade laser. *Nature* **492**, 229–233 (2012).
- <sup>131</sup> Okawachi, Y. *et al.* Octave-spanning frequency comb generation in a silicon nitride chip. *Optics Letters* **36**, 3398–3400 (2011).
- <sup>132</sup> Eikema, K. S. E. Frequency combs: Liberated from material dispersion. *Nature Photonics* **5**, 258–260 (2011).
- <sup>133</sup> Saha, K. *et al.* Broadband parametric frequency comb generation with a 1  $\mu\text{m}$  pump source. *Optics Express* **20**, 26935–26941 (2012).
- <sup>134</sup> Li, J., Lee, H., Chen, T. & Vahala, K. J. Low-Pump-Power, Low-Phase-Noise, and Microwave to Millimeter-wave Repetition Rate Operation in Microcombs. *Physical Review Letters* **109**, 233901 (2012).
- <sup>135</sup> Boyd, R. W. *Nonlinear Optics* (Academic Press, 3ed., 2007).
- <sup>136</sup> Manley, J. M. & Rowe, H. E. Some General Properties of Nonlinear Elements - Part I. General Energy Relations. *Proceedings of the IRE* **44**, 904–913 (1956).
- <sup>137</sup> He, L., Xiao, Y.-f., Zhu, J., Ozdemir, S. K. & Yang, L. Oscillatory thermal dynamics in high-Q PDMS-coated silica toroidal microresonators. *Optics Express* **17**, 9571–9581 (2009).
- <sup>138</sup> Savchenkov, A. A. *et al.* Kerr frequency comb generation in overmoded resonators. *Optics Express* **20**, 27290–27298 (2012).
- <sup>139</sup> Matsko, A. B., Savchenkov, A. A. & Maleki, L. Normal group-velocity dispersion Kerr frequency comb. *Optics Letters* **37**, 43–45 (2012).
- <sup>140</sup> Tomes, M. & Carmon, T. Photonic Micro-Electromechanical Systems Vibrating at X-band (11-GHz) Rates. *Physical Review Letters* **102**, 113601 (2009).
- <sup>141</sup> Matsko, A. B., Savchenkov, A. A., Strekalov, D., Ilchenko, V. S. & Maleki, L. Optical hyperparametric oscillations in a whispering-gallery-mode resonator: Threshold and phase diffusion. *Physical Review A* **71**, 33804 (2005).

- <sup>142</sup> Chembo, Y. K. K. & Yu, N. Modal expansion approach to optical-frequency-comb generation with monolithic whispering-gallery-mode resonators. *Physical Review A* **82**, 33801 (2010).
- <sup>143</sup> Chembo, Y. K., Strekalov, D. V. & Yu, N. Spectrum and Dynamics of Optical Frequency Combs Generated with Monolithic Whispering Gallery Mode Resonators. *Physical Review Letters* **104**, 103902 (2010).
- <sup>144</sup> Chembo, Y. K. & Yu, N. On the generation of octave-spanning optical frequency combs using monolithic whispering-gallery-mode microresonators. *Optics Letters* **35**, 2696–2698 (2010).
- <sup>145</sup> Chembo, Y. K. & Menyuk, C. R. Spatiotemporal Model for Kerr Comb Generation in Whispering Gallery Mode Resonators. *Physica* **87**, 053852 (2013).
- <sup>146</sup> Matsko, A., Savchenko, A. & Maleki, L. On Excitation of Breather Solitons in an Optical Microresonator. *Optics Letters* **37**, 4856–4858 (2012).
- <sup>147</sup> Coen, S., Randle, H. G., Sylvestre, T. & Erkintalo, M. Modeling of octave-spanning Kerr frequency combs using a generalized mean-field Lugiato-Lefever model. *Optics Letters* **38**, 37–39 (2013).
- <sup>148</sup> Coen, S. & Erkintalo, M. Universal scaling laws of Kerr frequency combs. *Optics letters* **38**, 1790–2 (2013).
- <sup>149</sup> Papp, S. B., Haye, P. D. & Diddams, S. A. Parametric seeding of a microresonator optical frequency comb. *arXiv* **1305.3262** (2013).
- <sup>150</sup> Oxborrow, M. Traceable 2-D Finite-Element Simulation of the Whispering-Gallery Modes of Axisymmetric Electromagnetic Resonators. *IEEE Transactions on Microwave Theory and Techniques* **55**, 1209–1218 (2007).
- <sup>151</sup> Braginsky, V. B. B., Gorodetsky, M. L. L. & Vyatchanin, S. P. P. Thermodynamical fluctuations and photo-thermal shot noise in gravitational wave antennae. *Physics Letters A* **264**, 1–10 (1999).
- <sup>152</sup> Gorodetsky, M. L. L. & Grudinin, I. S. S. Fundamental thermal fluctuations in microspheres. *Journal of the Optical Society of America B* **21**, 697–705 (2004).
- <sup>153</sup> Matsko, A. B., Savchenko, A. A., Yu, N. & Maleki, L. Whispering-gallery-mode resonators as frequency references. I. Fundamental limitations. *Journal of the Optical Society of America B* **24**, 1324–1335 (2007).
- <sup>154</sup> Rokhsari, H. & Vahala, K. J. Observation of Kerr nonlinearity in microcavities at room temperature. *Optics Letters* **30**, 427–429 (2005).

## Bibliography

---

- <sup>155</sup> Ma, R. *et al.* Radiation-pressure-driven vibrational modes in ultrahigh-Q silica microspheres. *Optics Letters* **32**, 2200–2202 (2007).
- <sup>156</sup> Savchenkov, A. A., Matsko, A. B., Ilchenko, V. S., Seidel, D. & Maleki, L. Surface Acoustic Wave Frequency Comb. *Optics Letters* **36**, 3338–3340 (2011).
- <sup>157</sup> Fomin, A. E., Gorodetsky, M. L., Grudinin, I. S. & Ilchenko, V. S. Nonstationary nonlinear effects in optical microspheres. *Journal of the Optical Society of America B* **22**, 459–465 (2005).
- <sup>158</sup> Bahl, G., Zehnpfennig, J., Tomes, M. & Carmon, T. Stimulated optomechanical excitation of surface acoustic waves in a microdevice. *Nature Communications* **2**, 403 (2011).
- <sup>159</sup> Carmon, T. & Vahala, K. J. Modal Spectroscopy of Optoexcited Vibrations of a Micron-Scale On-Chip Resonator at Greater than 1 GHz Frequency. *Physical Review Letters* **98**, 123901 (2007).
- <sup>160</sup> Agha, I. H., Okawachi, Y. & Gaeta, A. L. Theoretical and experimental investigation of broadband cascaded four-wave mixing in high-Q microspheres. *Optics Express* **17**, 16209–16215 (2009).
- <sup>161</sup> Wang, X., Vinjanampathy, S., Strauch, F. W. & Jacobs, K. Ultraefficient Cooling of Resonators: Beating Sideband Cooling with Quantum Control. *Physical Review Letters* **107**, 177204 (2011).
- <sup>162</sup> Liang, W. *et al.* Whispering gallery mode resonator based ultra-narrow linewidth external cavity semiconductor lasers. *Optics Letters* **35**, 2822–2824 (2010).
- <sup>163</sup> Carmon, T. *et al.* Static envelope patterns in composite resonances generated by level crossing in optical toroidal microcavities. *Physical Review Letters* **100**, 103905 (2008).
- <sup>164</sup> Thorpe, M. J., Moll, K. D., Jones, R. J., Safdi, B. & Ye, J. Broadband Cavity Ringdown Spectroscopy for Sensitive and Rapid Molecular Detection. *Science* **311**, 1595–1599 (2006).
- <sup>165</sup> Coddington, I., Swann, W. C. & Newbury, N. R. Coherent multiheterodyne spectroscopy using stabilized optical frequency combs. *Physical Review Letters* **100**, 13902 (2008).
- <sup>166</sup> Maddaloni, P., Malara, P., Gagliardi, G. & Natale, P. D. Mid-infrared fibre-based optical comb. *New Journal of Physics* **8**, 262 (2006).
- <sup>167</sup> Adler, F. *et al.* Phase-stabilized, 1.5 W frequency comb at 2.8–4.8  $\mu\text{m}$ . *Optics Letters* **34**, 1330–1332 (2009).



- <sup>168</sup> Leindecke, N., Marandi, A., Byer, R. L. & Vodopyanov, K. L. Broadband degenerate OPO for mid-infrared frequency comb generation. *Optics Express* **19**, 6296–6302 (2011).
- <sup>169</sup> Faist, J. *et al.* Quantum Cascade Laser. *Science* **264**, 553–556 (1994).
- <sup>170</sup> Wang, C. *et al.* Coherent instabilities in a semiconductor laser with fast gain recovery. *Physical Review A* **75**, 031802 (2007).
- <sup>171</sup> Wang, C. Y. *et al.* Mode-locked pulses from mid-infrared Quantum Cascade Lasers. *Optics Express* **17**, 12929–12943 (2009).
- <sup>172</sup> Oxborrow, M. How to simulate the whispering-gallery-modes of dielectric microresonators in FEMLAB/COMSOL. *Laser Resonators and Beam Control IX* **6452**, 64520J (2007).
- <sup>173</sup> Bernhardt, B. *et al.* Mid-infrared dual-comb spectroscopy with 2.4  $\mu\text{m}$  Cr:ZnSe femtosecond lasers. *Applied Physics B* **100**, 3–8 (2010).
- <sup>174</sup> Adler, F. *et al.* Mid-infrared Fourier transform spectroscopy with a broadband frequency comb. *Optics Express* **18**, 21861–21872 (2010).
- <sup>175</sup> Mägi, E. C. *et al.* Enhanced Kerr nonlinearity in sub-wavelength diameter As<sub>2</sub>Se<sub>3</sub> chalcogenide fiber tapers. *Optics Express* **15**, 2–7 (2007).
- <sup>176</sup> Thorpe, M. J. & Ye, J. Cavity-enhanced direct frequency comb spectroscopy. *Applied Physics B* **91**, 397–414 (2008).
- <sup>177</sup> Thorpe, M. J., Balslev-Clausen, D., Kirchner, M. S. & Ye, J. Cavity-enhanced optical frequency combspectroscopy: application to human breathanalysis. *Optics Express* **16**, 2387–2397 (2008).
- <sup>178</sup> Akhmediev, N. & Ankiewicz, A. *Dissipative Solitons: From Optics to Biology and Medicine* (Springer, 2008).
- <sup>179</sup> Grelu, P. & Akhmediev, N. Dissipative solitons for mode-locked lasers. *Nature Photonics* **6**, 84–92 (2012).
- <sup>180</sup> Wabnitz, S. Suppression of interactions in a phase-locked soliton optical memory. *Optics Letters* **18**, 601–603 (1993).
- <sup>181</sup> Leo, F. *et al.* Temporal cavity solitons in one-dimensional Kerr media as bits in an all-optical buffer. *Nature Photonics* **4**, 471–476 (2010).
- <sup>182</sup> Lugiato, L. A. & Lefever, R. Spatial Dissipative Structures in Passive Optical Systems. *Physical Review Letters* **21**, 2209–2211 (1987).

## Bibliography

---

- <sup>183</sup> Firth, W. J. & Weiss, C. O. Cavity and Feedback Solitons. *Optics and Photonics News* **13**, 54–58 (2002).
- <sup>184</sup> Segev, M. & Stegeman, G. Self-Trapping of Optical Beams: Spatial Solitons. *Physics Today* **51**, 42–48 (1998).
- <sup>185</sup> Ilchenko, V. S. & Gorodetsky, M. L. Thermal Nonlinear Effects in Optical Whispering Gallery Microresonators. *Laser Physics* **2**, 1004–1009 (1992).
- <sup>186</sup> Barashenkov, I. V. & Smirnov, Y. S. Existence and stability chart for the ac-driven, damped nonlinear Schrödinger solitons. *Physical Review E* **54**, 5707–5725 (1996).
- <sup>187</sup> Gasch, A., Wedding, B. & Jäger, D. Multistability and soliton modes in nonlinear microwave resonators. *Applied Physics Letters* **44**, 1105–1107 (1984).
- <sup>188</sup> Drever, R. W. P. *et al.* Laser Phase and Frequency Stabilization Using an Optical Resonator. *Applied Physics B* **31**, 97–105 (1983).
- <sup>189</sup> Maleki, L. *et al.* High performance, miniature hyper-parametric microwave photonic oscillator. In *Frequency Control Symposium (FCS), 2010 IEEE International*, 558–563 (2010).
- <sup>190</sup> Matsko, A. B., Savchenkov, A. A., Ilchenko, V. S., Seidel, D. & Maleki, L. Self-referenced stabilization of temperature of an optomechanical microresonator. *Physical Review A* **83**, 21801 (2011).
- <sup>191</sup> Matsko, A. B. *et al.* Mode-locked Kerr frequency combs. *Optics Letters* **36**, 2845–2847 (2011).
- <sup>192</sup> Dudley, J. *et al.* Complete characterization of ultrashort pulse sources at 1550 nm. *IEEE Journal of Quantum Electronics* **35**, 441–450 (1999).
- <sup>193</sup> Kane, D. J. Principal components generalized projections: a review. *Journal of the Optical Society of America B* **25**, A120–A132 (2008).
- <sup>194</sup> Salem, R. *et al.* High-speed optical sampling using a silicon-chiptemporal magnifier. *Optics Express* **17**, 4324–4329 (2009).
- <sup>195</sup> Kolner, B. H. & Nazarathy, M. Temporal imaging with a time lens. *Optics Letters* **14**, 630–632 (1989).
- <sup>196</sup> Dudley, J. M. & Coen, S. Coherence properties of supercontinuum spectra generated in photonic crystal and tapered optical fibers. *Optics Letters* **27**, 1180–1182 (2002).
- <sup>197</sup> Sun, Z. *et al.* Graphene mode-locked ultrafast laser. *ACS Nano* **4**, 803–810 (2010).

- <sup>198</sup> Gardiner, C. W. & Collett, M. J. Input and output in damped quantum systems: Quantum stochastic differential equations and the master equation. *Physical Review A* **31**, 3761–3774 (1985).
- <sup>199</sup> Zhang, T. C. *et al.* Quantum-noise of Free-running and Externally-stabilized Laser-diodes. *Quantum and Semiclassical Optics* **7**, 601–613 (1995).
- <sup>200</sup> Riehle, F. *Frequency Standards: Basics and Applications* (Wiley-VCH, 2005).
- <sup>201</sup> Landau, L. D. & Lifshitz, E. M. *Statistical Physics*. Course of Theoretical Physics (Pergamon Press, 1980), 3rd edn.
- <sup>202</sup> Kippenberg, T. J., Rokhsari, H., Carmon, T., Scherer, A. & Vahala, K. J. Analysis of radiation-pressure induced mechanical oscillation of an optical microcavity. *Physical Review Letters* **95**, 33901 (2005).
- <sup>203</sup> Kärtner, F. X., Jung, I. D. & Keller, U. Soliton mode-locking with saturable absorbers. *IEEE Journal Of Selected Topics In Quantum Electronics* **2**, 540–556 (1996).
- <sup>204</sup> Jung, I. D., Kärtner, F. X., Brovelli, L. R., Kamp, M. & Keller, U. Experimental verification of soliton mode locking using only a slow saturable absorber. *Optics Letters* **20**, 1892–1894 (1995).



**TOBIAS HERR****CURRICULUM VITAE**

---

Rue de Couvaloup 16	Citizenship:	German
1110 Morges	Email:	tobias.herr@epfl.ch
Switzerland	Phone:	+41 (0) 76 799 29 88

**EDUCATION**

---

<b>PhD in Photonics</b>	06/2010-06/2013
-------------------------	-----------------

Swiss Federal Institute of Technology Lausanne (EPFL)  
Lausanne, Switzerland and

Max-Planck Institute of Quantum Optics	05/2009-05/2010
--	-----------------

Garching, Germany

<b>Diploma in Physics</b>	10/2002-06/2008
---------------------------	-----------------

University of Heidelberg and  
Max-Planck-Institute for Nuclear Physics  
Heidelberg, Germany

<b>Academic Exchange Year</b>	08/2005-06/2006
-------------------------------	-----------------

University of Arizona  
Tucson, Arizona

<b>Abitur</b>	06/2001
---------------	---------

Gymnasium Karlsbad  
Karsbad, Germany

**PROFESSIONAL AND ACADEMIC EXPERIENCE**

---

<b>Teaching Assistant</b>	2010-2012
---------------------------	-----------

Swiss Federal Institute of Technology Lausanne (EPFL)  
Lausanne, Switzerland

<b>Research Assistant</b>	08/2008-12/2008
---------------------------	-----------------

Max-Planck-Institute for Nuclear Physics  
Heidelberg, Germany

<b>Civillian Service</b>	08/2001-05/2002
--------------------------	-----------------

Internationaler Bund  
Karlsruhe, Germany

**FELLOWSHIPS**

---

<b>German National Academic Foundation</b>	04/2003-06/2008
--	-----------------

<b>Fulbright</b>	08/2005-05/2006
------------------	-----------------